UNIVERSITY OF CALIFORNIA SAN DIEGO

Detection and Influence of Biological Aerosols in Marine and Coastal Environments

A dissertation submitted in partial satisfaction of the requirements for the degree Doctor of Philosophy

in

Chemistry

by

Brock Andrew Mitts

Committee in charge:

Professor Kimberly Prather, Chair
Professor Farooq Azam
Professor Vicki Grassian
Professor Valerie Schmidt
Professor Michael Tauber

2022

The Dissertation of Brock Andrew Mitts is approved, and it is acceptable in quality and form for publication on microfilm and electronically.

University of California San Diego

2022

DEDICATION

To my family and friends who have supported me throughout this journey.

EPIGRAPH

“The great tragedy of science – the slaying of a beautiful hypothesis by an ugly fact.”

-Thomas Henry Huxley

TABLE OF CONTENTS

LIST OF ABBREVIATIONS AND SYMBOLS

AF	asymmetry factor
AMS	aerosol mass spectrometer
APS	aerodynamic particle sizer
ATOFMS	aerosol time-of-flight mass spectrometer
A-ATOFMS	aircraft aerosol time-of-flight mass spectrometer
ART-2A	adaptive resonance theory, version 2a
A.U.	arbitrary units
α-pinene	alpha pinene
BC	black carbon
BEAST	biological effects on air sea transfer
Bioaerosols	biological aerosols
BF	Border Field
BVOC	biogenic volatile organic compound
CCN	cloud condensation nuclei
CFSR	climate forecast system reanalysis
Ch	channel
Chl A	chlorophyll a
cMA-ATOFMS	condensation matrix-assisted aerosol time-of-flight mass spectrometer
CPC	condensation particle counter
2,4-DHB	2,4-dihydroxybenzoic acid
DMA	differential mobility analyzer
DNA	deoxyribonucleic acid

DMS	dimethyl sulfide
DOC	dissolved organic carbon
DOM	dissolved organic matter
D_a	aerodynamic diameter
D_m	mobility diameter
D_{va}	vacuum aerodynamic diameter
EBC	equivalent black carbon
EC	electrostatic classifier
EEM	excitation-emission matrix
EEMs	excitation-emission matrices
EEMS	excitation-emission matrix spectroscopy
Em	emission
Ex	excitation
FA	ferulic acid
FATES	Flexible Analysis Toolkit for the Exploration of SPMS data
FCM	flow cytometry
FF	fluorescent fraction
FL1	fluorescent channel 1
FL2	fluorescent channel 2
FLEXPART	flexible particle dispersion model
guiFATES	graphical user interface of FATES
HB	heterotrophic bacteria
HEPA	high efficiency particulate air

HULIS	humic-like substance
IN	ice nuclei
INE	ice nucleating entity
INP	ice nucleating particle
KY	kynurenine
L	liters
(S)LPM	(standard) liters per minute
MALDI	matrix assisted laser desorption ionization
MART	marine aerosol reference tank
miniMART	miniature marine aerosol reference tank
MCP	microchannel plate
mDOM	marine dissolved organic matter
MeOH	methanol
MS	mass spectrometry
m/z	mass to charge ratio
NAD(P)H	nicotinamide-adenine dinucleotide (phosphate)
NCEP	United States National Centers for Environmental Prediction
Nd:YAG	Neodymium:YAG laser
NFK	N'-formyl kynurenine
N_{Fl}	number of fluorescent particles
N_{Tot}	number of total particles
n_s	ice nucleation active site density
O_3	ozone

OFR	oxidative flow reactors
OH	hydroxyl radical
PAH(s)	polycyclic aromatic hydrocarbon(s)
PAM-OFR	potential aerosol mass oxidative flow reactor
PMT(s)	photomultiplier tube(s)
RH	relative humidity
RNA	ribonucleic acid
SeaSCAPE	sea spray chemistry and particle evolution
SIO	Scripps Institution of Oceanography
SMA	secondary marine aerosol
SMPS	scanning mobility particle sizer
SPFS	single particle fluorescence spectrometer
SPMS	single particle mass spectrometer
SSA	sea spray aerosol
SSML	sea surface microlayer
TMGN	1,8-bis(tetramethylguanidino)naphthalene
UV	ultraviolet
Vis	visible
VOC	volatile organic compound
v_s	ice nucleation volume site density
WIBS	wideband integrated bioaerosol sensor
Xe1	Xenon lamp 1
Xe2	Xenon lamp 2

LIST OF FIGURES

LIST OF TABLES

ACKNOWLEDGEMENTS

First and foremost, I would like to thank Professor Kimberly Prather whose mentorship and support has allowed me to pursue incredible opportunities and investigate unique science questions. Kim has encouraged me to always think of the big picture and demonstrated, through science communication, how I can convey the relevance of my work. Kim has allowed me to work with a range of analytical instruments and taught me how to build/service these instruments, providing me with both a chemistry and an engineering experience. Her guidance has extended beyond work in the lab; she has taught me how to be a better mentor and leader in the workplace. I would also like to specifically thank Professor Grant Deane who worked with me on my first manuscript and showed me how to present my work in a peer-reviewed publication. I would like to thank my committee, Professor Vicki Grassian, Professor Michael Tauber, Professor Farooq Azam, and Professor Valerie Schmidt for their thoughtful feedback and advice as I have progressed through my graduate career.

Working in the Prather research group has been incredibly rewarding because of the enormously kind and talented graduate students, postdocs, and research scientists who assisted me in experiments and taught me new techniques. The day-to-day of graduate school was always brightened because of the network of peers. Their support with my presentations, papers, and experiment design has given me a range of skills that I will have beyond graduate school. I am grateful for the opportunity to pass these skills onto graduate students who have come after me and watch them excel in their graduate careers. For all your help and friendship, thank you to: Alexia Moore, Ke'La Kimble, Lucia Cancelada, Ben Rico, Matthew Pendergraft, Mitchell Santander, Raymond Leibensperger III, Sabrina Ufer, Sarah Amiri, Dolan Lucero, Ikran Ibrahim, Dr. Jonathan Sauer, Dr. Camille Sultana, Dr. Charlotte Beale, Dr. Christopher Lee, Dr. Daniel

Petras, Dr. Gavin Cornwell, Hashim Al-Mashat, Joseph Manson, Dr. Julie Dinasquet, Dr. Kathryn Mayer, Dr. Louise Kristensen, Dr. Olivia Ryder, Dr. Rebecca Simpson, and Dr. Xiaofei Wang. I would also like to thank the group machinist, Joe Mayer whose knowledge and expertise in instrument fabrication is unsurpassed. Joe has taught me both life skills as well as an attention to detail that is required for working with analytical instruments. I would like to thank Monica Castrejon whose kindness and support has been a shining light during my time in graduate school. She is always willing to help with a task, no matter the size, and has streamlined the logistics and coordination of graduate school.

Outside of the Prather research group, I have been fortunate enough to work with multiple researchers who have helped me through my studies and educated me on topics that were originally outside my field. Thank you to Professor Francesca Malfatti, Dr. Paul DeMott, Dr. Tom Hill, Dr. Christina McCluskey, Dr. Pedro Belda-Ferre, Dr. Allegra Aron, Dr. Daniel Crocker, Dr. Neal Arakawa, and Dr. Liora Mael.

Lastly, I would like to acknowledge all the support from my family and friends who encouraged me throughout graduate school and listened to me vent when times were tough. Thank you to my mother, Maureen, father, Daniel, and brother, Grant. You have always given me unconditional love and support whenever I needed it. Thank you to the friends I have made and kept throughout graduate school and a special thank you to Clare Morris whose support and reassurance has helped me throughout the final years of my PhD.

Chapter 2, in full, is a reprint of material as it appears in *Geophysical Research Letters*, 2021. Mitts, B. A., Wang, X., Lucero, D. D., Beall, C. M., Deane, G. B., DeMott, P. J., & Prather, K. A. (2021). “Importance of supermicron ice nucleating particles in nascent sea spray” *Geophysical Research Letters* 48, e2020GL089633. An edited version of this paper was published

by AGU. Copyright 2021 *American Geophysical Union*. The dissertation author is the primary investigator and author of this manuscript.

Chapter 3, in full, is a reprint of material with permission from *Environmental Science & Technology*, 2021. Santander, M. V., Mitts, B. A., Pendergraft, M. A., Dinasquet, J., Lee, C., Moore, A. N., Cancelada, L. B., Kimble, K. A., Malfatti, F., & Prather, K. A. (2021) "Tandem fluorescence measurements of organic matter and bacteria released in sea spray aerosols." *Environmental Science & Technology* 55 (8), 5171-5179. Copyright 2021 American Chemical Society. The dissertation author and Mitchell Santander are co-first authors of this manuscript. The dissertation author was the primary experimenter for all investigations involving the WIBS, primary analyst and figure generator for the WIBS datasets, and lead writer of sections describing the WIBS methods and results. Mitchell Santander was the primary experimenter for all investigations involving EEMS, primary analyst and figure generator for EEMS datasets, and lead writer of sections describing EEMS methods and results. The dissertation author and Mitchell Santander contributed equally to drafting the introduction, abstract, and implications sections of the manuscript and to revisions of all sections.

Chapter 4, in full, is currently being prepared for submission for publication of the material. Mitts, B. A., Santander, M. V., Ibrahim, I., Morris, C. K., Dinasquet, J., Mayer, K. J., Sauer, J. S., Lee, C., Malfatti, F. & Prather, K. A. (2022). "Single-particle fluorescence properties of oxidized sea spray aerosol." The dissertation author is the primary investigator and author of this manuscript.

Chapter 5, in full, is currently being prepared for submission for publication of the material. Mitts, B. A., Pendergraft, M. A., Morris, C. K., Belda-Ferre, P., Aron, A. T., Petras, D., & Prather, K. A. (2022). "Real-time fluorescence measurements of marine and continental aerosols in a

coastal environment." The dissertation author is the primary investigator and author of this manuscript.

Chapter 6, in full, is currently being prepared for submission for publication of the material. Kimble, K. A., Mitts, B. A., Li, L., Moore, A. M., Heilig, M., Hogan Jr., C. J., & Prather, K. A. (2022). "Optimization and application of a condensation matrix-assisted aerosol time-of-flight mass spectrometer." The dissertation author and Ke'La Kimble are co-first authors of this manuscript. The dissertation author contributed to experimental design and setup, designed and generated Figure 6.2, and was the lead writer for the abstract and results sections. The dissertation author contributed secondarily to writing the methods section and provided intellectual input and code for figure design. Ke'La Kimble was the primary experimenter, generated all other figures in the manuscript, was the lead writer of the methods section and secondary writer for the abstract and results sections. Both the dissertation author and Ke'La Kimble contributed equally to the writing of the introduction and conclusions, the generation of the graphical abstract, and to the review and editing process.

VITA

2016 Bachelor of Science, University of California Los Angeles

2016-2017 Teaching Assistant, University of California San Diego

2017-2022 Research Assistant, University of California San Diego

2018 Master of Science, Chemistry, University of California San Diego

2022 Doctor of Philosophy, Chemistry, University of California San Diego

AWARDS

San Diego Fellowship Fellow, UCSD, 2017, 2018

PUBLICATIONS

Mitts, B. A., Wang, X., Lucero, D. D., Beall, C. M., Deane, G. B., DeMott, P. J., Prather, K. A. (2021). Importance of supermicron ice nucleating particles in nascent sea spray. *Geophysical Research Letters*, 48, e2020GL089633, doi:10.1029/2020GL089633

*Santander, M. V., *Mitts, B. A., Pendergraft, M. A., Dinasquet, J., Lee, C., Moore, A. N., Cancelada, L. B., Kimble, K. A., Malfatti, F., Prather, K. A. (2021). Tandem fluorescence measurements of organic matter and bacteria released in sea spray aerosols. *Environmental Science & Technology*, 55 (8), 5171-5179, doi:10.1021/acs.est.0c05493

Mayer, K. J., Wang, X., Santander, M. V., Mitts, B. A., Sauer, J. S., Sultana, C. M., Cappa, C. D., Prather, K. A. (2020). Secondary marine aerosol plays a dominant role over primary sea spray aerosol in cloud formation. *ACS Central Science*, 6 (12), 2259-2266, https://doi.org/10.1021/acscentsci.0c00793

Sauer, J. S., Mayer, K. J., Lee, C., Alves, M. R., Amiri, S., Bahaveolos, C. J., Franklin, E. B., Crocker, D. R., Dang, D., Dinasquet, J., Garofalo, L. A., Kaluarachchi, C. P., Kilgour, D. B., Mael, L. E., Mitts, B. A., Moon, D. A., Moore, A. N., Morris, C. K., Mullenmeister, C. A., Ni, C., Pendergraft, M. A., Petras, D., Simpson, R. M. C., Smith, S., Tumminello, P. R., Walker, J. L., DeMott, P. J., Farmer, D. K., Goldstein, A. H., Grassian, V. H., Jaffe, J. S., Malfatti, F., Martz, T. R., Slade, J. H., Tivanski, A. V., Bertram, T. H., Cappa, C. D., Prather, K. A. (2022). The Sea Spray Chemistry and Particle Evolution Study (SeaSCAPE): Overview and experimental methods. *Environmental Science: Processes & Impacts*, 24, 290-315. https://doi.org/10.1039/D1EM00260K

Crocker, D. R., Deane, G. B., Cao, R., Santander, M. V., Morris, C. K., Mitts, B. A., Dinasquet, J., Amiri, S., Malfatti, F., Prather, K. A., Thiemens, M. H. (2022). Biologically induced changes in the partitioning of submicron particulates between bulk seawater and the sea surface microlayer. *Geophysical Research Letters,* 49 (2), e2021GL094587, https://doi.org/10.1029/2021GL094587

*Co-first authors.

PRESENTATIONS

Mitts, B. A., Santander, M. V., Pendergraft, M. A., Malfatti, F., Prather, K. A. (2019). Sea spray aerosol fluorescence: Intercomparison of excitation emission matrix spectroscopy and single particle integrated fluorescence measurements; AGU Fall Meeting, San Francisco, CA, 2019.

ABSTRACT OF THE DISSERTATION

Detection and Influence of Biological Aerosols in Marine and Coastal Environments

by

Brock Andrew Mitts

Doctor of Philosophy in Chemistry

University of California San Diego, 2022

Professor Kimberly Prather, Chair

Aerosols influence climate by directly scatter radiation and affecting cloud properties and lifetime. Biological aerosols (bioaerosols) act as cloud condensation nuclei and ice nucleating particles (INPs) and can impact human and ecosystem health. Oceans, which cover over 70% of the Earth's surface, comprise an important source of bioaerosols emitted in both primary sea spray aerosol (SSA) particles and formed as secondary organic aerosols (SOA) from biogenic volatile organic compounds (VOCs). However, the influence of marine bioaerosols on clouds and climate remains an area of high uncertainty. In this dissertation, bioaerosols from marine environments were measured in laboratory-based systems and the ambient coastal environment to analyze their impact on cloud formation and on local communities. Studies on the ice nucleating ability of SSA showed supermicron-size SSA particles, rather than submicron, were the predominant source of INPs released from a marine environment. The size of these particles suggests these INPs represented bioaerosols, like marine bacteria, their fragments, or exudates. Bioaerosol emissions

in SSA were measured with single-particle fluorescence spectrometry over the course of a mesocosm phytoplankton bloom and showed, for the first time, the fluorescence signature and size distribution of these particles in nascent SSA. To uncover how atmospheric oxidants impact the SSA fluorescence profile, an oxidative flow reactor was used to simulate days of atmospheric aging during a phytoplankton bloom study in an ocean-atmosphere system. This study revealed that aged SSA particles underwent chemical transformations from proteinaceous to humic-like particles, reflected in the loss of protein-like fluorescence and the production of humic-like fluorescence. Applying these online fluorescence methods to aerosols in an urban-coastal environment demonstrated the ability to distinguish and characterize marine and continental air masses. Lastly, we developed a novel system combining a sublimation-condensation flow tube with a matrix-assisted laser desorption ionization matrix and an aerosol time-of-flight mass spectrometer to identify sub-100 nm SOA produced from biogenic VOCs. By improving bioaerosol detection in marine environments and better understanding their ability to seed clouds, the findings from this work enable more accurate representations and parameterizations of marine emissions for global climate models.

Chapter 1. Introduction

1.1 Aerosols

Aerosols are solid or liquid particles suspended within a gas (Seinfeld and Pandis, 2016). Aerosol particles range in diameter from single nanometers up to hundreds of micrometers. Aerosols can remain in the atmosphere following emission and travel significant distances to influence distant locations. The number, morphology, biological composition, and chemical composition of aerosols have a significant influence on clouds, climate, and human and ecological health (Pöschl, 2005).

1.2 Aerosol Sources

Aerosols are generated from a variety of natural and anthropogenic sources and are typically categorized into primary aerosols and secondary aerosols. Primary aerosols are directly emitted from sources such as dust storms, anthropogenic combustion, volcanic eruptions, breaking ocean waves, and biogenic sources. Secondary aerosols are generated through the condensation of gaseous volatile organic compounds (VOCs), from both biological and anthropogenic sources, after reacting with atmospheric oxidants (Pandis et al., 1992). Following emission, aerosols can undergo chemical and morphological transformations upon exposure to solar radiation, reactions with atmospheric oxidants, interactions with SOA, and coagulation with other particles (Seinfeld and Pandis, 2016). Investigating the influence of different aerosol sources on atmospheric interactions is required to elucidate the impact of these particles on the climate and the environment.

1.3 Aerosol Interactions with Clouds and Climate

Aerosols can affect climate directly by absorbing and scattering solar and terrestrial radiation (Pöschl, 2005). Aerosols can also influence climate indirectly by acting as both cloud

condensation nuclei (CCN) and ice nucleating particles (INPs) (Andreae and Rosenfeld, 2008). The aerosol-cloud interaction currently represents one of the largest uncertainties in the global radiative budget (Boucher et al., 2013).

When the atmosphere becomes supersaturated with water (relative humidity greater than 100%), water condenses onto aerosol particles forming cloud droplets. Without a particle for water to condense onto, supersaturations would reach several hundred percent prior to the formation of cloud droplets (Yau and Rogers, 1996). The ability of an aerosol to act as a CCN is determined predominantly by its chemical composition and size, with more polar particles and larger particles acting as more efficient CCN (Köhler, 1936). CCN can influence cloud radiative properties and overall climate. High CCN concentrations can result in decreased cloud droplet diameter and therefore brighter clouds, increasing the back scatter of solar radiation and resulting in a net cooling effect (Twomey, 1974, 1977). Additionally, an increased number of cloud drops can decrease cloud precipitation, leading to longer cloud lifetimes, and affecting radiative forcing (Albrecht, 1989; Rosenfeld et al., 2014).

Aerosols can serve as INPs and seed supercooled clouds, those at temperatures below 0°C, leading to cloud glaciation (freezing). Although ice nucleating particles are rare in the troposphere, comprising only ~1 in $10^5 – 10^6$ particles, they have a significant impact on clouds and can result in glaciation even with low concentrations (DeMott et al., 2010). In the absence of an INP, clouds can remain supercooled until the homogeneous freezing temperature of water at -38°C (Heymsfield and Miloshevich, 1993), which would lead to vastly different cloud properties. However, with an effective INP, ice formation can occur at temperatures as warm as -1°C (Després et al., 2012). Because ice crystals grow faster than liquid cloud droplets, the presence of ice crystals can lead to shorter cloud lifetimes and increased precipitation (DeMott et al., 2010). The competing

effects of CCN and INPs on cloud formation result in the large uncertainty associated with aerosol-cloud interactions and require further research to elucidate the influence of different aerosol sources on cloud properties and global climate.

1.4 Measurements of Ice Nucleating Particles

Although INPs can induce freezing through multiple mechanisms, the dominant freezing method for mixed-phase clouds (clouds with both supercooled water and ice) is via immersion freezing, where an INP is immersed in a supercooled water droplet (Field et al., 2012; Hoose and Möhler, 2012; Murray et al., 2012; Westbrook and Illingworth, 2011; Vali et al., 2015). For immersion mode freezing analysis, INPs are typically collected onto filters, into liquid solutions, or from precipitation and subsequently measured offline. Filter samples are commonly resuspended in water and subsequently aliquoted into droplets or wells which are then cooled at a controlled rate (Hiranuma et al., 2015). Upon freezing, the temperature of each subsample is recorded, and a temperature profile is determined for the INPs within a sample. The number concentration of INPs at each freezing temperature is determined by the number of unfrozen wells at that temperature and the volume of sample in each well (Beall et al., 2017; Vali, 1971). These methods for measuring INP concentrations better constrain the impact of different aerosol sources on cloud glaciation.

When measuring the ice nucleating activity of particles from different sources, it is often important to understand the ice nucleating efficiency of those aerosols. A common method to describe the efficiency of an ice nucleating particle is the calculation of the active site density (n_s) or the volume site density (v_s) which normalize the INP concentration to the surface area or volume of a particle, respectively. These methods are based on the assumptions that ice nucleation is time-independent and determined by the number of active/ice nucleation sites on a particle which are

dependent on temperature or ice supersaturation (Vali, 1971; Alpert et al., 2011). These calculations can be determined from laboratory measurements (McCluskey et al., 2018a; DeMott et al., 2016; Niemand et al., 2012), or field measurements (McCluskey et al., 2018b), and then utilized in climate models for the simulation of INP freezing from a variety of sources (Vergara-Temprado et al., 2017, 2018b, a; McCluskey et al., 2019). Therefore, it is critical to measure the active site density and volume site density of different aerosol sources to better parameterize climate models and improve estimates of the global radiative budget.

INPs are emitted from a variety of different aerosol sources including dust storms (DeMott et al., 2010; Neimand et al., 2012) agricultural soils (Garcia et al., 2012; Hill et al., 2016), biomass burning (Friedman et al., 2011; Vergara-Temprado et al., 2018a), sea spray (DeMott et al., 2016; McCluskey et al., 2017) and biological sources (Fröhlich-Nowoisky et al., 2016). By number, dust particles, typically produced through major dust storm events, constitute the majority of INPs freezing at temperatures below -15°C (Vergara-Temprado et al., 2017). However, it has been shown that biological particles, especially those released in sea spray over remote oceans, can play a significant role in the INP budget when dust is not present (Burrows et al., 2013; Vergara-Temprado et al., 2017) and effectively nucleate ice at warmer freezing temperatures, with some biological species found to nucleate ice at temperatures warmer than -10°C (Huffman et al., 2013; Bowers et al., 2009; Knopf et al., 2011; Mason et al., 2015; Christner et al., 2008). The potentially significance of sea spray acting as INP in marine environments highlights the importance of studies on the composition and influence of these particles on cloud formation.

1.5 Sea Spray Aerosols

With oceans covering over 70% of the Earth, sea spray aerosol (SSA) particles constitute a significant portion of atmospheric aerosols (Gantt and Meskhidze, 2013; Textor et al., 2006).

SSA particles are often comprised of complex mixtures of inorganic salts, organic molecules, and biological particulates including bacteria, viruses, enzymes, and fragments of phytoplankton and diatoms (Cochran et al., 2017; Patterson et al., 2016; Malfatti et al., 2019). SSA particles are formed when breaking waves entrain bubbles which burst at the surface of the ocean (Lewis and Schwartz, 2004). Bubble bursting consists of two main mechanisms for aerosol release into the atmosphere: 1) film drop formation, where the bubble film ruptures and ejects numerous aerosols into the air; and 2) jet drop production, where the cavity of the bubble collapses, forming a fluid jet which can fragment and release aerosols (Lewis and Schwartz, 2004). These different production mechanisms result in different chemical compositions and size distributions for the jet and film drops (Wang et al., 2017). Additionally, bubble entrainment can lead to scavenging of surface-active and biological materials throughout the water column and result in an enrichment of these species at the sea surface and in SSA (Aller et al., 2005; Blanchard et al., 1981; Cunliffe et al., 2013; Rastelli et al., 2017; Weber et al., 1983). To better understand the release of biological particles from seawater, the composition of SSA, and the influence on clouds and climate, it is necessary to properly generate and characterize SSA in the laboratory and accurately identify SSA in the field.

Recent developments in SSA production methods for laboratory experiments have enabled more realistic investigations into SSA chemistry (Prather et al., 2013). Modern laboratory studies on SSA have utilized wave channels to generate a breaking wave in a controlled ocean-atmosphere system (Lee et al., 2015; Sauer et al., 2022). Additionally, small scale experiments can be performed using a marine aerosol reference tank (MART) or a miniature MART (miniMART) which utilize a plunging waterfall to generate SSA in an isolated system with accurate size distributions and production mechanisms (Stokes et al., 2013, 2016). As noted before, the

generation of SSA through proper bubble formation and production mechanisms resemblant of the real ocean is critical for accurate emissions of biological and chemical species. By employing these systems, laboratory-based experiments on SSA composition and concentration can proceed without the interference of anthropogenic or terrestrial aerosols.

1.6 Biological Aerosol Particles

Biological aerosols, bioaerosols, are comprised of bacteria, pollen, fungi, viruses, cells, spores, their fragments, and exudates (Després et al., 2012). Bioaerosols originate from a variety of sources including plants, soil, animals, and sea spray, and can range in size from nanometers up to millimeters (Fröhlich-Nowoisky et al., 2016). As noted, bioaerosols can act as both efficient INPs and CCN due to their size and chemical composition. In addition to their role in the hydrological cycle and climate, bioaerosols can have a significant impact on human and ecosystem health (Douwes et al., 2003; Fröhlich-Nowoisky et al., 2016). Bioaerosols can act as allergens and pathogens which may result in disease and the loss of crops and livestock (Šantl-Temkiv et al., 2020). Once in the atmosphere, bioaerosols can undergo further chemical and physical changes through interactions with solar radiation, atmospheric oxidants (Estillore et al., 2016; Santarpia et al., 2012; Pan et al., 2021), and other aerosols such as secondary aerosols formed from biogenic VOCs (Zhang et al., 2021; Huffman et al., 2012; Pöschl et al., 2010). These changes to the composition of bioaerosol can further affect their ability to act as cloud seeds and alter their infectivity or allergenic potential (Ariya et al., 2009; Shiraiwa et al., 2012). Because of their significance on the global climate, local precipitation, and environmental health, it is important to accurately identify bioaerosols and distinguish their sources.

1.7 Fluorescent Detection of Biological Species

A common way to detect bioaerosols and characterize their composition is through fluorescence-based measurements. Fluorescence occurs when a molecule is excited to a singlet electronic state from incoming radiation and, during the relaxation to the ground electronic state, emits a photon (Lakowicz, 2006). Fluorescence techniques for bioaerosol identification often exploit the intrinsic fluorescence of biomolecules such as the amino acids tryptophan, tyrosine, and phenylalanine found in proteins, as well as the biological cofactors nicotinamide adenine dinucleotide (phosphate) (NAD(P)H), and flavins such as riboflavin (Pöhlker et al., 2012). Other fluorescent biomolecules include chlorophyll, natural pigments, and even (deoxy)ribonucleic acid (DNA, RNA) (Pöhlker et al., 2012). In addition to fluorescent biomolecules, non-biological fluorophores can be characterized including combustion related particles that contain polycyclic aromatic hydrocarbons (PAHs) and humic-like substances (HULIS) which arise from the breakdown of organic material in terrestrial soils and water bodies such as lakes and oceans (Pöhlker et al., 2012). It is important when using fluorescence-based techniques to distinguish between different fluorescent molecule types and utilize the fluorescence signature to inform source apportionment of particle populations.

1.7.1 Single-Particle Detection with the WIBS

A common commercial instrument for real-time fluorescence measurements of bioaerosols is the wideband integrated bioaerosol sensor (WIBS). The WIBS is a portable, single-particle fluorescence spectrometer designed to detect bioaerosols by characterizing aerosol morphology and fluorescent profiles (Kaye et al., 2005). The WIBS has been utilized both in the field and in the laboratory to detect various types of bioaerosols, but only recently has it been used for detection of SSA (Gabey et al. 2010, 2011; Perring et al. 2015; Hernandez et al. 2016; Savage et al. 2017; Toprak and Schnaiter 2013; Crawford et al. 2014, 2016, 2017). The WIBS operates by first

detecting an incoming particle based on scattered light from a 635 nm continuous-wave laser. Side-scattered light is used to determine the optical diameter of a particle using a Mie scattering model calibrated with polystyrene latex spheres of known diameters (Gabey et al., 2010). Additionally, forward-scattered light is detected on a quadrant photomultiplier tube to determine the shape of a particle, known as the asymmetry factor, which ranges from a value of 1 (sphere) to 100 (rod-shaped particle) (Kaye et al., 2007). The detection of an incoming particle also triggers the firing of two sequential xenon lamps (Xe) used for the excitation of fluorescent biomolecules. These lamps are used in combination with bandpass filters to enable excitation at 280 nm (Xe1) and 370 nm (Xe2). Fluorescence emission is then detected in two wavelength bands, again using bandpass filters, between 300 – 400 nm (FL1) and between 420 – 650 nm (FL2). The combination of these fluorescence excitation and emission wavelengths results in three distinct excitation/emission (ex/em) "channels" (ch):

channel 1, Xe1:FL1 (ex/em: 280 nm / 300 – 400 nm)

channel 2, Xe1:FL2 (ex/em: 280 nm / 420 – 650 nm)

channel 3, Xe2:FL2 (ex/em: 370 nm / 420 – 650 nm)

These fluorescence channels were originally designed to detect the biological fluorophores tryptophan, riboflavin, and NAD(P)H for channels 1-3, respectively; however, as mentioned before, other fluorophores, such as HULIS, can be detected in these regions and benefit particle discrimination in a marine environment (Pöhlker et al., 2012). Fluorescent particles can be further defined based on the logical combination of these fluorescent channels into various classes (Perring et al. 2015). These classes are exclusive and use the following notation: class A (channel 1 only), class B (ch 2 only), class C (ch 3 only), class AB (ch 1 & 2), class AC (ch 1 & 3), class BC (ch 2 & 3), and class ABC (ch 1, 2, & 3), visualized in Figure 1.1. The breakdown of particle

populations into fluorescence classes can be useful for identifying particle sources; however, identification often requires characterization of the fluorescence signature of isolated sources.

1.7.2 Bulk Analysis with EEMS

Excitation emission matrix spectroscopy (EEMS) is a common technique for characterizing different chemical species within a bulk solution (Mostofa et al., 2013). EEMS can separate complex mixtures of fluorophores in solution because of its ability to scan through multiple excitation and emission wavelengths (Coble, 1996). Unlike the WIBS, EEMS has a higher resolution of fluorescence excitation and emission and wider excitation and emission wavelength ranges. EEMS can detect several fluorescent biomolecules commonly observed in seawater. These include chlorophyll-a which fluoresces from excitation at 400 – 440 nm and emits between 680 – 690 nm (Pöhlker et al., 2012). Chlorophyll-a is often used as a proxy for biological activity in seawater (Falkowski and Kiefer, 1985; Vignati et al., 2010; Rinaldi et al., 2013; Quinn et al., 2014) because of its production by phytoplankton and other marine autotrophic organisms. Furthermore, EEMS is capable of distinguishing between different protein-like substances, namely the amino acids tryptophan (ex/em: 275 – 280 nm / 330 – 350 nm) and tyrosine (ex/em: 275 nm / 300 – 310 nm) which are common in most biological species including bacteria, viruses, phytoplankton, and their exudates and fragments (Determann et al., 1998; Lakowicz, 2006; Mostofa et al., 2013; Pöhlker et al., 2012). Another common fluorophore detected with EEMS in marine and terrestrial aqueous systems is HULIS (ex/em: 280 – 400 nm / 380 – 550 nm) (Mostofa et al., 2013; Coble, 1996; Lee et al., 2015). HULIS is produced from the degradation of biological materials and recombination into extremely complex and often highly conjugated molecules (Hessen and Tranvik, 1998; Zhang et al., 2009). Detection and identification of HULIS is important in the marine environment because of its potential to act as a photosensitizer and impact the

heterogeneous chemistry in the atmosphere (Graber and Rudich, 2006; Shrestha et al., 2018; Tsui and Mcneill, 2018; Wang et al., 2020; Monge et al., 2012). EEMS represents a valuable complimentary measurement to the WIBS because together they can measure a bulk solution and the aerosol phase. Nevertheless, these two instruments have not yet been combined to measure the bulk and aerosol phases of a marine system.

1.8 Measuring Chemical Composition with ATOFMS

Another common method for online detection of bioaerosols and other atmospheric particles is single-particle mass spectrometry (SMPS). The Aerosol Time-of-Flight Mass Spectrometer (ATOFMS) is a well-established instrument for measuring the size-resolved chemical composition of single particles in real time (Prather et al., 1994; Gard et al., 1997). The ATOFMS has been used in many laboratory and field studies to detect particles originating from a variety of sources including dust storms, anthropogenic sources, cell cultures, SOA, and SSA (Pratt et al., 2009; Cahill et al., 2015; Creamean et al., 2013; Gaston et al., 2010; Sultana et al., 2017a). Aerosols entering the instrument are collimated into a particle stream using a nozzle and a series of skimmers or with an aerodynamic lens (Liu et al. 1995a, 1995b; X. Zhang et al. 2002, 2004). Aerosols then pass through a couple of visible-wavelength continuous-wave lasers (two 532 nm lasers or one 405 nm and one 488 nm laser) located 60 mm apart. As the particles pass through the lasers, they scatter light which is focused onto photomultiplier tubes (PMTs) for detection. The time delay between the scatter signal on each PMT is used to calculate the terminal velocity of the aerosol, which can then be converted to the vacuum aerodynamic diameter based on an external calibration with polystyrene latex spheres of known diameter for particles with diameters from 0.1 – 1 μm or 0.3 – 3 μm. The scattering signal and particle velocity are then used to trigger a pulsed 266 nm Nd:YAG desorption/ionization laser (operating between 0.1 – 1.3 mJ).

Following desorption and ionization, positive and negative ions are separated with a dual-polarity reflectron time-of-flight mass spectrometer and detected using microchannel plates. The ATOFMS represents an extremely powerful instrument for detecting individual particles from a variety of sources and analyzing their chemical composition and morphological traits.

Due to the large datasets generated by the ATOFMS (data on 1000s of single particles), different methods have been used to analyze and separate the data into meaningful outputs. Typical methods include clustering analyses, such as the adaptive neural network ATR-2a (Song et al., 1999; Rebotier and Prather, 2007), which cluster spectra based on the ion peak identities and intensities. Additionally, spectra can be visually inspected and grouped using the Flexible Analysis Toolkit for the Exploration of SPMS data (FATES) (Sultana et al., 2017b) which is a graphical user interface software designed in MATLAB (The MathWorks, Inc). Once clusters are generated, source assignments are designated based on previous laboratory work and field studies as references. These data analysis methods allow for the streamlined identification of particle sources and the detection of minor shifts in particle populations, including changes following atmospheric oxidation and heterogeneous reactions.

1.9 Simulated Atmospheric Aging with Oxidative Flow Reactors

The hydroxyl radical is one of the most important reactive species in the atmosphere and a significant source of atmospheric oxidation (Seinfeld and Pandis, 2016). Reactions involving the hydroxyl radical lead to the formation of SOA and can alter the chemical composition of primary aerosols (Kroll and Seinfeld, 2008). To understand the impact of the hydroxyl radical in a controlled laboratory setting, the oxidative flow reactor (OFR) was developed. OFRs simulate days of equivalent atmospheric aging over a period of minutes by generating high concentrations of hydroxyl radical. The potential aerosol mass oxidative flow reactor (PAM-OFR, Aerodyne Inc) is

a commercially available OFR that has been thoroughly characterized (Kang et al., 2007; Li et al., 2015; Peng et al., 2015). The PAM-OFR is a 13.3 L cylindrical reaction chamber that uses Hg lamps at wavelengths of 185 nm and 254 nm to generate the hydroxyl radical and simulate aging. The introduction of VOCs and particles into the PAM-OFR has been shown to generate SOA and initiate heterogenous reactions (Lambe et al., 2011). While OFRs have been used extensively to measure SOA formation and heterogeneous reactions, few studies have used OFRs to simulate aging of bioaerosols produced from a marine environment (Trueblood et al., 2020).

1.10 Dissertation Objectives

This dissertation focuses on the identification and characterization of biological aerosols released in marine and coastal environments through fluorescence and mass spectrometry techniques and assesses the impact of these bioaerosols on clouds and the environment. The main questions that will be addressed in this dissertation include:

1. What role do supermicron sea spray aerosols play in the marine ice nucleating particle budget?
2. What is the fluorescence signature of bioaerosols in SSA?
3. How does the fluorescence signature of SSA change with atmospheric aging and oxidation?
4. How are urban-coastal environments impacted by SSA and other atmospheric aerosols?
5. How do we measure the chemical composition of single-particle sub-100nm biogenic SOA?

1.11 Dissertation Synopsis

To address the questions laid out in this dissertation, both laboratory and field studies were conducted using a variety of different online and offline instruments and analyses. Chapter 2 of this dissertation investigates the size-dependent ice nucleating ability of SSA particles over the course of two different mesocosm phytoplankton blooms. This study showed that supermicron SSA were the dominant source of INPs released in sea spray throughout all phases of a phytoplankton bloom.

Chapter 3 describes the identification of bioaerosols released in SSA using fluorescence-based measurements. SSA were measured with the WIBS in tandem with EEMS of collected SSA to determine, for the first time, a fluorescence signature of bioaerosols released in nascent SSA. The size distribution of fluorescent SSA showed supermicron particles primarily had protein-like fluorescence, suggestive of marine bacteria, while submicron particles predominantly had humic-like fluorescence, indicating dissolved HULIS.

Chapter 4 expands on the results of Chapter 3 by observing the influence of atmospheric aging and oxidation on the fluorescence signature of SSA generated in a wave channel ocean-atmosphere system. Following exposure to atmospheric aging in an oxidative flow reactor (OFR), aged SSA showed the degradation of protein-like fluorescence and the production of humic-like fluorescence. The fluorescent particle profile of aged SSA was significantly different from nascent SSA after only ~3 days of equivalent aging.

Chapter 5 investigates the coastal fluorescent aerosol populations at two sampling sites in Southern California using the WIBS. A notable difference was observed between the fluorescence profiles of continental/anthropogenic aerosols and marine aerosols. Additionally, the fluorescence signatures of marine aerosols at both sampling sites were similar, and a potential fluorescence indicator of wastewater contaminated SSA was suggested.

Lastly, Chapter 6 describes the characterization and development of a novel application of the ATOFMS coupled with a sublimation-condensation laminar flow growth tube to grow sub-100 nm particles using a matrix-assisted laser desorption-ionization (MALDI) matrix. This condensation matrix-assisted ATOFMS (cMA-ATOFMS) system enabled the detection and ionization of particles with diameters as small as 20 nm, previously below the detection limit of the ATOFMS. The cMA-ATOFMS system was tested to optimize sub-100nm SOA particles detection and was capable of distinguishing between anthropogenic and biogenic sulfur containing secondary aerosols.

1.12 Acknowledgements

Mitchell Santander, Alexia Moore, and Dr. Liora Mael are acknowledged for their assistance in editing this chapter.

1.13 Figures

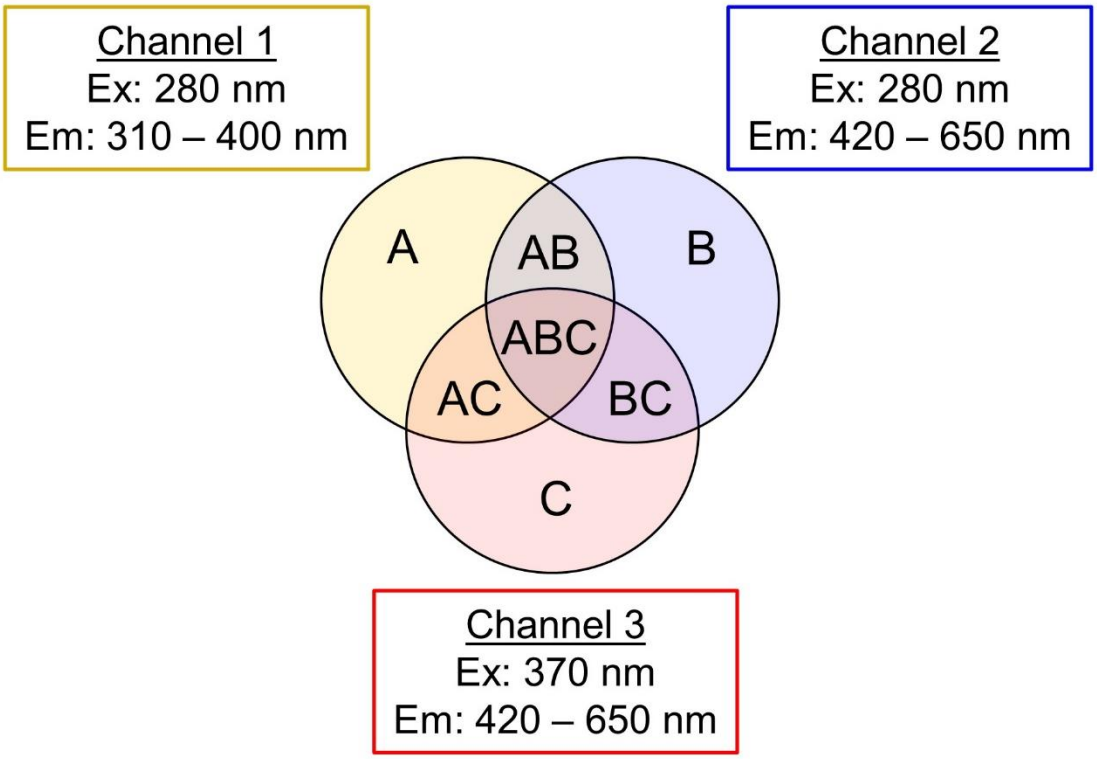

Figure 1.1. Breakdown of the different WIBS channels with the corresponding excitation (ex) and emission (em) wavelengths. Also shown are the different WIBS fluorescence classes color coordinated to show the fluorescence profile with channel 1 (yellow), channel 2 (blue), and channel 3 (red).

1.14 References

Albrecht, B. A.: Aerosols, Cloud Microphysics, and Fractional Cloudiness, Science (80-.)., 245, 1227–1230, https://doi.org/10.1126/SCIENCE.245.4923.1227, 1989.

Aller, J. Y., Kuznetsova, M. R., Jahns, C. J., and Kemp, P. F.: The sea surface microlayer as a source of viral and bacterial enrichment in marine aerosols, J. Aerosol Sci., 36, 801–812, https://doi.org/10.1016/j.jaerosci.2004.10.012, 2005.

Alpert, P. A., Aller, J. Y., and Knopf, D. A.: Ice nucleation from aqueous NaCl droplets with and without marine diatoms, Atmos. Chem. Phys., 11, 5539–5555, https://doi.org/10.5194/acp-11-5539-2011, 2011.

Andreae, M. O. and Rosenfeld, D.: Aerosol-cloud-precipitation interactions. Part 1. The nature and sources of cloud-active aerosols, Earth-Science Rev., 89, 13–41, https://doi.org/10.1016/j.earscirev.2008.03.001, 2008.

Ariya, P. A., Sun, J., Eltouny, N. A., Hudson, E. D., Hayes, C. T., and Kos, G.: Physical and chemical characterization of bioaerosols - Implications for nucleation processes, Int. Rev. Phys. Chem., 28, 1–32, https://doi.org/10.1080/01442350802597438, 2009.

Beall, C. M., Stokes, M. D., Hill, T. C., Demott, P. J., Dewald, J. T., and Prather, K. A.: Automation and heat transfer characterization of immersion mode spectroscopy for analysis of ice nucleating particles, Atmos. Meas. Tech, 10, 2613–2626, https://doi.org/10.5194/amt-10-2613-2017, 2017.

Blanchard, D. C., Syzdek, L. D., and Weber, M. E.: Bubble scavenging of bacteria in freshwater quickly produces bacterial enrichment in airborne jet drops1, Limnol. Oceanogr., 26, 961–964, https://doi.org/10.4319/lo.1981.26.5.0961, 1981.

Boucher, O., Randall, D., Artaxo, P., Bretherton, C., Feingold, G., Forster, P., Kerminen, V.-M. V.-M., Kondo, Y., Liao, H., Lohmann, U., Rasch, P., Satheesh, S. K., Sherwood, S., Stevens, B., Zhang, X. Y., and Zhan, X. Y.: Clouds and Aerosols, Clim. Chang. 2013 Phys. Sci. Basis. Contrib. Work. Gr. I to Fifth Assess. Rep. Intergov. Panel Clim. Chang., 571–657, https://doi.org/10.1017/CBO9781107415324.016, 2013.

Bowers, R. M., Lauber, C. L., Wiedinmyer, C., Hamady, M., Hallar, A. G., Fall, R., Knight, R., and Fierer, N.: Characterization of airborne microbial communities at a high-elevation site and their potential to act as atmospheric ice nuclei, Appl. Environ. Microbiol., 75, 5121–5130, https://doi.org/10.1128/AEM.00447-09/FORMAT/EPUB, 2009.

Burrows, S. M., Hoose, C., Pöschl, U., and Lawrence, M. G.: Ice nuclei in marine air: Biogenic particles or dust?, Atmos. Chem. Phys., 13, 245–267, https://doi.org/10.5194/acp-13-245-2013, 2013.

Cahill, J. F., Darlington, T. K., Fitzgerald, C., Schoepp, N. G., Beld, J., Burkart, M. D., and Prather,

K. A.: Online Analysis of Single Cyanobacteria and Algae Cells under Nitrogen-Limited Conditions Using Aerosol Time-of-Flight Mass Spectrometry, Anal. Chem., 87, 8039–8046, https://doi.org/10.1021/acs.analchem.5b02326, 2015.

Christner, B. C., Morris, C. E., Foreman, C. M., Cai, R., and Sands, D. C.: Ubiquity of biological ice nucleators in snowfall, Science (80-.)., 319, 1214, https://doi.org/10.1126/science.1149757, 2008.

Coble, P. G.: Characterization of marine and terrestrial DOM in seawater using excitation-emission matrix spectroscopy, Mar. Chem., 51, 325–346, https://doi.org/10.1016/0304-4203(95)00062-3, 1996.

Cochran, R. E., Laskina, O., Trueblood, J. V., Estillore, A. D., Morris, H. S., Jayarathne, T., Sultana, C. M., Lee, C., Lin, P., Laskin, J., Laskin, A., Dowling, J. A., Qin, Z., Cappa, C. D., Bertram, T. H., Tivanski, A. V., Stone, E. A., Prather, K. A., and Grassian, V. H.: Molecular Diversity of Sea Spray Aerosol Particles: Impact of Ocean Biology on Particle Composition and Hygroscopicity, 2, 655–667, https://doi.org/10.1016/J.CHEMPR.2017.03.007, 2017.

Crawford, I., Robinson, N. H., Flynn, M. J., Foot, V. E., Gallagher, M. W., Huffman, J. A., Stanley, W. R., and Kaye, P. H.: Characterisation of bioaerosol emissions from a Colorado pine forest: Results from the beachon-rombas experiment, Atmos. Chem. Phys., 14, 8559–8578, https://doi.org/10.5194/acp-14-8559-2014, 2014.

Crawford, I., Lloyd, G., Herrmann, E., Hoyle, C. R., Bower, K. N., Connolly, P. J., Flynn, M. J., Kaye, P. H., Choularton, T. W., and Gallagher, M. W.: Observations of fluorescent aerosol-cloud interactions in the free troposphere at the High-Altitude Research Station Jungfraujoch, Atmos. Chem. Phys., 16, 2273–2284, https://doi.org/10.5194/acp-16-2273-2016, 2016.

Crawford, I., Gallagher, M. W., Bower, K. N., Choularton, T. W., Flynn, M. J., Ruske, S., Listowski, C., Brough, N., Lachlan-Cope, T., Fleming, Z. L., Foot, V. E., and Stanley, W. R.: Real-time detection of airborne fluorescent bioparticles in Antarctica, Atmos. Chem. Phys., 17, 14291–14307, https://doi.org/10.5194/acp-17-14291-2017, 2017.

Creamean, J. M., Suski, K. J., Rosenfeld, D., Cazorla, A., Demott, P. J., Sullivan, R. C., White, A. B., Ralph, F., Minnis, P., Comstock, J. M., Tomlinson, J. M., and Prather, K. A.: Dust and Biological Aerosols from the Sahara and Asia Influence Precipitation in the Western U.S., Science (80-.)., 339, 1572–1578, https://doi.org/10.1126/science.1227279, 2013.

Cunliffe, M., Engel, A., Frka, S., Gašparović, B. Ž., Guitart, C., Murrell, J. C., Salter, M., Stolle, C., Upstill-Goddard, R., and Wurl, O.: Sea surface microlayers: A unified physicochemical and biological perspective of the air-ocean interface, https://doi.org/10.1016/j.pocean.2012.08.004, 2013.

DeMott, P. J., Prenni, A. J., Liu, X., Kreidenweis, S. M., Petters, M. D., Twohy, C. H., Richardson,

M. S., Eidhammer, T., and Rogers, D. C.: Predicting global atmospheric ice nuclei distributions and their impacts on climate, Proc. Natl. Acad. Sci. U. S. A., 107, 11217–11222, https://doi.org/10.1073/pnas.0910818107, 2010.

DeMott, P. J., Hill, T. C. J., McCluskey, C. S., Prather, K. A., Collins, D. B., Sullivan, R. C., Ruppel, M. J., Mason, R. H., Irish, V. E., Lee, T., Hwang, C. Y., Rhee, T. S., Snider, J. R., McMeeking, G. R., Dhaniyala, S., Lewis, E. R., Wentzell, J. J. B., Abbatt, J., Lee, C., Sultana, C. M., Ault, A. P., Axson, J. L., Martinez, M. D., Venero, I., Santos-Figueroa, G., Stokes, M. D., Deane, G. B., Mayol-Bracero, O. L., Grassian, V. H., Bertram, T. H., Bertram, A. K., Moffett, B. F., and Franc, G. D.: Sea spray aerosol as a unique source of ice nucleating particles, Proc. Natl. Acad. Sci. U. S. A., 113, 5797–5803, https://doi.org/10.1073/pnas.1514034112, 2016.

Després, V. R., Alex Huffman, J., Burrows, S. M., Hoose, C., Safatov, A. S., Buryak, G., Fröhlich-Nowoisky, J., Elbert, W., Andreae, M. O., Pöschl, U., and Jaenicke, R.: Primary biological aerosol particles in the atmosphere: A review, Tellus, Ser. B Chem. Phys. Meteorol., 64, 1–58, https://doi.org/10.3402/tellusb.v64i0.15598, 2012.

Determann, S., Lobbes, J. M., Reuter, R., and Rullkötter, J.: Ultraviolet fluorescence excitation and emission spectroscopy of marine algae and bacteria, Mar. Chem., 62, 137–156, https://doi.org/10.1016/S0304-4203(98)00026-7, 1998.

Douwes, J., Thorne, P., Pearce, N., and Heederik, D.: Bioaerosol Health Effects and Exposure Assessment: Progress and Prospects, Ann. Occup. Hyg., 47, 187–200, https://doi.org/10.1093/ANNHYG/MEG032, 2003.

Estillore, A. D., Trueblood, J. V., and Grassian, V. H.: Atmospheric chemistry of bioaerosols: Heterogeneous and multiphase reactions with atmospheric oxidants and other trace gases, https://doi.org/10.1039/c6sc02353c, 18 October 2016.

Falkowski, P. and Kiefer, D. A.: Chlorophyll a fluorescence in phytoplankton: relationship to photosynthesis and biomass, J. Plankton Res., 7, 715–731, https://doi.org/10.1093/PLANKT/7.5.715, 1985.

Field, P. R., Heymsfield, A. J., Shipway, B. J., Demott, P. J., Pratt, K. A., Rogers, D. C., Stith, J., and Prather, K. A.: Ice in clouds experiment-layer clouds. Part II: Testing characteristics of heterogeneous ice formation in lee wave clouds, J. Atmos. Sci., 69, 1066–1079, https://doi.org/10.1175/JAS-D-11-026.1, 2012.

Friedman, B., Kulkarni, G., Beránek, J., Zelenyuk, A., Thornton, J. A., Cziczo, D. J., Friedman, C. :, Kulkarni, G., Beránek, J., Zelenyuk, A., Thornton, J. A., and Cziczo, D. J.: Ice nucleation and droplet formation by bare and coated soot particles, J. Geophys. Res., 116, 17203, https://doi.org/10.1029/2011jd015999, 2011.

Fröhlich-Nowoisky, J., Kampf, C. J., Weber, B., Huffman, J. A., Pöhlker, C., Andreae, M. O., Lang-Yona, N., Burrows, S. M., Gunthe, S. S., Elbert, W., Su, H., Hoor, P., Thines, E.,

Hoffmann, T., Després, V. R., and Pöschl, U.: Bioaerosols in the Earth system: Climate, health, and ecosystem interactions, Atmos. Res., 182, 346–376, https://doi.org/10.1016/j.atmosres.2016.07.018, 2016.

Gabey, A. M., Gallagher, M. W., Whitehead, J., Dorsey, J. R., Kaye, P. H., and Stanley, W. R.: Measurements and comparison of primary biological aerosol above and below a tropical forest canopy using a dual channel fluorescence spectrometer, Atmos. Chem. Phys. Atmos. Chem. Phys., 10, 4453–4466, https://doi.org/10.5194/acp-10-4453-2010, 2010.

Gabey, A. M., Stanley, W. R., Gallagher, M. W., and Kaye, P. H.: The fluorescence properties of aerosol larger than 0.8 μm in urban and tropical rainforest locations, Atmos. Chem. Phys., 11, 5491–5504, https://doi.org/10.5194/acp-11-5491-2011, 2011.

Gantt, B. and Meskhidze, N.: The physical and chemical characteristics of marine primary organic aerosol: A review, Atmos. Chem. Phys., 13, 3979–3996, https://doi.org/10.5194/acp-13-3979-2013, 2013.

Garcia, E., Hill, T. C. J., Prenni, A. J., DeMott, P. J., Franc, G. D., and Kreidenweis, S. M.: Biogenic ice nuclei in boundary layer air over two U.S. High Plains agricultural regions, J. Geophys. Res. Atmos., 117, https://doi.org/10.1029/2012JD018343, 2012.

Gard, E., Mayer, J. E., Morrical, B. D., Dienes, T., Fergenson, D. P., and Prather, K. A.: Real-Time Analysis of Individual Atmospheric Aerosol Particles: Design and Performance of a Portable ATOFMS, Analytical Chemistry, 4083–4091 pp., https://doi.org/10.1021/ac970540n, 1997.

Gaston, C. J., Pratt, K. A., Qin, X., and Prather, K. A.: Real-Time Detection and Mixing State of Methanesulfonate in Single Particles at an Inland Urban Location during a Phytoplankton Bloom, Environ. Sci. Technol., 44, 1566–1572, https://doi.org/10.1021/es902069d, 2010.

Graber, E. R. and Rudich, Y.: Atmospheric Chemistry and Physics Atmospheric HULIS: How humic-like are they? A comprehensive and critical review, Atmos. Chem. Phys, 729–753 pp., 2006.

Hernandez, M., Perring, A. E., McCabe, K., Kok, G., Granger, G., and Baumgardner, D.: Chamber catalogues of optical and fluorescent signatures distinguish bioaerosol classes, Atmos. Meas. Tech., 9, 3283–3292, https://doi.org/10.5194/amt-9-3283-2016, 2016.

Hessen, D. O. and Tranvik, L. J.: Aquatic humic substances: ecology and biochemistry, Springer-Verlag Berlin Heidelberg, Berlin, 1998.

Heymsfield, A. J. and Miloshevich, L. M.: Homogeneous Ice Nucleation and Supercooled Liquid Water in Orographic Wave Clouds, https://doi.org/10.1175/1520-0469(1993)050<2335:HINASL>2.0.CO;2, 1993.

Hill, T. C. J., Demott, P. J., Tobo, Y., Fröhlich-Nowoisky, J., Moffett, B. F., Franc, G. D., and

Kreidenweis, S. M.: Sources of organic ice nucleating particles in soils, Atmos. Chem. Phys., 16, 7195–7211, https://doi.org/10.5194/ACP-16-7195-2016, 2016.

Hiranuma, N., Möhler, O., Yamashita, K., Tajiri, T., Saito, A., Kiselev, A., Hoffmann, N., Hoose, C., Jantsch, E., Koop, T., and Murakami, M.: Ice nucleation by cellulose and its potential contribution to ice formation in clouds, Nat. Geosci., 8, 273–277, https://doi.org/10.1038/ngeo2374, 2015.

Hoose, C. and Möhler, O.: Heterogeneous ice nucleation on atmospheric aerosols: A review of results from laboratory experiments, 9817–9854 pp., https://doi.org/10.5194/acp-12-9817-2012, 2012.

Huffman, J. A., Sinha, B., Garland, R. M., Snee-Pollmann, A., Gunthe, S. S., Artaxo, P., Martin, S. T., Andreae, M. O., and Pöschl, U.: Size distributions and temporal variations of biological aerosol particles in the Amazon rainforest characterized by microscopy and real-time UV-APS fluorescence techniques during AMAZE-08, Atmos. Chem. Phys. Atmos. Chem. Phys., 12, 11997–12019, https://doi.org/10.5194/acp-12-11997-2012, 2012.

Huffman, J. A., Prenni, A. J., Demott, P. J., Pöhlker, C., Mason, R. H., Robinson, N. H., Fröhlich-Nowoisky, J., Tobo, Y., Després, V. R., Garcia, E., Gochis, D. J., Harris, E., Müller-Germann, I., Ruzene, C., Schmer, B., Sinha, B., Day, D. A., Andreae, M. O., Jimenez, J. L., Gallagher, M., Kreidenweis, S. M., Bertram, A. K., and Pöschl, U.: High concentrations of biological aerosol particles and ice nuclei during and after rain, Atmos. Chem. Phys., 13, 6151–6164, https://doi.org/10.5194/acp-13-6151-2013, 2013.

Kang, E., Root, M. J., Toohey, D. W., and Brune, W. H.: Introducing the concept of Potential Aerosol Mass (PAM), Atmos. Chem. Phys, 7, 5727–5744, https://doi.org/https://doi.org/10.5194/acp-7-5727-2007, 2007.

Kaye, P. H., Stanley, W. R., Hirst, E., Foot, E. V., Baxter, K. L., and Barrington, S. J.: Single particle multichannel bio-aerosol fluorescence sensor, Opt. Express, 13, 3583, https://doi.org/10.1364/opex.13.003583, 2005.

Kaye, P. H., Aptowicz, K., Chang, R. K., Foot, V., and Videen, G.: Angularly Resolved Elastic Scattering From Airborne Particles, in: Optics of Biological Particles, Springer Netherlands, 31–61, https://doi.org/10.1007/978-1-4020-5502-7_3, 2007.

Knopf, D. A., Alpert, P. A., Wang, B., and Aller, J. Y.: Stimulation of ice nucleation by marine diatoms, Nat. Geosci., 4, 88–90, https://doi.org/10.1038/ngeo1037, 2011.

Köhler, H.: The nucleus in and the growth of hygroscopic droplets, Trans. Faraday Soc., 32, 1152–1161, https://doi.org/10.1039/TF9363201152, 1936.

Kroll, J. H. and Seinfeld, J. H.: Chemistry of secondary organic aerosol: Formation and evolution of low-volatility organics in the atmosphere, Atmos. Environ., 42, 3593–3624, https://doi.org/10.1016/j.atmosenv.2008.01.003, 2008.

Lakowicz, J. R.: Principles of fluorescence spectroscopy, Springer, 1–954 pp., https://doi.org/10.1007/978-0-387-46312-4, 2006.

Lambe, A. T., Ahern, A. T., Williams, L. R., Slowik, J. G., Wong, J. P. S., Abbatt, J. P. D., Brune, W. H., Ng, N. L., Wright, J. P., Croasdale, D. R., Worsnop, D. R., Davidovits, P., and Onasch, T. B.: Characterization of aerosol photooxidation flow reactors: heterogeneous oxidation, secondary organic aerosol formation and cloud condensation nuclei activity measurements, Atmos. Meas. Tech, 4, 445–461, https://doi.org/10.5194/amt-4-445-2011, 2011.

Lee, C., Sultana, C. M., Collins, D. B., Santander, M. V., Axson, J. L., Malfatti, F., Cornwell, G. C., Grandquist, J. R., Deane, G. B., Stokes, M. D., Azam, F., Grassian, V. H., and Prather, K. A.: Advancing Model Systems for Fundamental Laboratory Studies of Sea Spray Aerosol Using the Microbial Loop, J. Phys. Chem. A, 119, 8860–8870, https://doi.org/10.1021/acs.jpca.5b03488, 2015.

Lewis, E. R. and Schwartz, S. E.: Sea salt aerosol production: Mechanisms, methods, measurements and models—A critical review, American Geophysical Union, Washington, D. C., 1–408 pp., https://doi.org/10.1029/152GM01, 2004.

Li, R., Palm, B. B., Ortega, A. M., Hlywiak, J., Hu, W., Peng, Z., Day, D. A., Knote, C., Brune, W. H., De Gouw, J. A., and Jimenez, J. L.: Modeling the radical chemistry in an oxidation flow reactor: Radical formation and recycling, sensitivities, and the OH exposure estimation equation, J. Phys. Chem. A, 119, 4418–4432, https://doi.org/10.1021/JP509534K/SUPPL_FILE/JP509534K_SI_001.PDF, 2015.

Liu, P., Ziemann, P. J., Kittelson, D. B., and McMurry, P. H.: Generating particle beams of controlled dimensions and divergence: I. Theory of particle motion in aerodynamic lenses and nozzle expansions, Aerosol Sci. Technol., 22, 293–313, https://doi.org/10.1080/02786829408959748, 1995a.

Liu, P., Ziemann, P. J., Kittelson, D. B., and McMurry, P. H.: Generating particle beams of controlled dimensions and divergence: II. Experimental evaluation of particle motion in aerodynamic lenses and nozzle expansions, Aerosol Sci. Technol., 22, 314–324, https://doi.org/10.1080/02786829408959749, 1995b.

Malfatti, F., Lee, C., Tinta, T., Pendergraft, M. A., Celussi, M., Zhou, Y., Sultana, C. M., Rotter, A., Axson, J. L., Collins, D. B., Santander, M. V., Anides Morales, A. L., Aluwihare, L. I., Riemer, N., Grassian, V. H., Azam, F., and Prather, K. A.: Detection of Active Microbial Enzymes in Nascent Sea Spray Aerosol: Implications for Atmospheric Chemistry and Climate, Environ. Sci. Technol. Lett., 6, 171–177, https://doi.org/10.1021/acs.estlett.8b00699, 2019.

Mason, R. H., Si, M., Li, J., Chou, C., Dickie, R., Toom-Sauntry, D., Pöhlker, C., Yakobi-Hancock, J. D., Ladino, L. A., Jones, K., Leaitch, W. R., Schiller, C. L., Abbatt, J. P. D., Huffman, J. A., and Bertram, A. K.: Ice nucleating particles at a coastal marine boundary

layer site: correlations with aerosol type and meteorological conditions, Atmos. Chem. Phys, 15, 12547–12566, https://doi.org/10.5194/acp-15-12547-2015, 2015.

McCluskey, C. S., Hill, E. T. C. J., Sultana, C. M., Laskina, O., Trueblood, J., Santander, M. V., Beall, C. M., Michaud, J. M., Kreidenweis, S. M., Prather, K. A., Grassian, V., and Demott, P. J.: A mesocosm double feature: Insights into the chemical makeup of marine ice nucleating particles, J. Atmos. Sci., 75, 2405–2423, https://doi.org/10.1175/JAS-D-17-0155.1, 2018a.

McCluskey, C. S., Ovadnevaite, J., Rinaldi, M., Atkinson, J., Belosi, F., Ceburnis, D., Marullo, S., Hill, T. C. J., Lohmann, U., Kanji, Z. A., O'Dowd, C., Kreidenweis, S. M., and DeMott, P. J.: Marine and Terrestrial Organic Ice-Nucleating Particles in Pristine Marine to Continentally Influenced Northeast Atlantic Air Masses, J. Geophys. Res. Atmos., 123, 6196–6212, https://doi.org/10.1029/2017JD028033, 2018b.

McCluskey, C. S., DeMott, P. J., Ma, P. -L., and Burrows, S. M.: Numerical Representations of Marine Ice-Nucleating Particles in Remote Marine Environments Evaluated Against Observations, Geophys. Res. Lett., 46, 7838–7847, https://doi.org/10.1029/2018GL081861, 2019.

Monge, M. E., Rosenørn, T., Favez, O., Müller, M., Adler, G., Riziq, A. A., Rudich, Y., Herrmann, H., George, C., and D'Anna, B.: Alternative pathway for atmospheric particles growth, Proc. Natl. Acad. Sci. U. S. A., 109, 6840–6844, https://doi.org/10.1073/PNAS.1120593109/SUPPL_FILE/PNAS.1120593109_SI.PDF, 2012.

Mostofa, K. M. G., Liu, C., Mottaleb, M. A., Wan, G., Ogawa, H., Vione, D., Yoshioka, T., and Wu, F.: Photobiogeochemistry of Organic Matter, edited by: Mostofa, K. M. G., Yoshioka, T., Mottaleb, A., and Vione, D., Springer Berlin Heidelberg, Berlin, Heidelberg, 1–135 pp., https://doi.org/10.1007/978-3-642-32223-5, 2013.

Murray, B. J., O'sullivan, D., Atkinson, J. D., and Webb, M. E.: Ice nucleation by particles immersed in supercooled cloud dropletsw, Chem. Soc. Rev, 41, 6519–6554, https://doi.org/10.1039/c2cs35200a, 2012.

Niemand, M., Möhler, O., Vogel, B., Vogel, H., Hoose, C., Connolly, P., Klein, H., Bingemer, H., Demott, P., Skrotzki, J., and Leisner, T.: A particle-surface-area-based parameterization of immersion freezing on desert dust particles, J. Atmos. Sci., 69, 3077–3092, https://doi.org/10.1175/JAS-D-11-0249.1, 2012.

Pan, Y. Le, Kalume, A., Wang, C., and Santarpia, J.: Atmospheric aging processes of bioaerosols under laboratory-controlled conditions: A review, J. Aerosol Sci., 155, 105767, https://doi.org/10.1016/J.JAEROSCI.2021.105767, 2021.

Pandis, S. N., Harley, R. A., Cass, G. R., and Seinfeld, J. H.: Secondary organic aerosol formation and transport, Atmos. Environ. Part A, Gen. Top., 26, 2269–2282,

https://doi.org/10.1016/0960-1686(92)90358-R, 1992.

Patterson, J. P., Collins, D. B., Michaud, J. M., Axson, J. L., Sultana, C. M., Moser, T., Dommer, A. C., Conner, J., Grassian, V. H., Stokes, M. D., Deane, G. B., Evans, J. E., Burkart, M. D., Prather, K. A., and Gianneschi, N. C.: Sea spray aerosol structure and composition using cryogenic transmission electron microscopy, ACS Cent. Sci., 2, 40–47, https://doi.org/10.1021/acscentsci.5b00344, 2016.

Peng, Z., Day, D. A., Stark, H., Li, R., Lee-Taylor, J., Palm, B. B., Brune, W. H., and Jimenez, J. L.: HOx radical chemistry in oxidation flow reactors with low-pressure mercury lamps systematically examined by modeling, Atmos. Meas. Tech., 8, 4863–4890, https://doi.org/10.5194/AMT-8-4863-2015, 2015.

Perring, A. E., Schwarz, J. P., Baumgardner, D., Hernandez, M. T., Spracklen, D. V., Heald, C. L., Gao, R. S., Kok, G., McMeeking, G. R., McQuaid, J. B., and Fahey, D. W.: Airborne observations of regional variation in fluorescent aerosol across the United States, J. Geophys. Res. Atmos., 120, 1153–1170, https://doi.org/10.1002/2014JD022495, 2015.

Pöhlker, C., Huffman, J. A., and Pöschl, U.: Autofluorescence of atmospheric bioaerosols-fluorescent biomolecules and potential interferences, Atmos. Meas. Tech, 5, 37–71, https://doi.org/10.5194/amt-5-37-2012, 2012.

Pöschl, U.: Atmospheric aerosols: Composition, transformation, climate and health effects, Angew. Chemie - Int. Ed., 44, 7520–7540, https://doi.org/10.1002/ANIE.200501122, 2005.

Pöschl, U., Martin, S. T., Sinha, B., Chen, Q., Gunthe, S. S., Huffman, J. A., Borrmann, S., Farmer, D. K., Garland, R. M., Helas, G., Jimenez, J. L., King, S. M., Manzi, A., Mikhailov, E., Pauliquevis, T., Petters, M. D., Prenni, A. J., Roldin, P., Rose, D., Schneider, J., Su, H., Zorn, S. R., Artaxo, P., and Andreae, M. O.: Rainforest aerosols as biogenic nuclei of clouds and precipitation in the Amazon, Science (80-.)., 329, 1513–1516, https://doi.org/10.1126/SCIENCE.1191056, 2010.

Prather, K. A., Nordmeyer, T., Salt, K., and J Colloid, S. K.: Real-Time Characterization of Individual Aerosol Particles Using Time-of-Flight Mass Spectrometry, 66, 1403–1407, https://doi.org/https://doi.org/10.1021/ac00081a007, 1994.

Prather, K. A., Bertram, T. H., Grassian, V. H., Deane, G. B., Stokes, M. D., DeMott, P. J., Aluwihare, L. I., Palenik, B. P., Azam, F., Seinfeld, J. H., Moffet, R. C., Molina, M. J., Cappa, C. D., Geiger, F. M., Roberts, G. C., Russell, L. M., Ault, A. P., Baltrusaitis, J., Collins, D. B., Corrigan, C. E., Cuadra-Rodriguez, L. A., Ebben, C. J., Forestieri, S. D., Guasco, T. L., Hersey, S. P., Kim, M. J., Lambert, W. F., Modini, R. L., Mui, W., Pedler, B. E., Ruppel, M. J., Ryder, O. S., Schoepp, N. G., Sullivan, R. C., and Zhao, D.: Bringing the ocean into the laboratory to probe the chemical complexity of sea spray aerosol, Proc. Natl. Acad. Sci. U. S. A., 110, 7550–7555, https://doi.org/10.1073/pnas.1300262110, 2013.

Pratt, K. A., Mayer, J. E., Holecek, J. C., Moffet, R. C., Sanchez, R. O., Rebotier, T. P., Furutani, H., Gonin, M., Fuhrer, K., Su, Y., Guazzotti, S., and Prather, K. A.: Development and Characterization of an Aircraft Aerosol Time-of-Flight Mass Spectrometer, Anal. Chem., 81, 1792–1800, https://doi.org/10.1021/ac801942r, 2009.

Quinn, P. K., Bates, T. S., Schulz, K. S., Coffman, D. J., Frossard, A. A., Russell, L. M., Keene, W. C., and Kieber, D. J.: Contribution of sea surface carbon pool to organic matter enrichment in sea spray aerosol, Nat. Geosci. 2014 73, 7, 228–232, https://doi.org/10.1038/ngeo2092, 2014.

Rastelli, E., Corinaldesi, C., Dell'anno, A., Lo Martire, M., Greco, S., Cristina Facchini, M., Rinaldi, M., O'Dowd, C., Ceburnis, D., and Danovaro, R.: Transfer of labile organic matter and microbes from the ocean surface to the marine aerosol: An experimental approach, Sci. Rep., 7, https://doi.org/10.1038/s41598-017-10563-z, 2017.

Rebotier, T. P. and Prather, K. A.: Aerosol time-of-flight mass spectrometry data analysis: A benchmark of clustering algorithms, Anal. Chim. Acta, 585, 38–54, https://doi.org/10.1016/J.ACA.2006.12.009, 2007.

Rinaldi, M., Fuzzi, S., Decesari, S., Marullo, S., Santoleri, R., Provenzale, A., Von Hardenberg, J., Ceburnis, D., Vaishya, A., O'Dowd, C. D., and Facchini, M. C.: Is chlorophyll-a the best surrogate for organic matter enrichment in submicron primary marine aerosol?, J. Geophys. Res. Atmos., 118, 4964–4973, https://doi.org/10.1002/JGRD.50417, 2013.

Rosenfeld, D., Sherwood, S., Wood, R., and Donner, L.: Climate effects of aerosol-cloud interactions, Science (80-.)., 343, 379–380, https://doi.org/10.1126/SCIENCE.1247490/ASSET/1438E01A-DAE3-4035-9C4E-F5BC3F3FD8D1/ASSETS/GRAPHIC/343_379_F2.JPEG, 2014.

Santarpia, J. L., Pan, Y.-L., Hill, S. C., Baker, N., Cottrell, B., McKee, L., Ratnesar-Shumate, S., and Pinnick, R. G.: Changes in fluorescence spectra of bioaerosols exposed to ozone in a laboratory reaction chamber to simulate atmospheric aging, Opt. Express, 20, 29867, https://doi.org/10.1364/oe.20.029867, 2012.

Šantl-Temkiv, T., Sikoparija, B., Maki, T., Carotenuto, F., Amato, P., Yao, M., Morris, C. E., Schnell, R., Jaenicke, R., Pöhlker, C., DeMott, P. J., Hill, T. C. J., and Huffman, J. A.: Bioaerosol field measurements: Challenges and perspectives in outdoor studies, https://doi.org/10.1080/02786826.2019.1676395, 3 May 2020.

Sauer, J. S., Mayer, K. J., Lee, C., Alves, M. R., Amiri, S., Bahaveolos, C. J., Franklin, E. B., Crocker, D. R., Dang, D., Dinasquet, J., Garofalo, L. A., Kaluarachchi, C. P., Kilgour, D. B., Mael, L. E., Mitts, B. A., Moon, D. R., Moore, A. N., Morris, C. K., Mullenmeister, C. A., Ni, C.-M., Pendergraft, M. A., Petras, D., Simpson, R. M. C., Smith, S., Tumminello, P. R., Walker, J. L., DeMott, P. J., Farmer, D. K., Goldstein, A. H., Grassian, V. H., Jaffe, J. S., Malfatti, F., Martz, T. R., Slade, J. H., Tivanski, A. V., Bertram, T. H., Cappa, C. D., and Prather, K. A.: The Sea Spray Chemistry and Particle Evolution study (SeaSCAPE):

overview and experimental methods, Environ. Sci. Process. Impacts, 24, 290–315, https://doi.org/10.1039/D1EM00260K, 2022.

Savage, N. J., Krentz, C. E., Könemann, T., Han, T. T., Mainelis, G., Pöhlker, C., and Alex Huffman, J.: Systematic characterization and fluorescence threshold strategies for the wideband integrated bioaerosol sensor (WIBS) using size-resolved biological and interfering particles, Atmos. Meas. Tech., 10, 4279–4302, https://doi.org/10.5194/amt-10-4279-2017, 2017.

Seinfeld, J. H. and Pandis, S. N.: Atmospheric chemistry and physics : From air pollution to climate change, 3rd ed., Wiley, 2016.

Shiraiwa, M., Selzle, K., Yang, H., Sosedova, Y., Ammann, M., and Pöschl, U.: Multiphase chemical kinetics of the nitration of aerosolized protein by ozone and nitrogen dioxide, Environ. Sci. Technol., 46, 6672–6680, https://doi.org/10.1021/es300871b, 2012.

Shrestha, M., Luo, M., Li, Y., Xiang, B., Xiong, W., and Grassian, V. H.: Let there be light: stability of palmitic acid monolayers at the air/salt water interface in the presence and absence of simulated solar light and a photosensitizer, Chem. Sci., 9, 5716–5723, https://doi.org/10.1039/C8SC01957F, 2018.

Song, X. H., Hopke, P. K., Fergenson, D. P., and Prather, K. A.: Classification of single particles analyzed by ATOFMS using an artificial neural network, ART-2A, Anal. Chem., 71, 860–865, https://doi.org/10.1021/ac9809682, 1999.

Stokes, M. D., Deane, G. B., Prather, K., Bertram, T. H., Ruppel, M. J., Ryder, O. S., Brady, J. M., and Zhao, D.: A Marine Aerosol Reference Tank system as a breaking wave analogue for the production of foam and sea-spray aerosols, Atmos. Meas. Tech., 6, 1085–1094, https://doi.org/10.5194/amt-6-1085-2013, 2013.

Stokes, M. D., Deane, G., Collins, D. B., Cappa, C., Bertram, T., Dommer, A., Schill, S., Forestieri, S., and Survilo, M.: A miniature Marine Aerosol Reference Tank (miniMART) as a compact breaking wave analogue, Atmos. Meas. Tech., 9, 4257–4267, https://doi.org/10.5194/amt-9-4257-2016, 2016.

Sultana, C. M., Al-Mashat, H., and Prather, K. A.: Expanding Single Particle Mass Spectrometer Analyses for the Identification of Microbe Signatures in Sea Spray Aerosol, Anal. Chem., 89, 10162–10170, https://doi.org/10.1021/acs.analchem.7b00933, 2017a.

Sultana, C. M., Cornwell, G. C., Rodriguez, P., and Prather, K. A.: FATES: A flexible analysis toolkit for the exploration of single-particle mass spectrometer data, Atmos. Meas. Tech., 10, 1323–1334, https://doi.org/10.5194/AMT-10-1323-2017, 2017b.

Textor, C., Schulz, M., Guibert, S., Kinne, S., Balkanski, Y., Bauer, S., Berntsen, T., Berglen, T., Boucher, O., Chin, M., Dentener, F., Diehl, T., Easter, R., Feichter, H., Fillmore, D., Ghan, S., Ginoux, P., Gong, S., Grini, A., Hendricks, J., Horowitz, L., Huang, P., Isaksen, I.,

Iversen, T., Kloster, S., Koch, D., Kirkevåg, A., Kristjansson, J. E., Krol, M., Lauer, A., Lamarque, J. F., Liu, X., Montanaro, V., Myhre, G., Penner, J., Pitari, G., Reddy, S., Seland, Ø., Stier, P., Takemura, T., and Tie, X.: Analysis and quantification of the diversities of aerosol life cycles within AeroCom, Atmos. Chem. Phys, 6, 1777–1813, 2006.

Toprak, E. and Schnaiter, M.: Fluorescent biological aerosol particles measured with the Waveband Integrated Bioaerosol Sensor WIBS-4: Laboratory tests combined with a one year field study, Atmos. Chem. Phys., 13, 225–243, https://doi.org/10.5194/acp-13-225-2013, 2013.

Trueblood, J. V, Wang, X., Or, V. W., Alves, M. R., Santander, M. V, Prather, K. A., and Grassian, V. H.: The Old and the New: Aging of Sea Spray Aerosol and Formation of Secondary Marine Aerosol through OH Oxidation Reactions, https://doi.org/10.1021/acsearthspacechem.9b00087, 2020.

Tsui, W. G. and Mcneill, V. F.: Modeling Secondary Organic Aerosol Production from Photosensitized Humic-like Substances (HULIS), https://doi.org/10.1021/acs.estlett.8b00101, 2018.

Twomey, S.: Pollution and the planetary albedo, Atmos. Environ., 8, 1251–1256, https://doi.org/10.1016/0004-6981(74)90004-3, 1974.

Twomey, S.: The Influence of Pollution on the Shortwave Albedo of Clouds, J. Atmos. Sci., 34, 1149–1152, 1977.

Vali, G.: Quantitative Evaluation of Experimental Results an the Heterogeneous Freezing Nucleation of Supercooled Liquids, J. Atmos. Sci., 28, 402–409, https://doi.org/https://doi.org/10.1175/1520-0469(1971)028<0402:QEOERA>2.0.CO;2, 1971.

Vali, G., DeMott, P. J., Möhler, O., and Whale, T. F.: Technical Note: A proposal for ice nucleation terminology, Atmos. Chem. Phys., 15, 10263–10270, https://doi.org/10.5194/ACP-15-10263-2015, 2015.

Vergara-Temprado, J., Murray, B. J., Wilson, T. W., O'Sullivan, D., Browse, J., Pringle, K. J., Ardon-Dryer, K., Bertram, A. K., Burrows, S. M., Ceburnis, D., Demott, P. J., Mason, R. H., O'Dowd, C. D., Rinaldi, M., and Carslaw, K. S.: Contribution of feldspar and marine organic aerosols to global ice nucleating particle concentrations, Atmos. Chem. Phys., 17, 3637–3658, https://doi.org/10.5194/acp-17-3637-2017, 2017.

Vergara-Temprado, J., Holden, M. A., Orton, T. R., O'Sullivan, D., Umo, N. S., Browse, J., Reddington, C., Baeza-Romero, M. T., Jones, J. M., Lea-Langton, A., Williams, A., Carslaw, K. S., and Murray, B. J.: Is Black Carbon an Unimportant Ice-Nucleating Particle in Mixed-Phase Clouds?, J. Geophys. Res. Atmos., 123, 4273–4283, https://doi.org/10.1002/2017JD027831, 2018a.

Vergara-Temprado, J., Miltenberger, A. K., Furtado, K., Grosvenor, D. P., Shipway, B. J., Hill, A. A., Wilkinson, J. M., Field, P. R., Murray, B. J., and Carslaw, K. S.: Strong control of Southern Ocean cloud reflectivity by ice-nucleating particles, Proc. Natl. Acad. Sci. U. S. A., 115, 2687–2692, https://doi.org/10.1073/pnas.1721627115, 2018b.

Vignati, E., Facchini, M. C., Rinaldi, M., Scannell, C., Ceburnis, D., Sciare, J., Kanakidou, M., Myriokefalitakis, S., Dentener, F., and O'Dowd, C. D.: Global scale emission and distribution of sea-spray aerosol: Sea-salt and organic enrichment, Atmos. Environ., 44, 670–677, https://doi.org/10.1016/j.atmosenv.2009.11.013, 2010.

Wang, X., Deane, G. B., Moore, K. A., Ryder, O. S., Stokes, M. D., Beall, C. M., Collins, D. B., Santander, M. V., Burrows, S. M., Sultana, C. M., and Prather, K. A.: The role of jet and film drops in controlling the mixing state of submicron sea spray aerosol particles, Proc. Natl. Acad. Sci., 114, 6978–6983, https://doi.org/10.1073/pnas.1702420114, 2017.

Wang, X., Gemayel, R., Hayeck, N., Perrier, S., Charbonnel, N., Xu, C., Chen, H., Zhu, C., Zhang, L., Wang, L., Nizkorodov, S. A., Wang, X., Wang, Z., Wang, T., Mellouki, A., Riva, M., Chen, J., and George, C.: Atmospheric Photosensitization: A New Pathway for Sulfate Formation, Cite This Environ. Sci. Technol, 54, 3120, https://doi.org/10.1021/acs.est.9b06347, 2020.

Weber, M. E., Blanchard, D. C., and Syzdek, L. D.: The mechanism of scavenging of waterborne bacteria by a rising bubble, Limnol. Oceanogr., 28, 101–105, https://doi.org/10.4319/lo.1983.28.1.0101, 1983.

Westbrook, C. D. and Illingworth, A. J.: Evidence that ice forms primarily in supercooled liquid clouds at temperatures >-27°C, Geophys. Res. Lett., 38, https://doi.org/10.1029/2011GL048021, 2011.

Yau, M. K. and Rogers, R. R.: A Short Course in Cloud Physics, Elsevier Science, 1996.

Zhang, M., Su, H., Li, G., Kuhn, U., Li, S., Klimach, T., Hoffmann, T., Fu, P., Pöschl, U., and Cheng, Y.: High-Resolution Fluorescence Spectra of Airborne Biogenic Secondary Organic Aerosols: Comparisons to Primary Biological Aerosol Particles and Implications for Single-Particle Measurements, Environ. Sci. Technol., acs.est.1c02536, https://doi.org/10.1021/ACS.EST.1C02536, 2021.

Zhang, X., Smith, K. A., Worsnop, D. R., Jimenez, J., Jayne, J. T., and Kolb, C. E.: A numerical characterization of particle beam collimation by an aerodynamic lens-nozzle system: Part I. An individual lens or nozzle, Aerosol Sci. Technol., 36, 617–631, https://doi.org/10.1080/02786820252883856, 2002.

Zhang, X., Smith, K. A., Worsnop, D. R., Jimenez, J. L., Jayne, J. T., Kolb, C. E., Morris, J., and Davidovits, P.: Numerical characterization of particle beam collimation: Part II integrated aerodynamic-lens-nozzle system, Aerosol Sci. Technol., 38, 619–638, https://doi.org/10.1080/02786820490479833, 2004.

Zhang, Y., van Dijk, M. A., Liu, M., Zhu, G., and Qin, B.: The contribution of phytoplankton degradation to chromophoric dissolved organic matter (CDOM) in eutrophic shallow lakes: Field and experimental evidence, Water Res., 43, 4685–4697, https://doi.org/10.1016/J.WATRES.2009.07.024, 2009.

Chapter 2. Importance of Supermicron Ice Nucleating Particles in Nascent Sea Spray

2.1 Abstract

With oceans covering 71% of the Earth's surface, sea spray aerosol (SSA) particles play an important role in the global radiative budget by acting as cloud condensation nuclei and ice nucleating particles (INPs). By acting as INPs, SSA particles affect the structure and properties of mixed-phase clouds by inducing freezing at warmer temperatures than the homogeneous freezing temperature. Climate models that incorporate marine INPs use the emission of submicron SSA in INP parameterizations because these particles contain a higher fraction of organic mass. Here we show supermicron SSA particles, produced using a natural breaking wave analogue, are the major source of INPs throughout the lifecycle of a phytoplankton bloom. Additionally, supermicron SSA particles are shown to be more efficient INPs than submicron SSA particles, because they carry a greater number of ice active components. Thus, supermicron SSA needs to be incorporated in INP parameterizations for future climate models.

2.2 Introduction

Mixed-phase clouds, those containing both ice crystals and supercooled water, play a significant role in the global radiation budget due to their ubiquity, especially at high latitudes (Shupe et al., 2008). Aerosol particles affect mixed-phase cloud formation by acting as cloud condensation nuclei and ice nuclei. Ice nucleating particles (INPs) have been shown to glaciate mixed-phase clouds and change their radiative and physical properties (DeMott et al., 2010; Lohmann, 2002; Lohmann & Feichter, 2005). Without an effective particle upon which ice can form, water will remain supercooled in the atmosphere down to a temperature of −38°C, where homogeneous freezing occurs for dilute liquid aerosols (Heymsfield & Miloshevich, 1993). However, water will freeze in the atmosphere at temperatures as warm as −1°C with an effective

INP (Després et al., 2012). Determining the freezing conditions of different INPs is important for understanding cloud glaciation influenced by different aerosol populations. It is believed that the primary mechanism for freezing in mixed-phase clouds is through immersion of INPs into supercooled water droplets, known as the immersion freezing mode (Field et al., 2012; Hoose & Möhler, 2012; Murray et al., 2012; Westbrook & Illingworth, 2011).

Sea spray aerosols (SSA) particles have been shown to be a major source of INPs in the marine atmosphere (DeMott et al., 2016; Wilson et al., 2015). SSA particles are considered to be the most likely source of INPs in remote marine locations, representing up to 80% of INPs over the high latitude oceans when dust is not present (Burrows et al., 2013; Vergara-Temprado et al., 2017). Ice nucleating entities (INEs) are the chemical species in seawater that are transferred into SSA particles and can form INPs. Potential species that act as INEs include proteins, carbohydrates, and cell fragments which, along with other organic species, are often enriched in the sea surface microlayer (SSML, Aller et al., 2005; McCluskey et al., 2018b; Schnell & Vali, 1976; Wilson et al., 2015). Wilson et al. (2015) studied INEs in various locations and found the organic-rich SSML contains more INEs that nucleate ice at warmer temperatures than bulk seawater. They showed that, upon filtration of the SSML and subsequent measurement of the ice nucleating ability of the filtrate, INEs in the SSML are likely submicron in size. Using a slightly different sampling method, measurements of the bulk seawater and the SSML in the Canadian Arctic by Irish et al. (2017) concluded that INEs were biological material with diameters between 0.2 and 0.02 μm, supporting the measurements made by Wilson et al. (2015).

Breaking waves form bubbles which burst at the ocean surface to produce SSA. When bubbles rupture, INEs can be transferred from seawater to the atmosphere and serve as INPs in SSA. There are two main SSA production mechanisms: (1) the retraction and fragmentation of the

bubble cap, which ejects film drops and (2) the production of a fluid jet at the base of the bubble that fragments through a Plateau-Rayleigh instability and produces jet drops. These generation mechanisms produce droplets with different size distributions and distinct chemical compositions (Veron, 2015). Wang et al. (2017) investigated the impact of production mechanisms on submicron INP concentrations and found INPs generated by jet drops had higher concentrations than those generated by film drops, suggesting a potential size-differentiated distribution of INEs released in SSA particles. The compositional differences of SSA based on particle size, referred to as a size-resolved external mixing state, have motivated the study of the effect of SSA size on INP concentration. Previously, Rosinski, et al. (1986, 1987) suggested that marine INPs were submicron in size based on physical and chemical analysis of filter-collected INPs. However, Schnell and Vali (1976) discovered a source of "ocean derived nuclei" from seawater INEs that were micron-sized and suggested that these nuclei were responsible for increased INPs over regions of elevated ocean productivity.

There has been a recent resurgence in the number of studies measuring the size of INPs in marine locations, which include anthropogenic and terrestrial sources in addition to SSA (Creamean et al., 2019; Ladino et al., 2019; Mason et al., 2015, 2016; McCluskey et al., 2018a, 2018c; Si et al., 2018). These studies often show that the majority of INPs are supermicron in scale. Although Ladino et al. (2019) hypothesized that some of the supermicron INPs observed could consist of marine biological particles, there may have been other sources, such as mineral dust or terrestrial biological aerosols, making it impossible to definitively determine the origin of the INPs.

The approach here uses a unique system to produce isolated, nascent SSA in a laboratory setting, which excludes all other sources of INPs, to measure the size-resolved ice nucleating activity for immersion freezing. Previously, DeMott et al. (2016) and McCluskey et al. (2017,

2018b) investigated INPs from SSA generated in the laboratory in a wave flume and a Marine Aerosol Reference Tank (MART, Stokes et al., 2013). DeMott et al. (2016) found INP concentrations from laboratory-generated SSA were consistent with concentrations measured in remote marine locations. McCluskey et al. (2017) investigated nascent SSA from mesocosm blooms and observed an increase in INP concentrations after the senescence of phytoplankton bloom biomass. Through chemical analysis of the SSA, McCluskey et al. (2018b) hypothesized two sources of marine INPs: molecular INEs in dissolved organic carbon, and INEs as particulate organic carbon derived from marine microbes. None of these studies reported the size-resolved ice nucleating activity of nascent SSA without the influence of other aerosols. As discussed earlier, the size differentiation of INPs is important for understanding the composition and factors controlling the ice nucleating abilities of SSA particles. Therefore, the size range for the most active INP population was measured over the course of two phytoplankton blooms in natural seawater to better understand how biology and physical production processes affect the ice nucleating ability of SSA.

2.3 Materials and Methods

2.3.1 Overview of the Experiment

SSA was generated during two mesocosm phytoplankton blooms from June 18, 2017 to June 29, 2017 and September 20, 2017 to October 13, 2017. Blooms were induced in an outdoor tank through the addition of nutrients and sodium silicate to seawater collected from the Pacific Ocean. Water from the tank was transferred to a MART to generate SSA. Sampling days were chosen based on chlorophyll-a concentrations, a common indicator of phytoplankton growth. SSA sampling was performed at three critical times during the phytoplankton bloom: before the peak, during the peak, and after the peak of the bloom during senescence.

A schematic of the experiment setup is shown in Figure 2.5. SSA particles generated in the MART were sent into two main sampling lines, one for characterization of the size distribution and the other for collecting SSA on filters for off-line processing of INP activity. SSA particles were dried with silica diffusion driers, to ensure the relative humidity was below the deliquescence point, prior to measuring the size distribution with a scanning mobility particle sizer (SMPS) and an aerodynamic particle sizer (APS). SSA particles for off-line processing were collected onto 0.2 μm polycarbonate filters for a period of 18 h at a flow rate of 4.5 L/min. After collection, the INPs were eluted off the filters with a milliQ water wash and subsequently measured with an automated ice spectrometer, with controlled cooling from −5°C to −35°C, to determine the immersion freezing temperatures of the samples (Beall et al., 2017). The SSA particles were divided into two size ranges before reaching the filters: submicron, which excluded droplets greater than 1 μm dry diameter, and total, which included all droplets produced (both supermicron and submicron). Particles were removed from the submicron SSA population using a custom impactor with a 50% collection efficiency cut-off at an aerodynamic diameter of 2 μm near 80% relative humidity (RH). Particles with aerodynamic diameters of 1 μm at 80% RH passed through with close to 0% collection efficiency and particles with 3 μm diameters had a 90% collection efficiency through this impactor. Assuming spherical particles, there is a factor of 2 size reduction upon desiccation (Lewis & Schwartz, 2004). Therefore, once dried, the aerosol physical diameter at 50% collection efficiency is approximately 1 μm. The supermicron particles removed by the custom impactor were not collected for analysis. Additionally, measurements of seawater chlorophyll-a concentration, and bacterial and viral concentrations were performed on each day. Further details on the methods are in the supporting information and the data is available at: https://doi.org/10.6075/J0GM85TV.

2.4 Results

2.4.1 Conditions for Mesocosm Phytoplankton Blooms

Two phytoplankton blooms, representative of the microbial communities off La Jolla, California at different times of the year, were induced (Figures 2.1a, 2.1b). Both blooms reached chlorophyll-a maximum values in the range of 0.1–10 µg/L, typical of moderate phytoplankton blooms in the Pacific Ocean (Coale et al., 1996; McClain, 2009; Wernand et al., 2013). The first phytoplankton bloom, induced during the summer, reached a maximum chlorophyll-a concentration of 8.79 µg/L, 4 days after spiking with F/100 nutrients. The second phytoplankton bloom, in the fall, showed a minor increase in chlorophyll-a fluorescence after spiking with F/100 but required an additional spike with F/20 nutrients on October 3, 2017 to achieve a full bloom, with a peak concentration of 4.48 µg/L. The two blooms showed similar abundances of both bacteria and viruses, consistent with previous observations in marine environments (Bergh et al., 1989; Hara et al., 1991). Bacterial concentrations during both blooms were on the order of 10^6 mL^{-1} while virus concentrations ranged from 10^7 to 10^8 mL^{-1}.

Phytoplankton blooms follow a typical pattern known as the microbial loop, where the breakdown of phytoplankton coincides with bacterial growth (Azam et al., 1983). After peaking, bacterial concentrations decline due to viral lysis (Wilhelm & Suttle, 1999). Both blooms followed this pattern, with bacterial populations tracking the chlorophyll-a growth with a slight delay (Figures 2.1a, 2.1b). The viral growth progressed after the peak in the bacterial concentrations and generally increased throughout the course of the bloom into senescence. Presuming INEs are biological in origin (Alpert et al., 2011; Irish et al., 2017; Knopf et al., 2011, McCluskey et al., 2018b; Wilson et al., 2015), the concentration of INEs is expected to change throughout these biological growth and degradation processes.

2.4.2 Measured INP Concentrations

Figure 2.2 compares the INP concentrations of total SSA to submicron SSA for both blooms. The INP concentrations for total SSA were typically a factor of 10 higher than those measured for submicron SSA, demonstrating there was a larger abundance of species that form INPs in the supermicron SSA population. On October 2, 2017 the submicron INPs reached their highest concentrations and fell in the lower range of observed total INP concentrations. However, on this day, there were also elevated total INP concentrations and supermicron INPs remained the most abundant. Fisher's exact test was used to compare the significance of the INP concentrations for the total and submicron particle populations for each sampling day of both blooms (Fisher, 1922). The higher INP concentrations observed in total SSA were statistically significant (p-value <0.05) at all times throughout both blooms, independent of the stage of the bloom lifecycles.

The warmest temperatures at which significant differences occurred between total and submicron INP activities ranged from −14°C and −17°C (Table 2.1). At these mid-level temperatures and colder, total INPs were significantly higher in concentration. McCluskey et al. (2017) observed an increase in INP concentrations between temperatures of −15°C and −25°C after the peak of a phytoplankton bloom. Our results show that the predominant INP source in this temperature range was from supermicron particles. There were two observations, at −8°C and −11°C, of warm submicron INPs. Both data points were considerably warmer than the other submicron INP temperatures, indicating they may have been from a distinct source of biological INEs or, more likely, random variability or potential contamination. However, these two outliers did not represent the majority of the INP populations measured or change the conclusion that supermicron INPs dominate in the mid to cold temperatures.

2.4.3 Calculated Number and Volume Site Densities

The number site density, n_s, is often used to describe the efficiency of a single INP type by normalizing the INP concentration to the total dry aerosol surface area, calculated from the number size distribution (Figures 2.6a, 2.6b). The number site density has been used to parameterize INP concentrations from size distributions of SSA and dust INP types in an atmospheric model (McCluskey et al., 2019). In this study, we used the number site density to compare how efficient total INP and submicron INP populations were to one another. As shown in Figure 2.3a, the number site densities for both submicron and total aerosols fell within the values for lab generated SSA previously reported by DeMott et al. (2016). However, the total particles generally showed larger number site densities compared to submicron particles, indicating that submicron SSA are less efficient INPs in primary SSA. Additionally, this figure shows the range of number site density values measured by McCluskey et al. (2018c) for INPs collected in clean marine air masses at the Mace Head Research Station in Ireland.

Figure 2.3a shows the total INP number site densities measured in this laboratory study fell within the range of number site densities measured for ambient SSA. Total INP number site densities occurred at the upper end of those measured at Mace Head. This could be because marine events with enhanced INPs were excluded from the values reported by McCluskey et al. (2018c). This difference may also reflect the influence of atmospheric processes on INPs in the real atmosphere, such as aerosol scavenging through wet and dry deposition and/or secondary reactions. The results of this study are consistent with recent ambient observations suggesting supermicron sized particles play a major role acting as marine INPs.

After normalizing to the surface area, supermicron INPs had moderately higher number site densities compared to submicron particles. A subsequent normalization of the ice active sites to aerosol volume showed submicron and total particle populations had comparable volume site

densities, v_s (Figure 2.3b). A linear fit was generated using the volume site density data from both blooms based on the following equation: $\log_{10}(v_s) = a \cdot T + b$, where v_s is the volume site density (cm^{-3}) and T is the freezing temperature (°C). The fit parameters (±95% confidence intervals) based on this equation were −0.18 (±0.02) and 2.41 (±0.27), respectively, with a coefficient of determination of 0.71. This relationship supports the idea that the number of entrained INEs scales with SSA volume. Supermicron particles, which have larger volumes, therefore likely contain more INEs than submicron SSA particles.

2.4.4 INE Transfer to INP

INE concentrations measured during the second bloom using immersion freezing are reported for bulk seawater and SSML samples (Figure 2.4a, 2.4b). INE concentrations in the microlayer were greater than those in bulk seawater, a trend reported in previous studies (Irish et al., 2017; McCluskey et al., 2018b; Wilson et al., 2015). The concentrations of the INEs in the SSML and bulk seawater fall within those reported for seawater from the Pacific Ocean (McCluskey et al., 2018b). The number of INEs increased over the course of the phytoplankton bloom, which corresponded with the observed increase in total INP concentrations at the end of the bloom (Figure 2.4c); more INEs in the bulk was consistent with more INPs in the SSA. However, the lack of a clear trend between INE and INP concentrations suggests an increase in the number of INEs alone was not sufficient to explain the observed INP concentration behavior. We speculate that unidentified processes influence the selection of INEs into SSA particles. Although INEs were not size selected in our seawater samples, previous studies found that INEs within the SSML and bulk are between 0.02 and 0.2 µm (Irish et al., 2017; McCluskey et al., 2018b; Wilson et al., 2015). Additionally, these studies demonstrated that the INEs are likely biological in nature. It is known that bubbles scavenge both biological and surface-active particles,

resulting in an enrichment of these species at the sea surface (Blanchard et al., 1981; Cunliffe et al., 2013; Weber et al., 1983). Previously, Rastelli et al. (2017) showed supermicron SSA particles contain a higher overall abundance of biological species compared to submicron SSA particles. Furthermore, submicron jet drops were shown to have higher ice nucleating activity than submicron film drops; likely due to the different production mechanisms and different chemical compositions (Wang et al., 2017). A majority (60%–80%) of all submicron SSA particles are film drops (Wang et al., 2017), whereas jet drops are believed to comprise a majority of SSA particles with diameters from 1 to 25 μm (80% RH) (de Leeuw et al., 2011). Therefore, we suggest scavenging of INEs in surface-active material through rising bubbles and subsequent airborne transfer in supermicron sized SSA, likely through jet drops, as an important mode of transport (Figure 2.7).

2.5 Conclusions

Laboratory measurements comparing the ice nucleating activities of submicron versus total SSA particles in an isolated ocean/atmosphere study show supermicron SSA particles are the dominant source of INPs in nascent SSA. We show INPs in supermicron SSA have higher ice nucleation active site densities when normalized by surface area compared to INPs in submicron SSA. When the active sites were normalized to aerosol volume, submicron and total SSA populations showed comparable results, suggesting the transfer of INEs into SSA scales with particle volume. These measurements support the conclusion that supermicron SSA particles are the main source of INPs released from the ocean and marine INEs are predominantly transferred into these particles because they represent the bulk of SSA volume. The dominance of supermicron INPs in nascent SSA is consistent with prior studies, which quantified the important role of supermicron INPs in ambient environments but were unable to unambiguously show that SSA

particles led to the observed difference in activity. This laboratory study is the first to clearly show that supermicron SSA particles represent a key source of nascent INPs in marine environments. A caveat to this conclusion is that the ice nucleating properties of aged SSA are potentially quite different from the nucleating properties of the nascent SSA studied here. Assuming this is not the case, factors leading to changes in SSA production or biological processes resulting in an increased flux of supermicron SSA particles are likely to have a strong impact on marine clouds and climate.

A question remains as to which physical mechanism produces supermicron INPs. As discussed herein, SSA particles are produced via two bubble-bursting mechanisms: (1) the breakup of a jet formed at the base of a bursting bubble producing jet drops and (2) the fragmentation of the retracting bubble cap film producing film drops. Current wisdom is that most supermicron SSA particles, and therefore supermicron INPs, are produced via jet drops (Lewis & Schwartz, 2004). Additionally, it has been proposed that INEs are enriched in jet drops relative to film drops. Wang et al. (2017) analyzed the ice nucleating activity of submicron SSA and, upon normalization to the total aerosol surface area and volume, found INP concentrations from jet drops were greater than those from film drops. They suggested the observed dominance of INPs in submicron jet drops could be explained if the jet drop production mechanism concentrates INEs more than film drop production. Unlike the study by Wang et al. (2017), which used bubble generators, the results shown here on SSA generated using a breaking wave analogue do not suggest enhancement of INEs in supermicron particles after normalization to aerosol volume. However, the dominance of supermicron INPs indicates that jet drops serve as an efficient transfer method of INEs into SSA particles for the observed temperature regime (−26°C to −8°C).

Previous studies aimed at representing marine INPs in global climate models assumed all marine INPs were derived from submicron SSA particles (Burrows et al., 2013; Huang et al., 2018;

Vergara-Temprado et al., 2017). McCluskey et al. (2019) found model-observation closure for marine INPs using ice nucleating site densities that included all aerosol particle sizes. However, they highlighted the critical need for studies that resolve the size-dependence of marine aerosol composition on INP efficiency. Here, supermicron particles represent the major fraction of INPs in nascent SSA during two phytoplankton blooms. These results suggest that existing marine INP parameterizations need to include supermicron marine INPs in global climate models. Additionally, based on the volume scaling shown in this analysis, models should consider parameterizing INPs in SSA based on active sites normalized to dry particle volume as opposed to surface area. Without accounting for the impact of supermicron INPs, this study predicts an underestimation of the number of marine INPs by a factor of 10, which will lead to a subsequent misrepresentation of the effects on the global radiative budget. Future work focused on the composition of INEs and their transfer to the marine atmosphere as INPs will benefit model simulations of aerosol impacts on clouds and climate over remote marine locations, especially over the Southern Ocean.

2.6 Acknowledgments

This study was funded by the National Science Foundation through the NSF Center for Aerosol Impacts on Chemistry of the Environment (CAICE), a Center for Chemical Innovation (CHE-1801971). The authors thank Dr. Tom Hill (University of Colorado, Fort Collins) and Mitchell Santander (University of California, San Diego) for their helpful contributions. The authors also thank both anonymous reviewers who provided extremely helpful feedback and advice. All data supporting the conclusions are publicly available from the UC San Diego Library Digital Collections at: https://doi.org/10.6075/J0GM85TV The authors declare no conflicts of interest or financial interests regarding this work.

Chapter 2, in full, is a reprint of material as it appears in *Geophysical Research Letters*, 2021. Mitts, B. A., Wang, X., Lucero, D. D., Beall, C. M., Deane, G. B., DeMott, P. J., & Prather, K. A. (2021). "Importance of supermicron ice nucleating particles in nascent sea spray" *Geophysical Research Letters* 48, e2020GL089633. An edited version of this paper was published by AGU. Copyright 2021 *American Geophysical Union*. The dissertation author is the primary investigator and author of this manuscript.

2.7 Figures

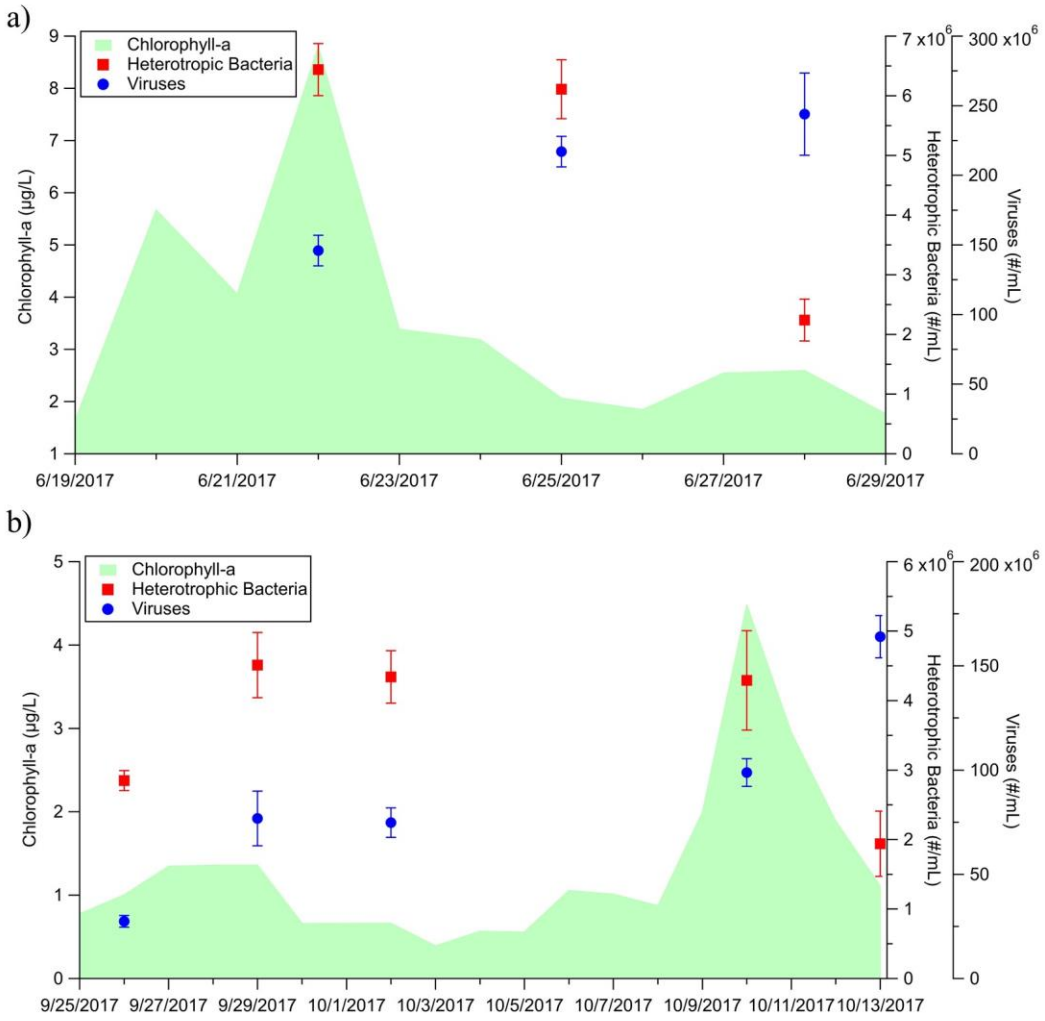

Figure 2.1. Temporal profiles of chlorophyll-a concentration, bacteria and virus concentrations in seawater for (a) Bloom 1 and (b) Bloom 2.

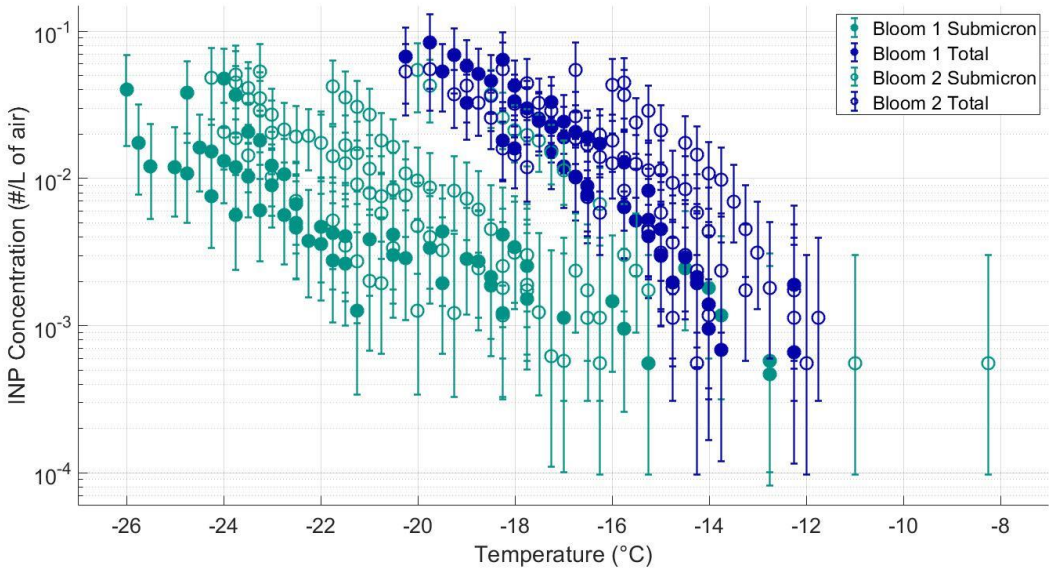

Figure 2.2. INP concentrations for submicron (teal) and total (navy) SSA populations plotted for both Bloom 1 (closed marker) and Bloom 2 (open marker).

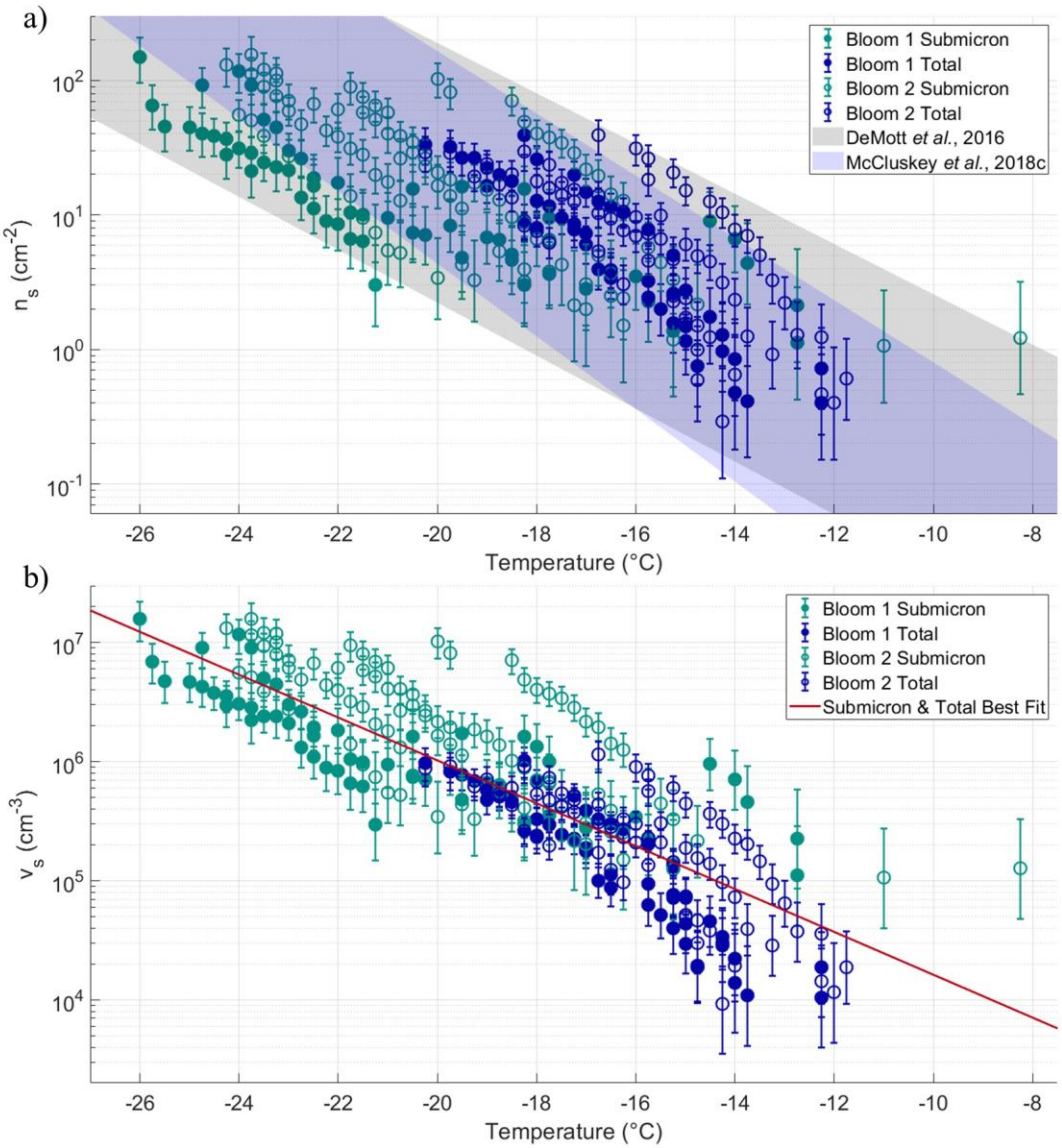

Figure 2.3. (a) Number site densities of the submicron (teal) and total (navy) populations plotted against freezing temperatures for Bloom 1 (closed markers) and Bloom 2 (open markers). For reference, the ranges are plotted for laboratory SSA values from DeMott et al. (2016) and ambient values by McCluskey et al. (2018c). (b) Volume site densities of submicron and total populations plotted against freezing temperatures for Bloom 1 and Bloom 2. A best fit ($R^2 = 0.71$) is shown for the combined total and submicron data from both blooms with the following equation: $\log_{10}(v_s) = -0.18 \cdot T + 2.41$, where v_s is the volume site density (cm^{-3}), and T is temperature (°C).

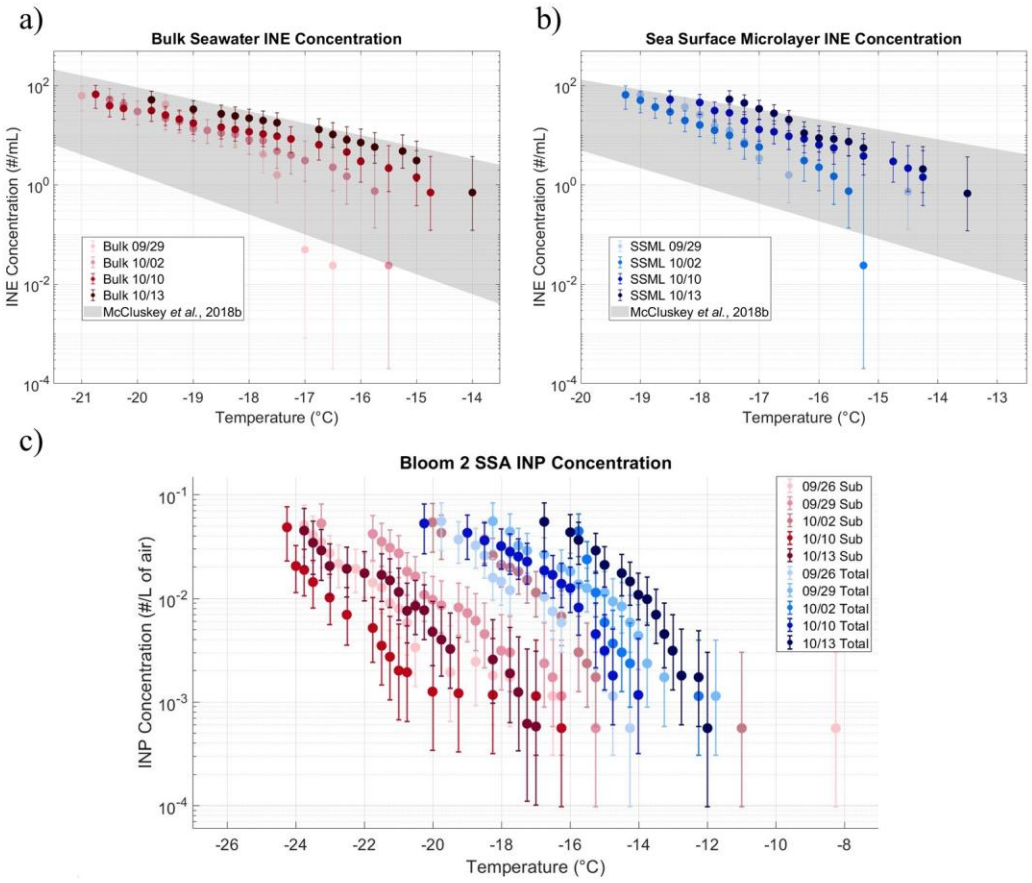

Figure 2.4. Daily INE concentration in (a) bulk seawater; and (b) sea surface microlayer during Bloom 2. (c) Daily INP concentration for Bloom 2 submicron (red) and total (blue) particles. For reference, the range of INE concentrations from bulk seawater and the sea surface microlayer measured by McCluskey et al. (2018b) are included.

2.8 Supplemental Information

2.8.1 Phytoplankton Bloom Experiments

110 gallons of seawater were collected at the Ellen Browning Scripps Memorial Pier (32.8663° N, 117.2546° W) and transported in 5-gallon water containers to the University of California, San Diego. After transport, the seawater was placed in a 300-gallon outdoor tank and spiked with 8.36 mL of sodium silicate and 1.08 mL of Guillard's F/2 algae food, creating an F/100 nutrient solution (Guillard & Ryther, 1962). These solutions contain the necessary metals and nutrients to support a phytoplankton bloom. The first nutrient additions occurred on 6/18/2017 for the first bloom, and on 9/25/2017 for the second phytoplankton bloom. A second addition of F/20 solution was added during the second bloom on 10/03/2017 to increase phytoplankton activity, which was weak. Chlorophyll-a fluorescence was measured using a handheld fluorometer (Turner Designs, AquaFluor) to evaluate phytoplankton activity during the bloom's lifecycle and determine when to sample the SSA. On sampling days, 30 gallons of water were transferred from the outdoor tank into a MART for SSA generation. The water was transferred back into the outdoor tank to continue growth at the end of the sampling period.

2.8.2 Measurement of the Microbial Counts

The microbial activity of both blooms was characterized by measuring the total bacterial and viral concentrations within the bulk seawater. Samples of the bulk seawater were collected on sampling days using a stainless steel spigot on the side of the MART. 1900 µL of each sample was aliquoted into a Cryovial (Simport, Model T311-4A) and fixed with 100 µL of 10% electron microscopy-grade glutaraldehyde. The Cryovials were cooled in a 4°C refrigerator for 15 minutes before flash freezing in liquid nitrogen for 15 minutes and finally placed in a −80°C freezer. For analysis, the samples were thawed and filtered onto 0.02 µm filters (Whatman, Anodisc 25) using

vacuum filtration kept below 5 inHg to prevent cell lysing. The filters were then stained for 15 minutes in the dark using a 25x concentrated Sybr Green II solution following previously described protocols by Noble & Fuhrman (1998). After staining, the filters were dried in a desiccator for 20 minutes and mounted onto a microscopy slide primed with 10 µL of antifade mountant (Invitrogen, SlowFade Gold). A slide cover with 10 µL of antifade mountant was placed atop of the filter to prevent degradation of the nucleic acid stain and then secured with clear nail polish. The slide was then placed into an epifluorescence microscope (Keyence BZ-X700) and illuminated with 470nm light to excite the stain and cause fluorescence emission. Pictures of 10 different sections of the filter were taken at 100X. Bacteria and viruses were then counted in each image and scaled to the size of the filter to represent the total concentration in the sample.

2.8.3 Marine Aerosol Reference Tank

The MART continuously generated an intermittent plunging waterfall (4 seconds on, 10 seconds off). This action produces a realistic size distribution of sea spray aerosols, further details of which can be found in Stokes et al. (2013). The MART allows for a completely isolated system to perform SSA experiments without the influence of anthropogenic aerosol sources. A zero-air generator (Sabio, Model 1001), which scrubs the air of particles, was used to supply clean air into the MART. The headspace of the MART was cleared of any particles before the start of SSA generation and sampling.

2.8.4 Particle Size Distributions

Particle populations were divided based on their size using a custom-built impactor. The impactor cut-off at 2 µm was accomplished with a flow rate of 4.5 L/minute; determined through empirical testing. At this flow rate, half of the population of aerosolized 2 µm polystyrene latex spheres made it through the impactor (50% collection efficiency). A 2 µm cut-off applied to the

SSA generated by the MART (RH ~80%) yielded a dried particle size cut-off of 1 µm (Lewis & Schwartz, 2004). To measure the size distribution of SSA for this experiment, both an SMPS and an APS were used in tandem to cover the particle sizes from 15 nm to 20 µm. The SMPS was composed of an electrostatic classifier (TSI, Model 3082), to size select the aerosols, attached to a water-based condensation particle counter (TSI, Model 3787) to count the number of particles within each size bin. The SMPS measured particle mobility diameter from approximately 14 nm up to 500 nm whereas the APS (TSI, Model 3321) measured the aerodynamic diameter of particles from approximately 500 nm up to 20 µm. To convert the aerodynamic diameter of the APS to the physical diameter, dried SSA were assumed to be spherical particles with a density of 1.8 $g \cdot cm^{-3}$, based on previous measurements (Stokes et al., 2013).

2.8.5 Ice Nucleating Particle Analysis

Prior to any particle collection, INP filters and filter holders were cleaned using 10% hydrogen peroxide for one hour, rinsed three times with milliQ filtered water, and left to dry in a closed, clean space. SSA were collected onto 0.2 µm polycarbonate filters (Whatman, Nuclepore Track Etched Membrane) for eighteen hours, overnight. The flow of air through each INP filter was set to 4.5 L/minute using a mass flow controller. On days with high particle loading, the flow rate dropped on the total filter below the set point of the mass flow controller. However, the original flow of 4.5 L/minute was used to calculate the INP particle concentration deposited on the filter. Therefore, the INP concentration reported for the total size population is effectively a lower limit. After aerosol collection, the filters were removed from the filter holders using hydrogen peroxide-cleaned Teflon forceps, placed into sterile petri dishes, and stored in a −20°C freezer to preserve the samples until analysis at a later date (Wex et al., 2019). For analysis, the filters were thawed and individually placed into sterile 15 mL conical centrifuge tubes (Corning, Falcon

polypropylene centrifuge tubes) along with 4 mL of milliQ filtered water. The tubes were then shaken using an orbital platform shaker (Ibi Scientific, The Belly Dancer) for 15 minutes, transferring the INPs into the liquid solution. Each sample was then pipetted into 30 wells of a 96-well plate, with 50 µL of solution per well. MilliQ water was also pipetted into 30 wells for each test and used as a blank for the INP concentrations. Once filled, the 96-well plate was placed into the automated ice spectrometer (AIS) to determine the immersion freezing temperature and concentration of the INPs in each well (Beall et al., 2017). Error bars associated with the INP concentrations represent the 95% confidence interval, derived from the score confidence interval (Agresti & Coull, 2012).

During the second phytoplankton bloom, bulk seawater and SSML samples were measured to calculate the daily INE concentrations in each sample. SSML samples were collected using the glass plate method and bulk seawater samples were taken from a spigot in the MART tank, located approximately 0.2 meters below the surface of the water (Cunliffe et al., 2013). To measure the INE concentrations, bulk seawater and SSML were pipetted into a 96-well plate and analyzed with the AIS in the same manner as the washed filter samples. Corrections for the freezing depression from salts within these samples were not applied in our analysis.

2.8.6 Number Site Density and Volume Site Density Calculations

The number site density, n_s (per square centimeter), is calculated by dividing the INP concentration (per liter of air) of each day, by the daily mean surface area (units of square micrometer per cubic centimeter). The n_s is calculated through the following equation:

$$n_s(T) = n_{INPs}(T)\left(\frac{10^5}{S_{tot}}\right) \qquad [2.1]$$

Where, in Eq. 2.1, $n_{INPs}(T)$ corresponds to the INP concentration at a given temperature, S_{tot} represents the daily mean surface area, and the 10^5 factor is applied to account for the INP units of

liters of air. Error for the number site density was propagated from the standard deviation of the surface area and the standard deviation of the INP concentrations. The standard deviation of the combined size distribution measured by the APS and the SMPS was calculated for the submicron and total particle population for each sampling day and propagated to the daily standard deviation of the surface area distribution. The standard deviation of the INP concentrations was calculated based on the score confidence interval equation (Agresti & Coull, 2012) using a z-score of 1 to get the 68% confidence interval, which was assumed as the standard deviation based on a normal distribution.

The volume site density v_s (per cubic centimeter) was calculated in the same manner as the number site density but by dividing by the daily mean volume (units of cubic micrometer per cubic centimeter). V_s is calculated through the following equation:

$$v_s(T) = n_{INPs}(T)\left(\frac{10^9}{V_{tot}}\right) \quad [2.2]$$

Where in Eq. 2.2, $n_{INPs}(T)$ again corresponds to the INP concentration at a given temperature, V_{tot} represents the daily mean volume, and the 10^9 factor accounts for the INP units of liters of air. Error for the volume site density was propagated in the same manner as the number site density but instead using the propagated standard deviation of the volume and the standard deviation of the INP concentrations.

2.9 Supplemental Figures

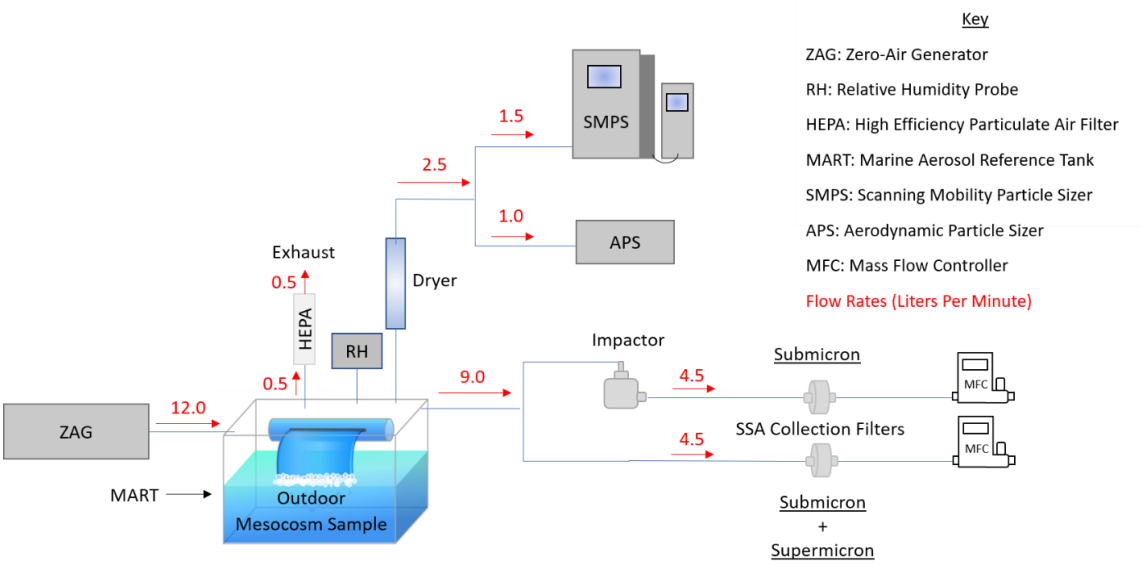

Figure 2.5. Experimental setup.

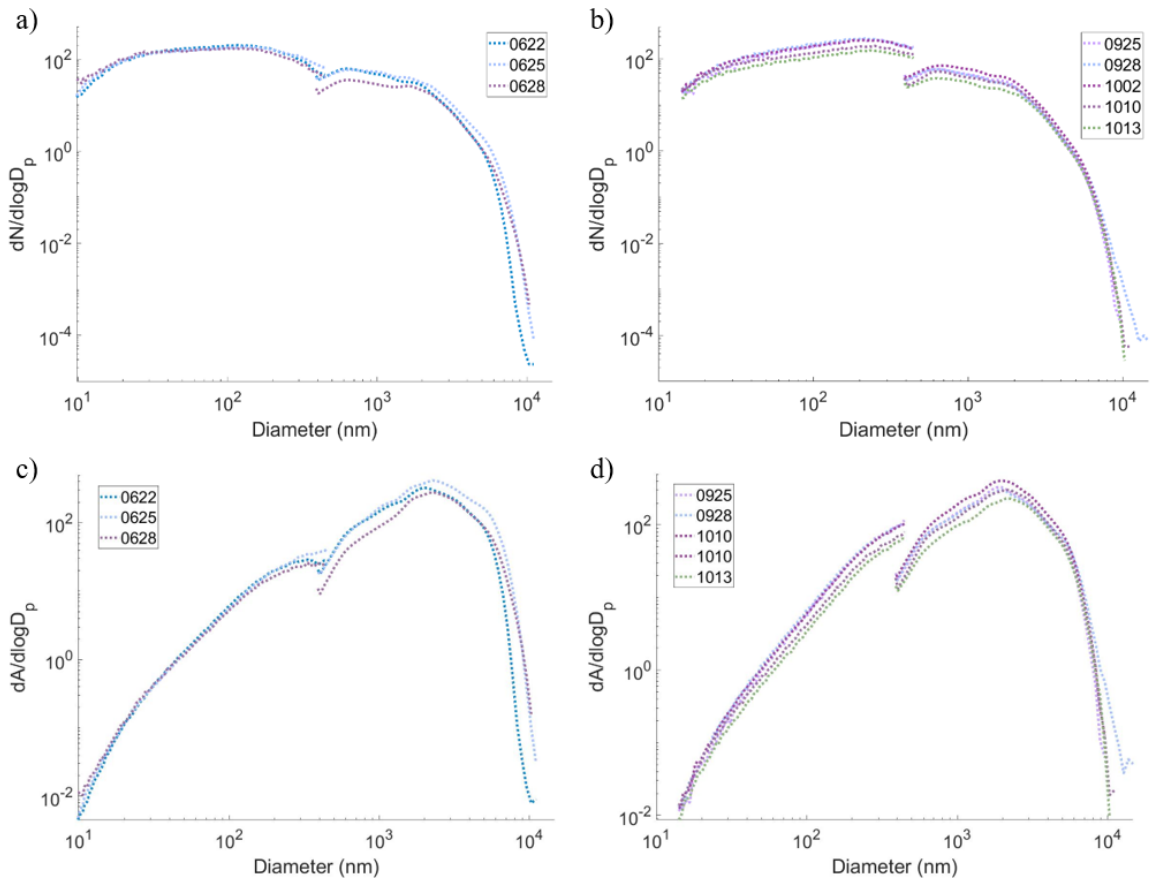

Figure 2.6. Dry diameter, number size distributions for (a) Bloom 1 and (b) Bloom 2 measured with an aerodynamic particle sizer and a scanning mobility particle sizer. Surface area distributions for (c) Bloom 1 and (d) Bloom 2.

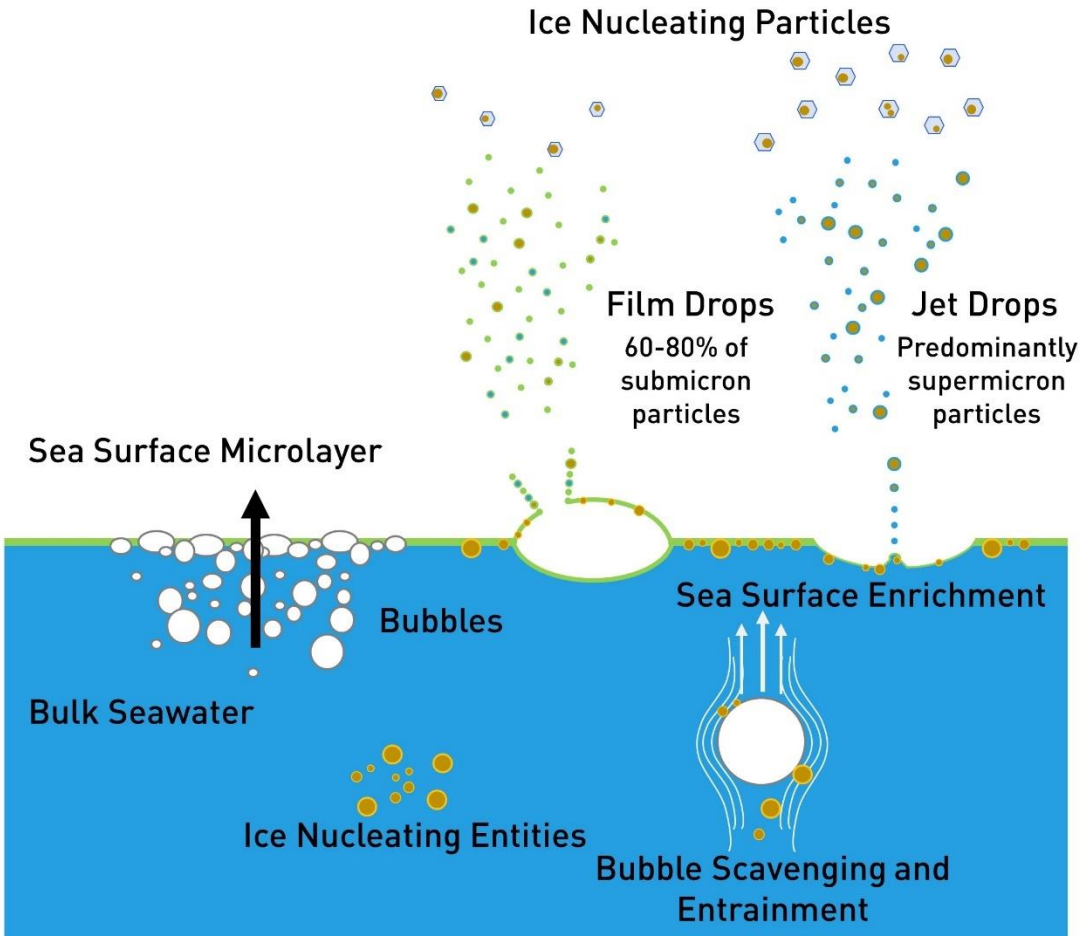

Figure 2.7. Schematic depicting a potential process by which ice nucleating entities are scavenged through rising bubbles and subsequently ejected through jet drops and film drops, resulting in ice nucleating particles.

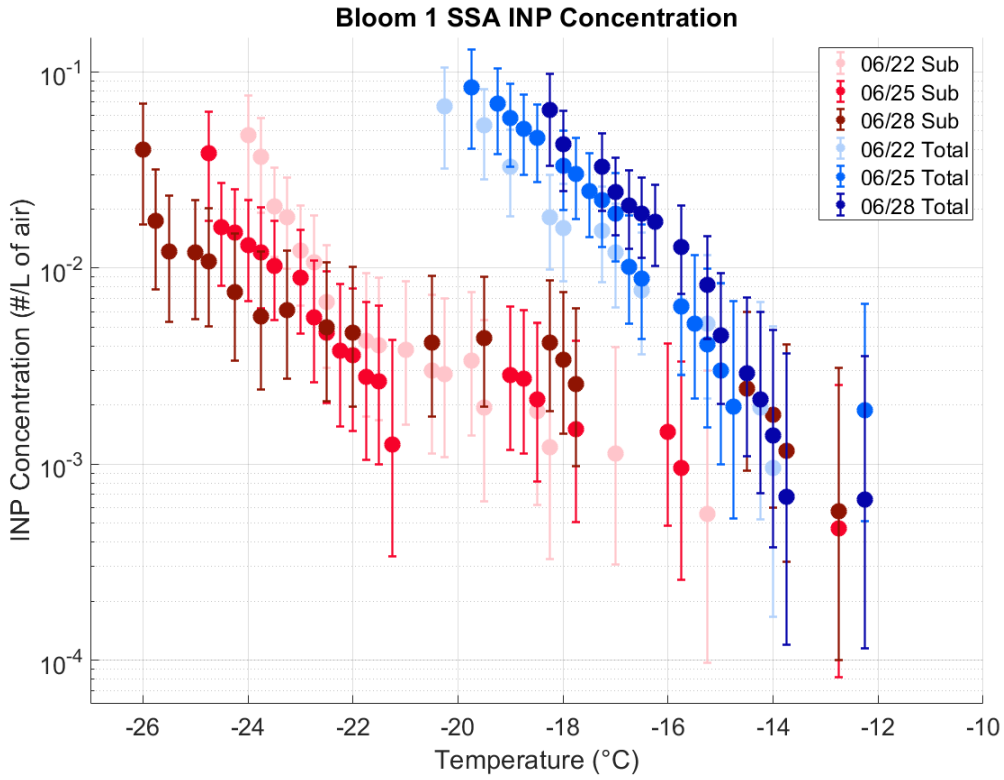

Figure 2.8. Daily INP concentrations for the Bloom 1 submicron (red) and total (blue) particle populations.

2.10 Supplemental Tables

Table 2.1. The warmest temperatures at which the differences between the total and submicron INP concentrations were statistically significant across each sampling day of both blooms. Significance was determined using the Fisher's exact test (Fisher, 1922).

Bloom 1 Date	Temperature (°C)
06/22/2017	−17
06/25/2017	−17
06/28/2017	−17
Bloom 2 Date	Temperature (°C)
09/26/2017	−17
09/29/2017	−14
10/02/2017	−15
10/10/2017	−16
10/13/2017	−14

2.11 References

Agresti, A., & Coull, B. A. (1998). Approximate is better than "exact" for interval estimation of binomial proportions. The American Statistician, 52(2), 119–126. https://doi.org/10.1080/00031305.1998.10480550

Aller, J. Y., Kuznetsova, M. R., Jahns, C. J., & Kemp, P. F. (2005). The sea surface microlayer as a source of viral and bacterial enrichment in marine aerosols. Journal of Aerosol Science, 36(5–6), 801–812. https://doi.org/10.1016/j.jaerosci.2004.10.012

Alpert, P. A., Aller, J. Y., & Knopf, D. A. (2011). Ice nucleation from aqueous NaCl droplets with and without marine diatoms. Atmospheric Chemistry and Physics, 11, 5539–5555. https://doi.org/10.5194/acp-11-5539-2011

Azam, F., Fenchel, T., Field, J., Gray, J., Meyer-Reil, L., & Thingstad, F. (1983). The ecological role of water-column microbes in the sea. Marine Ecology Progress Series, 10, 257–263. https://doi.org/10.3354/meps010257

Beall, C. M., Stokes, M. D., Hill, T. C., Demott, P. J., Dewald, J. T., & Prather, K. A. (2017). Automation and heat transfer characterization of immersion mode spectroscopy for analysis of ice nucleating particles. Atmospheric Measurement Techniques, 10, 2613–2626. https://doi.org/10.5194/amt-10-2613-2017

Bergh, Ø., Børsheim, K. Y., Bratbak, G., & Heldal, M. (1989). High abundance of viruses found in aquatic environments. Nature, 340(6233), 467–468. https://doi.org/10.1038/340467a0

Blanchard, D. C., Syzdek, L. D., & Weber, M. E. (1981). Bubble scavenging of bacteria in freshwater quickly produces bacterial enrichment in airborne jet drops. Limnology and Oceanography, 26(5), 961–964. https://doi.org/10.4319/lo.1981.26.5.0961

Burrows, S. M., Hoose, C., Pöschl, U., & Lawrence, M. G. (2013). Ice nuclei in marine air: Biogenic particles or dust? Atmospheric Chemistry and Physics, 13(1), 245–267. https://doi.org/10.5194/acp-13-245-2013

Coale, K. H., Johnson, K. S., Fitzwater, S. E., Gordon, R. M., Tanner, S., Chavez, F. P., Ferioli, L., Sakamoto, C., Rogers, P., Millero, F., Steinberg, P., Nightingale, P., Cooper, D., Cochlan, W. P., Landry, M. R., Constantinou, J., Rollwagen, G., Trasvina, A., & Kudela, R. (1996). A massive phytoplankton bloom induced by an ecosystem-scale iron fertilization experiment in the equatorial Pacific Ocean. Nature, 383(6600), 495-501. https://doi.org/10.1038/383495a0

Creamean, J. M., Cross, J. N., Pickart, R., McRaven, L., Lin, P., Pacini, A., Hanlon, R., Schmale, D. G., Ceniceros, J., Aydell, T., Colombi, N., Bolger, E., & DeMott, P. J. (2019). Ice nucleating particles carried from below a phytoplankton bloom to the Arctic atmosphere. Geophysical Research Letters, 46(14), 8572–8581. https://doi.org/10.1029/2019GL083039

Cunliffe, M., Engel, A., Frka, S., Gašparović, B. Ž., Guitart, C., Murrell, J. C., Salter, M., Stolle, C., Upstill-Goddard, R., & Wurl, O. (2013). Sea surface microlayers: A unified physicochemical and biological perspective of the air-ocean interface. Progress in Oceanography, 109, 104-116. https://doi.org/10.1016/j.pocean.2012.08.004

de Leeuw, G., Andreas, E. L., Anguelova, M. D., Fairall, C. W., Lewis, E. R., O'Dowd, C., Schulz, M., & Schwartz, S. E. (2011). Production flux of sea spray aerosol. Reviews of Geophysics, 49(2), RG2001. https://doi.org/10.1029/2010RG000349

DeMott, P. J., Prenni, A. J., Liu, X., Kreidenweis, S. M., Petters, M. D., Twohy, C. H., Richardson, M. S., Eidhammer, T., & Rogers, D. C. (2010). Predicting global atmospheric ice nuclei distributions and their impacts on climate. Proceedings of the National Academy of Sciences of the United States of America, 107(25), 11217–11222. https://doi.org/10.1073/pnas.0910818107

DeMott, P. J., Hill, T. C. J., McCluskey, C. S., Prather, K. A., Collins, D. B., Sullivan, R. C., Ruppel, M. J., Mason, R. H., Irish, V. E., Lee, T., Hwang, C. Y., Rhee, T. S., Snider, J. R., McMeeking, G. R., Dhaniyala, S., Lewis, E. R., Wentzell, J. J. B., Abbatt, J., Lee, C., Sultana, C. M., Ault, A. P., Axson, J. L., Diaz Martinez, M., Venero, I., Santos-Figueroa, G., Stokes, M. D., Deane, G. B., Mayol-Bracero, O. L., Grassian, V. H., Bertram, T. H., Bertram, A. K., Moffett, B. F., & Franc, G. D. (2016). Sea spray aerosol as a unique source of ice nucleating particles. Proceedings of the National Academy of Sciences of the United States of America, 113(21), 5797–5803. https://doi.org/10.1073/pnas.1514034112

Després, V. R., Huffman, J. A., Burrows, S. M., Hoose, C., Safatov, A. S., Buryak, G., Fröhlich-Nowoisky, J., Elbert, W., Andreae, M. O., Pöschl, U., & Jaenicke, R. (2012). Primary biological aerosol particles in the atmosphere: A review. Tellus, Series B: Chemical and Physical Meteorology, 64(1). https://doi.org/10.3402/tellusb.v64i0.15598

Field, P. R., Heymsfield, A. J., Shipway, B. J., Demott, P. J., Pratt, K. A., Rogers, D. C., Stith, J., & Prather, K. A. (2012). Ice in clouds experiment-layer clouds. Part II: Testing characteristics of heterogeneous ice formation in lee wave clouds. Journal of the Atmospheric Sciences, 69(3), 1066–1079. https://doi.org/10.1175/JAS-D-11-026.1

Fisher, R. A. (1922). On the interpretation of χ^2 from contingency tables, and the calculation of p. Journal of the Royal Statistical Society, 85(1), 87-94. https://doi.org/10.2307/2340521

Guillard, R. R. L., & Ryther, J. H. (1962). Studies of marine planktonic diatoms: I. Cyclotella nana Hustedt, and Detonula confervacea (Cleve) Gran. Canadian Journal of Microbiology, 8(2), 229–239. https://doi.org/10.1139/m62-029

Hara, S., Terauchi, K., & Koike, I. (1991). Abundance of viruses in marine waters: Assessment by epifluorescence and transmission electron microscopy. Applied and Environmental Microbiology, 57(9), 2731–2734. https://doi.org/10.1128/aem.57.9.2731-2734.1991

Heymsfield, A. J., & Miloshevich, L. M. (1993). Homogeneous ice nucleation and supercooled liquid water in orographic wave clouds. Journal of the Atmospheric Sciences, 50(15), 2335-2353. https://doi.org/10.1175/1520-0469(1993)050<2335:HINASL>2.0.CO;2

Hoose, C., & Möhler, O. (2012). Heterogeneous ice nucleation on atmospheric aerosols: A review of results from laboratory experiments. Atmospheric Chemistry and Physics, 12, 9817–9854. https://doi.org/10.5194/acp-12-9817-2012

Huang, W. T. K., Ickes, L., Tegen, I., Rinaldi, M., Ceburnis, D., & Lohmann, U. (2018). Global relevance of marine organic aerosol as ice nucleating particles. Atmospheric Chemistry and Physics, 18(15), 11423–11445. https://doi.org/10.5194/acp-18-11423-2018

Irish, V. E., Elizondo, P., Chen, J., Chou, C., Charette, J., Lizotte, M., Ladino, L. A., Wilson, T. W., Gosselin, M., Murray, B. J., Polishchuk, E., Abbatt, J. P. D., Miller, L. A., & Bertram, A. K. (2017). Ice-nucleating particles in Canadian Arctic sea-surface microlayer and bulk seawater. Atmospheric Chemistry and Physics, 17, 10583–10595. https://doi.org/10.5194/acp-17-10583-2017

Knopf, D. A., Alpert, P. A., Wang, B., & Aller, J. Y. (2011). Stimulation of ice nucleation by marine diatoms. Nature Geoscience, 4(2), 88–90. https://doi.org/10.1038/ngeo1037

Ladino, L. A., Raga, G. B., Alvarez, H., Rosas, I., Alvarez-Ospina, H., Andino-Enríquez, M. A., Martínez, L., Salinas, E., Miranda, J., Ramírez-Díaz, Z., Figueroa, B., Chou, C., Bertram, A. K., Quintana, E. T., Maldonado, L. A., García-Reynoso, A., Si, M., & Irish, V. E. (2019). Ice-nucleating particles in a coastal tropical site. Atmospheric Chemistry and Physics, 19, 6147–6165. https://doi.org/10.5194/acp-19-6147-2019

Lewis, E. R., & Schwartz, S. E. (2004). Sea salt aerosol production: Mechanisms, methods, measurements and models—A critical review. Geophysical Monograph Series (Vol. 152). Washington, D. C.: American Geophysical Union. https://doi.org/10.1029/152GM01

Lohmann, U. (2002). A glaciation indirect aerosol effect caused by soot aerosols. Geophysical Research Letters, 29(4), 11-1-11-4. https://doi.org/10.1029/2001GL014357

Lohmann, U., & Feichter, J. (2005). Global indirect aerosol effects: A review. Atmospheric Chemistry and Physics, 5(3), 715–737. https://doi.org/10.5194/acp-5-715-2005

Mason, R. H., Si, M., Chou, C., Irish, V. E., Dickie, R., Elizondo, P., Wong, R., Brintnell, M., Elsasser, M., Lassar, W. M., Pierce, K. M., Leaitch, W. R., Macdonald, A. M., Platt, A., Toom-Sauntry, D., Sarda-Estève, R., Schiller, C. L., Suski, K. J., Hill, T. C. J., Abbatt, J. P. D., Huffman, J. A., Demott, P. J., & Bertram, A. K. (2016). Size-resolved measurements of ice-nucleating particles at six locations in North America and one in Europe. Atmospheric Chemistry and Physics, 16, 1637–1651. https://doi.org/10.5194/acp-16-1637-2016

Mason, R. H., Si, M., Li, J., Chou, C., Dickie, R., Toom-Sauntry, D., Pöhlker, C., Yakobi-Hancock, J. D., Ladino, L. A., Jones, K., Leaitch, W. R., Schiller, C. L., Abbatt, J. P. D., Huffman, J. A., & Bertram, A. K. (2015). Ice nucleating particles at a coastal marine boundary layer site: correlations with aerosol type and meteorological conditions. Atmospheric Chemistry and Physics, 15, 12547–12566. https://doi.org/10.5194/acp-15-12547-2015

McClain, C. R. (2009). A decade of satellite ocean color observations. Annual Review of Marine Science, 1(1), 19–42. https://doi.org/10.1146/annurev.marine.010908.163650

McCluskey, C. S., DeMott, P. J., Ma, P. L., & Burrows, S. M. (2019). Numerical representations of marine ice-nucleating particles in remote marine environments evaluated against observations. Geophysical Research Letters, 46(13), 7838–7847. https://doi.org/10.1029/2018GL081861

McCluskey, C. S., Hill, T. C. J., Humphries, R. S., Rauker, A. M., Moreau, S., Strutton, P. G., Chambers, S. D., Williams, A. G., McRobert, I., Ward, J., Keywood, M. D., Harnwell, J., Ponsonby, W., Loh, Z. M., Krummel, P. B., Protat, A., Kreidenweis, S. M., & DeMott, P. J. (2018a). Observations of ice nucleating particles over Southern Ocean waters. Geophysical Research Letters, 45(21), 11,989-11,997. https://doi.org/10.1029/2018GL079981

McCluskey, C. S., Hill, E. T. C. J., Sultana, C. M., Laskina, O., Trueblood, J., Santander, M. V., Beall, C. M., Michaud, J. M., Kreidenweis, S. M., Prather, K. A., Grassian, V., & Demott, P. J. (2018b). A mesocosm double feature: Insights into the chemical makeup of marine ice nucleating particles. Journal of the Atmospheric Sciences, 75(7), 2405–2423. https://doi.org/10.1175/JAS-D-17-0155.1

McCluskey, C. S., Hill, T. C. J., Malfatti, F., Sultana, C. M., Lee, C., Santander, M. V., Beall, C. M., Moore, K. A., Cornwell, G. C., Collins, D. B., Prather, K. A., Jayarathne, T., Stone, E. A., Azam, F., Kreidenweis, S. M., & DeMott, P. J. (2017). A dynamic link between ice nucleating particles released in nascent sea spray aerosol and oceanic biological activity during two mesocosm experiments. Journal of the Atmospheric Sciences, 74(1), 151–166. https://doi.org/10.1175/JAS-D-16-0087.1

McCluskey, C. S., Ovadnevaite, J., Rinaldi, M., Atkinson, J., Belosi, F., Ceburnis, D., Marullo, S., Hill, T. C. J., Lohmann, U., Kanji, Z. A., O'Dowd, C., Kreidenweis, S. M., & DeMott, P. J. (2018c). Marine and terrestrial organic ice-nucleating particles in pristine marine to continentally influenced northeast Atlantic air masses. Journal of Geophysical Research: Atmospheres, 123(11), 6196–6212. https://doi.org/10.1029/2017JD028033

Murray, B. J., O'sullivan, D., Atkinson, J. D., & Webb, M. E. (2012). Ice nucleation by particles immersed in supercooled cloud droplets. Chemical Society Reviews, 41, 6519–6554. https://doi.org/10.1039/c2cs35200a

Noble, R. T., & Fuhrman, J. A. (1998). Use of SYBR Green I for rapid epifluorescence counts of marine viruses and bacteria. Aquatic Microbial Ecology, 14(2), 113–118. https://doi.org/10.3354/ame014113

Rastelli, E., Corinaldesi, C., Dell'anno, A., Martire, M. L., Greco, S., Facchini, M. C., Rinaldi, M., O'Dowd, C., Ceburnis, D., & Danovaro, R. (2017). Transfer of labile organic matter and microbes from the ocean surface to the marine aerosol: An experimental approach. Scientific Reports, 7(1). https://doi.org/10.1038/s41598-017-10563-z

Rosinski, J., Haagenson, P. L., Nagamoto, C. T., & Parungo, F. (1986). Ice-forming nuclei of maritime origin. Journal of Aerosol Science, 17(1), 23–46. https://doi.org/10.1016/0021-8502(86)90004-2

Rosinski, J., Haagenson, P. L., Nagamoto, C. T., & Parungo, F. (1987). Nature of ice-forming nuclei in marine air masses. Journal of Aerosol Science, 18(3), 291–309. https://doi.org/10.1016/0021-8502(87)90024-3

Schnell, R. C., & Vali, G. (1976). Biogenic Ice Nuclei: Part 1. Terrestrial and marine sources. Journal of the Atmospheric Sciences, 33(8), 1554–1564. https://doi.org/10.1175/1520-0469(1976)033<1554:BINPIT>2.0.CO;2

Shupe, M. D., Daniel, J. S., de Boer, G., Eloranta, E. W., Kollias, P., Long, C. N., Luke, E. P., Turner, D. D., & Verlinde, J. (2008). A focus on mixed-phase clouds The status of ground-based observational methods. American Meteorological Society, 89(10), 1549-1562. https://doi.org/10.1175/2008BAMS2378.1

Si, M., Irish, V. E., Mason, R. H., Vergara-Temprado, J., Hanna, S., Ladino, L. A., Yakobi-Hancock, J. D., Schiller, C. L., Wentzell, J. J. B., Abbatt, J. P. D., Carslaw, K. S., Murray, B. J., & Bertram, A. K. (2018). Ice-nucleating efficiency of aerosol particles and possible sources at three coastal marine sites. Atmospheric Chemistry and Physics, 18, 15669–15685. https://doi.org/10.5194/acp-2018-81

Stokes, M. D., Deane, G. B., Prather, K., Bertram, T. H., Ruppel, M. J., Ryder, O. S., Brady, J. M., and Zhao, D.: A Marine Aerosol Reference Tank system as a breaking wave analogue for the production of foam and sea-spray aerosols, Atmos. Meas. Tech., 6, 1085–1094, https://doi.org/10.5194/amt-6-1085-2013, 2013.

Vergara-Temprado, J., Murray, B. J., Wilson, T. W., O'Sullivan, D., Browse, J., Pringle, K. J., Ardon-Dryer, K., Bertram, A. K., Burrows, S. M., Ceburnis, D., Demott, P. J., Mason, R. H., O'Dowd, C. D., Rinaldi, M., & Carslaw, K. S. (2017). Contribution of feldspar and marine organic aerosols to global ice nucleating particle concentrations. Atmospheric Chemistry and Physics, 17(5), 3637–3658. https://doi.org/10.5194/acp-17-3637-2017

Veron, F. (2015). Ocean Spray. Annual Review of Fluid Mechanics, 47(1), 507–538. https://doi.org/10.1146/annurev-fluid-010814-014651

Wang, X., Deane, G. B., Moore, K. A., Ryder, O. S., Stokes, M. D., Beall, C. M., Collins, D. B., Santander, M. V., Burrows, S. M., Sultana, C. M., & Prather, K. A.. (2017). The role of jet and film drops in controlling the mixing state of submicron sea spray aerosol particles. Proceedings of the National Academy of Sciences of the United States of America, 114(27), 6978–6983. https://doi.org/10.1073/pnas.1702420114

Weber, M. E., Blanchard, D. C., & Syzdek, L. D. (1983). The mechanism of scavenging of waterborne bacteria by a rising bubble. Limnology and Oceanography, 28(1), 101–105. https://doi.org/10.4319/lo.1983.28.1.0101

Wernand, M. R., van der Woerd, H. J., & Gieskes, W. W. C. (2013). Trends in ocean colour and chlorophyll concentration from 1889 to 2000, worldwide. PLoS ONE, 8(6), e63766. https://doi.org/10.1371/journal.pone.0063766

Westbrook, C. D., & Illingworth, A. J. (2011). Evidence that ice forms primarily in supercooled liquid clouds at temperatures > −27°C. Geophysical Research Letters, 38(14). https://doi.org/10.1029/2011GL048021

Wex, H., Huang, L., Zhang, W., Hung, H., Traversi, R., Becagli, S., Sheesley, R. J., Moffett, C. E., Barrett, T. E., Bossi, R., Skov, H., Hünerbein, A., Lubitz, J., Löffler, M., Linke, O., Hartmann, M., Herenz, P., & Stratmann, F. (2019). Annual variability of ice-nucleating particle concentrations at different Arctic locations. Atmospheric Chemistry and Physics, 19, 5293–5311. https://doi.org/10.5194/acp-19-5293-2019

Wilhelm, S. W., & Suttle, C. A. (1999). Viruses and nutrient cycles in the sea. BioScience, 49(10), 781–788. https://doi.org/10.2307/1313569

Wilson, T. W., Ladino, L. A., Alpert, P. A., Breckels, M. N., Brooks, I. M., Browse, J., J., Burrows, S. M., Carslaw, K. S., Huffman, J. A., Judd, C., Kilthau, W. P., Mason, R. H., McFiggans, G., Miller, L. A., Najera, J. J., Polishchuk, E., Rae, S., Schiller, C. L., Si, M., Temprado, J. V., Whale, T. F., Wong, J. P. S., Wurl, O., Yakobi-Hancock, J. D., Abbatt, J. P. D., Aller, J. Y., Bertram, A. K., Knopf, D. A., & Murray, B. J. (2015). A marine biogenic source of atmospheric ice-nucleating particles. Nature, 525(7568), 234–238. https://doi.org/10.1038/nature14986

Chapter 3. Tandem fluorescence measurements of organic matter and bacteria released in sea spray aerosols

3.1 Abstract

Biological aerosols, typically identified through their fluorescence properties, strongly influence clouds and climate. Sea spray aerosol (SSA) particles are a major source of biological aerosols, but detection in the atmosphere is challenging due to potential interference from other sources. Here, the fluorescence signature of isolated SSA, produced using laboratory-based aerosol generation methods, was analyzed and compared with two commonly used fluorescence techniques: excitation−emission matrix spectroscopy (EEMS) and the wideband integrated bioaerosol sensor (WIBS). A range of dynamic biological ocean scenarios were tested to compare EEMS and WIBS analyses of SSA. Both techniques revealed similar trends in SSA fluorescence intensity in response to changes in ocean microbiology, demonstrating the potential to use the WIBS to measure fluorescent aerosols alongside EEMS bulk solution measurements. Together, these instruments revealed a unique fluorescence signature of isolated, nascent SSA and, for the first time, a size-segregated emission of fluorescent species in SSA. Additionally, the fluorescence signature of aerosolized marine bacterial isolates was characterized and showed similar fluorescence peaks to those of SSA, suggesting that bacteria are a contributor to SSA fluorescence. Through investigation of isolated SSA, this study provides a reference for future identification of marine biological aerosols in a complex atmosphere.

3.2 Introduction

Biological aerosols, or bioaerosols, are particles that include organisms, biological fragments, excretions, or dispersal units (Fröhlich-Nowoisky et al., 2016). These particles are ubiquitous in the atmosphere and can have profound effects on clouds and climate by acting as

cloud condensation nuclei and ice nuclei in clouds (Fröhlich-Nowoisky et al., 2016). Therefore, there is a strong interest to identify bioaerosols and understand their atmospheric dynamics. A widely used method for bioaerosol identification is fluorescence spectroscopy, which exploits the intrinsically fluorescent biomolecules found in these aerosols (Pöhlker et al., 2012). However, aerosols in the atmosphere are often externally mixed populations from different sources, making it a challenge to separate particle types based on fluorescence alone. Thus, it is necessary to characterize the fluorescence of isolated particle sources to disentangle the impact of different bioaerosols in the atmosphere.

The oceans have been shown to be a major source of bioaerosols, via sea spray aerosol (SSA) particles (Fröhlich-Nowoisky et al., 2016; Després et al., 2012). SSA particles are produced when bubbles, entrained by breaking waves, burst at the sea surface. SSA composition can vary depending on the biological state of the ocean (Wang et al., 2015; Prather et al., 2013; Rinaldi et al., 2013). Previous studies have shown that SSA particles contain bacteria, cell fragments, viruses, enzymes, and other biomolecules that can influence the climate and relevant cloud properties (Patterson et al., 2016; Malfatti et al., 2019). Despite the potential for marine bioaerosols to play a major role in climate, very few studies have used fluorescence as a tool to identify bioaerosols released during nascent SSA production (Kasparian et al., 2017; Toprak and Schnaiter, 2013; Yue et al., 2019; Mostofa et al., 2013). This is, in part, due to the difficulty of using fluorescence to study SSA in the real atmosphere without a basic understanding of the fluorescence signature of SSA.

Here, the fluorescence characterization for isolated, laboratory-generated SSA is reported. Two common fluorescence methods were used to characterize SSA: excitation−emission matrix spectroscopy (EEMS) and a wideband integrated bioaerosol sensor (WIBS). EEMS has been

widely used to characterize organic matter in a variety of aqueous environments, including seawater (Mostofa et al., 2013; Zhang et al., 2011; Nebbioso and Piccolo, 2013). EEMS has the advantage of taking direct, full-spectrum fluorescence measurements of aqueous samples and can be used to investigate offline, bulk aerosol chemistry. The WIBS collects online, single-particle fluorescence measurements at lower resolution and has been increasingly used to investigate the dynamics of atmospheric bioaerosols in both the laboratory and the field (Toprak and Schnaiter, 2013; Gabey et al., 2010; Crawford et al., 2017; Savage et al., 2017; Hernandez et al., 2016). However, no studies have used the WIBS to directly measure isolated, nascent SSA in a laboratory setting. In the present study, single-particle and bulk aerosol fluorescence were used to evaluate realistic SSA and determine how SSA fluorescence changes under dynamic ocean biological conditions (e.g., during a phytoplankton bloom). Additionally, these techniques were used to characterize the contribution of marine bacteria to SSA fluorescence through controlled experiments involving isolated marine bacteria and abiotic seawater. This study provides a framework for using a fluorescence approach to investigate how temporal changes in biological species affect SSA released into the environment.

3.3 Methods

3.3.1 Aerosol Generation and Experiment Design

SSA particles were generated using three different methods: a wave channel located at the Scripps Institution of Oceanography (Wang et al., 2015; Prather et al., 2013), a Marine Aerosol Reference Tank (MART) (Stokes et al., 2013; Lee et al., 2015), or a miniature Marine Aerosol Reference Tank (miniMART) (Stokes et al., 2016). Each of these aerosol generation methods are isolated systems, without the influence of non-biological fluorescent particles from terrestrial or anthropogenic sources. Additionally, each of these methods produces aerosol size distributions

and chemical compositions which mimic that of a breaking ocean wave (Stokes et al., 2016; Collins et al., 2014). The three experimental methods also differed in biological activity in the seawater: (1) seawater without a phytoplankton bloom; (2) seawater with Guillard's nutrient medium added to generate a phytoplankton bloom with natural marine microbial communities (Guillard and Ryther, 1962); and (3) control scenarios consisting of either abiotic seawater or cultured marine bacterial strains in a phosphate buffered saline solution (4× PBS). Details of the three experiments are provided in Table 3.1 and Supporting Information.

3.3.2 Aerosol and Seawater Sample Collection

Aerosol samples were measured in real time with the WIBS and collected into a liquid solution for EEMS measurements. Prior to detection with the WIBS, aerosols were dried using inline silica diffusion driers to maintain a relative humidity of <20% throughout all experiments. As a result of drying and partial quenching of the fluorophores, it is possible that a fraction of fluorescent particles was below the fluorescence threshold. While channel 1 may not be affected due to the strong emission of tryptophan, humic-like substances (HULIS) can show decreased emission when in a powder state (Pöhlker et al., 2012). However, SSA particles have been shown to be semisolid below the efflorescence point (Lee et al., 2020), therefore, drying should not have a significant effect on the observed trends.

For EEMS analysis of the bulk aerosol, collection involved a liquid spot sampler (Aerosol Devices Inc., 110A), which uses a water condensation growth tube to collect particles directly into a liquid medium with high efficiency (Eiguren Fernandez et al., 2014). Aerosols passing through the spot sampler were collected in ultrapure water. Although collection into ultrapure water could potentially change the fluorescence intensity due to bacterial lysis and subsequent solvent exposure, these changes would be slight, due to the lack of new tryptophan formation/breakdown.

Additionally, any changes would be consistent throughout the course of these experiments. SSA particles were collected for experiments 1 and 2 at a flow rate of 1.5 liters per minute (LPM) for 1 h on the MART or overnight (12 h) on the wave channel. No aerosols were collected for EEMS analysis for experiment 3 (miniMART).

Seawater collection for EEMS analysis was performed for each experiment. For all experiments, seawater samples were collected into either 15 or 50 mL sterile, polypropylene tubes. Seawater samples were collected during aerosol generation for experiment 2 and either prior to, or immediately after, aerosol generation for the other experiments. Excitation−emission matrices (EEMs) were generally measured within 20 min of collection.

3.3.3 Bacterial Isolate Culture Preparation

Three different marine-relevant bacterial isolates were chosen due to their presence in the coastal waters off of Scripps Pier: AltSIO, ATW7, and BBFL7 (Bidle and Azam, 2001; Pedler et al., 2014). All isolates were originally derived from the Pacific Ocean off the Scripps Pier in La Jolla, California and isolated by the Azam laboratory at the Scripps Institution of Oceanography. For this experiment, bacterial isolates were streaked out from a frozen glycerol stock onto ZoBell medium. After 24 h, colonies were picked and grown in liquid ZoBell medium at room temperature on a shaker (130 rpm). The next day, the cultures were harvested through 5 min of centrifugation at 9000g and washed with PBS to remove the supernatant (spent medium). Optical density was measured at 600 nm in order to have a 1:1:1 (AltSIO/ATW7/BBFL7) ratio of the three cultures in the inoculum with a concentration of 1×10^9 cells/mL. The final concentration of bacterial cells in the miniMART was $\sim 1.6 \times 10^5$ cells/mL, which is on the order of known bacterial concentrations in the ocean, especially in oligotrophic regions (Azam et al., 1983).

3.3.4 Fluorescence Measurements

3.3.4.1 WIBS

Online, single-particle fluorescence measurements were taken using a WIBS (Droplet Measurement Technologies, WIBS-NEO). The WIBS operation has been described previously in detail (Gabey et al., 2010). Briefly, the WIBS utilizes two xenon lamps with bandpass filters to generate two excitation wavelengths at 280 nm (Xe1) and 370 nm (Xe2). These excitation wavelengths are intended to target the fluorescence excitation of the amino acid tryptophan and the biological cofactor nicotinamide adenine dinucleotide (NADH), respectively (Kaye et al., 2005). The WIBS collects the fluorescence emission from a particle using two photomultiplier tubes (PMTs) with bandpass filters from 310 to 400 nm (FL1) and from 420 to 650 nm (FL2). This arrangement creates three main combinations of fluorescence excitation and emission "channels," with different target molecules. These channels are labeled here as channel 1 (Xe1/FL1; Ex/Em = 280 nm/310−400 nm; targeting tryptophan), channel 2 (Xe1/FL2; 280 nm/420−650 nm; targeting riboflavin), and channel 3 (Xe2/FL2; 370 nm/420− 650 nm, targeting NADH). We focus primarily on channels 1 and 3 as these channels coincide with the EEM peaks representing the fluorescence from protein-like and HULIS, respectively. Additionally, we exclude channel 2 from most of our discussion due to the potential cross-sensitivity of this channel with the other two channels, as reported previously (Toprak and Schnaiter, 2013; Gabey et al., 2011).

A forced trigger sampling period, where the sample flow is off and the xenon lamps are fired, was performed at the start of each day to provide a blank for the fluorescent particle detection. Particles are deemed fluorescent if they exceed a minimum threshold

$$E_{Threshold_i} = 3\sigma_i + \bar{E}_i \qquad [3.1]$$

where $\bar{E}_i$ is the mean background fluorescence from the forced trigger data and σ_i is the standard deviation of the background for each fluorescence channel (FL_i), as described in previous studies

(Toprak and Schnaiter, 2013). The fluorescence values for particles detected by the WIBS were then subtracted by the forced trigger thresholds for each individual channel. The WIBS-NEO has greater dynamic range compared to previous models, which prevents saturation of the detector for highly fluorescent particles (Forde et al., 2019). The intensity values reported are in arbitrary units; however, the mean SSA intensity values were converted to mass equivalents of tryptophan (channel 1) and quinine (channel 2 and 3) based on a similar calibration to that defined by Robinson et al. (2017) (Supporting Information, Figure 3.7) (Robinson et al., 2017) .

The WIBS uses a 635 nm continuous-wave laser to detect, size, and determine the shape of single particles. Optical diameter measurements, from 0.5 to 50 μm, are based on detection of side-scattered light with the FL2 PMT. Analysis of forward-scattered light on a quadrant PMT determines the asymmetry factor (AF) for each particle. The AF is a measure of the shape of a particle, with an AF < 10−15 indicative of nearly spherical particles, an AF of 15−30 for aspherical particles, and an AF > 30 for rod- or fiber-shaped particles (Crawford et al., 2017; Kaye et al., 2007). The single-particle optical diameter, measured with the WIBS, was used to calculate the size distribution of fluorescent particles in each channel. Polystyrene latex spheres were used to verify the accuracy of the WIBS optical diameter measurements. For the size distribution measurements, size bins were divided into 32 bins per decade of optical diameter. Particle counts are displayed as the number concentration of fluorescent particles per liter of air divided by the logarithm of the bin width ($dN/d\log D_p$). In addition to the forced trigger fluorescence threshold, a size threshold was applied to all particles measured with the WIBS. Particles with optical diameters less than $D_p = 0.8$ μm were excluded from these analyses because of previously reported inaccuracies in the fluorescence detector sensitivity and counting efficiency of smaller particles (Crawford et al., 2017; Gabey et al., 2011). For bacterial isolate size distributions, a fluorescence

cutoff of 2.5 standard deviations above the mean background PBS fluorescence in channel 1 was applied to eliminate most PBS particles.

3.3.4.2 EEMS

Offline, bulk fluorescence EEMs of seawater and SSA collected with the liquid spot sampler were measured with an Aqualog spectrophotometer (HORIBA Scientific, extended range). Collection periods of at least 1 h on a MART at 1.5 LPM or approximately 12 h at 1.5 LPM on the wave channel were used to obtain an adequate fluorescence signal from the protein-like region and often sufficient signal for the HULIS region, depending on seawater biology and chemistry. No processing of seawater samples was necessary to acquire fluorescence signals. Excitation wavelengths ranged from 230 to 500 nm, while the emission collection bands ranged from 250 to 800 nm, both in ~5 nm increments. Background spectra acquired using ultrapure water or PBS solution were subtracted from all EEMs. EEMs were then corrected for inner filter effects based on the absorbance spectra measured simultaneously. Rayleigh scattering (1st and 2nd order) was removed from all spectra. EEMs were normalized to the area of the Raman scattering peak of water at 350 nm excitation to convert fluorescence intensities to Raman Units (Lawaetz and Stedmon, 2009; Murphy, 2011). A comparison between the EEM spectrum and the WIBS channels is highlighted in Figure 3.8.

3.4 Results

Three different experiments, with varying biological complexity and activity, were studied in order to compare the fluorescence measurements of EEMS and the WIBS. Experiment 1 used a wave channel and fresh seawater to replicate SSA production of the natural microbial community in coastal seawater with low phytoplankton biomass. Experiment 2 involved a MART for aerosolization of seawater induced with a phytoplankton bloom, typical of realistic bloom

conditions with high biomass. Experiment 3 was used as a control of two different scenarios involving a miniMART: abiotic seawater and a pure bacterial system in a salt solution.

3.4.1 Experiment 1: Bulk Aerosol and Single-Particle Fluorescence of Nascent SSA

EEMs for seawater showed fluorescence in regions that are commonly detected for marine systems (Figure 3.2a) (Mostofa et al., 2013; Coble, 1996). Specifically, three fluorescence regions were present, representing three different classes of organic molecules. Fluorescence in the region at excitation/ emission wavelengths 400−440 nm/680−690 nm is indicative of chlorophyll *a* (Mostofa et al., 2013). Fluorescence at excitation/emission wavelengths <235 nm and 275−280 nm/330−350 nm is attributed to protein-like substances and typically indicates fluorescence from the amino acid tryptophan. In this study, the 275−280 nm excitation was used as an indicator for protein-like fluorescence because of the excitation bounds of the EEMs. Components that emit in this region range from bacteria cells to viruses to proteinaceous gels (Mostofa et al., 2013; Determann et al., 1998; Lakowicz, 2006). EEM features near 260 nm or 360 nm/450−455 nm and at 325 nm/410 nm are indicative of HULIS, complex mixtures of organic molecules produced during the breakdown of organisms and larger biomolecules (Mostofa et al., 2013; Coble, 1996; Hessen and Tranvik, 1998).

EEMs for SSA collected from the wave channel showed different fluorescence signatures than those in seawater, indicating chemical species are selectively transferred into SSA (Figure 3.2b). In contrast to seawater, SSA EEMs did not show chlorophyll *a* signatures, suggesting that larger phytoplankton species are not efficiently transferred. While both seawater and SSA EEMs showed protein-like and humic-like signatures, SSA EEMs were primarily dominated by protein-like fluorescence with a smaller contribution from HULIS. The ratio of the protein-like peak (Ex: 275 nm/Em: 330 nm) to the humic-like peak (Ex: 360 nm/Em: 450 nm) was evaluated for both

samples. The protein-to-humic intensity ratio for seawater was 12.87, whereas the ratio for SSA was 15.63, confirming the increased contribution of protein-like fluorescence in SSA. Additionally, the SSA EEMs showed a shift in the protein-like emission spectra when compared to the protein-like fluorescence in seawater. While seawater showed fluorescence primarily from tryptophan, with an emission peak close to 350 nm, SSA EEMs showed a major peak in the emission spectra closer to 300 nm, indicative of fluorescence from the amino acid tyrosine. Tyrosine fluorescence suggests the presence of marine gels or exopolymeric substances in SSA (Liu et al., 2017). The tyrosine peak lies outside the range of wavelengths detected by the WIBS (310−400 nm), thus some portion of SSA fluorescence was not captured using this analytical method. However, the protein peak in SSA extended to longer wavelengths, suggesting that tryptophan fluorescence was also present and therefore detectable with the WIBS.

Across 7 days of sampling nascent SSA particles generated from the wave channel, the WIBS measured over 100,000 individual fluorescent particles each day. The fluorescent fraction in this low biomass scenario represented 0.87 ± 0.09% of all particles measured with optical diameters greater than D_p = 0.8 μm. The fluorescent fraction measured was relatively low compared to ambient measurements which range from 1.9% to upward of 40% but are often influenced by terrestrial bioaerosols (Crawford et al., 2017; Fennelly et al., 2018). In order to define a distinct fluorescence signature for isolated SSA, mean fluorescence intensities of the different fluorescence channels were calculated from all sampling days combined (Figure 3.2c). Additionally, the channel-specific mean AF and diameter were calculated for fluorescent SSA particles. Particles across all three channels had low AF (~6), with channel 3 particles showing the lowest AF. These low AFs demonstrate that most of the fluorescent particles detected were spherical or spheroidal in shape. The mean diameter of SSA measured in channel 1 was, in general,

larger than those in channel 3, indicating different chemical species are transferred into different particle sizes.

The mean daily size distributions of SSA particles generated by the wave channel were measured with the WIBS and separated based on the fluorescence channels (Figure 3.3). The size distributions measured with the WIBS showed a bimodal distribution for channel 1, with a peak optical diameter around D_p = 2.6 μm and a second mode near D_p = 1 μm. The larger-sized mode is suggestive of proteinaceous molecules ejected in supermicron-sized aerosols. Bacteria, which contain a high protein content, have been observed in coarse mode aerosols measured in nascent SSA and off coastal regions (Rastelli et al., 2017; Shaffer and Lighthart, 1997). Previous WIBS studies show that bacteria have dominant fluorescence emission in channel 1 due to the amino acid tryptophan (Savage et al., 2017; Hernandez et al., 2016). Additionally, a fraction of particles that fluoresced in channel 1 also fluoresced in channel 3 (*ca.* 7% of all channel 1 particles). The particles that fluoresced in both channels 1 and 3 showed a size distribution resembling the main mode for channel 1 fluorescent particles, slightly shifted to larger sizes (Figure 3.9). The size distribution and fluorescence signature of the particles that fluoresced in both channels 1 and 3 suggest that these particles may be metabolically active bacteria, with enhanced NADH. Furthermore, bacteria bound to gels and transparent exopolymeric particles have been observed in this size range (Mari and Kiørboe, 1996; Aller et al., 2005). Bound bacteria are often larger and enzymatically active which may explain the shift to larger sizes for particles that fluoresce in both channels 1 and 3 (Smith, D., Simon, M., Alldredge, A., Azam, F., 1992).

For particles fluorescing in the WIBS channel 3, a peak in the size distribution was observed near D_p = 1 μm with a tail extending into the larger sizes (Figure 3.3). In an ambient setting, fluorescence in this channel is often associated with pollen and fungal spores. However,

in this study of isolated, nascent SSA, fluorescence in this channel was likely indicative of HULIS, as shown in previous work by Savage et al. (2017) (Savage et al., 2017). Measurements on the molecular weight of marine-based HULIS show that it typically consists of small molecules, with 90% of the measured HULIS mass falling below 5 kDa (Grzybowski, 1996). HULIS, by nature, is part of dissolved organic matter in the ocean and is therefore expected to be released across particles of all sizes (Benner et al., 1992). The shape of the total particle size distribution (combined fluorescent and non-fluorescent), measured for SSA generated by the wave channel, was similar to that of channel 3 (Figure 3.10). This similarity further suggests that the channel 3 measurements by the WIBS are indicative of dissolved HULIS in SSA.

3.4.2 Experiment 2: Changes in Fluorescence Signatures During a Phytoplankton Bloom

SSA fluorescence was measured with both the WIBS and EEMS throughout an induced phytoplankton bloom to investigate the effect of a changing marine biological state on SSA. The microbial dynamics were measured throughout the course of the phytoplankton bloom (Figure 3.11). The experiment occurred over 9 days with *in vivo* chlorophyll *a* fluorescence indicating a peak in phytoplankton growth on the third day, followed by senescence for the remainder of the experiment. Heterotrophic bacteria concentrations peaked on the fifth day and declined afterward. Virus concentrations tracked the heterotrophic bacteria concentrations and increased after the peak in the phytoplankton bloom (Figure 3.11).

WIBS measurements of the SSA fluorescence intensity corresponded with SSA EEMs throughout the phytoplankton bloom (Figure 3.4). WIBS channel 1 (protein-like) showed a general decrease in fluorescence intensity over time. The decreasing fluorescence trend was also observed for the SSA EEMs upon integrating over the same wavelengths of WIBS channel 1. The trends in

WIBS channel 1 and EEM protein-like region revealed a disconnect between the fluorescence observed in SSA and the fluorescence in seawater over the course of the bloom (Figure 3.4). However, when the WIBS channel 3 measurements were compared to the corresponding seawater HULIS-region fluorescence measured with EEMS, the SSA mean fluorescence intensity generally agreed with that in the seawater (Figure 3.12). The difference in enrichment for HULIS and protein-like species into the aerosol indicates a chemical-specific transfer. More studies are required to determine which factors affect the selective transfer of fluorescent species from seawater to SSA. Nevertheless, the similarity between the WIBS and EEMS measurements of SSA over time reveals that single-particle fluorescence, in combination with seawater analysis, can provide unique insights on SSA composition throughout a wide range of ocean biological conditions.

3.4.3 Experiment 3: Characterizing the Fluorescence of Abiotic Seawater and Bacterial Isolates

In order to probe the contribution of marine bacteria to SSA fluorescence, the WIBS and EEMS were used to measure fluorescence under two controlled scenarios: (1) natural seawater vs filtered, autoclaved seawater (FASW) and (2) marine bacterial isolates in a salt solution. As mentioned previously, seawater used for the FASW experiment was taken from a separate phytoplankton bloom experiment and the bacterial isolate experiment was run with a PBS medium to minimize background fluorescence.

To better understand the underlying fluorescence signature of SSA, changes in both seawater and SSA fluorescence were measured with EEMS and the WIBS before and after sterilization of the seawater. The FASW EEMs showed an increase in the humic-like fluorescence intensity compared to natural seawater EEMs, suggesting an enhanced production of HULIS

during the autoclaving process (Figure 3.5a) (Andersson et al., 2018). The enhanced production of HULIS or a potential change in the selectivity, leading to aerosol enrichment, might explain the increase in the WIBS channel 3 size distribution for FASW SSA (Figure 3.5b). Additionally, WIBS measurements on FASW SSA showed a decrease in the D_p = 2−3 μm sized mode in the channel 1 fluorescence size distribution compared to natural SSA (Figure 3.5d), suggesting a lack of large, protein-containing particulates in FASW SSA. The decrease in the WIBS channel 1 size distribution was not as significant as the diminishment in the EEM protein-like feature (Figure 3.5c), likely because the fluorescent material (reduced but still detected by EEMS) was detected by the WIBS and contributed to the fluorescence size distribution. However, the trends of both instruments further suggest that marine microbes are contributing to the large size mode observed in the WIBS channel 1 size distribution measured for SSA.

To further elucidate the contribution of marine bacteria to SSA fluorescence, the bulk and aerosol fluorescence signatures were characterized for a solution containing three marine bacterial isolates (AltSIO, ATW7, and BBFL7) (Figure 3.6). The bacterial EEMs showed high fluorescence in the protein region, with no noticeable humic-like fluorescence above the background 4× PBS (Figure 3.6a). This spectrum shared similar characteristics to previously measured EEMs of marine bacteria (Determann et al., 1998). The three individual bacteria were also analyzed separately using EEMS and showed similar spectra with fluorescence predominantly in the protein region and negligible fluorescence in the HULIS region (Figure 3.13). This result indicates that the fluorescence signature of the marine bacterial solution containing all three bacteria was not dominated by one species. The tryptophan-like fluorescence regions from marine bacterial EEMs were also present in seawater and SSA EEMs, suggesting that bacteria are a component in SSA fluorescence.

The WIBS fluorescence measurements of the bacteria aerosolized with a miniMART showed similar signatures to those detected by EEMS. The bacterial isolates showed an increased mean fluorescence intensity in channel 1 compared to the 4× PBS medium (Figure 3.14). These results were similar to previous WIBS studies, which found that terrestrial bacterial cultures fluoresce strongly in channel 1 (Hernandez et al., 2016). Moreover, the increase in mean fluorescence intensity was not seen in the other two channels measured by the WIBS. The WIBS fluorescence signature for aerosolized marine bacteria paralleled the EEMs of the bacteria in solution, further highlighting the capability of single-particle fluorescence for SSA characterization.

WIBS channel 1 size distribution for the aerosolized bacterial isolates was generated in the same manner to those generated for the wave channel. The background-corrected, fluorescent particle size distribution showed that the bacterial isolates were ejected into predominantly larger particles with the peak of the distribution near D_p = 2.4 μm (Figure 3.6b). The mode of the size distribution for the bacterial isolates was resemblant of the protein-like, nascent SSA measured from the wave channel, indicating that the particles detected in the wave channel likely included bacteria (Figure 3.6b). Slight differences in the size distributions between the seawater and the bacterial isolates might be explained by the proteinaceous constituents in chemically complex seawater compared to the 4× PBS and the formation of proteinaceous aggregates in natural SSA (Aller et al., 2005). While further work is necessary to fully elucidate the contribution of marine bacteria in SSA and their transport pathways, it is clear that marine bacteria can be ejected into the atmosphere via SSA particles and detected using fluorescence techniques.

3.4.4 Implications

When evaluating which fluorescence technique is appropriate for a specific measurement, multiple factors should be considered. Due to the additional steps necessary in measuring SSA using EEMS, such as impinging the aerosols into a bulk medium, this instrument is better suited for measurements of bulk seawater. However, the WIBS is a useful instrument for characterizing real-time changes in single-particle SSA and shows comparable trends to fluorescence measured with EEMS. Therefore, WIBS aerosol measurements, in tandem with EEMS analysis of bulk solutions, can provide a thorough investigation of fluorescent particle production. Possible modifications to the optics of the WIBS for improved characterization of SSA may involve extending the fluorescence emission collection of channel 1 to include the major peak of tyrosine fluorescence, shown to be significant in the SSA EEMs.

SSA particles represent one of the most abundant natural aerosols in the atmosphere (Gantt and Meskhidze, 2013), but only during the past decade have their role as primary biological aerosols been a major focus of investigation. The unique ability of bioaerosols to affect clouds and climate becomes especially important in remote marine locations where SSA particles can dominate as cloud condensation nuclei or ice nuclei (Fröhlich-Nowoisky et al., 2016; Burrows et al., 2013; Vergara-Temprado et al., 2017; Andreae and Rosenfeld, 2008). With growing interest in the atmospheric dynamics of bioaerosols, uncovering the role of SSA has become increasingly critical to our understanding of how bioaerosols influence climate. Our investigations on isolated systems provide a basis for the fluorescence signature of SSA to help unravel the complex trends observed in the atmosphere and move toward identification of marine bioaerosols in the natural environment.

3.5 Acknowledgements

The authors would like to thank the National Science Foundation Center for Aerosol Impacts on the Chemistry of the Environment (NSF CAICE), a Center for Chemical Innovation (CHE-1801971) for funding this project. We thank Kathryn J. Mayer and Michael R. Alves for their thoughtful contributions and edits to this manuscript. We also thank the anonymous reviewers for their helpful comments and advice.

Chapter 3, in full, is a reprint of material with permission from *Environmental Science & Technology*, 2021. Santander, M. V., Mitts, B. A., Pendergraft, M. A., Dinasquet, J., Lee, C., Moore, A. N., Cancelada, L. B., Kimble, K. A., Malfatti, F., & Prather, K. A. (2021) "Tandem fluorescence measurements of organic matter and bacteria released in sea spray aerosols." *Environmental Science & Technology* 55 (8), 5171-5179. Copyright 2021 American Chemical Society. The dissertation author and Mitchell Santander are co-first authors of this manuscript. The dissertation author was the primary experimenter for all investigations involving the WIBS, primary analyst and figure generator for the WIBS datasets, and lead writer of sections describing the WIBS methods and results. Mitchell Santander was the primary experimenter for all investigations involving EEMS, primary analyst and figure generator for EEMS datasets, and lead writer of sections describing EEMS methods and results. The dissertation author and Mitchell Santander contributed equally to drafting the introduction, abstract, and implications sections of the manuscript and to revisions of all sections.

3.6 Figures

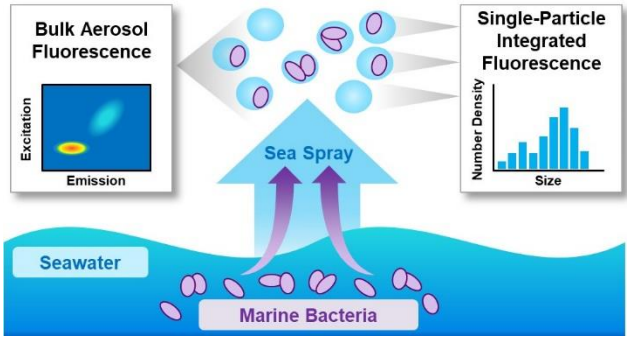

Figure 3.1. Graphical abstract.

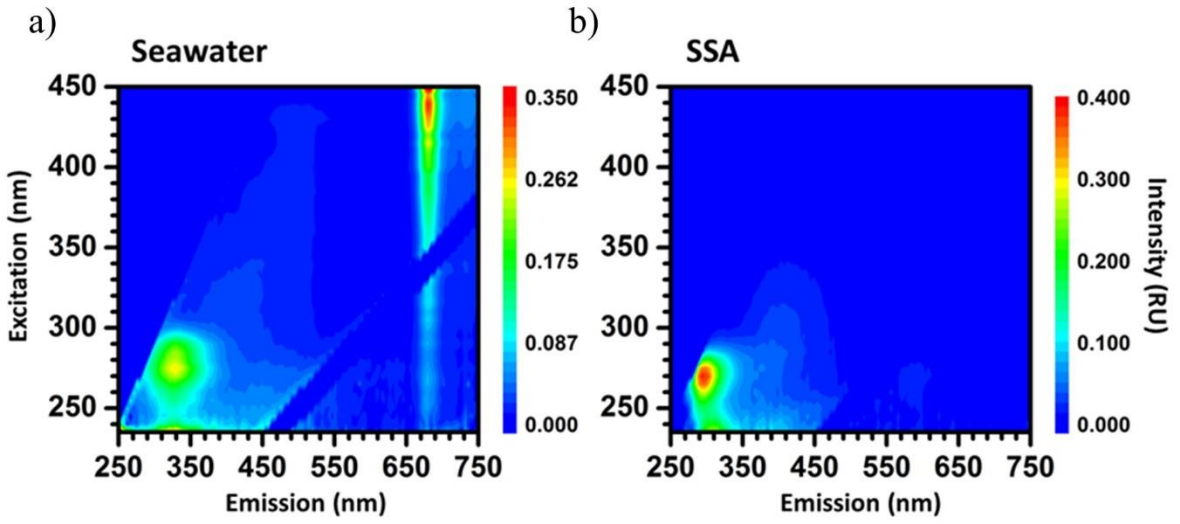

c)	Channel 1 (280 nm/310-400 nm)	Channel 2 (280 nm/420-650 nm)	Channel 3 (370 nm/420-650 nm)
Intensity (a.u.)	1.245e5 ± 5.368e5	2.491e4 ± 6.560e4	3.608e4 ± 1.045e5
Diameter (μm)	2.19 ± 1.01	2.03 ± 0.93	1.63 ± 0.816
AF (a.u.)	6.23 ± 3.25	6.10 ± 3.14	5.57 ± 2.79

Figure 3.2. Selected EEMs for a) seawater and b) nascent SSA collected from the wave channel. c) WIBS measurements of the mean fluorescence intensity, optical diameter, and asymmetry factor (AF) for each fluorescence channel (excitation/emission) for the SSA generated by the wave channel.

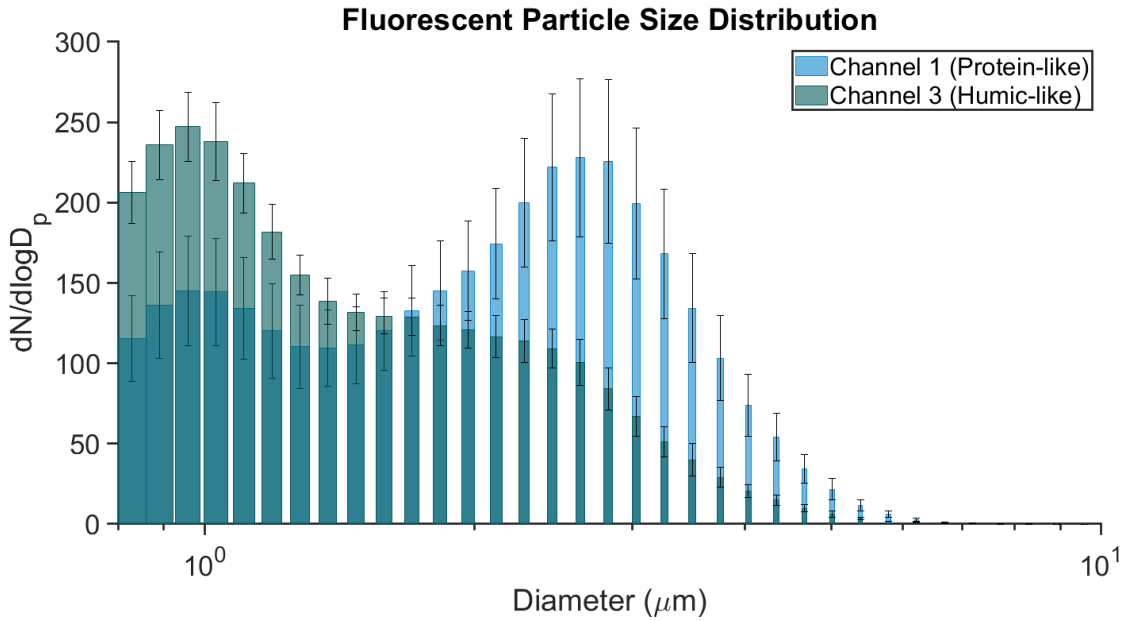

Figure 3.3. SSA size distributions separated by fluorescence channels measured with the WIBS. Channel 1 (protein-like) is in blue with channel 3 (humic-like) overlaid in green. Both size distributions shown are the daily mean particle counts (#/L) normalized to the bin widths and the error bars represent one standard deviation from the mean.

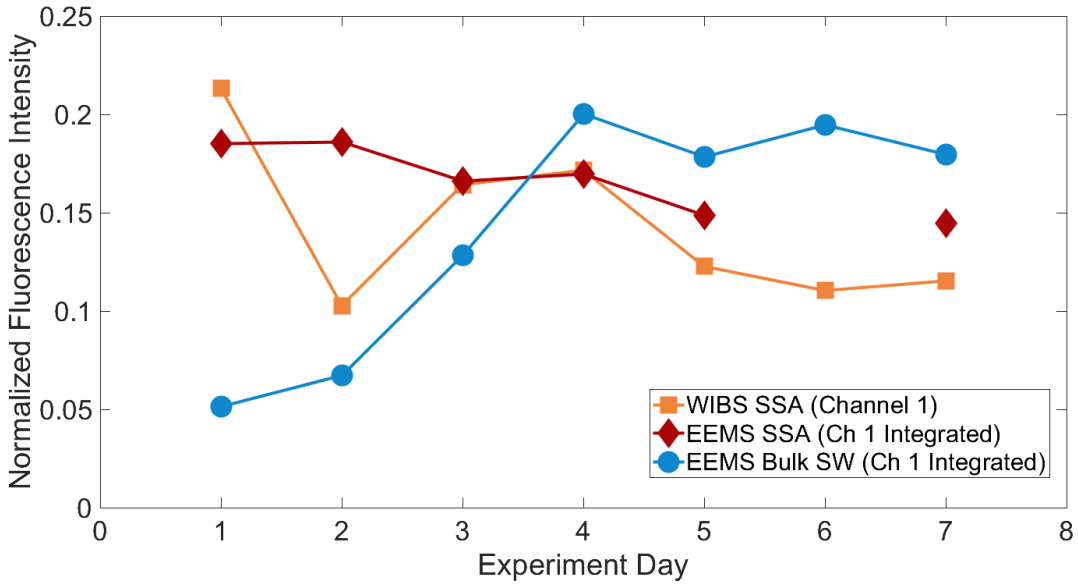

Figure 3.4. WIBS fluorescence channel 1 (protein-like) graphed over time during a phytoplankton bloom. EEM emission integrated over the same wavelengths measured by the WIBS shown over time for both bulk seawater (Bulk SW) and SSA over the course of a phytoplankton bloom. All values are normalized to the sum of intensities for each measurement across all the days of the experiment.

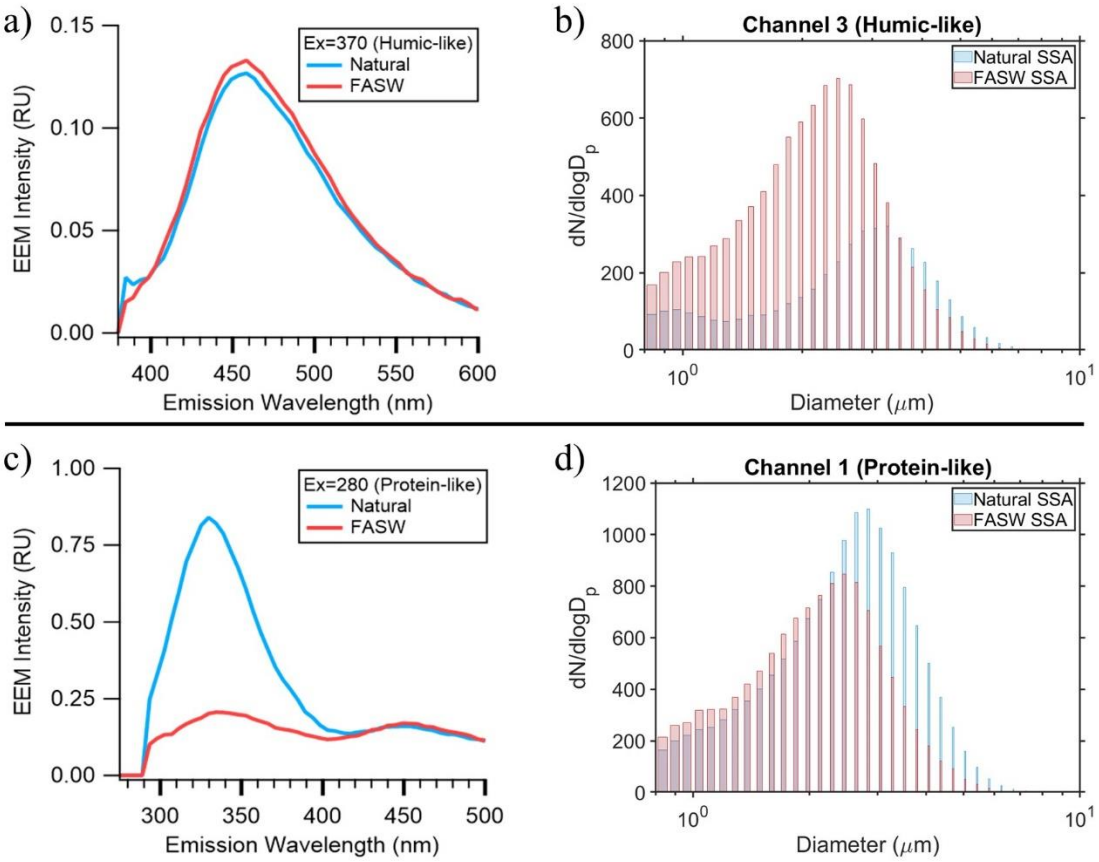

Figure 3.5. Emission spectra from the EEMs of the natural seawater and FASW corresponding to the excitation wavelengths for (a) WIBS channel 3 and (c) WIBS channel 1. Fluorescence size distributions of SSA before and after filtering and autoclaving for (b) WIBS channel 3 (d) WIBS channel 1.

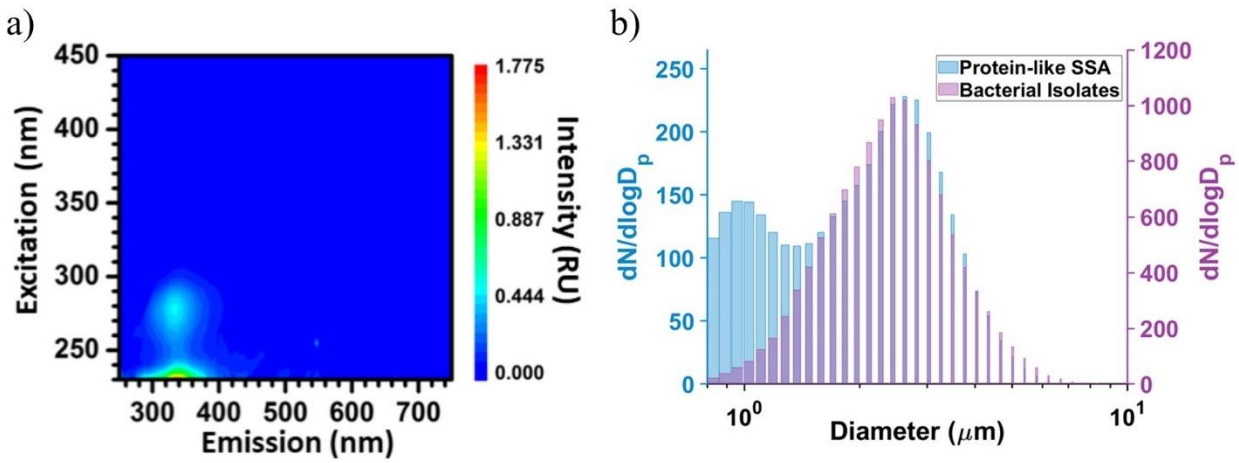

Figure 3.6. Fluorescence of the bacterial isolate mixture measured by a) EEMS (adjusted to the blank EEM of the 4xPBS solution). b) WIBS channel 1 fluorescence size distribution of the bacterial isolates that fluoresced above the PBS background (purple), overlaid on the mean channel 1 size distribution of the wave channel SSA (blue).

3.7 Tables

Table 3.1. Layout of the three experimental setups used in this study.

Experiment Number	**Bulk Solution**	**Additions**	**Aerosol Generation**	**Fluorescence Measurements**
Experiment 1	Seawater	None	Wave channel	EEMS bulk solution, EEMS & WIBS aerosol
Experiment 2	Seawater	F/100 nutrients, sodium silicate	MART	EEMS bulk solution, EEMS & WIBS aerosol
Experiment 3a	Seawater & filtered, autoclaved seawater	F/2 nutrients	miniMART	EEMS bulk solution & WIBS aerosol
Experiment 3b	4xPBS with bacterial isolates	None	miniMART	EEMS bulk solution & WIBS aerosol

3.8 Supporting Information

3.8.1 Experimental Designs

Experiment 1. A wave channel was used to produce SSA from natural seawater (Wang et al., 2015; Prather et al., 2013). The wave channel contained 13,000 L of natural seawater taken from Ellen Browning Scripps Memorial Pier (Scripps Pier; 32-52'00" N, 117-15’21" W). During this experiment, a phytoplankton bloom was not induced, therefore the seawater contained the natural microbial community in different growth stages and in a state of low biomass. SSA were produced by paddle-generated waves breaking on an artificial beach, and were measured continuously using the WIBS. SSA were collected for EEMS analysis for one 12-hour time period using an aerosol-to-liquid collection method.

Experiment 2. A Marine Aerosol Reference Tank (MART) was used to generate SSA over the course of a phytoplankton bloom (Stokes et al., 2013; Lee et al., 2015). A large outdoor tank (2200L) was filled with seawater from Scripps Pier and used to supply seawater to the MART. A phytoplankton bloom was induced in order to investigate the role of ocean microbiology on SSA composition and represent a system with high biomass. To initiate the phytoplankton bloom, Guillard’s F/2 medium, diluted to F/100, and sodium silicate were added to the outdoor tank of seawater (Guillard and Ryther, 1962). Phytoplankton biomass, indicated by *in vivo* chlorophyll *a* fluorescence, was measured using a handheld fluorometer (Turner Designs, Aquafluor) and converted to chlorophyll *a* concentration. Each day, 120 L of tank water was transferred to the MART, where aerosol generation occurred via a periodic plunging waterfall. After sample collection, the seawater was cycled back into the outdoor tank to allow the phytoplankton to continue growing. The SSA generated by the MART were measured by the WIBS in one- to two-hour intervals each day. Simultaneously, SSA were collected for approximately 1 hour each day

for EEMs analysis. Seawater was also collected daily for EEMs analysis prior to SSA collection. The EEMS intensities for Experiment 2 were compared to the WIBS intensities by normalizing to the sum of intensities for each method across all the sampled days of the phytoplankton bloom. This normalization allowed for a comparison between the relative trends in intensity measured using both instruments.

Experiment 3. To elucidate the role of microbes on SSA fluorescence, two control scenarios were investigated using a miniMART, which uses a water-wheel (mill) to produce a periodic plunging waterfall and generate aerosols (Stokes et al., 2016). In the first scenario, seawater fluorescence was compared before and after filtration and autoclaving. Seawater collected off Scripps Pier was spiked with Guillard's F/2 medium, to induce a mesocosm phytoplankton bloom in a 19 L carboy. During the senescence phase of the bloom, 12 days after spiking the seawater with nutrients, 7 L of water was added to the miniMART for aerosolization and sampling. The remaining seawater from the carboy was filtered using a 0.2 μm filter and then autoclaved for sterilization. After sampling the fresh seawater, the miniMART was drained, cleaned with 70% ethanol, rinsed with milliQ water, and filled with the filtered, autoclaved seawater for SSA generation.

The second scenario involved the aerosolization of bacterial isolates added to a 4x phosphate-buffered saline solution. Three marine bacterial isolates were used to investigate the fluorescence signature of aerosolized bacteria without the influence of background seawater fluorescence. The bacterial strains were in the same physiological state of exponential growth upon addition to the miniMART.

3.8.2 Enumeration of Heterotrophic Bacteria and Viruses

The seawater samples were fixed with a solution of glutaraldehyde at 0.05% final concentration and stored at -80°C after flash freezing (Noble and Fuhrman, 1998). Heterotrophic bacteria and virus counts were obtained using flow-cytometry at The Scripps Research Institute (TSRI) Flow Core Facility with a BIO-RAD, ZE5 Cell Analyzer. Samples for heterotrophic bacteria were diluted (1:10) in 1xTE buffer (pH 8) and stained with SYBR Green I (1:100 dilution of the commercial stock) at room temperature for 10 minutes in the dark. Viruses were diluted (1:50) in 1xTE buffer and stained (at a 1:50 dilution of the commercial SYBR Green I stock) in the dark for 10 minutes at 80°C (Gasol and Del Giorgio, 2000). Heterotrophic bacteria and virus populations were discriminated based on their signature in the fluorescence (488 nm laser, green fluorescence) versus side-scatter specific cytograms. Signals in the blank samples were subtracted from the sample signals.

3.8.3 Calibration of WIBS Intensities

To compare the SSA mean intensities detected by the WIBS to other WIBS instruments, we applied a calibration similar to that described by Robinson et al. (2017) (Robinson et al., 2017). This method compares WIBS fluorescence intensity to the equivalent mass of fluorophore atomized from a standard solution. Tryptophan was used as the fluorophore for channel 1 with ammonium sulfate as a non-fluorescent filler for particle generation. Quinine was used to calibrate channels 2 and 3. For the first standard solution, 0.0212 g of tryptophan and 0.9157 g of ammonium sulfate were added to 150 mL of milliQ water (tryptophan mass percent = 2.26%). For the quinine solution, 0.865 g of quinine were added to 150 mL of milliQ water (quinine mass percent = 100%). Particles were generated with a custom atomizer using particle-free air produced from a zero air generator (Sabio, Model 1001). The particles were dried using silica diffusion driers to an RH <21% before entering the WIBS. Dried particles were assumed to have the same fluorophore mass

percent to that in the bulk standard solution. The particle population was a polydisperse distribution, sized using the WIBS. Particles were divided into 5 nm size bins from 0.8 μm to 3 μm and the average particle optical diameter for each size bin was calculated. Assuming the particles were spheres, the particle volume was calculated for each size bin and converted to mass using the particle density: 1.77 g/cm3 for tryptophan particles (assuming ammonium sulfate density) and 1.36 g/cm3 for quinine particles (value provided by supplier).

A log-log linear relationship was observed between the calculated fluorophore mass and the measured WIBS intensity. Regressions were calculated for the first 150 size bins due to higher particle counts in this range. The R^2 values for the regressions of the three channels were: 0.928, 0.84, and 0.831 for channels 1-3, respectively. Both quinine calibrations showed a deviation from the fitted line at the higher mass values (Figure 3.7b, c), which was also observed in the calibration by Robinson et al. (2017) and previously accounted for by assuming an excitation penetration depth of 90 nm (Robinson et al., 2017). However, in this study, when a shell penetration depth was assumed, only a slight increase in the R^2 value was observed for both quinine regressions. Therefore, the deviation in the fit at higher quinine concentrations was ascribed to the lower particle counts in these size bins. Using the calculated regression fits, the mean values from the SSA generated by the wave channel were converted to the equivalent fluorophore mass (Figure 3.7a-c). The mean intensity ± the standard deviation for nascent SSA in channel 1 was equivalent to 2.331 ± 34.596 fg of tryptophan and for channels 2 and 3 were equivalent to 0.0537 ± 0.400 and 0.116 ± 1.050 fg of quinine, respectively (Figure 3.7d). As a note, the measured intensities for the SSA samples are blank-subtracted. In order to determine the measured limits of detection (LOD), the calibration curves were generated without subtracting out the blank from the fluorescence values. Based on the forced trigger thresholds for this experiment and the calibration curves

without the blank subtracted, the LOD for WIBS channel 1 was equivalent to 1.88 fg of tryptophan and the LOD for channels 2 & 3 were equivalent to 0.0216 fg of quinine and 0.103 fg of quinine, respectively.

3.9 Supplemental Figures

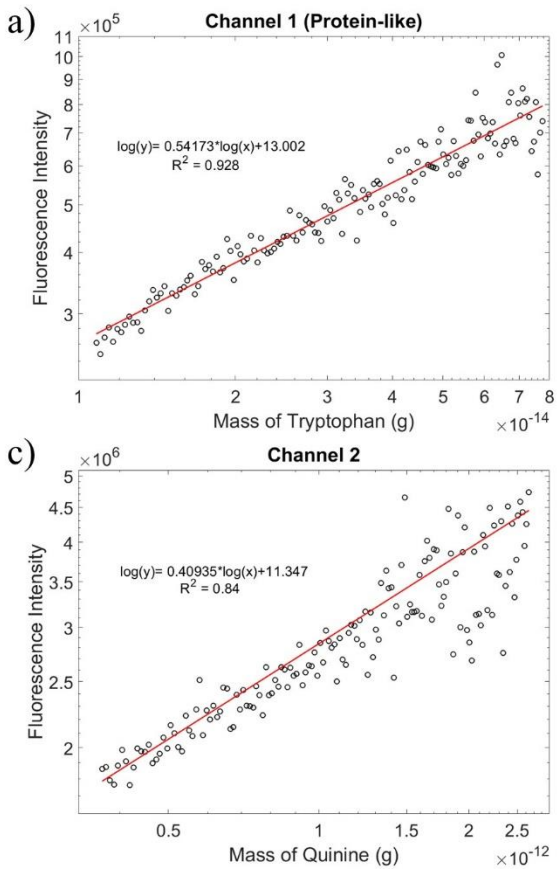

d)

WIBS Channels	Equivalent Fluorophore Mass
Channel 1 (280 nm/310-400 nm)	2.331 ± 34.596 femtograms of tryptophan
Channel 2 (280 nm/420-650 nm)	0.0537 ± 0.400 femtograms of quinine
Channel 3 (370 nm/420-650 nm)	0.116 ± 1.050 femtograms of quinine

Figure 3.7. WIBS calibration regressions comparing fluorophore mass to the WIBS fluorescence intensity for a) channel 1, b) channel 3, c) channel 2. d) Conversion of the WIBS mean fluorescence intensities to the fluorophore equivalent masses for SSA generated by the wave channel.

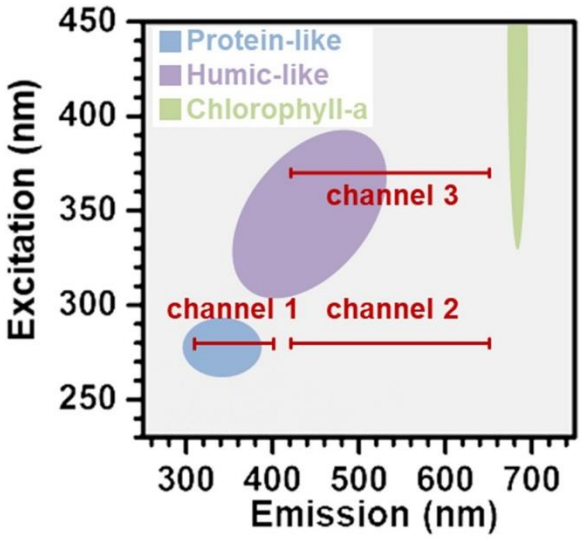

Figure 3.8. Overlay of the WIBS channels compared to an excitation emission matrix. Also labeled are the different fluorescence regions associated with seawater and sea spray aerosols.

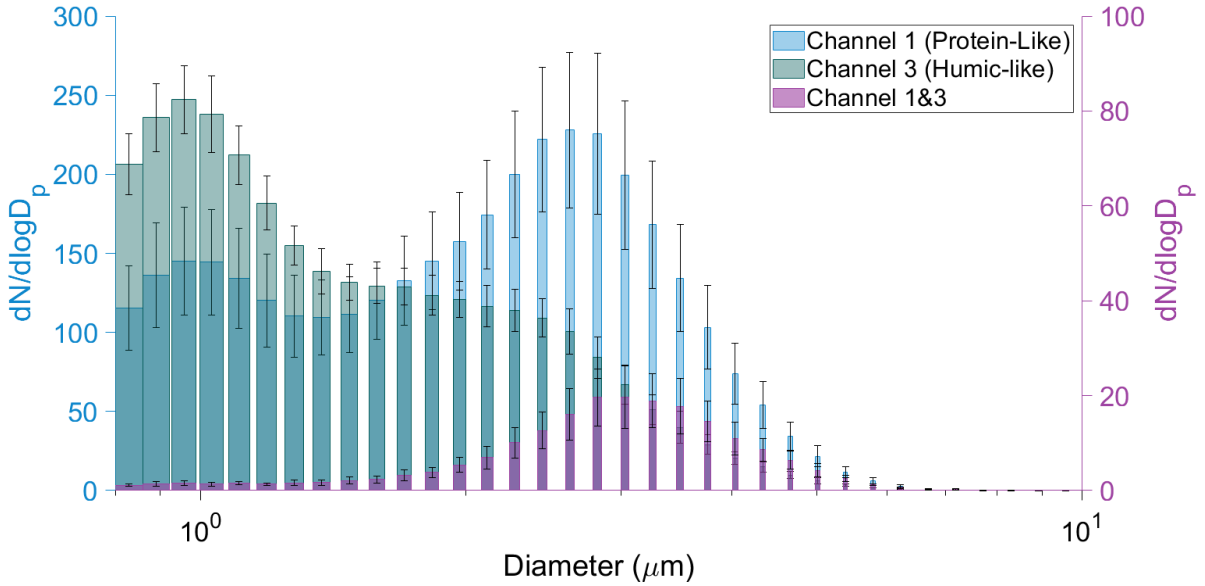

Figure 3.9. SSA size distributions separated by fluorescence channels measured with the WIBS. Channel 1 (protein-like) is in blue, channel 3 (humic-like) overlaid in green, and particles which fluoresced in both channels 1&3 are overlaid in purple. The size distributions shown are the daily mean particle counts (#/L) normalized to the bin widths and the error bars represent one standard deviation from the mean.

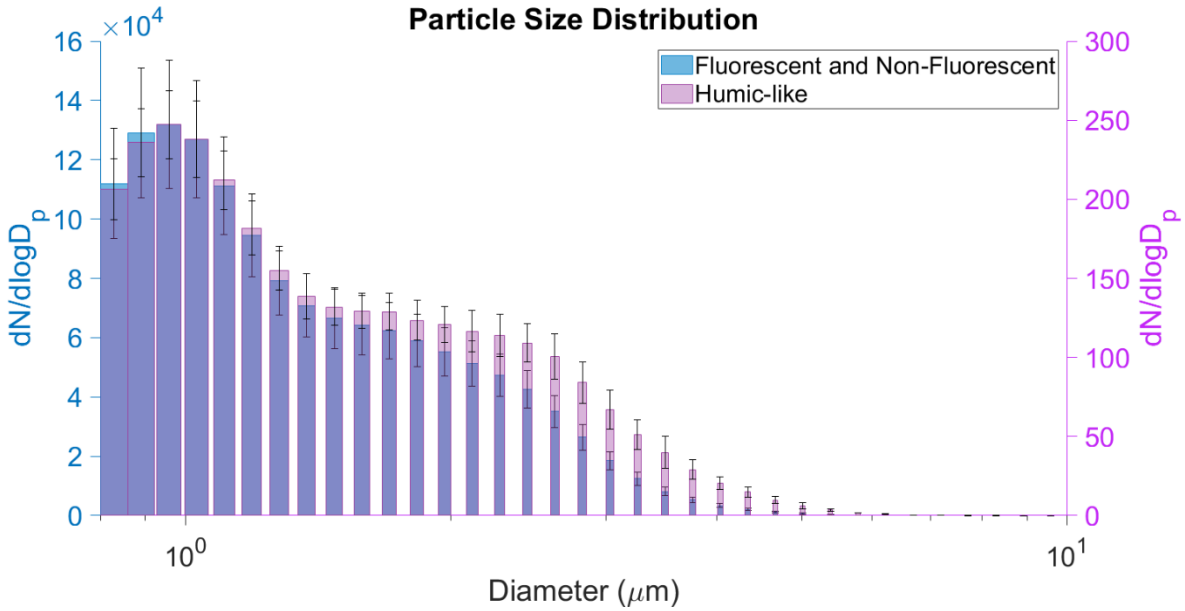

Figure 3.10. Particle size distribution of the SSA generated by the wave channel. Shown are the mean daily size distributions for total particles (fluorescent and non-fluorescent) (blue) as well as humic-like particles (pink). Averages along with standard deviations are derived from the seven days of sampling SSA from the wave channel.

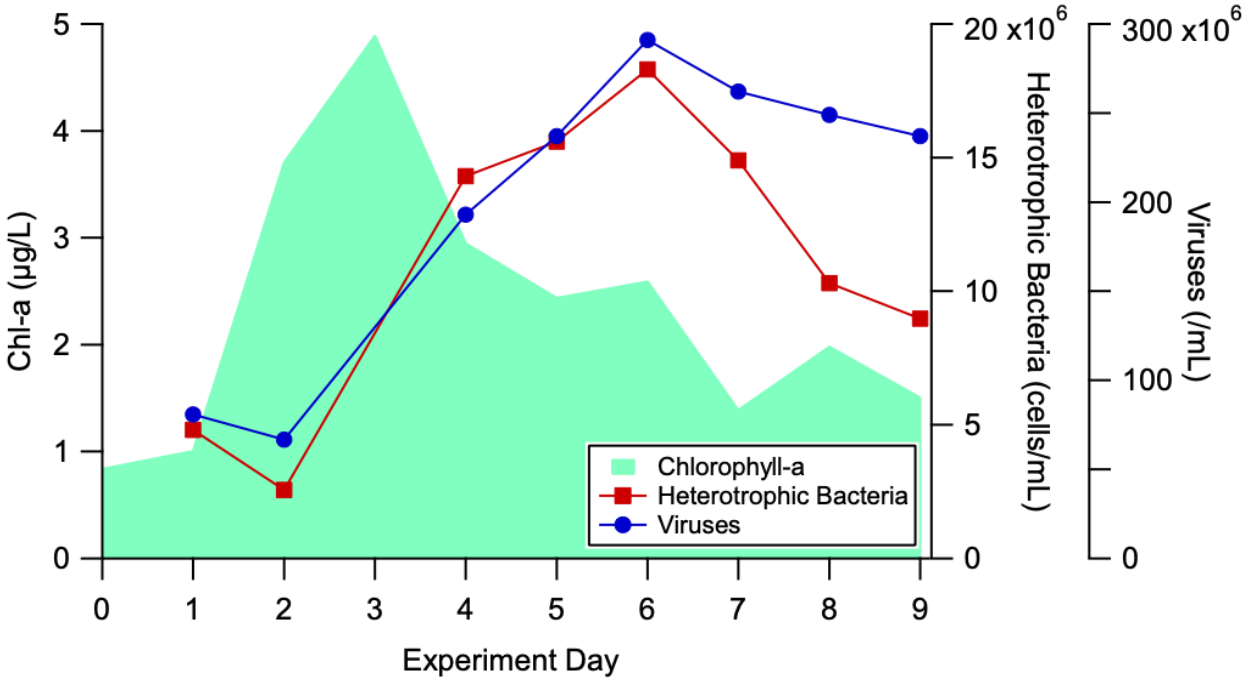

Figure 3.11. Microbial changes in the mesocosm phytoplankton bloom experiment. Chlorophyll *a* (green area), heterotrophic bacteria (red squares), and viruses (blue circles) concentrations are measured over time.

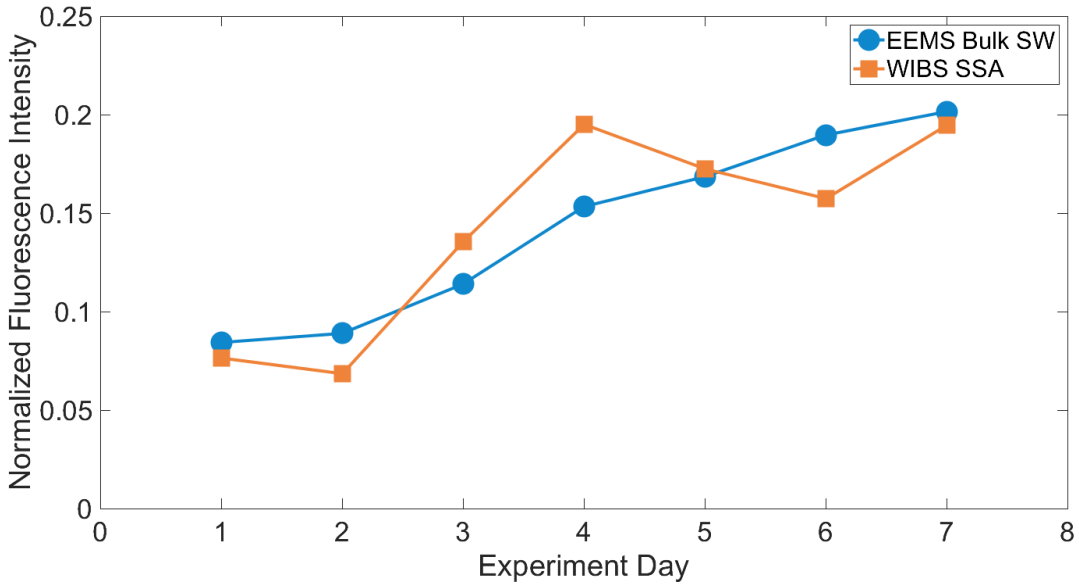

Figure 3.12. WIBS SSA mean intensity values for channel 3 (orange squares) compared to the EEMs mean intensity for the bulk seawater corresponding to the excitation and emission wavelengths of the WIBS channel 3 (blue circles). Experiment days refer to the day of the phytoplankton bloom experiment.

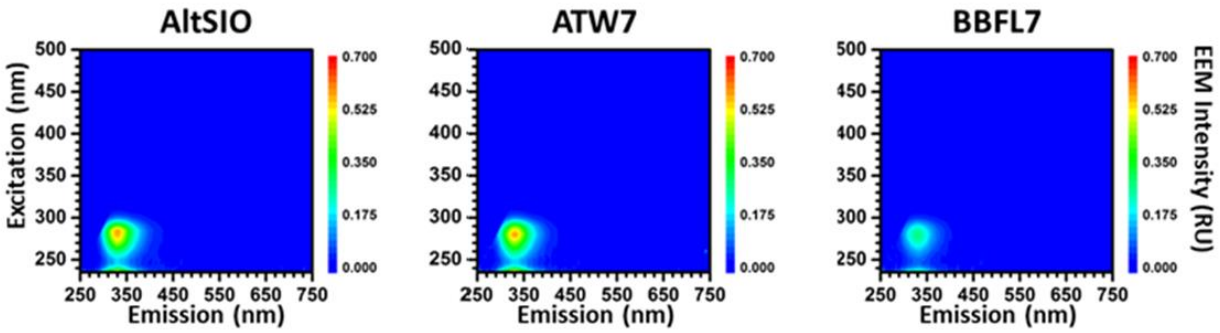

Figure 3.13. Selected EEMs for three different bacterial isolates: AltSIO, ATW7, and BBFL7.

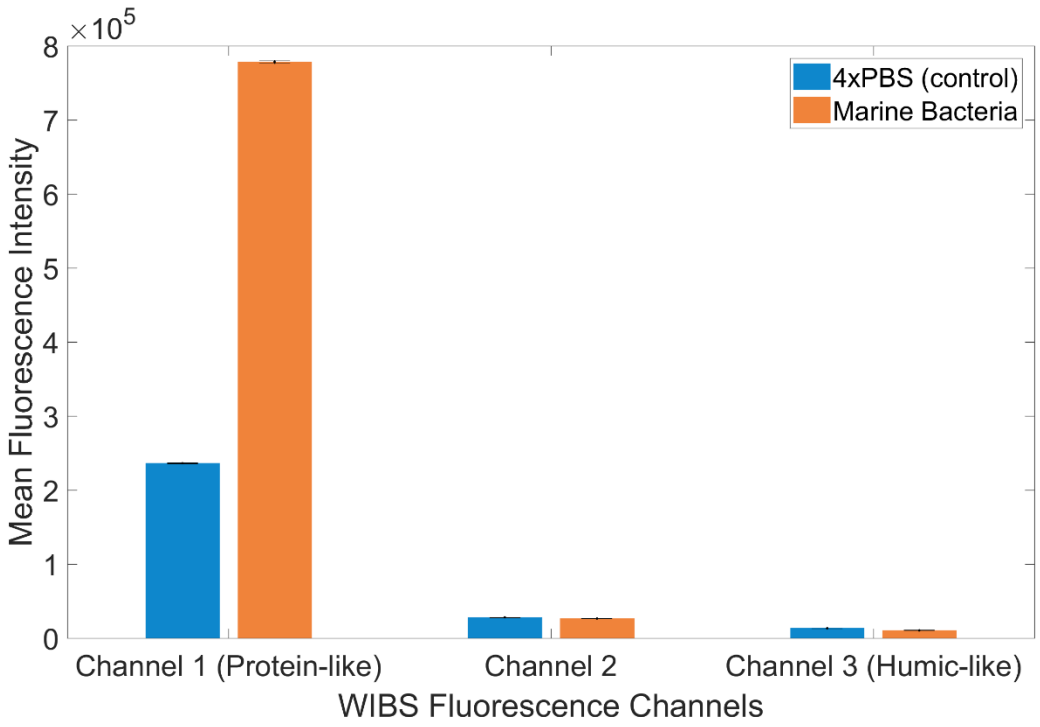

Figure 3.14. WIBS mean fluorescence intensity across each channel for the marine bacterial isolates compared to the 4xPBS solution (background). Error bars shown represent the standard error for each measurement.

3.10 References

Aller, J. Y., Kuznetsova, M. R., Jahns, C. J., and Kemp, P. F.: The sea surface microlayer as a source of viral and bacterial enrichment in marine aerosols, J. Aerosol Sci., 36, 801–812, https://doi.org/10.1016/j.jaerosci.2004.10.012, 2005.

Andersson, M., Catalán, N., Rahman, Z., Tranvik, L., and Lindström, E.: Effects of sterilization on dissolved organic carbon (DOC) composition and bacterial utilization of DOC from lakes, Aquat. Microb. Ecol., 82, 199–208, https://doi.org/10.3354/ame01890, 2018.

Andreae, M. O. and Rosenfeld, D.: Aerosol-cloud-precipitation interactions. Part 1. The nature and sources of cloud-active aerosols, Earth-Science Rev., 89, 13–41, https://doi.org/10.1016/j.earscirev.2008.03.001, 2008.

Azam, F., Fenchel, T., Field, J., Gray, J., Meyer-Reil, L., and Thingstad, F.: The Ecological Role of Water-Column Microbes in the Sea, Mar. Ecol. Prog. Ser., 10, 257–263, https://doi.org/10.3354/meps010257, 1983.

Benner, R., Pakulski, J. D., McCarthy, M., Hedges, J. I., and Hatcher, P. G.: Bulk chemical characteristics of dissolved organic matter in the ocean, Science (80-.)., 255, 1561–1564, https://doi.org/10.1126/science.255.5051.1561, 1992.

Bidle, K. and Azam, F.: Bacterial control of silicon regeneration from diatom detritus: Significance of bacterial ectohydrolases and species identity, Limnol. Oceanogr., 46, 1606–1623, 2001.

Burrows, S. M., Hoose, C., Pöschl, U., and Lawrence, M. G.: Ice nuclei in marine air: Biogenic particles or dust?, Atmos. Chem. Phys., 13, 245–267, https://doi.org/10.5194/acp-13-245-2013, 2013.

Coble, P. G.: Characterization of marine and terrestrial DOM in seawater using excitation-emission matrix spectroscopy, Mar. Chem., 51, 325–346, https://doi.org/10.1016/0304-4203(95)00062-3, 1996.

Collins, D. B., Zhao, D. F., Ruppel, M. J., Laskina, O., Grandquist, J. R., Modini, R. L., Stokes, M. D., Russell, L. M., Bertram, T. H., Grassian, V. H., Deane, G. B., and Prather, K. A.: Direct aerosol chemical composition measurements to evaluate the physicochemical differences between controlled sea spray aerosol generation schemes, Atmos. Meas. Tech., 7, 3667–3683, https://doi.org/10.5194/amt-7-3667-2014, 2014.

Crawford, I., Gallagher, M. W., Bower, K. N., Choularton, T. W., Flynn, M. J., Ruske, S., Listowski, C., Brough, N., Lachlan-Cope, T., Fleming, Z. L., Foot, V. E., and Stanley, W. R.: Real-time detection of airborne fluorescent bioparticles in Antarctica, Atmos. Chem. Phys., 17, 14291–14307, https://doi.org/10.5194/acp-17-14291-2017, 2017.

Després, V., Huffman, Ja., Burrows, S. M., Hoose, C., Safatov, A., Buryak, G., Fröhlich-Nowoisky, J., Elbert, W., Andreae, M., Pöschl, U., Jaenicke, R., Huffman, A., Viviane

Despré S, B. R., Alex Huffman, J., Safatov, A. S., Fro, J., and Andreae, M. O.: Primary biological aerosol particles in the atmosphere: a review, https://doi.org/10.3402/tellusb.v64i0.15598, 2012.

Determann, S., Lobbes, J. M., Reuter, R., and Rullkötter, J.: Ultraviolet fluorescence excitation and emission spectroscopy of marine algae and bacteria, Mar. Chem., 62, 137–156, https://doi.org/10.1016/S0304-4203(98)00026-7, 1998.

Eiguren Fernandez, A., Lewis, G. S., and Hering, S. V.: Design and laboratory evaluation of a sequential spot sampler for time-resolved measurement of airborne particle composition, Aerosol Sci. Technol., 48, 655–663, https://doi.org/10.1080/02786826.2014.911409, 2014.

Fennelly, M., Sewell, G., Prentice, M., O'Connor, D., and Sodeau, J.: Review: The Use of Real-Time Fluorescence Instrumentation to Monitor Ambient Primary Biological Aerosol Particles (PBAP), Atmosphere (Basel)., 9, https://doi.org/10.3390/atmos9010001, 2018.

Forde, E., Gallagher, M., Walker, M., Foot, V., Attwood, A., Granger, G., Sarda-Estève, R., Stanley, W., Kaye, P., and Topping, D.: Intercomparison of Multiple UV-LIF Spectrometers Using the Aerosol Challenge Simulator, Atmos. 2019, Vol. 10, Page 797, 10, 797, https://doi.org/10.3390/ATMOS10120797, 2019.

Fröhlich-Nowoisky, J., Kampf, C. J., Weber, B., Huffman, J. A., Pöhlker, C., Andreae, M. O., Lang-Yona, N., Burrows, S. M., Gunthe, S. S., Elbert, W., Su, H., Hoor, P., Thines, E., Hoffmann, T., Després, V. R., and Pöschl, U.: Bioaerosols in the Earth system: Climate, health, and ecosystem interactions, Atmos. Res., 182, 346–376, https://doi.org/10.1016/J.ATMOSRES.2016.07.018, 2016.

Gabey, A. M., Gallagher, M. W., Whitehead, J., Dorsey, J. R., Kaye, P. H., and Stanley, W. R.: Measurements and comparison of primary biological aerosol above and below a tropical forest canopy using a dual channel fluorescence spectrometer, Atmos. Chem. Phys. Atmos. Chem. Phys., 10, 4453–4466, https://doi.org/10.5194/acp-10-4453-2010, 2010.

Gabey, A. M., Stanley, W. R., Gallagher, M. W., and Kaye, P. H.: The fluorescence properties of aerosol larger than 0.8 μm in urban and tropical rainforest locations, Atmos. Chem. Phys., 11, 5491–5504, https://doi.org/10.5194/acp-11-5491-2011, 2011.

Gantt, B. and Meskhidze, N.: The physical and chemical characteristics of marine primary organic aerosol: A review, Atmos. Chem. Phys., 13, 3979–3996, https://doi.org/10.5194/acp-13-3979-2013, 2013.

Gasol, J. M. and Del Giorgio, P. A.: Using flow cytometry for counting natural planktonic bacteria and understanding the structure of planktonic bacterial communities, in: Scientia Marina, 197–224, https://doi.org/10.3989/scimar.2000.64n2197, 2000.

Grzybowski, W.: Selected properties of different molecular size fractions of humic substances

isolated from surface Baltic water in the Gdańsk Deep area, 38, 33–47, 1996.

Guillard, R. R. L. and Ryther, J. H.: Studies of Marine Planktonic Diatoms: I. Cyclotella Nana Hustedt, and Detonula Confervacea (Cleve) Gran., Can. J. Microbiol., 8, 229–239, https://doi.org/10.1139/m62-029, 1962.

Hernandez, M., Perring, A. E., McCabe, K., Kok, G., Granger, G., and Baumgardner, D.: Chamber catalogues of optical and fluorescent signatures distinguish bioaerosol classes, Atmos. Meas. Tech., 9, 3283–3292, https://doi.org/10.5194/amt-9-3283-2016, 2016.

Hessen, D. O. and Tranvik, L. J.: Aquatic humic substances: ecology and biochemistry, Springer-Verlag Berlin Heidelberg, Berlin, 1998.

Kasparian, J., Hassler, C., Ibelings, B., Berti, N., Bigorre, S., Djambazova, V., Gascon-Diez, E., Giuliani, G., Houlmann, R., Kiselev, D., De Laborie, P., Le, A. D., Magouroux, T., Neri, T., Palomino, D., Pfändler, S., Ray, N., Sousa, G., Staedler, D., Tettamanti, F., Wolf, J. P., and Beniston, M.: Assessing the Dynamics of Organic Aerosols over the North Atlantic Ocean, Sci. Rep., 7, https://doi.org/10.1038/srep45476, 2017.

Kaye, P. H., Stanley, W. R., Hirst, E., Foot, E. V., Baxter, K. L., and Barrington, S. J.: Single particle multichannel bio-aerosol fluorescence sensor, Opt. Express, 13, 3583, https://doi.org/10.1364/opex.13.003583, 2005.

Kaye, P. H., Aptowicz, K., Chang, R. K., Foot, V., and Videen, G.: Angularly Resolved Elastic Scattering From Airborne Particles, in: Optics of Biological Particles, Springer Netherlands, 31–61, https://doi.org/10.1007/978-1-4020-5502-7_3, 2007.

Lakowicz, J. R.: Principles of fluorescence spectroscopy, Springer, 1–954 pp., https://doi.org/10.1007/978-0-387-46312-4, 2006.

Lawaetz, A. J. and Stedmon, C. A.: Fluorescence intensity calibration using the Raman scatter peak of water, Appl. Spectrosc., 63, 936–940, https://doi.org/10.1366/000370209788964548, 2009.

Lee, C., Sultana, C. M., Collins, D. B., Santander, M. V., Axson, J. L., Malfatti, F., Cornwell, G. C., Grandquist, J. R., Deane, G. B., Stokes, M. D., Azam, F., Grassian, V. H., and Prather, K. A.: Advancing Model Systems for Fundamental Laboratory Studies of Sea Spray Aerosol Using the Microbial Loop, J. Phys. Chem. A, 119, 8860–8870, https://doi.org/10.1021/acs.jpca.5b03488, 2015.

Lee, H. D., Morris, H. S., Laskina, O., Sultana, C. M., Lee, C., Jayarathne, T., Cox, J. L., Wang, X., Hasenecz, E. S., Demott, P. J., Bertram, T. H., Cappa, C. D., Stone, E. A., Prather, K. A., Grassian, V. H., and Tivanski, A. V.: Organic Enrichment, Physical Phase State, and Surface Tension Depression of Nascent Core-Shell Sea Spray Aerosols during Two Phytoplankton Blooms, ACS Earth Sp. Chem., 4, 650–660, https://doi.org/10.1021/acsearthspacechem.0c00032, 2020.

Liu, L., Huang, Q., Zhang, Y., Qin, B., and Zhu, G.: Excitation-emission matrix fluorescence and parallel factor analyses of the effects of N and P nutrients on the extracellular polymeric substances of Microcystis aeruginosa, 63, 18–26, https://doi.org/10.1016/j.limno.2016.10.006, 2017.

Malfatti, F., Lee, C., Tinta, T., Pendergraft, M. A., Celussi, M., Zhou, Y., Sultana, C. M., Rotter, A., Axson, J. L., Collins, D. B., Santander, M. V., Anides Morales, A. L., Aluwihare, L. I., Riemer, N., Grassian, V. H., Azam, F., and Prather, K. A.: Detection of Active Microbial Enzymes in Nascent Sea Spray Aerosol: Implications for Atmospheric Chemistry and Climate, Environ. Sci. Technol. Lett., 6, 171–177, https://doi.org/10.1021/acs.estlett.8b00699, 2019.

Mari, X. and Kiørboe, T.: Abundance, size distribution and bacterial colonization of transparent exopolymeric particles (TEP) during spring in the Kattegat, J. Plankton Res., 18, 969–986, https://doi.org/10.1093/plankt/18.6.969, 1996.

Mostofa, K. M. G., Liu, C., Mottaleb, M. A., Wan, G., Ogawa, H., Vione, D., Yoshioka, T., and Wu, F.: Photobiogeochemistry of Organic Matter, edited by: Mostofa, K. M. G., Yoshioka, T., Mottaleb, A., and Vione, D., Springer Berlin Heidelberg, Berlin, Heidelberg, 1–135 pp., https://doi.org/10.1007/978-3-642-32223-5, 2013.

Murphy, K. R.: A note on determining the extent of the water Raman peak in fluorescence spectroscopy, Appl. Spectrosc., 65, 233–236, https://doi.org/10.1366/10-06136, 2011.

Nebbioso, A. and Piccolo, A.: Molecular characterization of dissolved organic matter (DOM): A critical review, https://doi.org/10.1007/s00216-012-6363-2, January 2013.

Noble, R. T. and Fuhrman, J. A.: Use of SYBR Green I for rapid epifluorescence counts of marine viruses and bacteria, Aquat. Microb. Ecol., 14, 113–118, https://doi.org/10.3354/ame014113, 1998.

Patterson, J. P., Collins, D. B., Michaud, J. M., Axson, J. L., Sultana, C. M., Moser, T., Dommer, A. C., Conner, J., Grassian, V. H., Stokes, M. D., Deane, G. B., Evans, J. E., Burkart, M. D., Prather, K. A., and Gianneschi, N. C.: Sea spray aerosol structure and composition using cryogenic transmission electron microscopy, ACS Cent. Sci., 2, 40–47, https://doi.org/10.1021/acscentsci.5b00344, 2016.

Pedler, B. E., Aluwihare, L. I., and Azam, F.: Single bacterial strain capable of significant contribution to carbon cycling in the surface ocean, Proc. Natl. Acad. Sci. U. S. A., 111, 7202–7207, https://doi.org/10.1073/pnas.1401887111, 2014.

Pöhlker, C., Huffman, J. A., and Pöschl, U.: Autofluorescence of atmospheric bioaerosols-fluorescent biomolecules and potential interferences, Atmos. Meas. Tech, 5, 37–71, https://doi.org/10.5194/amt-5-37-2012, 2012.

Prather, K. A., Bertram, T. H., Grassian, V. H., Deane, G. B., Stokes, M. D., DeMott, P. J.,

Aluwihare, L. I., Palenik, B. P., Azam, F., Seinfeld, J. H., Moffet, R. C., Molina, M. J., Cappa, C. D., Geiger, F. M., Roberts, G. C., Russell, L. M., Ault, A. P., Baltrusaitis, J., Collins, D. B., Corrigan, C. E., Cuadra-Rodriguez, L. A., Ebben, C. J., Forestieri, S. D., Guasco, T. L., Hersey, S. P., Kim, M. J., Lambert, W. F., Modini, R. L., Mui, W., Pedler, B. E., Ruppel, M. J., Ryder, O. S., Schoepp, N. G., Sullivan, R. C., and Zhao, D.: Bringing the ocean into the laboratory to probe the chemical complexity of sea spray aerosol, Proc. Natl. Acad. Sci. U. S. A., 110, 7550–7555, https://doi.org/10.1073/pnas.1300262110, 2013.

Rastelli, E., Corinaldesi, C., Dell'anno, A., Lo Martire, M., Greco, S., Cristina Facchini, M., Rinaldi, M., O'Dowd, C., Ceburnis, D., and Danovaro, R.: Transfer of labile organic matter and microbes from the ocean surface to the marine aerosol: An experimental approach, Sci. Rep., 7, https://doi.org/10.1038/s41598-017-10563-z, 2017.

Rinaldi, M., Fuzzi, S., Decesari, S., Marullo, S., Santoleri, R., Provenzale, A., Von Hardenberg, J., Ceburnis, D., Vaishya, A., O'Dowd, C. D., and Facchini, M. C.: Is chlorophyll-a the best surrogate for organic matter enrichment in submicron primary marine aerosol?, J. Geophys. Res. Atmos., 118, 4964–4973, https://doi.org/10.1002/JGRD.50417, 2013.

Robinson, E. S., Gao, R.-S., Schwarz, J. P., Fahey, D. W., and Perring, A. E.: Fluorescence calibration method for single-particle aerosol fluorescence instruments, Atmos. Meas. Tech, 10, 1755–1768, https://doi.org/10.5194/amt-10-1755-2017, 2017.

Savage, N. J., Krentz, C. E., Könemann, T., Han, T. T., Mainelis, G., Pöhlker, C., and Alex Huffman, J.: Systematic characterization and fluorescence threshold strategies for the wideband integrated bioaerosol sensor (WIBS) using size-resolved biological and interfering particles, Atmos. Meas. Tech., 10, 4279–4302, https://doi.org/10.5194/amt-10-4279-2017, 2017.

Shaffer, B. T. and Lighthart, B.: Survey of culturable airborne bacteria at four diverse locations in Oregon: Urban, rural, forest, and coastal, Microb. Ecol., 34, 167–177, https://doi.org/10.1007/s002489900046, 1997.

Smith, D., Simon, M., Alldredge, A., Azam, F.: Intense hydrolytic enzyme activity on marine aggregates and implications for rapid particle dissolution, Nature, 359, 139–142, https://doi.org/https://doi.org/10.1038/359139a0, 1992.

Stokes, M. D., Deane, G. B., Prather, K., Bertram, T. H., Ruppel, M. J., Ryder, O. S., Brady, J. M., and Zhao, D.: A Marine Aerosol Reference Tank system as a breaking wave analogue for the production of foam and sea-spray aerosols, Atmos. Meas. Tech., 6, 1085–1094, https://doi.org/10.5194/amt-6-1085-2013, 2013.

Stokes, M. D., Deane, G., Collins, D. B., Cappa, C., Bertram, T., Dommer, A., Schill, S., Forestieri, S., and Survilo, M.: A miniature Marine Aerosol Reference Tank (miniMART) as a compact breaking wave analogue, Atmos. Meas. Tech., 9, 4257–4267, https://doi.org/10.5194/amt-9-4257-2016, 2016.

Toprak, E. and Schnaiter, M.: Fluorescent biological aerosol particles measured with the Waveband Integrated Bioaerosol Sensor WIBS-4: Laboratory tests combined with a one year field study, Atmos. Chem. Phys., 13, 225–243, https://doi.org/10.5194/acp-13-225-2013, 2013.

Vergara-Temprado, J., Murray, B. J., Wilson, T. W., O'Sullivan, D., Browse, J., Pringle, K. J., Ardon-Dryer, K., Bertram, A. K., Burrows, S. M., Ceburnis, D., Demott, P. J., Mason, R. H., O'Dowd, C. D., Rinaldi, M., and Carslaw, K. S.: Contribution of feldspar and marine organic aerosols to global ice nucleating particle concentrations, Atmos. Chem. Phys., 17, 3637–3658, https://doi.org/10.5194/acp-17-3637-2017, 2017.

Wang, X., Sultana, C. M., Trueblood, J., Hill, T. C. J., Malfatti, F., Lee, C., Laskina, O., Moore, K. A., Beall, C. M., McCluskey, C. S., Cornwell, G. C., Zhou, Y., Cox, J. L., Pendergraft, M. A., Santander, M. V., Bertram, T. H., Cappa, C. D., Azam, F., DeMott, P. J., Grassian, V. H., and Prather, K. A.: Microbial control of sea spray aerosol composition: A tale of two blooms, ACS Cent. Sci., 1, 124–131, https://doi.org/10.1021/acscentsci.5b00148, 2015.

Yue, S., Ren, L., Song, T., Li, L., Xie, Q., Li, W., Kang, M., Zhao, W., Wei, L., Ren, H., Sun, Y., Wang, Z., Ellam, R. M., Liu, C., Kawamura, K., and Fu, P.: Abundance and Diurnal Trends of Fluorescent Bioaerosols in the Troposphere over Mt. Tai, China, in Spring, J. Geophys. Res. Atmos., 124, 4158–4173, https://doi.org/10.1029/2018JD029486, 2019.

Zhang, Y., Yin, Y., Feng, L., Zhu, G., Shi, Z., Liu, X., and Zhang, Y.: Characterizing chromophoric dissolved organic matter in Lake Tianmuhu and its catchment basin using excitation-emission matrix fluorescence and parallel factor analysis, Water Res., 45, 5110–5122, https://doi.org/10.1016/j.watres.2011.07.014, 2011.

Chapter 4. Single-Particle Fluorescence Properties of Oxidized Sea Spray Aerosol

4.1 Abstract

Biological aerosols (bioaerosols), typically detected in real time using fluorescence techniques, impact clouds and climate. Sea spray aerosol (SSA) particles act as a major source of bioaerosols, especially over remote marine and coastal regions. Accurate identification of marine bioaerosols is critical for proper representation in climate models; however, atmospheric aging, including oxidation, heterogeneous reactions, and the influence of secondary organic aerosols, can affect the fluorescence properties of nascent bioaerosols. Here, we simulated the equivalent of 3 – 16 days of atmospheric aging on SSA generated from a wave channel during two induced phytoplankton mesocosm blooms to identify the effects of oxidation on the fluorescence signature of naturally produced SSA. Aged particle populations showed a significant increase in the fraction of particles with humic-like fluorescence (excitation/emission: 280 nm/ 420 – 600 nm and 370 nm/ 420 – 600 nm), 1.2 – 7.5 times that of nascent SSA after 3 days of equivalent aging. Additionally, oxidation decreased single-particle protein-like fluorescence intensity (ex/em: 280 nm/ 310 – 400 nm) and increased humic-like fluorescence intensity, indicative of protein degradation and humic-like substance production in aged SSA. These controlled experiments on the oxidation of SSA highlight the impact of atmospheric aging on marine bioaerosol discrimination and the resulting chemical transformations that may affect the ability of SSA to seed clouds.

4.2 Introduction

Biological aerosols (bioaerosols, e.g., bacteria, viruses, pollen, fungi, and their fragments) affect clouds and climate directly by scattering and absorbing radiation, and indirectly by influencing cloud formation and cloud radiative properties (Fröhlich-Nowoisky et al., 2016). With oceans covering over two-thirds of the Earth, sea spray aerosol (SSA) particles comprise an

important source of bioaerosols in both remote marine and coastal regions (Després et al., 2012). Marine bioaerosols can have global implications; recent estimates report marine emission comprise ~30-70% of all airborne eukaryotes and prokaryotes (Mayol et al., 2017). It is therefore important to accurately detect and identify bioaerosols in the ambient marine environment to better understand their effect on local and global scales.

Real-time detection of bioaerosols is commonly performed using fluorescence-based techniques which detect intrinsically fluorescent biological molecules in these aerosols. Intrinsically fluorescent molecules include the aromatic amino acids tryptophan, tyrosine, and phenylalanine, as well as biological cofactors such as nicotinamide-adenine dinucleotide (phosphate) (NADH, NADPH) and riboflavin (Pöhlker et al., 2012). Recent studies have observed changes in bioaerosol fluorescence upon exposure to several factors including ozone, relative humidity (RH), solar simulated light, and interactions with secondary organic aerosol (SOA) formed from volatile organic compounds (VOCs) (Santarpia et al., 2012; Ratnesar-Shumate et al., 2015; Kinahan et al., 2019; Pan et al., 2014; Zhang et al., 2021). These studies report a reduction in protein-like fluorescence and an increase in Vis-excited visible fluorescence attributed to the oxidation of tryptophan and formation of N-formyl kynurenine and kynurenine under conditions of high RH and ozone (Ignatenko et al., 1982; Ignatenko, 1988). Because of the influence of these environmental factors on aerosol fluorescence, further research is required to better understand the effect of atmospheric aging on bioaerosol measurement and detection (Estillore et al., 2016; Santarpia, 2016; Huffman et al., 2020; Pan et al., 2021).

Few studies have measured the effect of atmospheric oxidants on primary SSA (Trueblood et al., 2020), and despite recent studies on the fluorescence signature of isolated, nascent SSA (Lee et al., 2015; Santander et al., 2021), no studies have observed the influence of oxidants on the

fluorescence properties of SSA. These experiments are necessary to relate laboratory data with field studies in ambient marine environments which use fluorescence-based techniques to identify bioaerosols released in SSA (Kasparian et al., 2017; Morrison et al., 2020; Kawana et al., 2021; Moallemi et al., 2021). To better characterize biological SSA in the ambient environment and therefore inform both instrument development and parameterizations of marine bioaerosols in climate models, an improved understanding of the influence of oxidants on SSA is required.

Here, we help bridge the gap between laboratory-based studies on the fluorescence of nascent SSA and field studies in marine environments by measuring the changes to fluorescent SSA after oxidation in a controlled system. In this study, an ocean-atmosphere wave channel was used to generate SSA from natural seawater and fluorescent SSA particles were detected with a wideband integrated bioaerosol sensor (WIBS). The WIBS was used to characterize and monitor the fluorescence of SSA generated throughout the course of two phytoplankton mesocosm blooms. Nascent SSA and marine VOCs were passed through an oxidative flow reactor (OFR), which simulates atmospheric oxidation at various days of equivalent aging (Kang et al., 2007), to produce aged SSA. Both nascent and aged SSA were then measured with the WIBS at different stages of the bloom. The fluorescence properties of aged SSA were monitored throughout changing seawater biological conditions. This study demonstrates the effect of atmospheric aging on the fluorescence properties of SSA over the course of a phytoplankton bloom.

4.3 Methods

4.3.1 Phytoplankton Mesocosm Blooms and Aerosol Generation

Two phytoplankton blooms were induced in an ocean-atmosphere wave channel during the summer of 2019 as part of the Sea Spray Chemistry and Particle Evolution (SeaSCAPE) campaign. Full details on the experimental conditions of the SeaSCAPE campaign can be found in Sauer et

al. (2022) (Sauer et al., 2022). Briefly, a 11,800 L wave channel was filled with filtered seawater (50 µm Nitex mesh) collected from the Pacific Ocean and used to generate an accurate distribution of natural SSA (Stokes et al., 2013; Lee et al., 2015). During SeaSCAPE, a total of three phytoplankton blooms were induced, however, WIBS measurements were only collected during the last two blooms, which we will refer to herein as experiment 1 and experiment 2. In experiment 1, from July 12th-July 19th, 2019, seawater was spiked with f/20 nutrient mixture and sodium metasilicate to induce a phytoplankton bloom (Guillard and Ryther, 1962). The seawater in this experiment was doubly filtered, resulting in a system dominated by smaller cells such as marine bacteria. Experiment 2, from July 24th-August 13th, 2019, was inoculated with a final concentration of f/2 nutrients and sodium metasilicate (Guillard and Ryther, 1962). Due to low initial phytoplankton growth, a 1,135 L infusion of inoculated seawater grown with natural sunlight was added to the tank on August 1st, 2019, to increase the overall bioactivity. Here, we focus primarily on experiment 2 which captured all phases of a phytoplankton bloom progression.

4.3.2 Wideband Integrated Bioaerosol Sensor (WIBS)

The single-particle fluorescence spectrometer used in this study was a wideband integrated bioaerosol sensor (WIBS-NEO, Droplet Measurement Techniques). The operation of the WIBS instruments have been described in detail in other publications (Gabey et al., 2010), and details on this model have been described previously (Forde et al., 2019; Santander et al., 2021). Briefly, the WIBS uses a 635 nm continuous-wave laser to measure the shape of fluorescent and non-fluorescent particles in the form of an asymmetry factor (AF) ranging from 1 – 100 for spheres to rods, respectively, and determine the optical diameter of each particle ranging from 0.5 to 50 µm, based on calibrations with polystyrene latex spheres. Two consecutive xenon lamps are used as excitation sources at 280 nm (Xe1) and 370 nm (Xe2). Fluorescence emission is collected using

two photomultiplier tubes with optical filters that transmit light from 310 – 400 nm (FL1) and 420 – 650 nm (FL2). The combination of these excitation sources and emission detection bands leads to three distinct fluorescence channels (channel 1: Xe1/FL1, channel 2: Xe1/FL2, channel 3: Xe2/FL2). We follow a common method of particle classification described in Perring et al. (2015) where particles are divided into seven different classes based on their fluorescence in any combination of the three channels (Perring et al., 2015). Following this method, the 3 fluorescence channels are defined as type A (channel 1), type B (channel 2), and type C (channel 3) along with the logical combinations (AB, AC, BC, ABC). Here, when particles are defined according to their channels (i.e., channels 1-3) they are inclusive of all fluorescent particles in that channel regardless of any overlap between the three channels. However, when defined by the different classes following Perring et al. (2015), particles with fluorescence in one of the primary classes (A, B, C) are defined as fluorescing in one channel exclusively. Figure 4.6 provides further details regarding the different classification schemes.

To determine the background fluorescence for the WIBS, a forced trigger is performed where the xenon lamps fire into an empty optical chamber. Individual particles are considered fluorescent if their fluorescence intensity is greater than three standard deviations above the mean forced trigger intensity for a specific channel (Toprak and Schnaiter, 2013). During this study, the forced trigger was performed before sampling each day and on an eight-hour schedule throughout the sampling period. The background signal was derived from the average forced trigger value for each sample. The forced trigger threshold for each channel was subtracted from the reported fluorescence intensities, therefore, each intensity is the fluorescence above the threshold. In addition to the fluorescence intensity threshold, the data were selected for particles with optical

diameters greater than 0.8 μm to account for possible counting inaccuracies at the lower end of the WIBS size range (Gabey et al., 2011; Crawford et al., 2017; Lieberherr et al., 2021).

4.3.3 Potential Aerosol Mass Oxidative Flow Reactor Operation

A potential aerosol mass oxidative flow reactor (OFR, Aerodyne Inc) was used to simulate atmospheric aging through oxidation and heterogeneous reactions of the gases and aerosols coming out of the wave channel. The operation and design of the OFR has been described in detail in other publications (Kang et al., 2007; Lambe et al., 2011), and the OFR used in this study has previously been described (Sauer et al., 2022). Here, the OFR was operated in 185 nm mode, which illuminates 185 nm and 254 nm UV lamps to generate both ozone (O_3) and the hydroxy radical (OH). Although the UV lamps have the potential to affect SSA fluorescence via photo-oxidation, supplemental experiments (Supplemental Information, Figure 4.7) demonstrated that the influence of radiation was minimized compared to the effect of the oxidants under normal operations. The OH exposure in the OFR at specific lamp voltages was calculated from the oxidation and loss of carbon monoxide (CO analyzer: APMA-370, Horiba Ltd.), which has a known reaction rate with OH (Chen and Marcus, 2006). A calibration curve was generated to describe the OH exposure and calculate the days of equivalent aging based on typical ambient OH concentrations (1.0×10^6 molec·cm^{-3}) (Figure 4.8) (Wolfe et al., 2019). Throughout these experiments, lamp voltages were set to represent ~3.2, 9.9 and 16.6 days of equivalent aging. OFR lamp voltages were cycled to allow measurements of nascent, 3.2, 9.9, and 16.6 days of equivalent aging for ~72 min each before the subsequent cycle. To account for this, WIBS data points with the shortest separation of time were selected to compare the effects of aging.

The total flow rate through the OFR in these experiments was set to 6 liters per minute (LPM). At this flow rate, with an internal volume of the OFR equal to 13.3 liters and assuming a plug flow,

the total residence time within the OFR was equal to about 133 seconds. Throughout the experiment, the relative humidity (RH) inside the OFR was maintained at 50-70% which is required for proper ozone and OH formation. Aerosols exiting the OFR were passed through a denuder to remove excess ozone (Carulite-200, Ozone Solutions) and subsequently dried through a silica diffusion drier to maintain an RH <20% prior to aerosol measurements.

4.3.4 Measurements of Biological Activity

In situ chlorophyll-a concentrations were measured with a homemade continuous flow sampling system which utilized a fluorescence sensor (ECO-Triplet-BBFL2, Sea Bird Scientific) with an excitation/emission of 470/695 nm to measure chlorophyll-a fluorescence. Measurements were made on a 1-minute time interval and reported concentrations represent 10-minute averages ± one standard deviation. This system was calibrated using extracted chlorophyll-a fluorescence measurements from bulk seawater following conventional protocols (Holm-Hansen et al., 1965).

Heterotrophic bacteria concentrations were measured in bulk seawater. Samples were fixed using 5% glutaraldehyde, flash-frozen in liquid nitrogen, and stored in a −80°C freezer to be preserved prior to analysis (Gasol and Del Giorgio, 2000). Samples were then thawed, diluted 10-fold using 1x TE buffer (pH 8) and stained using SYBR Green I for 10 minutes in the dark prior to enumeration using a flow cytometer (FACSCanto II, BD) (Noble and Fuhrman, 1998). Daily measurements of the bacterial concentration were made in triplicate for experiment 2 and the average ± one standard deviation is reported. Samples from experiment 1 represent a single daily measurement.

4.4 Results & Discussion

4.4.1 Mesocosm Phytoplankton Blooms Overview

In experiment 1, low chlorophyll-a concentrations were observed throughout the course of the experiment. Despite low phytoplankton growth, heterotrophic bacteria concentrations representative of a natural system were observed with the highest concentrations at the start of the experiment (Figure 4.9) (Azam and Malfatti, 2007). The nascent fluorescent particle fraction during this experiment varied from approximately 2% to 3.5% (Figure 4.9).

Experiment 2 began with relatively low concentrations of chlorophyll-a until the mesocosm was spiked on August 1, 2019, with a tank of inoculated seawater grown in natural sunlight (Figure 4.2). Following the addition of the outdoor tank, chlorophyll-a concentration quickly rose and reached a peak on August 3, 2019, ensued by a rapid decline. Experiment 2 adhered to previously observed patterns of a phytoplankton bloom with chlorophyll-a growth and senescence followed by bacterial growth, which reached a maximum on August 7, 2019 (Buchan et al., 2014; Azam et al., 1983).

To better define the different biological stages of this phytoplankton bloom, we separated it into three distinct time periods: pre-bloom which occurs from the initial inoculation of the bloom on July 24th, 2019, until the addition of the outdoor tank on August 1st; peak-bloom following the addition of the tank until the decline in the chlorophyll-a concentrations on August 5th; and post-bloom from August 5th until August 14th during phytoplankton senescence and bacterial growth.

Throughout this phytoplankton bloom, the nascent fluorescent particle fraction varied from 1.3% to 2.5% with the highest fluorescent fractions occurring in the pre-bloom and post-bloom phases, during periods of heterotrophic bacteria growth (Figure 4.2). The daily fluorescent fractions observed in this study were comparable to the fraction of fluorescent particles measured over the ocean (1.3% - 1.6% for particles > 1 μm) (Moallemi et al., 2021; Kawana et al., 2021). The fluorescent particle fractions measured in experiments 1 and 2 were higher than those

previously reported for nascent SSA generated in a laboratory setting under low biomass conditions (Santander et al., 2021). These differences suggest that increased biomass in the bulk seawater (i.e., phytoplankton cells and bacteria) may result in higher fluorescent particle fractions in SSA, due to the transfer of more fluorescent biological material in the aerosol phase.

4.4.2 Impact of Increased Aging on Particle Fluorescence Intensity

Aging influenced the fluorescence intensities in channels 1 – 3 for all fluorescent particles in experiment 2 (Figure 4.3). In channel 1, the number of particles with fluorescence intensities between 10^3 and 10^6 arbitrary units (A.U.) decreased after aging in the OFR. The greatest change in the fraction of particles fluorescent in channel 1 occurred at 3.2 days of equivalent aging (the lowest aging condition). Subsequent aging to 9.9 equivalent days resulted in a further decline in the number of particles with fluorescence in channel 1, especially for particles with fluorescence between 10^4 and 10^5 A.U. Between 9.9 and 16.6 days of equivalent aging, there was little change in the number of particles with fluorescence in channel 1, suggesting the greatest effect of aging on fluorescence in channel 1 occurred in the initial aging period. These changes were also reflected in the daily mean fluorescence intensity for channel 1 (Figure 4.10). Throughout the course of the phytoplankton bloom, a general decrease in the mean intensity was observed for the aged particle populations, with the most notable shift observed for the lowest aging conditions (3.2 equivalent days).

The decrease in particles with high fluorescence intensity within this channel is likely attributed to the oxidation of tryptophan within SSA. The fluorescence intensity of tryptophan, the main fluorescent component within channel 1, has been shown to decrease when oxidized by ozone under high RH (50% & 80%) (Pan et al., 2014). Additionally, tryptophan is known to degrade following reactions with OH (Maskos et al., 1992; Berlett and Stadtman, 1997). The OFR, which

produces ozone and OH, was maintained at an RH between 50-70% throughout these experiments, thus providing the proper conditions for tryptophan oxidation and degradation. Control experiments with aerosolized tryptophan and ammonium sulfate particles showed a substantial decrease in the number of particles with fluorescence in channel 1 after aging (Figure 4.11). The decrease in fluorescent fraction for tryptophan particles was much greater than the decrease observed for aged SSA. Unlike tryptophan in SSA, which can be embedded within proteins, exopolymeric substances, and microbes, the tryptophan in the control experiment was likely more exposed to oxidants leading to increased degradation.

Fluorescent particles in channel 2 and channel 3 showed similar trends following aging in the OFR. For both channels, an increase in the fraction of particles with high fluorescence intensity was observed following aging. Moreover, after 3.2 days of equivalent aging, the mode of particles with fluorescence in channels 2 shifted to a higher fluorescence intensity than nascent SSA. With increased exposure to oxidants, the fraction of particles fluorescent in channel 2 continued to shift to higher fluorescent values. This was reflected in the mean fluorescence intensity measurements which showed a more pronounced increase in fluorescence intensity for channel 2 following aging compared to channel 3 (Figure 4.10). The increase in fluorescence intensity within these channels is consistent with the oxidation of tryptophan and resulting production of N-formylkynurenine (NFK) and kynurenine (KY) (Ignatenko et al., 1982; Fukunaga et al., 1982). NFK and KY have absorbance peaks around 320 nm and 360 nm, respectively, which extend to 280 nm, and emission maxima of 430 nm and 480 nm, respectively, therefore aligning with the fluorescence detection of WIBS channels 2 and 3 (Ignatenko et al., 1982; Fukunaga et al., 1982). The formation of these fluorophores in oxidized SSA was supported by the control experiment with tryptophan and

ammonium sulfate particles (described above), where an increase in the number of particles with fluorescence in channels 2 and 3 was observed at the lowest aging scheme (Figure 4.11).

The fluorescence emission from NFK and KY has been reported in multiple studies involving ozonolysis of cells and peptides containing tryptophan (Kinahan et al., 2019; Pan et al., 2014). Both UV-excited, visible-wavelength fluorescence intensity (like WIBS channel 2) and vis-excited, visible-wavelength fluorescence (like WIBS channel 3) have been previously reported and associated with a degradation of tryptophan signal intensity (Kinahan et al., 2019; Pan et al., 2014). In general, reactivity of gas-phase oxidants increases with higher RH (Shiraiwa et al., 2011), and the conversion of tryptophan to NFK and KY has been shown to increase with increasing RH and exposure to ozone (Pan et al., 2014). As previously stated, the OFR conditions here allowed for sufficient hydrolysis and oxidation of tryptophan into NFK and KY. Thus, the decrease in channel 1 fluorescence and simultaneous increase in channels 2 and 3 observed in SSA were likely due to the reaction of tryptophan with oxidants in the OFR to form NFK, KY, and further reacted products such as hydroxykynurenine (Pan et al., 2014; Berlett and Stadtman, 1997).

4.4.3 Changes in Fluorescent Particle Morphology After Aging

In addition to the impact on fluorescence intensity, we investigated changes in the fluorescent particle size distribution between nascent SSA and aged SSA. Nascent SSA showed similar size distributions between the three different fluorescence channels (Figure 4.4). These size distributions generally showed a peak around 0.9-1 μm with a tail tapering off at larger diameters and reflect the distribution measured for all particles (Figure 4.12). The distributions measured here differ from previous measurements from a wave channel, which show a particle mode around 2-3 μm indicative of marine bacteria (Santander et al., 2021). The lack of this mode is likely due to particle losses from the OFR and the sampling lines, both of which impact particles with larger

diameters/mass compared to smaller particles. However, the mode seen in this study is consistent with the mode around 1 μm that was observed in Santander et al. (2021) (Santander et al., 2021).

Aging in the OFR altered the size distributions for the different fluorescent channels. Specifically, aging caused a decrease in the size distribution for channel 1 across most of the size range. Comparing the different aging conditions, the channel 1 size distribution remained relatively consistent with further aging. For both channels 2 and 3, aging resulted in an increase in the size distributions. Channel 2 saw a larger increase in the size distribution than channel 3 with an increase of ~20-40 particles/L compared to ~10 particles/L, respectively. Whereas channel 3 did not show any major changes in the distribution after the initial period of aging, channel 2 showed an increase in the size distribution for 9.9 days of equivalent aging followed by a decrease at 16.6 days of equivalent aging. The decrease in channel 1 and increase in channels 2 and 3 size distributions supports the hypothesis that molecules fluorescing in channel 1 underwent reactions in the OFR to form molecules fluorescent in channels 2 and 3. Additionally, the changes in the size distributions suggest that these reactions occurred consistently across fluorescent particles of all sizes.

The mean asymmetry factor (AF) for the fluorescent, nascent SSA was 5.89 ± 2.86 indicative of spherical particles (Toprak and Schnaiter, 2013). These AF values agree with previous measurements of nascent SSA generated in a laboratory setting which showed AF values of ~6 (Santander et al., 2021). Additionally, these values align with measurements of SSA over the remote marine ocean which showed modal AF values of 5 – 6 for SSA particles less than 5 μm in optical diameter (Moallemi et al., 2021). In this study, most particles observed had diameters less than 5 μm. The aged, fluorescent SSA had a similar AF to the nascent SSA with mean values of 5.86 ± 2.78, 5.74 ± 2.68, and 5.69 ± 2.66 for 3.2, 9.9, and 16.6 days of equivalent aging,

respectively. Thus, although increased aging appeared to lower the AF slightly, the similarity of the AF values before and after aging suggests atmospheric aging processes do not have a considerable effect on the shape of SSA particles. The consistency of AF values before and after oxidation/heterogeneous reactions suggests this measurement may be beneficial for identification of SSA in an ambient environment.

4.4.4 Aged Fluorescent Particle Fraction Throughout Bloom Phases

The fluorescence classes, first defined by Perring et al. (2015), are a common method used in WIBS analysis for classifying fluorescent particle types and providing information on the fluorescence behavior and biomolecules within these particles (Perring et al., 2015). Here, we observed the relative changes in the fraction of particles fluorescent in each class over the course of the phytoplankton bloom in experiment 2. The fluorescent class fraction was derived by dividing the number of particles fluorescent within each class by the total number of fluorescent and non-fluorescent particles, as shown in Eq 4.1:

$$FF_i = \frac{N_{Fl,i}}{N_{Tot}} \qquad [4.1]$$

Where FF_i represents the fluorescent fraction of fluorescence class i, $N_{Fl,i}$ represents the number of fluorescent particles in class i, and N_{Tot} represents the total number of fluorescent and non-fluorescent particles. N_{Tot} is used here instead of the total number of fluorescent particles to prevent skewing the data from an increase or decrease of a specific fluorescence class. The class-specific fluorescent fraction was calculated for both the nascent SSA and the aged SSA at the three different aging schemes. Classes ABC and AC are omitted from this discussion due to low particles counts throughout the experiment.

To determine if there was a significant change in the fluorescent fraction after aging in the OFR, a Student's t-test with unequal variance was used to compare the nascent and aged data over

the entire phytoplankton bloom. Table 4.1 summarizes the results of the t-test with the determined *p*-value shown for each fluorescence class at the different days of equivalent aging. The fluorescence classes B, C, AB, and BC showed statistically significant (p-value < 0.05) fluorescent fractions at all levels of aging compared to nascent particles. Class A only showed a significant difference at the highest level of aging and difference at a confidence interval of 90% for 9.9 days of equivalent aging. Thus, the simulated aging in the OFR resulted in significant changes in the fluorescent particle population and suggests that, in the real environment, atmospherically aged SSA may have a different fluorescent particle composition compared to nascent SSA.

To further distinguish between the fluorescent class fraction of nascent SSA compared to the fluorescent class fraction of aged SSA, we calculated the ratio of the aged fluorescent fraction to the nascent fluorescent fraction according to Eq 4.2:

$$Fluorescent\ Fraction\ Ratio_i = \frac{FF_{i,Aged}}{FF_{i,Nascent}} \qquad [4.2]$$

Here, the fluorescent fraction ratio for an individual fluorescence class, i, is the fluorescent fraction of class i for aged SSA ($FF_{i,Aged}$) divided by the fluorescent fraction of class i for nascent SSA ($FF_{i,Nascent}$). Based on this equation, if the aged SSA contained a higher/lower fluorescent fraction than nascent SSA, for a specific fluorescence class, than the value of the ratio would be greater/less than one. Box plots of the ratios were plotted for the fluorescence classes A, B, C, AB, and BC throughout the different bloom phases of experiment 2 (Figure 4.5). Included in these plots are a horizontal line at the 1:1 ratio to better highlight the changes that occurred following oxidation in the OFR.

Throughout all phases of the phytoplankton bloom, the fraction of particles fluorescent in class A decreased with simulated aging, especially for SSA aged at 9.9 and 16.6 equivalent days of aging (Figure 4.5a). This trend is relatively consistent with the other observations of the

degradation of channel 1 fluorescence with aging. Unlike class A, aged SSA generally had a higher fluorescent fraction for class B and class C compared to the nascent SSA. The fluorescent fraction of aged SSA in class B increased throughout the progression of the phytoplankton bloom and at times reached a median value twice that of nascent SSA (Figure 4.5b). The fluorescent fraction of aged SSA in class C was consistently higher by ~1.2 times that of nascent SSA throughout the course of the bloom (Figure 4.5c). In most cases, increased aging led to a decrease in the fluorescent fraction for particles in both class B and C, potentially due to increased degradation of fluorophores.

Notable changes in the fluorescent fraction of class AB were observed following oxidation (Figure 4.5d). In the pre-bloom phase of experiment 2, oxidation of the SSA resulted in a decrease in the class AB fluorescent fraction of aged SSA to less than half that of nascent SSA. However, for the peak-bloom and post-bloom phases, the influence of aging on the fluorescent fraction of class AB particles was less apparent. Additionally, the class AB fluorescent fraction of nascent SSA during peak- and post-bloom phases was generally less than that of the pre-bloom period, suggesting a change in the SSA fluorophores following the outdoor tank addition (Figure 4.13). Particles in class AB showed a consistent decrease in the median fluorescent fraction ratio associated with increased aging indicating a degradation of the fluorescent biomolecules in these SSA particles.

Class BC showed the greatest changes in the fluorescent particle fraction over the course of the phytoplankton bloom (Figure 4.5e). Throughout experiment 2, aging led to an increase in the overall fluorescent fraction of particles in class BC. The fluorescence fraction of aged SSA continued to increase throughout the progression of the phytoplankton bloom going from ~2.5 to ~7.5 times that of the nascent SSA in the lowest aging scheme (3.2 days). Additionally, increased

aging in the OFR resulted in an increase of the fluorescent particle fraction, suggesting continued production of fluorophores in these channels with more intense aging. Previous measurements by Yue et al. (2019) observed a shift in the diurnal fluorescent population marked by a decrease in class A particles and an increase in the class BC particles (Yue et al., 2019). The authors attributed this shift to oxidation of the protein-like material (class A) and transformation to humic-like substances (class BC) (Yue et al., 2019). The results shown here suggest a similar oxidation and conversion of protein-like fluorophores to humic-like fluorophores for SSA under atmospheric aging conditions.

The changes in the fluorescent fraction for each class reflect the trends observed for the fluorescence intensity measurements, where aging led to an increase of the number of particles in channels 2 and 3 and a decrease of the number of particles in channel 1. Furthermore, similar changes were observed in experiment 1 which showed lower fluorescent fraction ratios for classes A and AB and higher ratios for classes B, C, and BC (Figure 4.14). Based on these controlled experiments, atmospheric aging leads to the degradation of protein-like organic matter and production of humic-like substances within SSA particles in the ambient environment, as previously reported in field measurements over the Pacific Ocean (Miyazaki et al., 2018). The results from the fluorescent fraction analysis indicate that measurements of aged SSA may vary significantly from measurements of nascent SSA emitted from the same source, especially with further aging. Additionally, an increase in the fraction of humic-like particles (classes B and BC) associated with atmospheric aging may be more prominent during the later stages of natural phytoplankton blooms. The changes associated with biological state suggest the chemical composition of SSA can influence the reactivity of fluorescent compounds with atmospheric oxidants.

4.4.5 Implications

This study demonstrates the potential changes in fluorescent SSA following oxidation from OH and ozone over timescales of 3 to 16 days of equivalent aging under RH conditions representative of the marine boundary layer (Baumgardner and Clarke, 1998). Therefore, these results represent a first look at the influence of atmospheric oxidants on the fluorescence properties of SSA especially in a coastal environment. The significant changes to the fluorescent fractions reported here indicate that atmospheric aging may alter the fluorescent particle population of SSA, especially as more time elapses from the particle generation. These changes have implications for both detection and identification of bioaerosols in a marine environment using fluorescence techniques. Because fluorescence classes are often used to help distinguish between broad categories of known bioaerosols at the population level (Hernandez et al., 2016), changes to the class fractions will impact bioaerosol discrimination. We show here that SSA can undergo transformations leading to an increase in the fraction of particles with humic-like fluorescence, from an increase of 1.2 – 2 times the amount of particles fluorescent in classes B and C to up to 7.5 times the number of particles for class BC depending on the state of the phytoplankton bloom. The increase in humic-like substances following oxidation aligns with previous fluorescence measurements including those in a marine environment (Yue et al., 2019; Miyazaki et al., 2018). Humic-like substance formation may affect the ability of SSA to act as both CCN and INP and therefore impact cloud formation within marine environments (Sun and Ariya, 2006; Ariya et al., 2009). Detailed information on bioaerosol production and influence on cloud formation is necessary for global climate modeling (Burrows et al., 2009). Continued research on the transformation of marine bioaerosols following atmospheric aging will provide deeper insights into the role of SSA on the global atmosphere.

4.5 Acknowledgements

The authors would like to thank the SeaSCAPE team, especially Prof. Chris Cappa and Prof. Timothy Bertram for designing and overseeing the campaign. This study was funded by the National Science Foundation Center for Aerosol Impacts on Chemistry of the Environment (NSF-CAICE), an NSF Center for Chemical Innovation (CHE-1801971). Data availability supporting the conclusions is publicly available from the UC San Diego Library Digital Collections at:

Chapter 4, in full, is currently being prepared for submission for publication of the material. Mitts, B. A., Santander, M. V., Ibrahim, I., Morris, C. K., Dinasquet, J., Mayer, K. J., Sauer, J. S., Lee, C., Malfatti, F. & Prather, K. A. (2022). “Single-Particle Fluorescence Properties of Oxidized Sea Spray Aerosol” The dissertation author is the primary investigator and author of this manuscript.

4.6 Figures

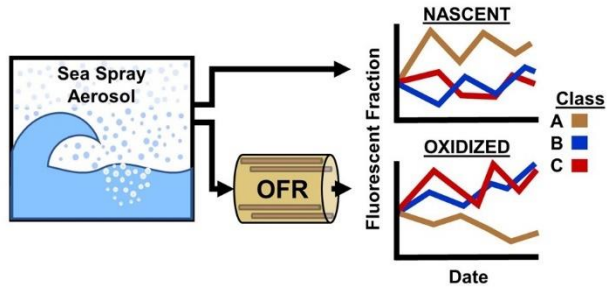

Figure 4.1. Graphical abstract.

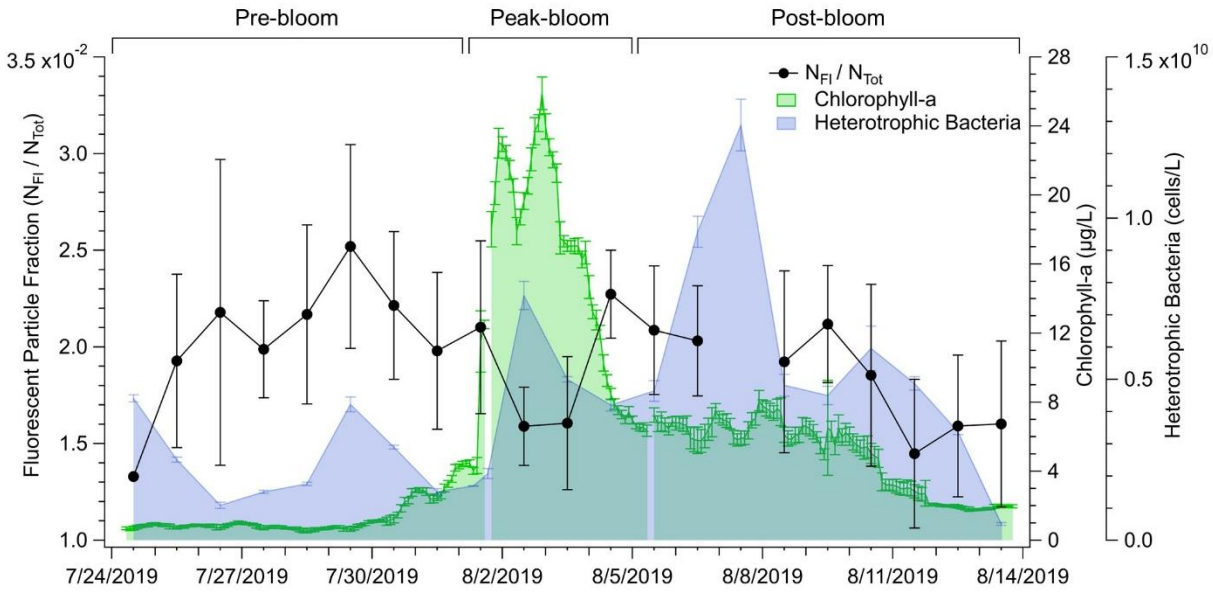

Figure 4.2. Time series of experiment 2 showing the daily average fluorescent particle fraction of nascent SSA measurements (black line) ± one standard deviation (error bars). The first day consisted of only one nascent sampling period, and therefore does not have associated error bars. Included are chlorophyll-a (green) and heterotrophic bacteria concentrations (blue). The phases of the phytoplankton bloom are denoted above the figure.

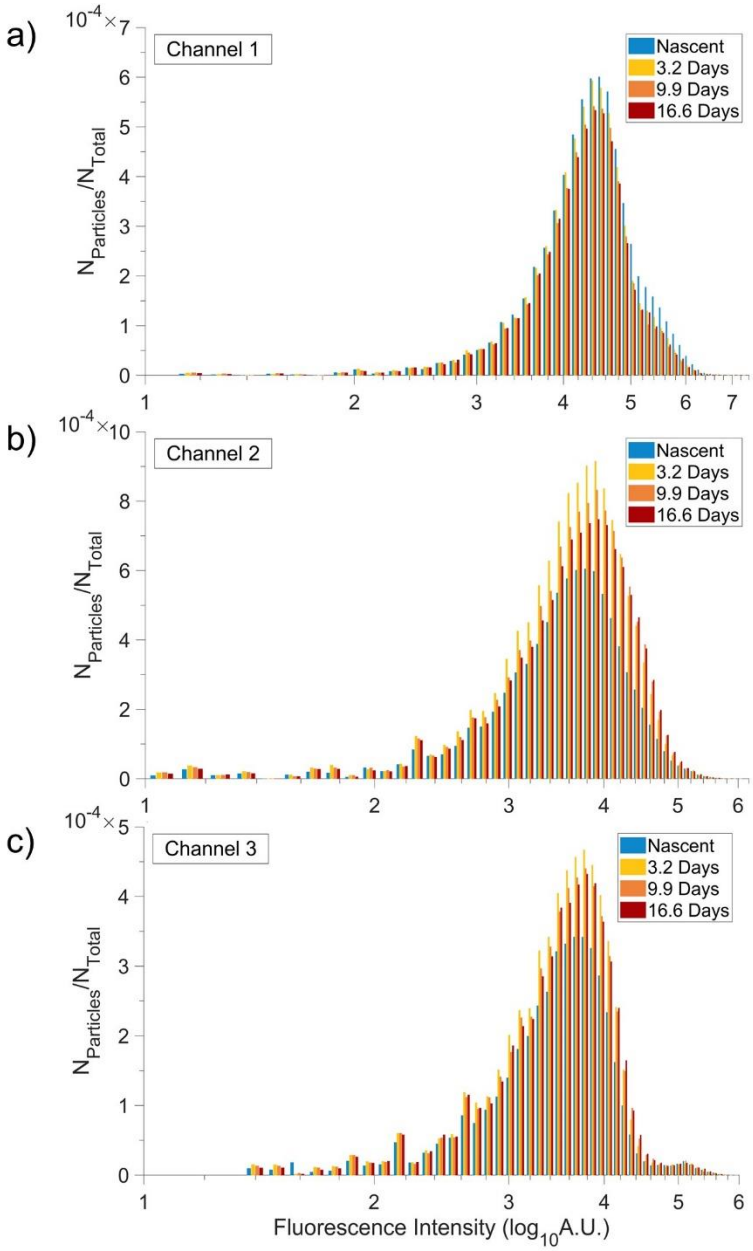

Figure 4.3. Histograms of the single-particle fluorescent intensity normalized to the total number of particles for channel 1 (a), channel 2 (b), and channel 3 (c). Included in each plot are histograms for nascent SSA (blue) and aged SSA exposed to 3.2 days of equivalent aging (yellow), 9.9 equivalent days (orange), and 16.6 equivalent days (red).

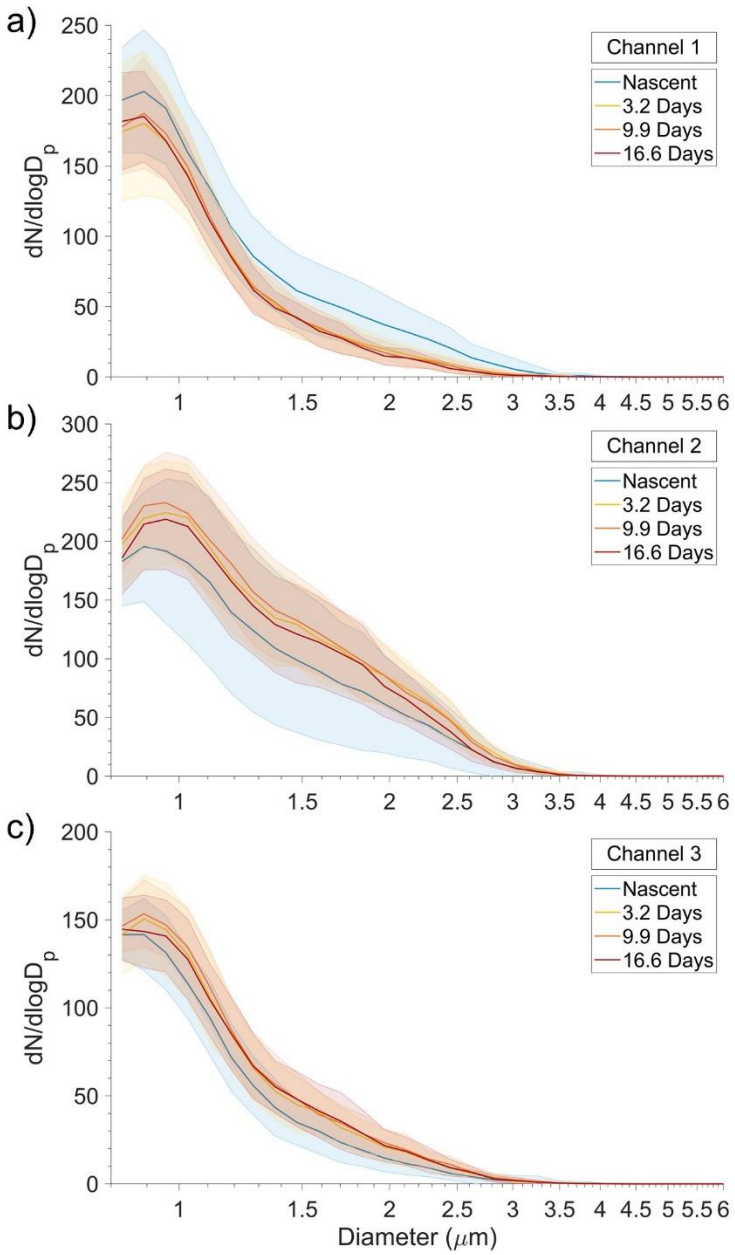

Figure 4.4. Probability density functions of the size distributions for the mean daily particle counts (#/L) normalized to the bin widths (solid line) along with one standard deviation (shaded) for channel 1 (a), channel 2 (b), and channel 3 (c). Included in each plot are traces for nascent SSA (blue) and aged SSA exposed to 3.2 (yellow), 9.9 (orange), and 16.6 (red) days of equivalent aging.

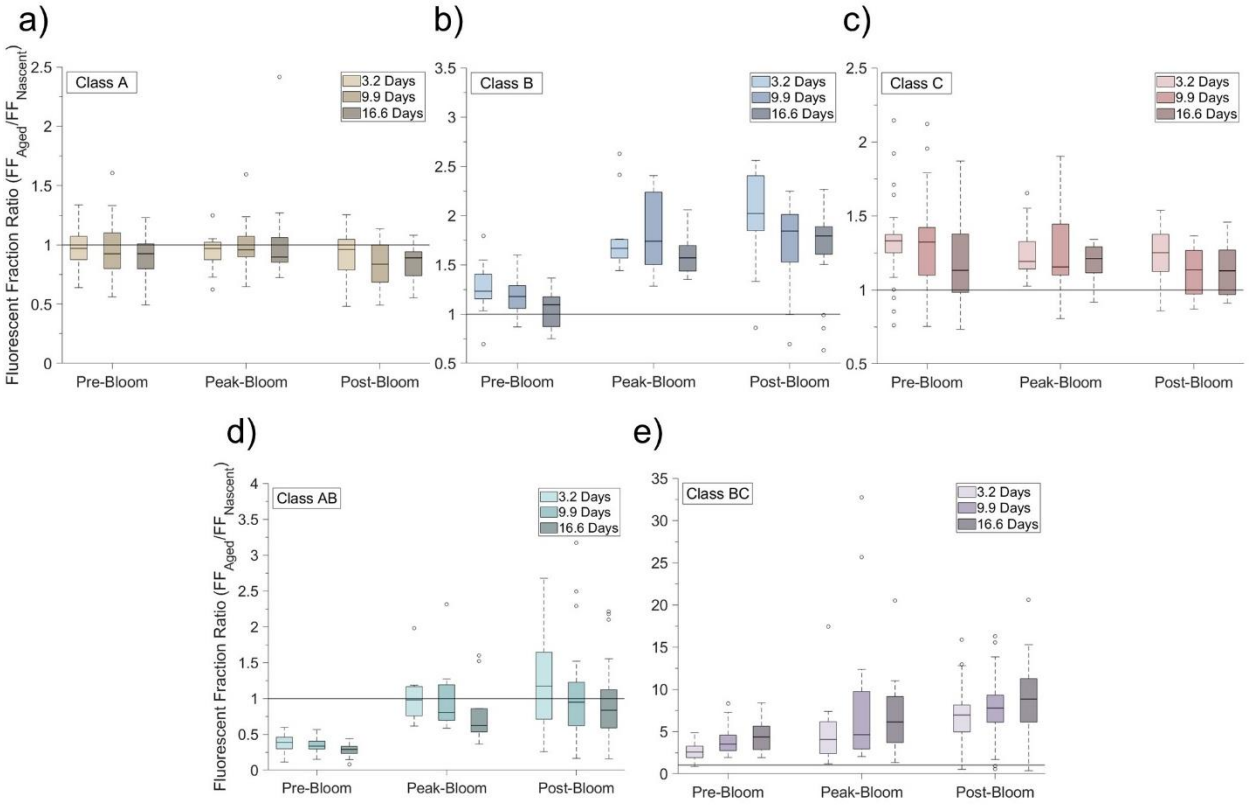

Figure 4.5. Fluorescent fraction ratio across different phytoplankton bloom phases (pre-bloom, peak-bloom, post-bloom) and different aging schemes (3.2, 9.9, and 16.6 days of equivalent aging). Shown are the box plots for the fluorescent classes A (a), B (b), C (c), AB (d), and BC (e) along with a 1:1 line plotted with each graph. Boxes depict the median fluorescent fraction ratio (black line) along with the interquartile range and whiskers correspond to the 5th and 95th percentile with open markers indicating outliers.

4.7 Tables

Table 4.1. *P*-values reported from the Student's t-test with unequal variance comparing the fluorescent fraction of aged SSA to nascent SSA across different fluorescence classes. *P*-values less than 0.05 are bolded to highlight statistical significance.

Fluorescence Class	*p*-value: 3.2 days	*p*-value: 9.9 days	*p*-value: 16.6 days
A	0.235	0.0878	**0.0239**
B	**2.52e-15**	**8.79e-12**	**6.77e-07**
C	**2.75e-07**	**7.13e-05**	**5.44e-03**
AB	**1.63e-07**	**1.50e-08**	**1.17e-10**
BC	**1.07e-20**	**1.74e-23**	**2.16e-22**

4.8 Supplemental Information

The operation of the OFR requires UV light at wavelengths not normally experienced in the troposphere which can cause photooxidation of molecules in SSA particles. Therefore, we chose to analyze the effect of these lights on aerosol fluorescence under dry conditions (RH<10%), ensuring significantly lower OH concentrations (Kang et al., 2007). Under these low RH conditions, we found exposure of SSA and exposure of tryptophan and ammonium sulfate particles to the UV radiation showed drastically different results in the channel 1 fluorescence intensity compared to standard operation with the OFR. Instead of a decrease in the channel 1 fluorescence intensity, as was observed during normal OFR operation (see Section 4.4.2), there was a substantial increase in the channel 1 fluorescence intensity under the low RH conditions (Figure 4.7), likely due to the high molar absorptivity of tryptophan at 185 nm (Wetlaufer, 1963). The lack of this increase in channel 1 intensity during normal operation of the OFR indicates that the effect of the UV radiation on the particles was minimized. Instead, degradation of the channel 1 fluorescence suggests that, under the standard operation of the OFR, the reactions with OH and other oxidants are the dominant effect on incoming particles.

4.9 Supplemental Figures

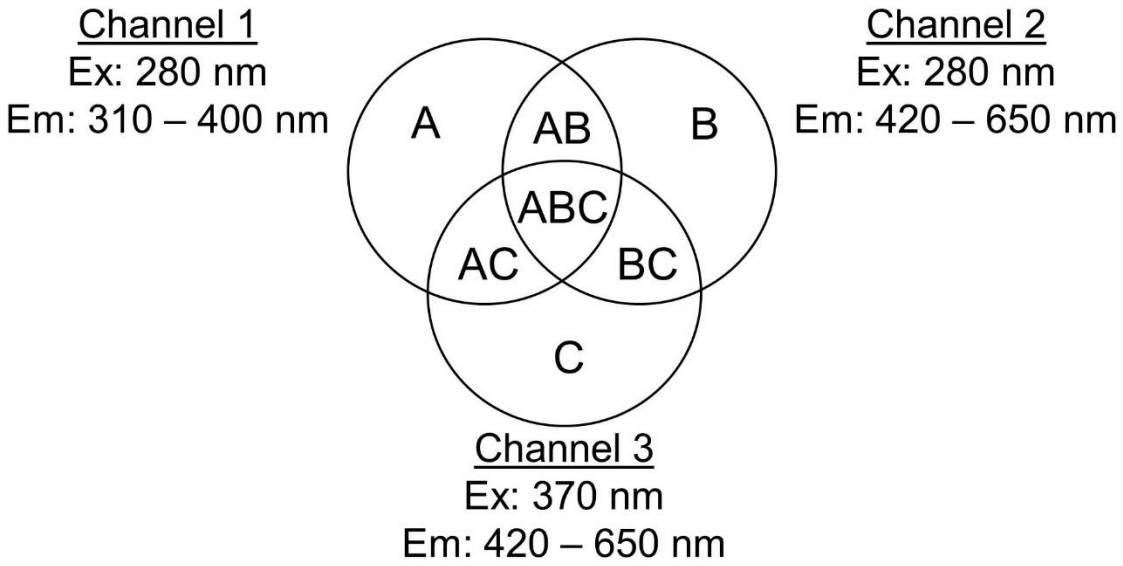

Fluorescence Class	Fluorescence Class Definition
A	Fluorescence in channel 1 but not channels 2 or 3
B	Fluorescence in channel 2 but not channels 1 or 3
C	Fluorescence in channel 3 but not channels 1 or 2
AB	Fluorescence in channels 1 and 2 but not channel 3
AC	Fluorescence in channels 1 and 3 but not channel 2
BC	Fluorescence in channels 2 and 3 but not channel 1
ABC	Fluorescence in channels 1, 2 and 3
Channel 1: Excitation: 280 nm / Emission: 310 – 400 nm Channel 2: Excitation: 280 nm / Emission: 420 – 650 nm Channel 3: Excitation: 370 nm / Emission: 420 – 650 nm	

Figure 4.6. Venn diagram showing the overlap of the different fluorescence classes measured with the WIBS. Fluorescence classes defined based on which channels detect fluorescence above the threshold.

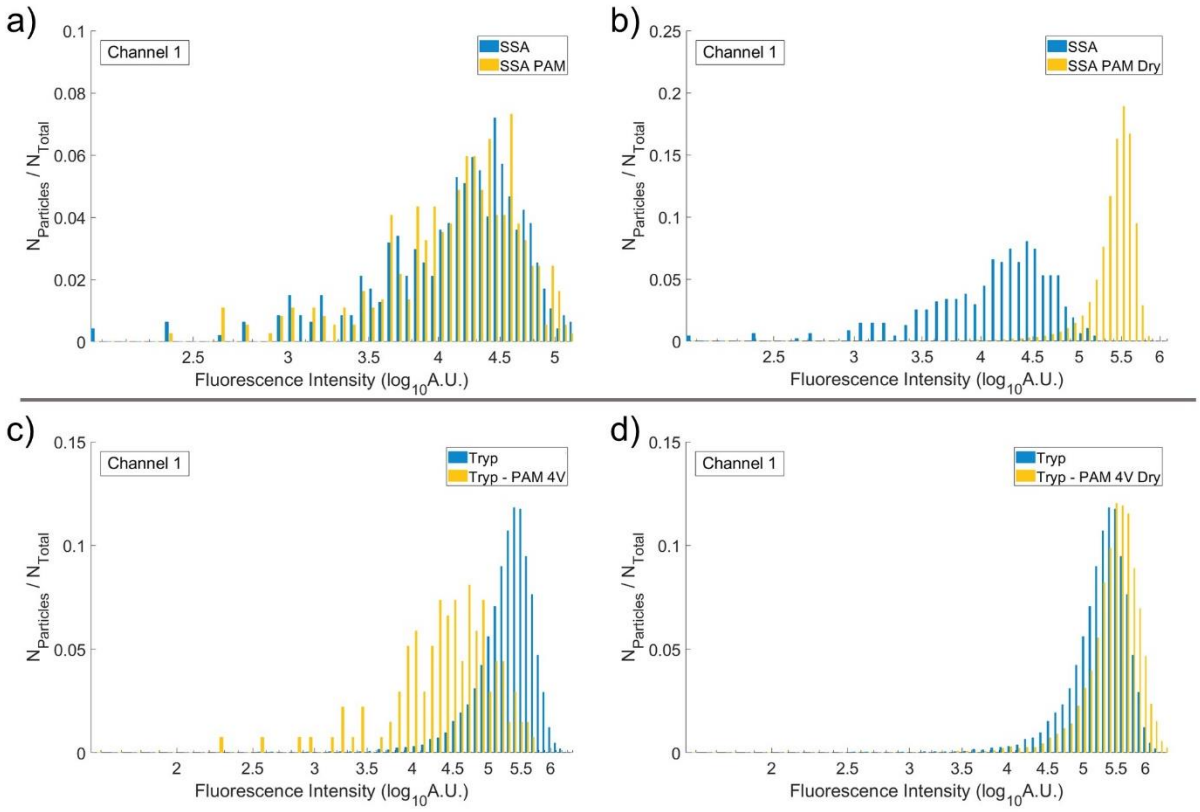

Figure 4.7. Histograms of the single-particle fluorescent intensity normalized to the total number of particles in channel 1 for: nascent SSA and OFR operations under normal conditions (a), nascent SSA and OFR operations under low RH conditions (b), tryptophan and ammonium sulfate particles with the OFR off and under normal OFR conditions (c), and tryptophan and ammonium sulfate particles with the OFR off and under normal OFR conditions (d). For each plot, the nascent or OFR off conditions are in blue while the OFR on conditions are in yellow.

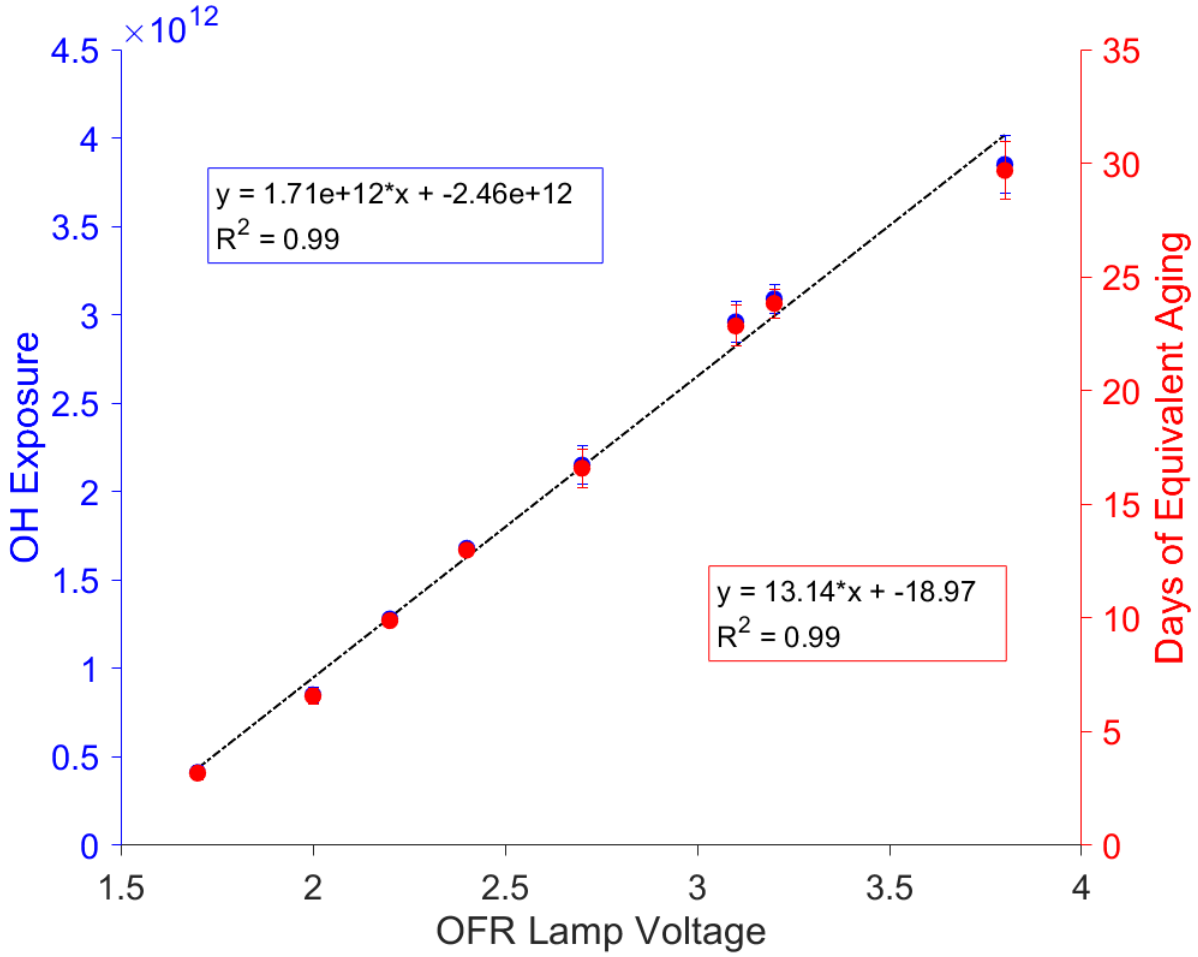

Figure 4.8. Calibration curve for the OFR to determine the relationship between lamp voltage and OH exposure (blue) and the days of equivalent aging (red). Linear fits for each are included along with the coefficient of determination.

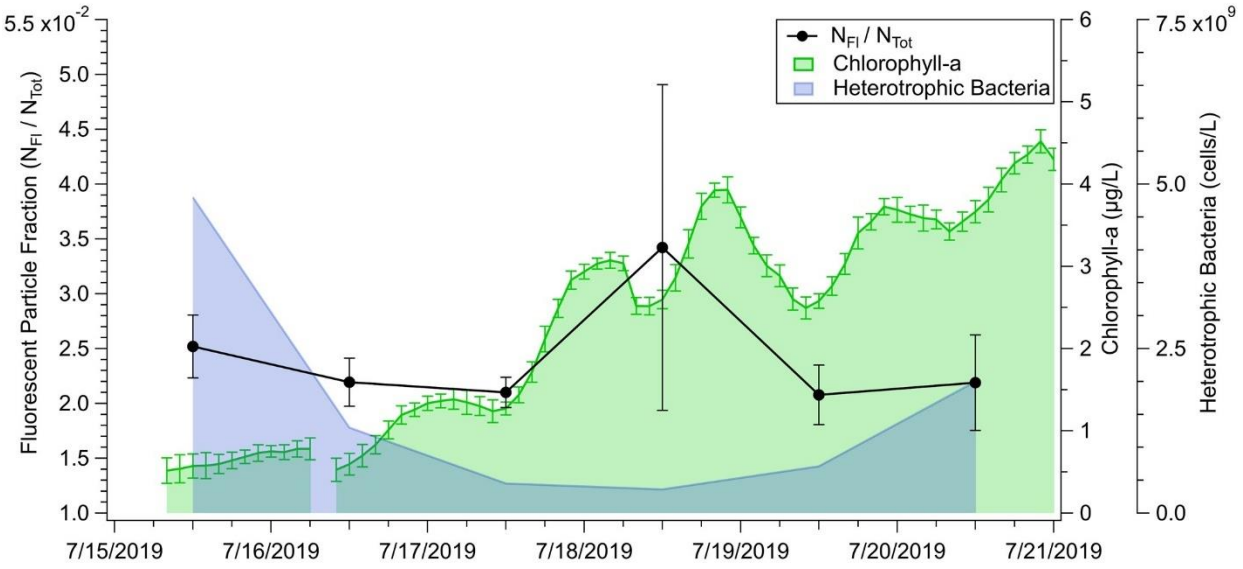

Figure 4.9. Time series of experiment 1 showing the fluorescent particle fraction (black line) along with one standard deviation (error bars) and the chlorophyll-a concentration (green) and heterotrophic bacteria concentration (blue) throughout the course of each phytoplankton bloom.

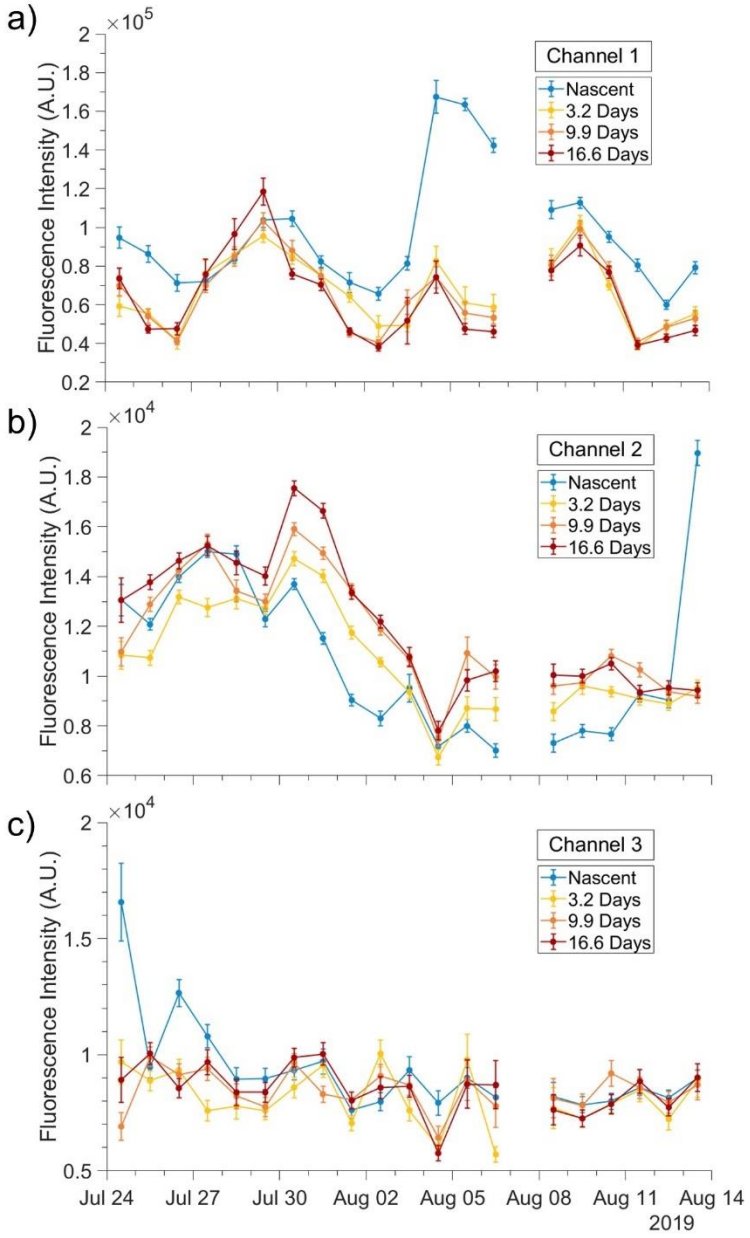

Figure 4.10. Daily mean fluorescence intensities shown with the standard error of the mean (error bars) for channel 1 (a), channel 2 (b), and channel 3 (c). Included in each plot are the values for the nascent SSA (blue), SSA exposed to 3.2 days of equivalent aging (yellow), 9.9 equivalent days (orange), and 16.6 equivalent days (red).

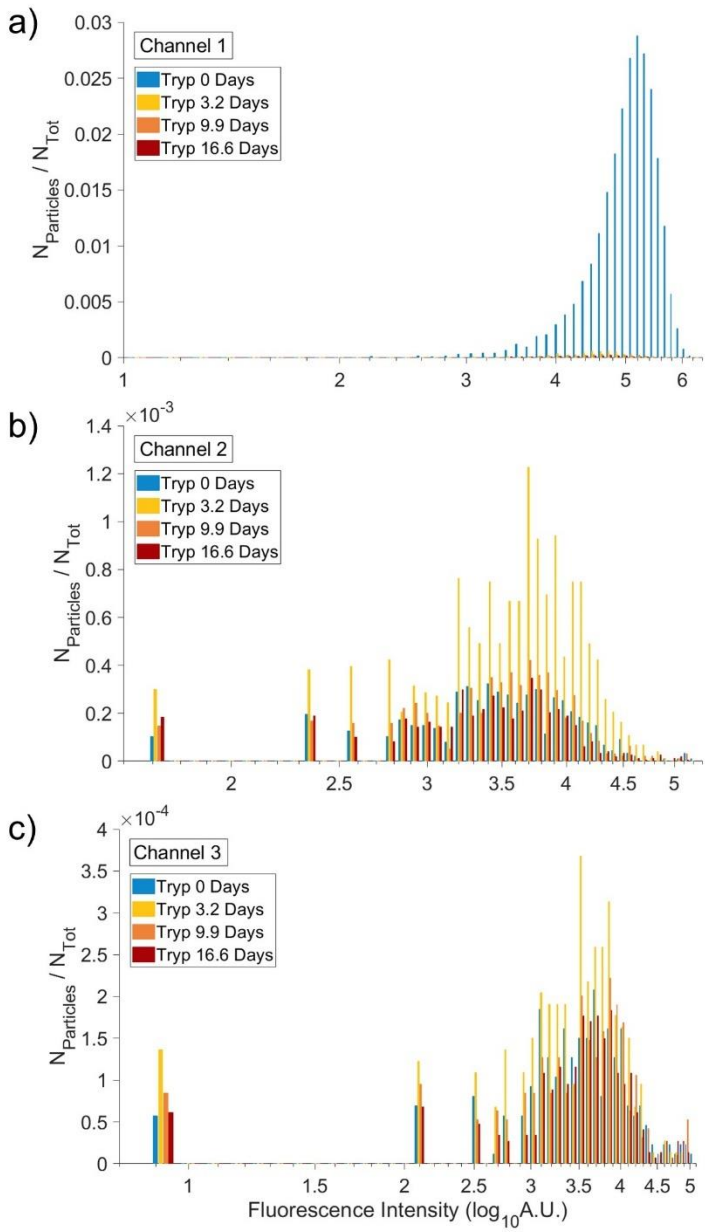

Figure 4.11. Histograms of the single-particle fluorescent intensity of tryptophan and ammonium sulfate particles normalized to the total number of particles in channel 1 (a), channel 2 (b), and channel 3 (c). Included in each plot are histograms for the OFR lamps off (blue) and aged tryptophan and ammonium sulfate particles exposed to 3.2 days of equivalent aging (yellow), 9.9 equivalent days (orange), and 16.6 equivalent days (red).

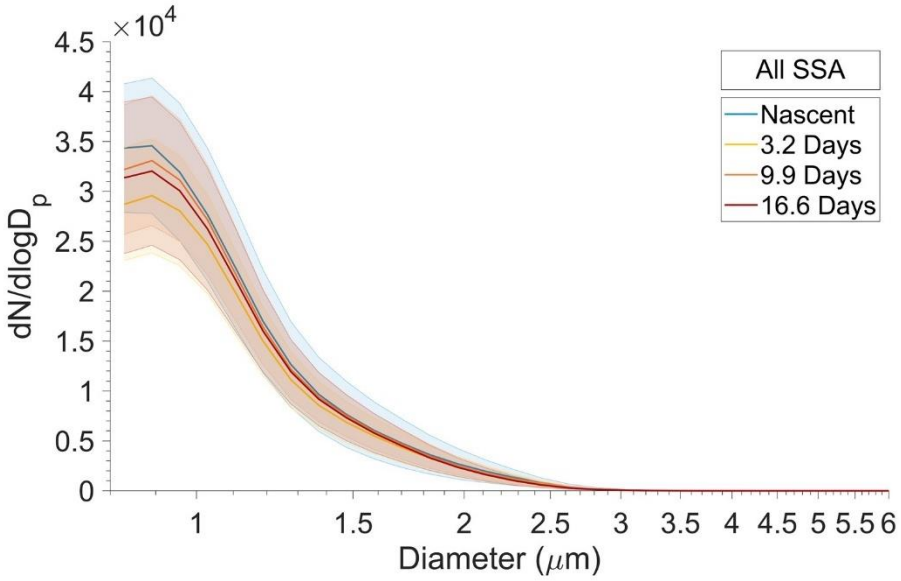

Figure 4.12. Probability density functions of the size distributions of the mean daily particle counts normalized to the bin width (solid line) along with one standard deviation (shaded) for nascent SSA (blue), aged SSA exposed to 3.2 (yellow), 9.9 (orange), and 16.6 (red) days of equivalent aging.

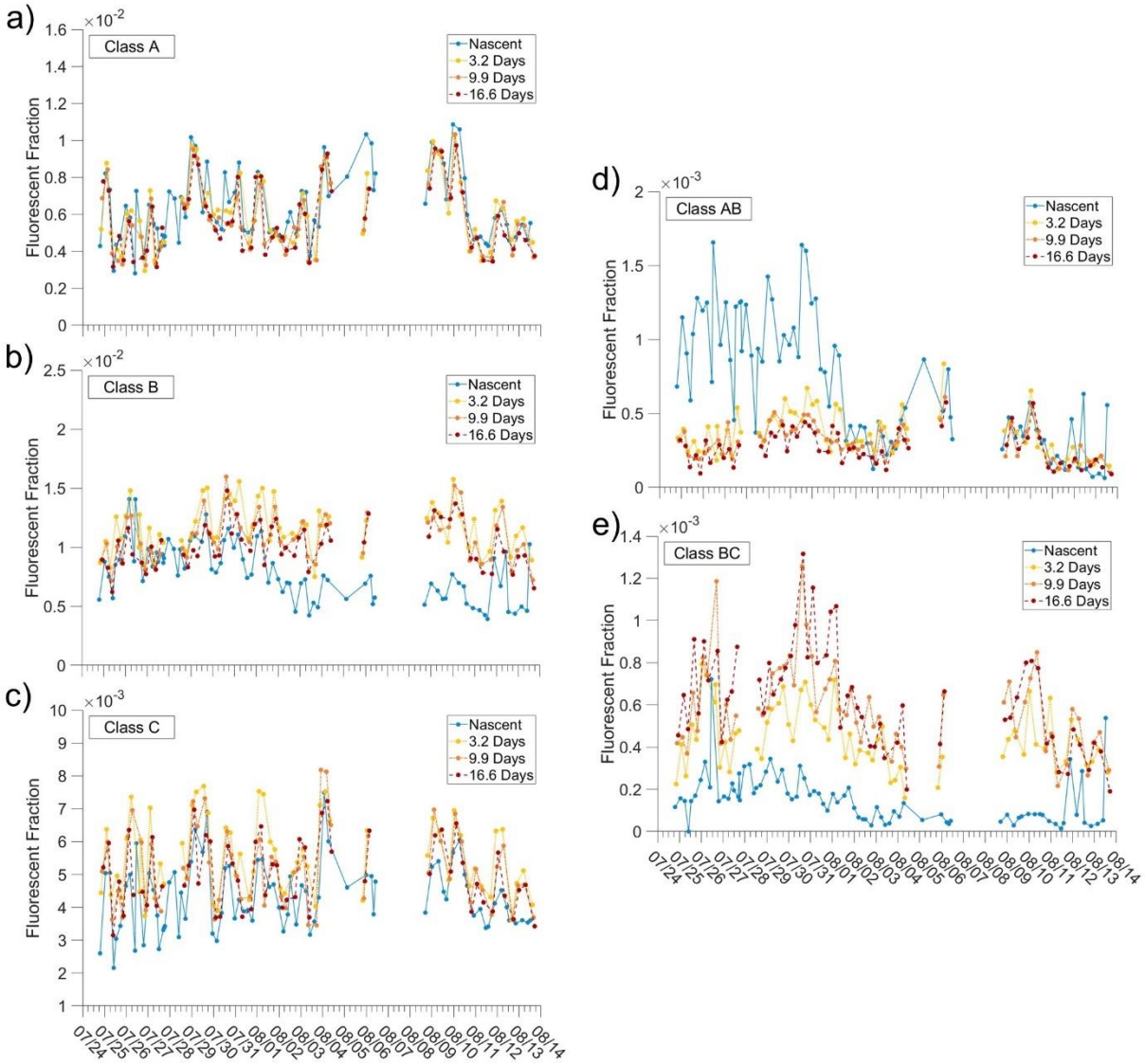

Figure 4.13. Fluorescent fractions of the fluorescence classes A (a), B (b), C (c), AB (d), and BC (e) plotted over the course of experiment 2. Each point represents a sampling period and included in each plot are nascent SSA (blue), aged SSA exposed to 3.2 (yellow), 9.9 (orange), and 16.6 (red) days of equivalent aging.

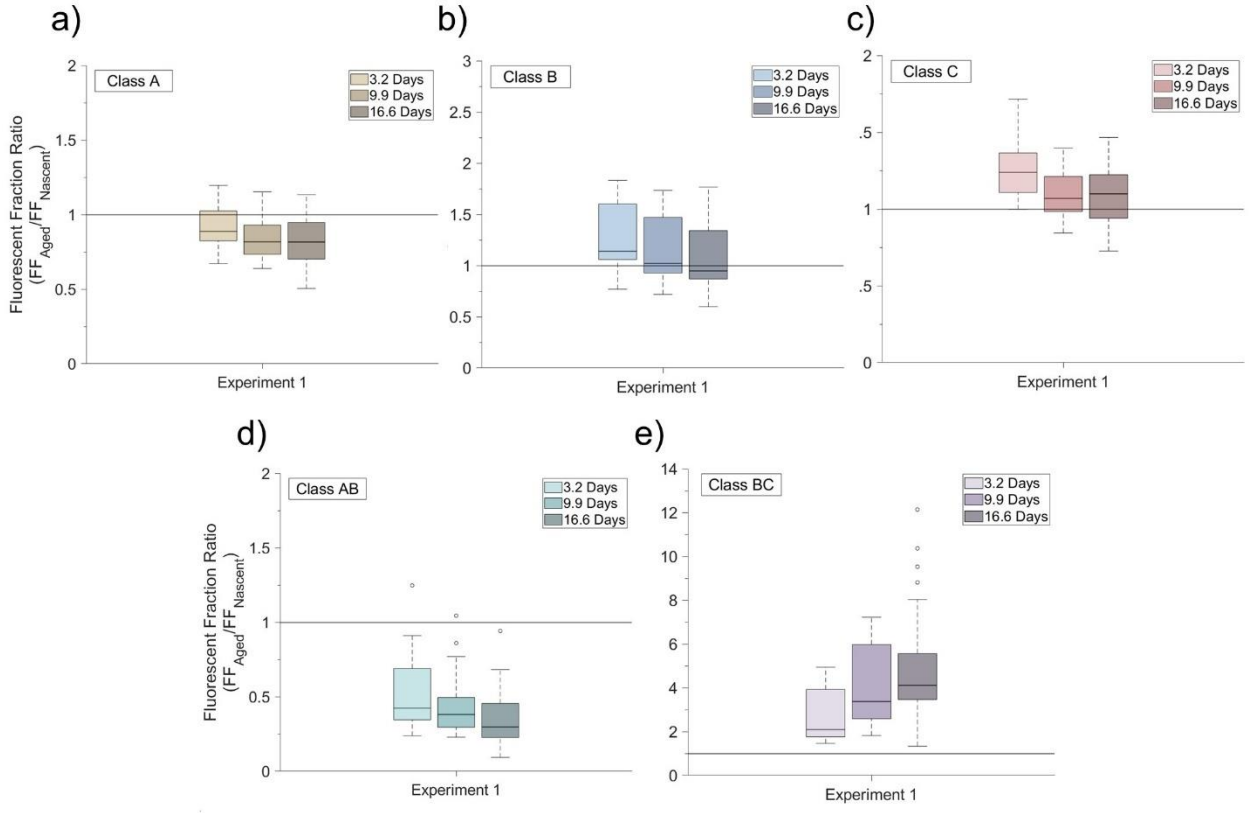

Figure 4.14. Fluorescent fraction ratio for experiment 1 during different aging schemes (3.2, 9.9, and 16.6 days of equivalent aging). Shown are the box plots for the fluorescent classes A (a), B (b), C (c), AB (d), and BC (e) along with a 1:1 line plotted with each graph. Boxes depict the median fluorescent fraction ratio (black line) along with the interquartile range and whiskers correspond to the 5th and 95th percentile with open markers indicating outliers.

4.10 References

Ariya, P. A., Sun, J., Eltouny, N. A., Hudson, E. D., Hayes, C. T., and Kos, G.: Physical and chemical characterization of bioaerosols - Implications for nucleation processes, Int. Rev. Phys. Chem., 28, 1–32, https://doi.org/10.1080/01442350802597438, 2009.

Azam, F. and Malfatti, F.: Microbial structuring of marine ecosystems, https://doi.org/10.1038/nrmicro1747, 2007.

Azam, F., Fenchel, T., Field, J., Gray, J., Meyer-Reil, L., and Thingstad, F.: The Ecological Role of Water-Column Microbes in the Sea, Mar. Ecol. Prog. Ser., 10, 257–263, https://doi.org/10.3354/meps010257, 1983.

Baumgardner, D. and Clarke, A.: Changes in aerosol properties with relative humidity in the remote southern hemisphere marine boundary layer, J. Geophys. Res. Atmos., 103, 16525–16534, https://doi.org/10.1029/98JD00688, 1998.

Berlett, B. S. and Stadtman, E. R.: Protein oxidation in aging, disease, and oxidative stress, J. Biol. Chem., 272, 20313–20316, https://doi.org/10.1074/jbc.272.33.20313, 1997.

Buchan, A., LeCleir, G. R., Gulvik, C. A., and González, J. M.: Master recyclers: features and functions of bacteria associated with phytoplankton blooms, Nat. Rev. Microbiol. 2014 1210, 12, 686–698, https://doi.org/10.1038/nrmicro3326, 2014.

Burrows, S. M., Elbert, W., Lawrence, M. G., and Pöschl, U.: Bacteria in the global atmosphere – Part 1: Review and synthesis of literature data for different ecosystems, Atmos. Chem. Phys., 9, 9263–9280, https://doi.org/10.5194/acp-9-9263-2009, 2009.

Chen, W. C. and Marcus, R. A.: On the theory of the reaction rate of vibrationally excited CO molecules with OH radicals, J. Chem. Phys., 124, 024306, https://doi.org/10.1063/1.2148408, 2006.

Crawford, I., Gallagher, M. W., Bower, K. N., Choularton, T. W., Flynn, M. J., Ruske, S., Listowski, C., Brough, N., Lachlan-Cope, T., Fleming, Z. L., Foot, V. E., and Stanley, W. R.: Real-time detection of airborne fluorescent bioparticles in Antarctica, Atmos. Chem. Phys., 17, 14291–14307, https://doi.org/10.5194/acp-17-14291-2017, 2017.

Després, V., Huffman, Ja., Burrows, S. M., Hoose, C., Safatov, A., Buryak, G., Fröhlich-Nowoisky, J., Elbert, W., Andreae, M., Pöschl, U., Jaenicke, R., Huffman, A., Viviane Despré S, B. R., Alex Huffman, J., Safatov, A. S., Fro, J., and Andreae, M. O.: Primary biological aerosol particles in the atmosphere: a review, https://doi.org/10.3402/tellusb.v64i0.15598, 2012.

Estillore, A. D., Trueblood, J. V., and Grassian, V. H.: Atmospheric chemistry of bioaerosols: Heterogeneous and multiphase reactions with atmospheric oxidants and other trace gases, https://doi.org/10.1039/c6sc02353c, 18 October 2016.

Forde, E., Gallagher, M., Walker, M., Foot, V., Attwood, A., Granger, G., Sarda-Estève, R., Stanley, W., Kaye, P., and Topping, D.: Intercomparison of Multiple UV-LIF Spectrometers Using the Aerosol Challenge Simulator, Atmos. 2019, Vol. 10, Page 797, 10, 797, https://doi.org/10.3390/ATMOS10120797, 2019.

Fröhlich-Nowoisky, J., Kampf, C. J., Weber, B., Huffman, J. A., Pöhlker, C., Andreae, M. O., Lang-Yona, N., Burrows, S. M., Gunthe, S. S., Elbert, W., Su, H., Hoor, P., Thines, E., Hoffmann, T., Després, V. R., and Pöschl, U.: Bioaerosols in the Earth system: Climate, health, and ecosystem interactions, Atmos. Res., 182, 346–376, https://doi.org/10.1016/j.atmosres.2016.07.018, 2016.

Fukunaga, Y., Katsuragi, Y., Izumi, T., and Sakiyama, F.: Fluorescence characteristics of kynurenine and N'-formylkynurenine, their use as reporters of the environment of tryptophan 62 in hen egg-white lysozyme, J. Biochem., 92, 129–141, https://doi.org/10.1093/oxfordjournals.jbchem.a133909, 1982.

Gabey, A. M., Gallagher, M. W., Whitehead, J., Dorsey, J. R., Kaye, P. H., and Stanley, W. R.: Measurements and comparison of primary biological aerosol above and below a tropical forest canopy using a dual channel fluorescence spectrometer, Atmos. Chem. Phys. Atmos. Chem. Phys., 10, 4453–4466, https://doi.org/10.5194/acp-10-4453-2010, 2010.

Gabey, A. M., Stanley, W. R., Gallagher, M. W., and Kaye, P. H.: The fluorescence properties of aerosol larger than 0.8 μm in urban and tropical rainforest locations, Atmos. Chem. Phys., 11, 5491–5504, https://doi.org/10.5194/acp-11-5491-2011, 2011.

Gasol, J. M. and Del Giorgio, P. A.: Using flow cytometry for counting natural planktonic bacteria and understanding the structure of planktonic bacterial communities, in: Scientia Marina, 197–224, https://doi.org/10.3989/scimar.2000.64n2197, 2000.

Guillard, R. R. L. and Ryther, J. H.: Studies of Marine Planktonic Diatoms: I. Cyclotella Nana Hustedt, and Detonula Confervacea (Cleve) Gran., Can. J. Microbiol., 8, 229–239, https://doi.org/10.1139/m62-029, 1962.

Hernandez, M., Perring, A. E., McCabe, K., Kok, G., Granger, G., and Baumgardner, D.: Chamber catalogues of optical and fluorescent signatures distinguish bioaerosol classes, Atmos. Meas. Tech., 9, 3283–3292, https://doi.org/10.5194/amt-9-3283-2016, 2016.

Holm-Hansen, O., Lorenzen, C. J., Holmes, R. W., and Strickland, J. D. H.: Fluorometric Determination of Chlorophyll, ICES J. Mar. Sci., 30, 3–15, https://doi.org/10.1093/ICESJMS/30.1.3, 1965.

Huffman, J. A., Perring, A. E., Savage, N. J., Clot, B., Crouzy, B., Tummon, F., Shoshanim, O., Damit, B., Schneider, J., Sivaprakasam, V., Zawadowicz, M. A., Crawford, I., Gallagher, M., Topping, D., Doughty, D. C., Hill, S. C., and Pan, Y.: Real-time sensing of bioaerosols: Review and current perspectives, https://doi.org/10.1080/02786826.2019.1664724, 3 May 2020.

Ignatenko, A. V.: Use of the method of tryptophan fluorescence to characterize disruptions of the structure of ozonized proteins, J. Appl. Spectrosc., 49, 691–695, https://doi.org/10.1007/BF00662905, 1988.

Ignatenko, A. V., Tatarinov, B. A., Khovratovich, N. N., Khrapovitskii, V. P., and Cherenkevich, S. N.: Spectral-fluorescent investigation of the action of ozone on aromatic amino acids, J. Appl. Spectrosc., 37, 781–784, https://doi.org/10.1007/BF00663829, 1982.

Kang, E., Root, M. J., Toohey, D. W., and Brune, W. H.: Introducing the concept of Potential Aerosol Mass (PAM), Atmos. Chem. Phys, 7, 5727–5744, https://doi.org/https://doi.org/10.5194/acp-7-5727-2007, 2007.

Kasparian, J., Hassler, C., Ibelings, B., Berti, N., Bigorre, S., Djambazova, V., Gascon-Diez, E., Giuliani, G., Houlmann, R., Kiselev, D., De Laborie, P., Le, A. D., Magouroux, T., Neri, T., Palomino, D., Pfändler, S., Ray, N., Sousa, G., Staedler, D., Tettamanti, F., Wolf, J. P., and Beniston, M.: Assessing the Dynamics of Organic Aerosols over the North Atlantic Ocean, Sci. Rep., 7, https://doi.org/10.1038/srep45476, 2017.

Kawana, K., Matsumoto, K., Taketani, F., Miyakawa, T., and Kanaya, Y.: Fluorescent biological aerosol particles over the central Pacific Ocean: covariation with ocean surface biological activity indicators, Atmos. Chem. Phys., 21, 15969–15983, https://doi.org/10.5194/acp-21-15969-2021, 2021.

Kinahan, S. M., Tezak, M. S., Siegrist, C. M., Lucero, G., Servantes, B. L., Santarpia, J. L., Kalume, A., Zhang, J., Felton, M., Williamson, C. C., and Pan, Y. Le: Changes of fluorescence spectra and viability from aging aerosolized E. coli cells under various laboratory-controlled conditions in an advanced rotating drum, Aerosol Sci. Technol., 53, 1261–1276, https://doi.org/10.1080/02786826.2019.1653446, 2019.

Lambe, A. T., Ahern, A. T., Williams, L. R., Slowik, J. G., Wong, J. P. S., Abbatt, J. P. D., Brune, W. H., Ng, N. L., Wright, J. P., Croasdale, D. R., Worsnop, D. R., Davidovits, P., and Onasch, T. B.: Characterization of aerosol photooxidation flow reactors: Heterogeneous oxidation, secondary organic aerosol formation and cloud condensation nuclei activity measurements, Atmos. Meas. Tech., 4, 445–461, https://doi.org/10.5194/AMT-4-445-2011, 2011.

Lee, C., Sultana, C. M., Collins, D. B., Santander, M. V., Axson, J. L., Malfatti, F., Cornwell, G. C., Grandquist, J. R., Deane, G. B., Stokes, M. D., Azam, F., Grassian, V. H., and Prather, K. A.: Advancing Model Systems for Fundamental Laboratory Studies of Sea Spray Aerosol Using the Microbial Loop, J. Phys. Chem. A, 119, 8860–8870, https://doi.org/10.1021/acs.jpca.5b03488, 2015.

Lieberherr, G., Auderset, K., Calpini, B., Clot, B., Crouzy, B., Gysel-Beer, M., Konzelmann, T., Manzano, J., Mihajlovic, A., Moallemi, A., O'connor, D., Sikoparija, B., Sauvageat, E., Tummon, F., and Vasilatou, K.: Assessment of real-time bioaerosol particle counters using reference chamber experiments, Atmos. Meas. Tech., 14, 7693–7706,

https://doi.org/10.5194/amt-14-7693-2021, 2021.

Maskos, Z., Rush, J. D., and Koppenol, W. H.: The hydroxylation of tryptophan, Arch. Biochem. Biophys., 296, 514–520, https://doi.org/10.1016/0003-9861(92)90605-V, 1992.

Mayol, E., Arrieta, J. M., Jiménez, M. A., Martínez-Asensio, A., Garcias-Bonet, N., Dachs, J., González-Gaya, B., Royer, S. J., Benítez-Barrios, V. M., Fraile-Nuez, E., and Duarte, C. M.: Long-range transport of airborne microbes over the global tropical and subtropical ocean, Nat. Commun., 8, https://doi.org/10.1038/s41467-017-00110-9, 2017.

Miyazaki, Y., Yamashita, Y., Kawana, K., Tachibana, E., Kagami, S., Mochida, M., Suzuki, K., and Nishioka, J.: Chemical transfer of dissolved organic matter from surface seawater to sea spray water-soluble organic aerosol in the marine atmosphere, Sci. Rep., 8, https://doi.org/10.1038/s41598-018-32864-7, 2018.

Moallemi, A., Landwehr, S., Robinson, C., and Simó, R.: Sources, Occurrence and Characteristics of Fluorescent Biological Aerosol Particles Measured Over the Pristine Southern Ocean, J. Geophys. Res., 2021.

Morrison, D., Li, J., Crawford, I., Che, W., Flynn, M., Chan, M. N., Lau, A. K. H., Fung, J. C. H., Topping, D., Yu, J., and Gallagher, M.: The Observation and Characterisation of Fluorescent Bioaerosols Using Real-Time UV-LIF Spectrometry in Hong Kong from June to November 2018, Atmos. 2020, Vol. 11, Page 944, 11, 944, https://doi.org/10.3390/ATMOS11090944, 2020.

Noble, R. T. and Fuhrman, J. A.: Use of SYBR Green I for rapid epifluorescence counts of marine viruses and bacteria, Aquat. Microb. Ecol., 14, 113–118, https://doi.org/10.3354/ame014113, 1998.

Pan, Y. Le, Santarpia, J. L., Ratnesar-Shumate, S., Corson, E., Eshbaugh, J., Hill, S. C., Williamson, C. C., Coleman, M., Bare, C., and Kinahan, S.: Effects of ozone and relative humidity on fluorescence spectra of octapeptide bioaerosol particles, J. Quant. Spectrosc. Radiat. Transf., 133, 538–550, https://doi.org/10.1016/J.JQSRT.2013.09.017, 2014.

Pan, Y. Le, Kalume, A., Wang, C., and Santarpia, J.: Atmospheric aging processes of bioaerosols under laboratory-controlled conditions: A review, J. Aerosol Sci., 155, 105767, https://doi.org/10.1016/J.JAEROSCI.2021.105767, 2021.

Perring, A. E., Schwarz, J. P., Baumgardner, D., Hernandez, M. T., Spracklen, D. V., Heald, C. L., Gao, R. S., Kok, G., McMeeking, G. R., McQuaid, J. B., and Fahey, D. W.: Airborne observations of regional variation in fluorescent aerosol across the United States, J. Geophys. Res. Atmos., 120, 1153–1170, https://doi.org/10.1002/2014JD022495, 2015.

Pöhlker, C., Huffman, J. A., and Pöschl, U.: Autofluorescence of atmospheric bioaerosols – fluorescent biomolecules and potential interferences, Atmos. Meas. Tech, 5, 37–71, https://doi.org/10.5194/amt-5-37-2012, 2012.

Ratnesar-Shumate, S., Pan, Y. Le, Hill, S. C., Kinahan, S., Corson, E., Eshbaugh, J., and Santarpia, J. L.: Fluorescence spectra and biological activity of aerosolized bacillus spores and MS2 bacteriophage exposed to ozone at different relative humidities in a rotating drum, J. Quant. Spectrosc. Radiat. Transf., 153, 13–28, https://doi.org/10.1016/J.JQSRT.2014.10.003, 2015.

Santander, M. V., Mitts, B. A., Pendergraft, M. A., Dinasquet, J., Lee, C., Moore, A. N., Cancelada, L. B., Kimble, K. A., Malfatti, F., and Prather, K. A.: Tandem Fluorescence Measurements of Organic Matter and Bacteria Released in Sea Spray Aerosols, Environ. Sci. Technol., 55, 5171–5179, https://doi.org/10.1021/ACS.EST.0C05493/SUPPL_FILE/ES0C05493_SI_001.PDF, 2021.

Santarpia, J. L.: Bioaerosols in the environment: Populations, measurement and processes, in: Issues in Toxicology, The Royal Society of Chemistry, 219–247, https://doi.org/10.1039/9781849735940-00219, 2016.

Santarpia, J. L., Pan, Y.-L., Hill, S. C., Baker, N., Cottrell, B., McKee, L., Ratnesar-Shumate, S., and Pinnick, R. G.: Changes in fluorescence spectra of bioaerosols exposed to ozone in a laboratory reaction chamber to simulate atmospheric aging, Opt. Express, 20, 29867, https://doi.org/10.1364/oe.20.029867, 2012.

Sauer, J. S., Mayer, K. J., Lee, C., Alves, M. R., Amiri, S., Bahaveolos, C. J., Franklin, E. B., Crocker, D. R., Dang, D., Dinasquet, J., Garofalo, L. A., Kaluarachchi, C. P., Kilgour, D. B., Mael, L. E., Mitts, B. A., Moon, D. R., Moore, A. N., Morris, C. K., Mullenmeister, C. A., Ni, C.-M., Pendergraft, M. A., Petras, D., Simpson, R. M. C., Smith, S., Tumminello, P. R., Walker, J. L., DeMott, P. J., Farmer, D. K., Goldstein, A. H., Grassian, V. H., Jaffe, J. S., Malfatti, F., Martz, T. R., Slade, J. H., Tivanski, A. V., Bertram, T. H., Cappa, C. D., and Prather, K. A.: The Sea Spray Chemistry and Particle Evolution study (SeaSCAPE): overview and experimental methods, Environ. Sci. Process. Impacts, 24, 290–315, https://doi.org/10.1039/D1EM00260K, 2022.

Shiraiwa, M., Ammann, M., Koop, T., and Pöschl, U.: Gas uptake and chemical aging of semisolid organic aerosol particles, Proc. Natl. Acad. Sci., 108, 11003–11008, https://doi.org/10.1073/PNAS.1103045108, 2011.

Stokes, M. D., Deane, G. B., Prather, K., Bertram, T. H., Ruppel, M. J., Ryder, O. S., Brady, J. M., and Zhao, D.: A Marine Aerosol Reference Tank system as a breaking wave analogue for the production of foam and sea-spray aerosols, Atmos. Meas. Tech., 6, 1085–1094, https://doi.org/10.5194/amt-6-1085-2013, 2013.

Sun, J. and Ariya, P. A.: Atmospheric organic and bio-aerosols as cloud condensation nuclei (CCN): A review, https://doi.org/10.1016/j.atmosenv.2005.05.052, February 2006.

Toprak, E. and Schnaiter, M.: Fluorescent biological aerosol particles measured with the Waveband Integrated Bioaerosol Sensor WIBS-4: Laboratory tests combined with a one

year field study, Atmos. Chem. Phys., 13, 225–243, https://doi.org/10.5194/acp-13-225-2013, 2013.

Trueblood, J. V, Wang, X., Or, V. W., Alves, M. R., Santander, M. V, Prather, K. A., and Grassian, V. H.: The Old and the New: Aging of Sea Spray Aerosol and Formation of Secondary Marine Aerosol through OH Oxidation Reactions, https://doi.org/10.1021/acsearthspacechem.9b00087, 2020.

Wolfe, G. M., Nicely, J. M., Clair, J. M. S., Hanisco, T. F., Liao, J., Oman, L. D., Brune, W. B., Miller, D., Thames, A., Abad, G. G., Ryerson, T. B., Thompson, C. R., Peischl, J., McCain, K., Sweeney, C., Wennberg, P. O., Kim, M., Crounse, J. D., Hall, S. R., Ullmann, K., Diskin, G., Bui, P., Chang, C., and Dean-Day, J.: Mapping hydroxyl variability throughout the global remote troposphere via synthesis of airborne and satellite formaldehyde observations, Proc. Natl. Acad. Sci. U. S. A., 116, 11171–11180, https://doi.org/10.1073/PNAS.1821661116, 2019.

Yue, S., Ren, L., Song, T., Li, L., Xie, Q., Li, W., Kang, M., Zhao, W., Wei, L., Ren, H., Sun, Y., Wang, Z., Ellam, R. M., Liu, C. Q., Kawamura, K., and Fu, P.: Abundance and Diurnal Trends of Fluorescent Bioaerosols in the Troposphere over Mt. Tai, China, in Spring, J. Geophys. Res. Atmos., 124, 4158–4173, https://doi.org/10.1029/2018JD029486, 2019.

Zhang, M., Su, H., Li, G., Kuhn, U., Li, S., Klimach, T., Hoffmann, T., Fu, P., Pöschl, U., and Cheng, Y.: High-Resolution Fluorescence Spectra of Airborne Biogenic Secondary Organic Aerosols: Comparisons to Primary Biological Aerosol Particles and Implications for Single-Particle Measurements, Environ. Sci. Technol., acs.est.1c02536, https://doi.org/10.1021/ACS.EST.1C02536, 2021.

Chapter 5. Real-Time Fluorescence Measurements of Marine and Continental Aerosols in a Coastal Environment

5.1 Abstract

Biological aerosols are known to affect clouds, climate, and human and ecosystem health. Urbanized coastlines represent a convergence zone of bioaerosols originating from terrestrial, anthropogenic, and marine sources that change with wind direction on short timescales and require observational techniques with high time resolution to measure the dynamic atmospheric environment. High time resolution measurements are especially important along coastlines that are impacted by wastewater and pollution runoff which can be aerosolized through breaking waves. Here, a Wideband Integrated Bioaerosol Sensor (WIBS) was used to measure the compositions and concentrations of fluorescent particles at two sites along the Southern California coast to characterize air masses originating from continental and marine sources and investigate the impact of wastewater and pollution runoff on coastal bioaerosol populations. Fluorescence measurements revealed significant changes in atmospheric composition consistent with the diurnal the land/sea breeze cycle. Fluorescent particles in onshore winds comprised 5.3 ± 4.6% of all particles > 0.8 μm while fluorescent particles in offshore winds made up 16 ± 12% of all particles. Offshore winds contained particles with fluorescent and morphological profiles indicative of anthropogenic combustion sources, which were highly correlated with effective black carbon concentrations. In contrast, onshore winds often contained particles with fluorescence signatures and size distributions consistent with marine bacteria and humic-like substances released in sea spray aerosol particles. Marine air masses measured at two separate coastal sites showed dramatically different fluorescence profiles compared to continental air masses, highlighting the capability of the WIBS to provide real-time information on bioparticle sources. Furthermore, by

comparing marine air masses from a clean coastal site to a wastewater polluted coastal site, we show higher fluorescent particle fractions and larger fluorescent particle diameters indicative of microbial bioaerosols associated with marine air masses originating from sewage contaminated seawater. Increased wastewater outflow into the ocean correlated with higher fluorescent fractions and strongly correlated with the fraction of fluorescent particles with humic-like fluorescence, suggesting this as a potential fluorescence indicator of polluted SSA. These results demonstrate the use of online fluorescence techniques to distinguish between particle populations derived from anthropogenic aerosol sources, clean marine sources, and wastewater polluted marine sources in urban coastal environments.

5.2 Introduction

Biological aerosols, or bioaerosols, are aerosols which are comprised of microbes, microbial fragments, excrements, and spores (Fröhlich-Nowoisky et al., 2016). Bioaerosols are present throughout the atmosphere and come from a variety of different sources including plants, fungi, and oceans. Because of their size, they can travel far distances and have both local and global influence (Després et al., 2012). Bioaerosols impact clouds and climate, acting as cloud condensation nuclei and ice nuclei, and have the potential to influence precipitation and radiative flux (Fröhlich-Nowoisky et al., 2016; Pratt et al., 2009). Bioaerosols, in the form of pathogenic bacteria and viruses, can also affect human health and ecological systems resulting in hospitalization and financial losses (Douwes et al., 2003).

Wastewater is known to contain human pathogenic species such as *Escherichia coli (E. coli), hepatitis A,* and *enterovirus,* which can survive in marine environments (Griffin et al., 2003; Gersberg et al., 2006). When wastewater is released into the coastal ocean and trapped in the surf zone, pathogens can be aerosolized in sea spray aerosol (SSA) particles through breaking waves

and bubble bursting (Baylor et al., 1977; Graham et al., 2018; Michaud et al., 2018). Furthermore, bubble scavenging leads to enrichment of biological species including bacteria and viruses at the sea surface and in SSA (Aller et al., 2005; Rastelli et al., 2017; Michaud et al., 2018). Previous studies have demonstrated the potential for coastal waters to be aerosolized and transmitted over land in sea spray aerosols (Pendergraft et al., 2021).

At the border between Imperial Beach, USA and Tijuana, Mexico, stormwater and wastewater runoff from the Tijuana River flow into the Pacific Ocean (Gersberg et al., 2006). At the mouth of the Tijuana Estuary, currents carry the sewage contaminated water along the coastline where it causes beach closures and has the potential to be aerosolized through breaking waves (Feddersen et al., 2021; Zimmer-Faust et al., 2021). Although measurements of sewage related bacteria are commonly used for seawater pollution detection, few studies focus on the release of bioaerosols from polluted waters and the potential impact on local communities (Graham et al., 2018).

Bioaerosols are often collected onto filters and subsequently analyzed offline through culturing or genomic sequencing. However, these measurements require long collection periods and often extensive time for offline processing. An alternative method for bioaerosol detection with near real-time detection is online fluorescence spectroscopy, which detects naturally fluorescent biomolecules including select amino acids (tryptophan, tyrosine, phenylalanine) and biological cofactors (riboflavin, nicotinamide adenine dinucleotide (phosphate); NAD(P)H) (Pöhlker et al., 2012). Fluorescence spectroscopy can also detect non-biological fluorescent particles such as polycyclic aromatic hydrocarbons (PAHs), often found in combustion related aerosols, and humic-like substances, formed through the decomposition of biological molecules in marine and terrestrial systems (Pöhlker et al., 2012). High temporal resolution of fluorescent

particle detection allows for comparisons to changing meteorological and environmental conditions, therefore providing more informative results to local communities. Recently, single-particle fluorescence spectrometers have been used in ambient and laboratory settings for the online identification of fluorescent particles (Santarpia, 2016; Fennelly et al., 2018; Huffman et al., 2020; and references within), including those derived from SSA (Kawana et al., 2021; Moallemi et al., 2021; Santander et al., 2021). However, the fluorescence detection of SSA often occurs in remote marine environments or isolated laboratory settings and has yet to be observed in an urban-coastal environment influenced by land/sea breezes and anthropogenic and terrestrial sources.

Here, a single-particle fluorescence spectrometer, the Wideband Integrated Bioaerosol Sensor (WIBS) was used to detect fluorescent particles in the air near the mouth of the Tijuana Estuary during the wet season of 2019, when coastal water quality is heavily impacted by raw wastewater and pollution runoff. Utilizing the WIBS along with a suite of other instruments in an urban-coastal setting, meteorological and fluorescent aerosol measurements were used to study the conditions leading to the impact of contaminated ocean water and anthropogenic aerosol sources on local air quality. Background air measurements were made on the Ellen Browning Scripps Memorial Pier in La Jolla, a coastal location ~23 miles north of the Tijuana Estuary and less affected by wastewater sources, to compare the influence of sewage runoff on marine bioaerosol emissions. We discuss the ability of the WIBS to characterize and distinguish between aerosol populations derived from continental, clean marine, and polluted marine sources using online fluorescence and morphological measurements.

5.3 Methods

5.3.1 Sampling Sites

Measurements for this study were made along the coast of the Pacific Ocean in San Diego, CA, USA at two different sampling sites, located ~23 miles apart (Figure 5.1). The main sampling location was at the International Friendship Park (32°32'06.5"N 117°07'19.6"W), located within Border Field State Park in the Tijuana River National Estuarine Research Reserve, herein designated as BF sampling site (Figure 5.1c). Sampling took place from Feb 28, 2019, to Apr 24, 2019. This park is located at the border between Imperial Beach, USA, with the urban center ~2.5 miles to the north, and Tijuana, Mexico, ~330 ft to the south, with the Pacific Ocean to the west. The major Mexican Federal Highway (1D) is located ~0.81 miles to the southeast, and the Naval Outlying Landing Field Airport is located ~2.2 miles to the northeast. The sampling site was located at an elevation of approximately 66 ft above sea level and about 330 ft from the ocean. This location was chosen due to its proximity to the mouth of the Tijuana River which intersects the Pacific Ocean around 1.3 miles to the northwest of the sampling site (Figure 5.1c).

The second sampling site was located at the Scripps Institution of Oceanography (SIO) on the Ellen Browning Scripps Memorial Pier (32°51'58.9"N, 117°15'17.2"W) (SIO sampling site, Figure 5.1b). The location of the SIO site was directly above the shoreline along the east end of the pier at an elevation of 36 ft above sea level. Sampling at SIO took place from May 15, 2019, until May 27, 2019. The SIO location was chosen as a reference site with little wastewater pollution and less influence from anthropogenic aerosols because of its distance from major stormwater outflows (~4.6 miles from Los Penasquitos Watershed) and major metropolitan centers (11.5 miles from San Diego), respectively.

5.3.2 Instrumentation

WIBS: Single-particle fluorescence was measured using a Wideband Integrated Bioaerosol Sensor (Droplet Measurement Technologies, WIBS-NEO). The operation of the WIBS has been

previously described in detail (Gabey et al., 2010; Forde et al., 2019). Briefly, the WIBS utilizes two xenon lamps with bandpass filters to generate two excitation wavelengths: 280 nm (Xe1) and 370 nm (Xe2). The WIBS then collects fluorescence emission using two photomultiplier tubes (PMTs) with in-line bandpass filters at the wavelength bands 310 – 400 nm (FL1) and 420 – 650 nm (FL2). The combination of excitation wavelengths and emission collection bands yields three fluorescence "channels" (Ch) measured by the WIBS. The three channels are: channel 1 (Xe1/FL1; excitation/emission = 280 nm/310 – 400 nm; targeting tryptophan), channel 2 (Xe1/FL2; 280 nm/420 – 650 nm; targeting riboflavin), and channel 3 (Xe2/FL2; 370nm/420 – 650 nm, targeting NAD(P)H). Fluorescence in one or more of these channels can be further categorized into seven different fluorescence classes, originally described by Perring et al. (2015). These classes are exclusive and denoted as follows: class A (Ch 1 fluorescence only), B (Ch 2 only), C (Ch 3 only), AB (Ch 1 & 2), AC (Ch 1 & 3), BC (Ch 2 & 3), and ABC (Ch 1, 2, & 3) (Figure 5.8).

To determine the background fluorescence of the WIBS optical chamber, a "forced trigger" is performed where the xenon lamps are flashed while the sample flow is off. The forced trigger ran for 5 minutes on an 8-hour scheduler throughout the study. Particles were deemed fluorescent if their fluorescence intensity was greater than a set threshold according to the following equation:

$$E_{Threshold_i} = 3\sigma_i + \bar{E}_i \qquad [5.1]$$

where $\bar{E}_i$ is the mean forced trigger intensity and σ_i is the standard deviation of the mean for each fluorescence channel (i), similar to previous studies (Healy et al., 2012a; Hernandez et al., 2016). The threshold was then subtracted from the particle fluorescence for each channel. Here, the mean threshold for the study was used because there was little drift observed in the measured threshold.

In addition to the fluorescence measurements, the WIBS measures the optical diameter and the asymmetry factor (AF) of each particle using the scattered light from a 635 nm continuous-

wave laser. Side scattered light is detected on the FL2 detector and the optical diameter from 0.5 – 50 µm is derived based on calibrations using polystyrene latex spheres. The AF value is obtained from forward scattered light onto a quadrant PMT and ranges from 1 – 100 with lower values (<10 – 15) corresponding to spherical shapes and higher values (>30) relating to more rod-like particles (Kaye et al., 2007; Crawford et al., 2017). In addition to the fluorescence threshold that was set for this study, we selected particles greater than 0.8 µm due to the lower counting efficiency of the WIBS below this diameter (Healy et al., 2012b; Crawford et al., 2017; Lieberherr et al., 2021) and to minimize the potential influence of non-biological fluorescent sources such as PAHs which are often in the submicron size range (Bond et al., 2013).

Aethalometer: A seven-wavelength aethalometer (Magee Scientific, Model AE31, λ = 370, 470, 520, 590, 660, 880, and 950 nm) was used to record the optical absorption of aerosol particles in 5-minute time intervals to determine the black carbon content. Here, we use the terminology suggested by Petzold et al. (2013) for optical absorption methods and report the equivalent black carbon mass concentrations (EBC) using the absorption of light from the λ = 880 nm lamp. This wavelength was chosen because it compares to single wavelength aethalometers and is less influenced by ultraviolet absorbing species, such as PAHs and mineral dust, that can increase the absorption at lower wavelengths (Weingartner et al., 2003). The principles of the aethalometer were originally described by Hansen et al. (1984) and the operation and function of the multiwavelength aethalometer has been described in detail in subsequent articles (Hansen, 2005; Fialho et al., 2005; Weingartner et al., 2003). Briefly, the aethalometer is based on the principles of Beer-Lambert's law and measures the attenuation of source light by aerosols collected onto a quartz filter compared a reference spot without aerosols according to Eq. 5.2:

$$ATN = \ln\left(\frac{I_0}{I}\right) * 100 \qquad [5.2]$$

Where I_0 is intensity of the incoming light at a specific wavelength without collected aerosols, and I is the intensity of light after passing through an aerosol-laden filter. The aerosol attenuation coefficient is described by Eq. 5.3:

$$b_{ATN} = \frac{A}{Q}\frac{\Delta ATN}{\Delta t} \quad [5.3]$$

Where A is the spot area of collected aerosols, 1.67 cm^2, Q refers to the flow rate of 4.9 liters per minute, ΔATN is the change in the attenuation over the time base, Δt, which was set to 5 minutes (Hansen et al., 2005). The non-corrected equivalent mass concentration of black carbon, EBC_{NC}, is then derived from the attenuation coefficient based on Eq. 5.4:

$$EBC_{NC}(\frac{ng}{m^3}) = \frac{b_{ATN}}{\sigma_{ATN}} \quad [5.4]$$

In Eq. 5.4, σ_{ATN} represents the specific attenuation cross section at the measured wavelength of light and is provided by the manufacture (Hansen, 2005).

Aethalometer Data Corrections: It is well known that single spot aethalometers, such as the AE31, can be biased by a number of factors including: 1) noise at low black carbon concentrations due to fluctuations in the digitized signals that result in negative ATN and EBC values, 2) fluctuations resulting in very high values followed by comparatively low values 3) enhanced absorption due to scattering from the fiber filter, and 4) increased loading of aerosols on the filter resulting in lower attenuation values than on a new filter. To account for these biases, the following post-processing analysis was applied to the data: 1) negative ATN and EBC values due to very low black carbon concentrations at the start of a filter change were set to zero; 2) fluctuations resulting in high and low values were corrected using the Optimized Noise-reduction Averaging Algorithm defined by Hagler et al. (2011) to retain the time base of 5 minutes; 3) scattering from the filter and 4) the increased loading were both corrected for using the Weingartner et al. (2003) method suggested in Collaud Coen et al. (2010) for data that do not

contain scattering coefficients measurements. The Weingartner correction method is further described in the Supplement.

Here, we designated three different ranges to distinguish the level of air pollution based on EBC concentrations: 1) low-EBC corresponds to EBC < 100 ng/m^3, 2) medium-EBC represents periods with EBC ≥ 100 ng/m^3 and ≤ 1000 ng/m^3, and 3) high-EBC when EBC > 1000 ng/m^3. The low-EBC category, representing clean air masses, was selected based on the concentrations of EBC at the reference location (SIO). The medium-EBC air masses can be considered somewhat influenced by anthropogenic sources, and the high-EBC air masses are assumed to be heavily influenced by the anthropogenic sources.

Meteorological Station: Meteorological data were collected using a meteorological station (Columbia Weather Systems, Inc., Magellan MX600) which collected precipitation rate, relative humidity, temperature, wind speed and wind direction data at the sampling location. The sensor for the meteorological station (met station) was elevated ~1 m above the roof of the trailer to put the met station sensor at the same height as the inlet to the WIBS and the aethalometer.

River Flow Data: Information on the flow of the Tijuana River was acquired from the International Boundary and Water Commission (waterdata.ibwc.gov). The data on the river discharge were selected for the Tijuana River at the International Boundary (location: 11013300) for the time periods when measurements were performed at the BF sampling site (Feb 28 – Apr 24, 2019). The 5-minute discharge recordings were used for this analysis to maintain high temporal resolution.

Back Trajectory Analysis Three-day (72-hour) back trajectories were calculated using the Flexible Particle (FLEXPART) dispersion model, a Lagrangian particle dispersion model. FLEXPART was run backwards in time and simulated the transport of aerosols and gases in the

atmosphere based on meteorological data (Stohl et al., 1998, 2005). Here, the meteorological data inputs used in FLEXPART were collected from the United States National Centers for Environmental Prediction (NCEP) Climate Forecast System Reanalysis (CFSR) 6-hour products. For each FLEXPART simulation, 2000 "air parcels" were released from a height of 66 ft from the BF sampling location coordinates and a height of 33 ft from the SIO sampling coordinates. The data outputs from each simulation included the latitude, longitude, and vertical distribution of the "air parcels" for each hour of the back trajectory. For these analyses, we focused on the horizontal spatial information to characterize the origin of the air mass. The data output from each 72-hour back trajectory was analyzed to determine the percentage of "air parcels" with latitudinal and longitudinal coordinates positioned over the ocean. Back trajectories were then classified as predominantly marine origin if the percentage of "air parcels" with positions over the ocean was greater than or equal to 80%.

5.3.3 Air Mass Selection

To identify air masses with different source influences at both BF and SIO, a combination of both local meteorological information and back trajectory analysis was used. Five-minute air masses were primarily selected based on the average wind direction and the EBC concentrations. Onshore winds (blowing from the west) were more likely to contain a larger fraction of freshly emitted SSA particles, and offshore winds (blowing from the east) were more likely to be influenced by terrestrial and anthropogenic sources. The EBC concentrations were used as a proxy to identify periods of high versus low local airborne pollution. Two main air mass types at BF were isolated with these parameters: 1) Polluted, continental air masses which were described as air masses blowing from the east (0° – 180°) with EBC concentrations > 1000 ng/m^3 (BF Continental), and 2) Clean, marine air masses selected as air masses blowing from the northwest

(270° – 330°, highlighted in section 5.4.2) with EBC concentrations < 100 ng/m^3 (BF Marine). At SIO, we identified air masses with similar conditions to the clean, marine air masses measured at BF, but with winds blowing from the west (180° – 360°) and with EBC concentrations < 100 ng/m^3 (SIO Marine).

Then 72-hour back trajectories were run for the periods when local marine conditions were met to further confirm the origin of these air masses. When gaps between local marine conditions were greater than 2 hours, a new back trajectory was run. If the local conditions persisted for more than 4 hours, additional back trajectories were run every 4 hours to ensure no major changes in the air mass origin. Back trajectory plots for both BF Marine and SIO Marine air masses are shown in Figures 5.9 and 5.10.

5.4 Results and Discussion

5.4.1 Timeseries of fluorescent particle populations

Throughout the course of the field campaign at BF, there was daily variability in the particle populations and meteorological conditions. As shown in Figure 5.2a, the 6-hour averages of the wind speed and direction show strong diurnal trends throughout the course of the study. Wind direction varied from around 90° (E) to 315° (NW) and on average the wind speed was around 1.58 ± 1.02 m/s. There was a notable amount of variability in the 30-minute averaged EBC concentrations with higher counts often observed over the course of the weekend, likely due to increased activity at the beach and local traffic in the area (Figure 5.2b). In general, 30-minute averages for the fluorescent particle counts (N_{Fl}) tracked those of the total particle counts (N_{Tot}) (Figure 5.2c). However, the 30-minute fluorescent particle fraction (N_{Fl}/N_{Tot}) highlights periods of variable fluorescent particle concentrations within the aerosol population (Figure 5.2d). Throughout the study average fluorescent particle concentrations and total particle concentrations

were 289 ± 247 L^{-1} and 5559 ± 5901 L^{-1}, respectively, while the fluorescent fraction was on average 0.086 ± 0.090 and reached a maximum of 0.65 on April 5, 2019. These counts are in the range of previous studies measuring the fluorescent fraction of aerosols in an urban environment (Gabey et al., 2011; Yue et al., 2017, 2019; Calvo et al., 2018). Notably, higher fluorescent particle fractions, 0.16 ± 0.12, (Figure 5.2d) often occurred during offshore winds (blowing from the east; 0° – 180°) compared to onshore winds (180° – 360°), 0.053 ± 0.046. This discrepancy reflects the different aerosol sources, with offshore winds comprised of terrestrial bioaerosols and non-biological fluorescent particles and onshore winds primarily consisting of marine bioaerosols, which have been previously shown to contain lower bacterial concentrations compared to urban environments (Shaffer and Lighthart, 1997).

The fluorescent and total particle concentrations measured at the SIO location were lower than at BF, with average fluorescent and total particle counts of 67 ± 35 L^{-1} and 3028 ± 2213 L^{-1}, respectively, over 30-minute sampling periods (Figure 5.11c). The lower total particle counts are likely the result of cleaner conditions at SIO with lower anthropogenic influences; evident from the average EBC concentrations of 102.1 ± 155.7 ng/m^3 compared to BF, 996.6 ± 1924.3 ng/m^3 (Figure 5.11b). In addition to the lower overall counts, the fluorescent particle fraction of the aerosol population at SIO (0.026 ± 0.013) was lower than that at the BF location (0.086 ± 0.090), suggesting less influence by bioaerosols and/or non-biological fluorescent sources (Figure 5.11d). The wind direction at the SIO site was primarily from the west (onshore) and the measured fluorescent fraction agrees with values previously reported for SSA (Kawana et al., 2021; Moallemi et al., 2021; Santander et al., 2021), indicating a predominant source of marine derived bioaerosols.

To better understand the sources of particle populations at BF, fluorescent particles were characterized according to the classification scheme presented by Perring et al. (2015) (Figure 5.8) into their respective fluorescent classes for each 30-min interval. This classification system creates a fluorescence signature to help distinguish between different particle sources and gather information on the fluorescent biomolecules present in the aerosols. In general, the 30-min fluorescence class profiles (fraction of fluorescent particles represented by each class) varied with offshore and onshore winds, indicting different sources of fluorescent particles depending on wind direction. In offshore winds, the fluorescent particle populations were largely comprised of class ABC (~20 – 40%) and class BC (~ 20%) particles (Figure 5.2e). In contrast, during onshore winds, the fluorescent populations largely consisted of class A particles (~20 – 40%) as well as class C particles (~10 – 20%) similar to previous measurements of bioaerosols in SSA (Moallemi et al., 2021; Santander et al., 2021). By using this classification method to define the fluorescence profile of particle populations, WIBS measurements can help discriminate between air masses derived from different sources in an urban-coastal environment.

The 30-min fluorescence class profiles at the SIO location were more consistent compared to BF, suggesting a single bioaerosol source for most of the sampling campaign (Figure 5.11e). The fluorescence profile observed throughout most of the SIO sampling period matched the signature measured at BF during the onshore periods, with primarily class A particles (~20%) and class C particles (10 – 20%), suggesting marine derived particles were the predominant aerosol source at SIO. Similar to BF, offshore winds were often associated with increases in the overall fluorescent particle fraction (N_{Fl}/N_{Tot}) and an increase in the fraction of class ABC and class BC fluorescent particles, indicating a continental fluorescent particle source from these wind directions. The similarities between the fluorescence class signatures at both SIO and BF for

onshore and offshore winds indicate this classification method is valuable for separating fluorescent particle sources at different coastal sites.

5.4.2 Links between fluorescent particles and local environmental conditions

To gain insight into the local sources contributing to the fluorescent particle classes at BF, we plotted the fluorescent classes as a function of wind speed and wind direction (Figure 5.3). It is clear from these plots that class A particles made up a large fraction (~20 – 30%) of the fluorescent particles in winds blowing from the west and thus had a heavy marine influence (Figure 5.3a). Furthermore, class A particles represented a notable fraction of the fluorescent particles in winds blowing from about 270° – 330° (W-NNW) for all wind speeds. With the Tijuana River mouth to the northwest of the sampling site, winds from this direction likely contained marine aerosols generated from wastewater contaminated seawater. The high fluorescent fraction of class A particles, indicating protein-like fluorescence, suggests a prominent source of marine bacteria, which have been previously observed in nascent SSA (Santander et al., 2021). Additionally, winds from the northwest had moderate fractions of class C particles (~15%), a known indictor of marine humic-like substances in SSA (Figure 5.3c) (Santander et al., 2021). Class A and class C particles have been previously related to conditions of SSA production in both laboratory (Santander et al., 2021) and ambient settings (Kawana et al., 2021), suggesting particle populations from the northwest at BF were heavily influenced by marine aerosols derived from wastewater contaminated SSA.

In contrast, both class ABC and class BC made up a large fraction of fluorescent particles from the south and the east of the sampling site. Shown in Figure 5.3e and 5.3f, these classes account for a higher fraction of fluorescent particles from ~60° (ENE) – 210° (SSW), therefore, they are likely an indicator of either terrestrial or anthropogenic sources. Pollens and pollen

fragments commonly comprise fluorescent particles in these classes and occasionally fungal spores have been observed to fluoresce in these classes (Gosselin et al., 2016; Hernandez et al., 2016; Savage et al., 2017; Hughes et al., 2020). Additionally, anthropogenic aerosols such as soot containing PAHs can fluoresce in these regions, and therefore may represent the primary source of fluorescent particles from these wind directions (Pöhlker et al., 2012; Savage et al., 2017).

To determine whether the class ABC and class BC particles were from anthropogenic or biological origin, correlations between the EBC concentrations and the fluorescent class fractions were calculated and the EBC concentrations were plotted as a function of wind speed and direction (Figure 5.4). Figure 5.4a highlights the Pearson correlation coefficients between the different fluorescent class fractions and the $\log_{10}$-tranformed EBC concentrations, all of which were statistically significant (*p-value* <0.05). Here, we follow the correlation terminology laid out by Dancey and Reidy (2011) where coefficient values from 0.1 – 0.3, 0.4 – 0.6, and 0.7 – 0.9 represent weak, moderate, and strong correlations, respectively.

The fluorescent class fractions for class ABC and class BC showed moderate positive correlations with the EBC concentrations, 0.58 and 0.62, respectively (Figure 5.4a). These correlations follow the trends observed with the polar plot of the EBC concentrations, where the highest concentrations were during the offshore winds (Figure 5.4b). Additionally, the positive correlations of class ABC and class BC suggest these particles are predominately anthropogenic combustion sources in winds from the south and the east. Previously, Yu et al., (2016) showed classes A, AB, and ABC had moderate to strong correlations with anthropogenic sources, but class BC showed only a weak correlation. Contrary to the results from Yu et al., we did not observe a moderate correlation with the fraction of class A or class AB particles and EBC concentrations. This difference indicates the fluorescent molecules in anthropogenic aerosols differed between the

two studies, with the fluorescent particles here containing PAHs such as pyrene and phenanthrene, which fluoresce strongly in both WIBS channels 2 and 3, and a minor influence from naphthalene which fluoresces in channel 1 (Pöhlker et al., 2012; Savage et al., 2017). The complimentary aethalometer measurements help confirm the initial conclusions made with the WIBS, that the high fractions of particles fluorescent in classes ABC and BC represented predominantly anthropogenic sources during offshore winds.

5.4.3 Relating particle fluorescence to air mass origin

Following the information gathered from the WIBS in relation to the environmental factors from the meteorological station and aethalometer, we decided to separate out air masses that were indicative of both marine and anthropogenic sources to compare their fluorescent and morphological particle properties. These categories were separated according to the criteria described in the methods section on air mass separation (Section 5.3.3). Here, we will refer to air masses at BF that occurred during low EBC concentrations, winds from the northwest, and marine origins (based on back trajectories) as "BF Marine" aerosols. Air masses measured at BF during conditions of high EBC and winds from the east will be referred to as "BF Continental". Lastly, for the SIO site, which serves as a reference for coastal aerosol containing SSA from non-polluted waters, we designate the term "SIO Marine" to represent air masses with low EBC, winds from the west, and marine back trajectories.

Figure 5.5 displays box-and-whisker plots of the morphological and fluorescent properties for the aerosols in each category. The differences between BF Continental and BF Marine are apparent based on the fluorescent particle fraction, with median fluorescent particle fractions of ~20% and ~4% for BF Continental and BF Marine, respectively (Figure 5.5a). Both air masses at BF had higher fluorescent particle fractions than SIO Marine which had a median fluorescent

fraction of ~2% (Figure 5.5a). The high fluorescent particle fraction of BF Continental, which had largely anthropogenic air masses, aligns with previous fluorescence measurements in polluted areas (Wei et al., 2016; Yue et al., 2017) and indicates that non-biological fluorescent particles can be a significant fluorescent particle source in an urban environment. The lower fluorescent fraction of BF Marine more closely compares to SIO Marine air masses, suggesting generally lower fluorescent fractions from marine sources compared to terrestrial sources (Gabey et al., 2011; Huffman et al., 2012; Perring et al., 2015). Previous studies on the fluorescent fractions of SSA report percentages of 0.87% for particles > 0.8 µm, and 1.3% – 1.6% for particles > 1 µm which compare well to the measurements made here, especially those of SIO Marine (Kawana et al., 2021; Moallemi et al., 2021; Santander et al., 2021). The higher fluorescent fraction measured for BF Marine likely resulted from the aerosolization of wastewater from the Tijuana River outflow. Wastewater is known to contain high bacterial and fungal concentrations as well as dissolved organic material that can contribute to the fluorescent population (Bauer et al., 2002; Tian et al., 2020). A moderate correlation (0.57) was observed between the fluorescent particle fraction and Tijuana River outflow during the BF Marine measurement periods, suggesting increased runoff into the coastal ocean led to the higher fluorescent particle fractions (Table 5.2). Additionally, during this period of increased outflow, there were rain events (Figure 5.13) which can increase SSA production when rain drops impact the ocean surface (Lewis and Schwartz, 2004).

In addition to the differences in the fluorescent fraction, the different air masses showed variability in particle morphology (Figure 5.5b, 5.5c). BF Continental particles had the smallest median optical diameter, with a value of ~1.3 µm. Comparatively, BF Marine particles showed a median diameter of ~2 µm and SIO Marine particles had a median diameter of ~1.5 µm. The small median diameter associated with BF Continental likely reflects a greater contribution from

anthropogenic soot aerosols, which often have submicron diameters (Jones and Harrison, 2004; Bond et al., 2013; Savage et al., 2017). The higher median optical diameters of BF Marine and SIO Marine suggest bioaerosol emissions from SSA (Santander et al., 2021). Furthermore, the difference between the median diameters of BF Marine and SIO Marine likely results from the polluted coastal waters near BF and the increased ejection of microbes, which are known to comprise SSA with larger diameters (Santander et al., 2021). While it is possible that the BF location was influenced by other sources of fluorescent aerosols with larger diameters such as fungal spores, which are common in terrestrial sources (O'Connor et al., 2015; Perring et al., 2015; Hernandez et al., 2016), the onshore winds and marine back trajectories suggest these bioaerosols originated from marine sources.

The fluorescence intensities across all three WIBS channels highlight the compositional differences between the three air masses (Figure 5.5e-f). The median fluorescence intensities of all three channels were highest for BF Continental air masses likely because PAHs, the fluorescent components in combustion aerosols, are known to have high quantum yields and strong fluorescence emission (Pöhlker et al., 2012; Savage et al., 2017). In contrast, the two marine air masses, BF Marine and SIO Marine, showed similar fluorescence intensities across the three channels measured with the WIBS. Notably, BF Marine showed a slightly higher protein-like fluorescence intensity in channel 1 compared to SIO Marine suggesting BF Marine had higher protein concentrations, common to microbial bioaerosols. Through WIBS fluorescence and morphological measurements, the compositional differences between particle populations belonging to continental sources as well as polluted and clean marine sources can be distinguished from one another.

5.4.4 Fluorescent class fraction of air masses

To better characterize the fluorescent particles from the BF Continental, BF Marine, and SIO Marine air masses, we report the fluorescent class profile of each air mass. With this classification scheme, a clear separation appears between the different air masses based on the fraction of fluorescent particles in each fluorescence class (Figure 5.6). Both BF Marine and SIO Marine air masses have a median class A fluorescent fraction of around 0.3 while BF Continental has a median class A fraction of around 0.03. Similarly, class C shows comparable median fluorescent fractions between BF Marine (0.14) and SIO Marine (0.14) that was much higher than the BF Continental aerosols (0.03). The spread of the fluorescent fraction of class C particles in BF Marine air masses was much larger than that of SIO Marine, with the 75^{th} percentile extending to 0.24. The greater variability likely results from the influence of wastewater runoff into the coastal waters at BF and fluctuations in the dissolved organic matter from the input of the Tijuana River. A strong Pearson's correlation coefficient of 0.79 was determined when the Tijuana River flow rate was compared to the class C fluorescent fraction for BF Marine air masses. It is possible that this increase may have been the result of rainfall during this period and the aerosolization of bioaerosols or humic-like substances from rain drops impacting the ocean and land, as previously observed (Huffman et al., 2013; Yue et al., 2016). However, the class C particles during this study appeared to persist after the rain events, in contrast to the short duration of previous observations. This suggests class C particles originated from SSA generated from local waters that remained polluted for days following rain events (Figure 5.13). Additionally, due to onshore winds during these measurements and proximity to the ocean, the BF site should have been more influence by aerosols produced from the ocean compared to aerosols from rain impaction on the land.

Contrary to the class A and class C fractions, BF Continental showed a much higher fluorescent class fraction for class BC and class ABC particles with median values of 0.18 and

0.22, respectively. Both BF Marine and SIO Marine have median fluorescent fractions of < 0.05 in these classes. As previously noted, classes BC and ABC correlated with EBC and showed fluorescent properties consistent with anthropogenic combustion sources; therefore, these higher fluorescent class fractions would be expected for the continental air masses compared to marine air masses. Here, classes A and C were effective at distinguishing marine particle sources, whereas classes BC and ABC were effective at identifying continental sources, supporting the initial observations made for onshore and offshore winds. Additionally, the strong correlation between the Tijuana River outflow and the class C fluorescent fraction measured for BF Marine air masses suggests this may be a helpful indicator of wastewater pollution into the coastal ocean.

5.4.5 Fluorescent class attributions of air masses

Fluorescent particles measured with the WIBS can be further characterized based on their optical diameters. As shown in Figure 5.7, the size distributions of each fluorescence class depended on the air mass origin. Notably, for BF Continental, particles in classes BC and ABC have a primary mode in the submicron range, highlighting that these particles were predominantly derived from anthropogenic combustion sources (Figure 5.7a). This trend follows observations by Yu et al. (2016), where combustion-related products with fluorescence in channel 3 showed higher correlations with decreasing particle size.

BF Marine showed drastically different size distributions across all fluorescent classes compared to the BF Continental distributions, highlighting the ability of the WIBS to distinguish between these different particle sources (Figure 5.7b). Class A and class B aerosols showed bimodal distributions with a mode around 0.8 – 0.9 μm and a second mode between 2 – 3 μm. The size modes for these classes reflect those previously measured for marine bacteria and SSA particles (Santander et al., 2021). Class C showed a less pronounced supermicron mode compared

to class A and class B although a slight increase around 2 µm is noticeable. SSA particles with humic-like substances have been shown to fluoresce in class C and comprise smaller particles in the SSA population (Santander et al., 2021). Class AB, BC, and ABC showed similar size distributions, with a primary mode observed around 3 µm. These fluorescent particle types have been previously detected in marine air masses with similar size distributions (Kawana et al., 2021), suggesting they represent a common bioaerosol produced in SSA from microbial origin. We note that other studies have shown fungal spores and pollen fragments with diameters around 3 µm and fluorescence in classes AB, BC, and ABC, however, these bioaerosols would more likely be expected in terrestrial air masses (Hernandez et al., 2016). Regardless, these distributions are substantially different than those reported for BF Continental air masses, demonstrating how fluorescent size distributions can help distinguish marine and continental particle sources.

The primary mode of classes A and B for SIO Marine had a maximum in the submicron range and, unlike BF Marine, only show a slight mode in the distribution around 2 – 3 µm (Figure 5.7c). This difference is likely due to the high concentrations of microbes present in wastewater runoff and therefore the increased ejection of bacteria in SSA from breaking ocean waves near the BF site (Bauer et al., 2002; Aller et al., 2005). Fluorescent particles in classes AB, BC, and ABC from both BF Marine and SIO Marine show similar size distributions indicative of bioaerosols emitted from the ocean into SSA. However, BF Marine showed higher particle counts in these classes compared to SIO Marine, suggesting greater microbial emissions in SSA due to wastewater runoff into the surf zone. The WIBS is uniquely suited to detect periods of increased microbial activity in local emission sources and distinguish between polluted and clean marine sources because of its ability to measure single-particle fluorescence and optical diameter.

5.5 Conclusions

Discriminating between different fluorescent aerosol sources, such as bioaerosols and combustion related aerosols, is important for assessing both local health implications and cloud interactions. This is especially true for locations such as Imperial Beach, California, where wastewater and stormwater runoff can be carried into the coastal waters and aerosolized in SSA through breaking waves (Pendergraft et al., 2021). Here, we demonstrate that online fluorescence and morphological measurements made using a WIBS can provide meaningful information to distinguish marine from continental sources. During this study, we show that classes BC and ABC track EBC concentrations, indicating they can be used to assess anthropogenic influences. Air masses with substantial fluorescent fractions of class BC and class ABC particles were further shown to have high fluorescence intensities and submicron size distributions, highlighting that these sources contained combustion related particles with fluorescent PAHs. In comparison, marine air masses contained higher fractions of class A and class C fluorescent particles and were often comprised of fluorescent particles with larger optical diameters because of their biological origin.

We observed lower overall fluorescent particle fractions in air masses of marine origin compared to the periods of continental influence and compared to previous studies of terrestrial based fluorescent particles. The low fluorescent fractions measured in ocean-derived particles are consistent with previous measurements of SSA (Kawana et al., 2021; Moallemi et al., 2021; Santander et al., 2021) and suggest that, in general, a lower fluorescence particle fraction, $\leq \sim 10\%$ with the thresholds used, may be a useful metric for identifying marine air masses in an urban-coastal environment. However, we show that marine air masses from wastewater polluted coastal waters resulted in higher fluorescent particle fractions ($6.8 \pm 4.6\%$), often over double those from clean coastal waters ($2.1 \pm 0.071\%$). Furthermore, the fraction of fluorescent particles increased

during periods of wastewater runoff and rain events. Higher concentrations of fluorescent particles with size distributions and fluorescent profiles consistent with microbes were observed in marine air masses from polluted water sources. Additionally, increased wastewater runoff positively correlation with the fraction of class C particles, suggesting runoff may act as a source of humic-like fluorescent species in coastal waters and SSA. We have shown here that the measurements from the WIBS can reliably separate continental, wastewater polluted marine, and clean marine air masses in urban-coastal environments. Online fluorescence techniques with real-time bioaerosol detection and source apportionment may provide an early-warning system of hazardous air conditions for coastal communities.

5.6 Acknowledgements

This project was supported by the Understanding and Protecting the Planet initiative from the University of California San Diego, the Betty and Gordon Moore Foundation to ATA, and by the German Research Foundation (DFG) with Grant PE 2600/1 to DP.

Chapter 5, in full, is currently being prepared for submission for publication of the material. Mitts, B. A., Pendergraft, M. A., Morris, C. K., Belda-Ferre, P., Aron, A. T. Petras, D., Prather, K. A. (2022).” Online Fluorescence Characterization of Marine and Continental Aerosols in a Coastal Environment” The dissertation author is the primary investigator and author of this manuscript.

5.7 Figures

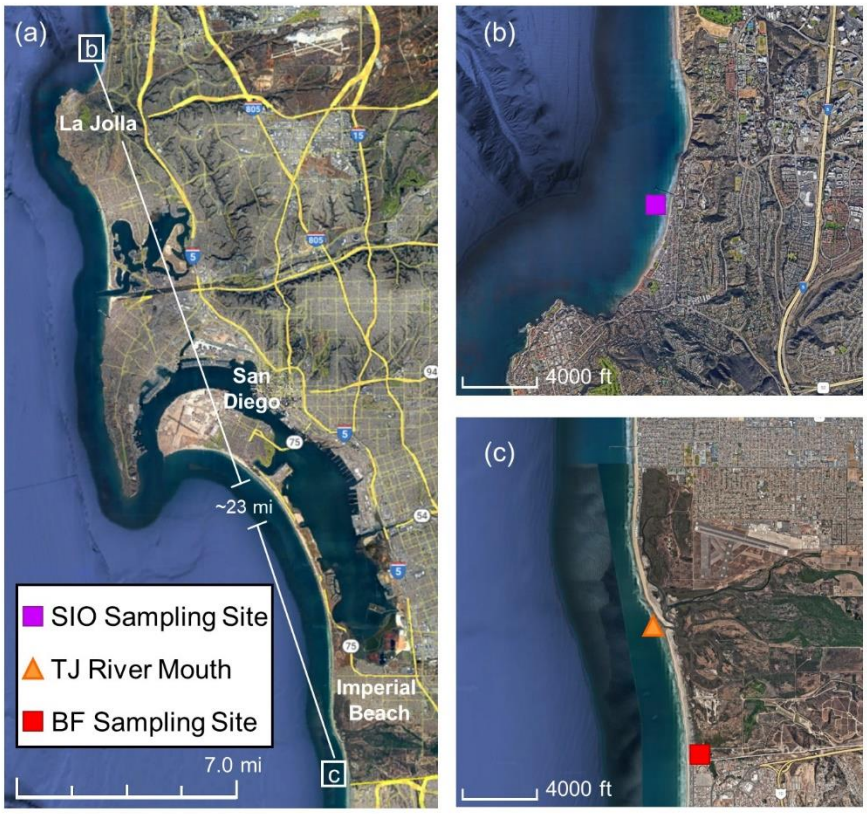

Figure 5.1. Images of the sampling locations. (a) Image of both sampling locations in Southern California: (b) the Scripps Institution of Oceanography (SIO) location (purple square), and (c) the Border Field location at the US-Mexico border (red square) as well as the Tijuana (TJ) river mouth (orange triangle) to show the proximity to a wastewater pollution source.

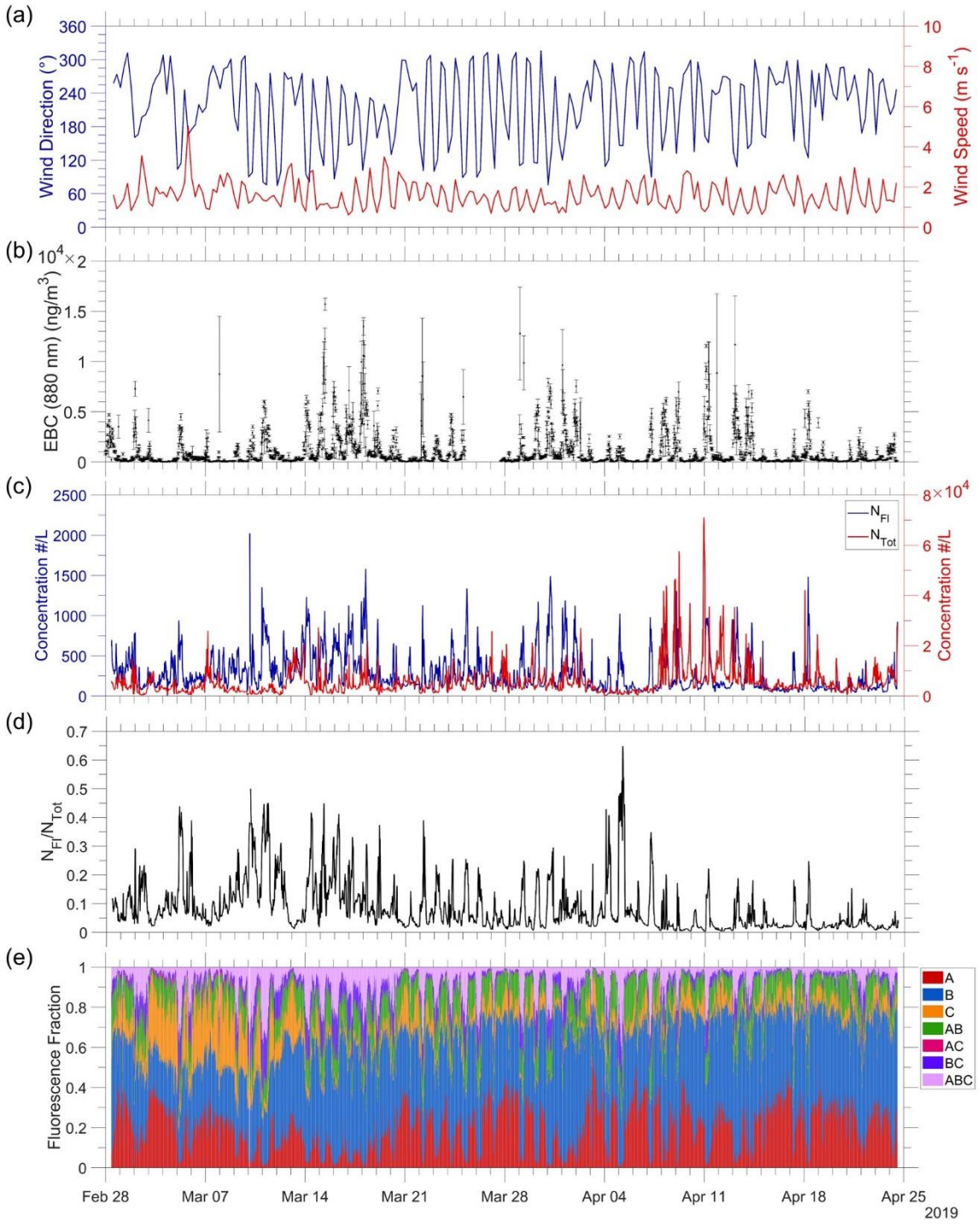

Figure 5.2. Timeseries of the sampling at the Border Field location. Measurements include (a) 6-hour averages of wind speed (red) and wind direction (blue), and 30-minute averages of the following: (b) EBC concentration; (c) fluorescent particle (blue) and total particle (red) concentrations; (d) fluorescent particle fraction; (e) fluorescent class fraction.

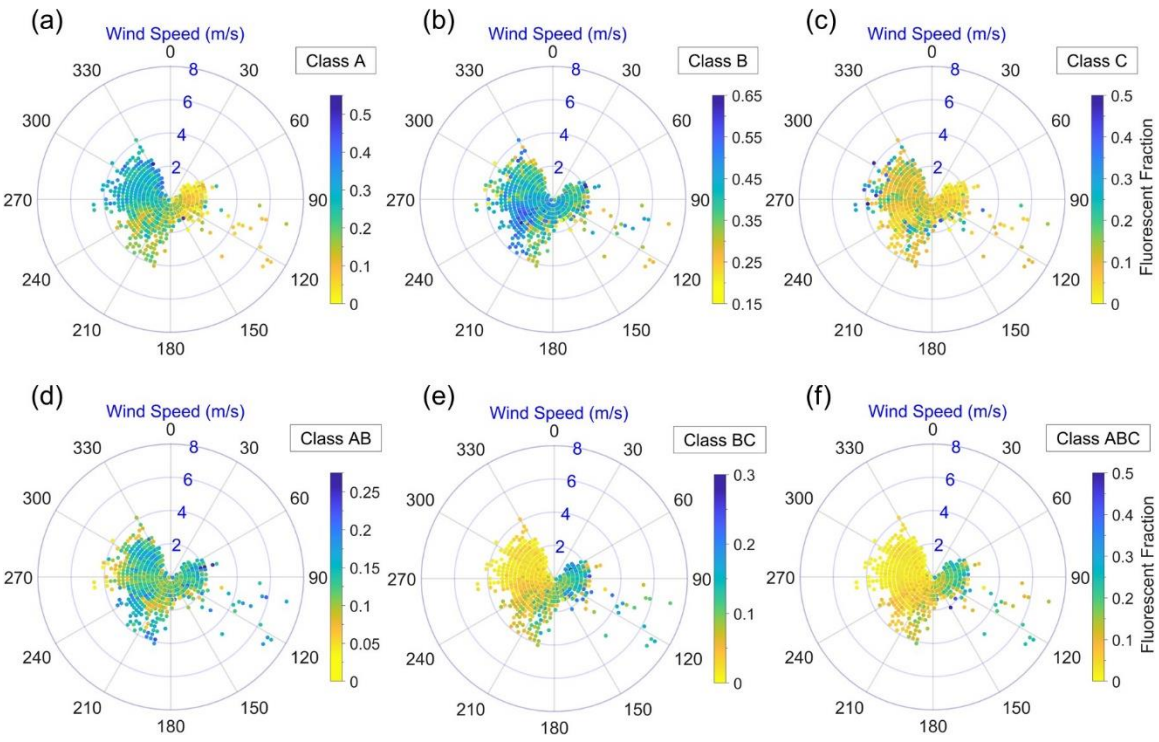

Figure 5.3. Polar plots of the fraction of fluorescent particles belonging to the fluorescent classes (a) A, (b) B, (c) C, (d) AB, (e) BC, (f) ABC over 30-minute time periods measured at the Border Field location. The fluorescent class fraction is plotted as a function of wind direction (°; 0° N) and wind speed (blue concentric circles).

(a)

Fluorescence Class	Correlation Coefficient
Class A	-0.70
Class B	0.22
Class C	-0.40
Class AB	0.13
Class AC	-0.55
Class BC	0.62
Class ABC	0.58

(b)

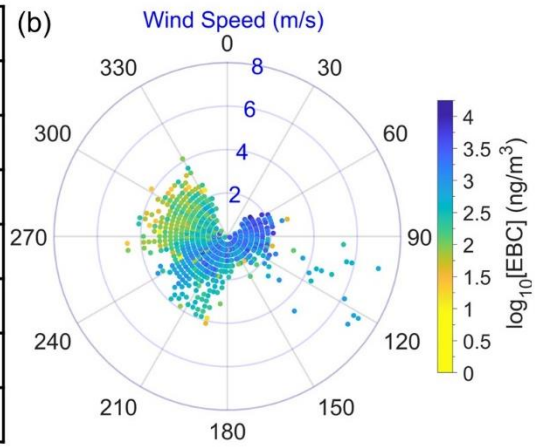

Figure 5.4. (a) Pearson correlation coefficients of the different fluorescent class fractions to the log_{10}-transformed EBC concentrations measured at the Border Field sampling site. All correlations were statistically significant with a *p-value* < 0.05. (b) Log_{10}-transformed EBC concentrations plotted as a function of wind speed (blue concentric circles) and wind direction (°; 0° N) at the Border Field sampling site.

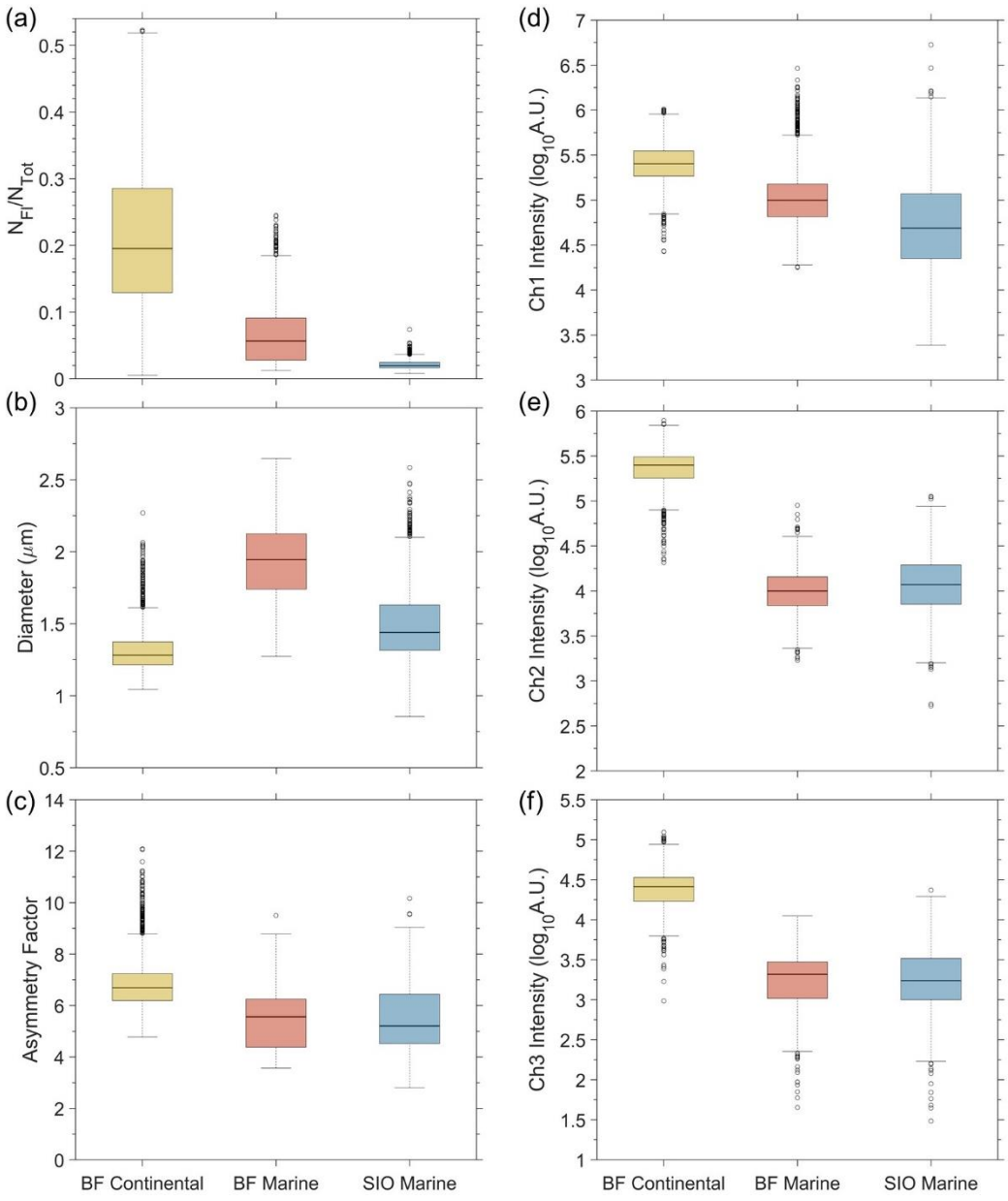

Figure 5.5. Box and whisker plots of the (a) fluorescent particle fraction, (b) fluorescent particle optical diameter, (c) fluorescent particle AF, (d) Ch1 fluorescence intensity, (e) Ch2 fluorescence intensity, (f) Ch3 fluorescence intensity for the BF Continental particles, the BF Marine particles, and the SIO Marine particles. Each box represents the median value (black line) and the interquartile range, while the whiskers indicate the 5th and 95th percentiles and outliers are open markers for the average 5-minute air masses corresponding to the different particle types.

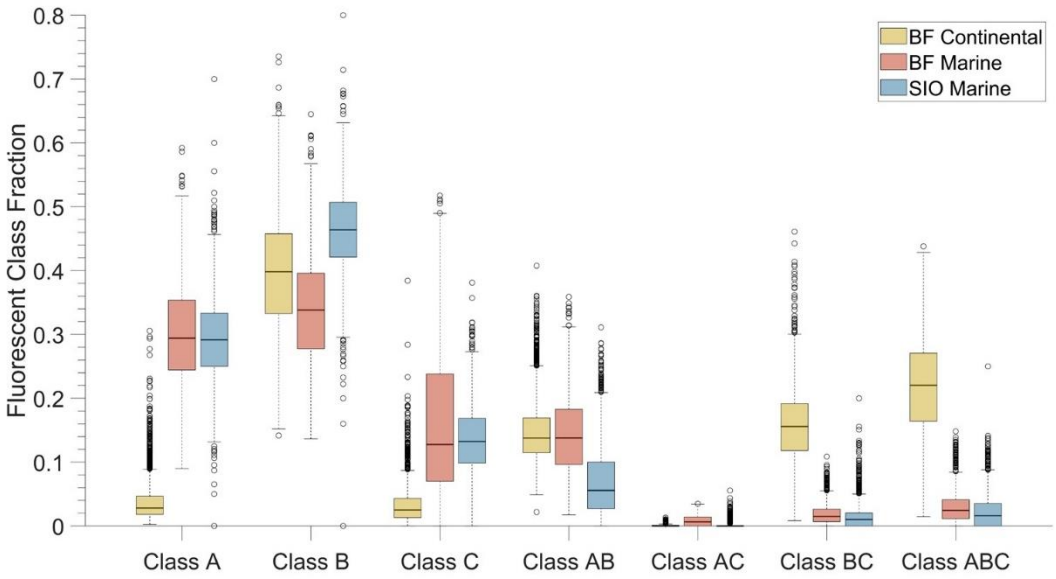

Figure 5.6. Box plots of the fluorescent class fraction of each fluorescent class for the 3 different air masses: BF Continental (yellow), BF Marine (red), and SIO Marine (blue). Each boxplot contains the median fluorescent class fraction (black line) along with the interquartile range (box), the 5th and 95th percentile (whiskers) and the outliers (open circles).

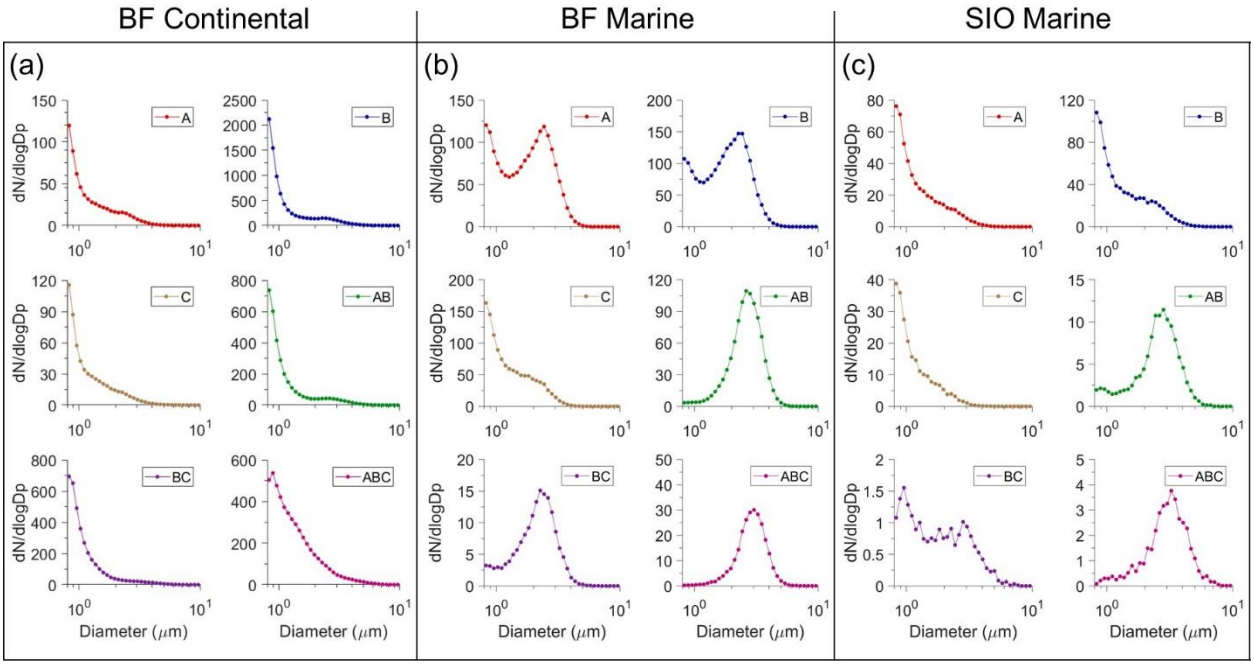

Figure 5.7. Size distributions of the different air masses (a) BF Continental, (b) BF Marine, and (c) SIO Marine. Shown are the single-particle size distributions of the concentration (#/L) normalized to the bin width for the fluorescence classes comprising each air mass.

5.8 Supplement

For the correction method described by Weingartner et al. (2003), two calibration factors are introduced, C and $R(ATN)$, to account for the multiple scattering effect of the fiber filters and the filter aerosol loading effect, respectively. The correction factor, C, was set to 2.14 based on the derivation by Weingartner et al. (2003) on fresh soot particles and due to the quartz fiber filter used in this study (Drinovec et al., 2015). $R(ATN)$ is described by Eq. 5.5:

$$R(ATN) = \left(\frac{1}{f} - 1\right) \cdot \left(\frac{\ln(ATN) - \ln(10)}{\ln(50) - \ln(10)}\right) + 1 \qquad [5.5]$$

Where the parameter, f, accounts for the error when the loading effect is disregarded. To derive f, we minimized the difference between the ratio of b_{ATN} values before and after the filter change (Sandradewi et al., 2008). For statistical reasons, the average of three b_{ATN} values on each side of the filter change were used in the derivation. The median f values were then fit with a linear regression and the linear f values were used to derive $R(ATN)$. The linear f values for each wavelength were: $f_{370} = 1.423$, $f_{470} = 1.368$, $f_{520} = 1.342$, $f_{590} = 1.304$, $f_{660} = 1.267$, $f_{880} = 1.150$, $f_{950} = 1.112$. These f values follow a common trend of lower values for longer wavelengths (Sandradewi et al., 2008; Drinovec et al., 2015; Resquin et al., 2018). For this study, the f values were derived from the filter changes that occurred at the Border Field sampling location because, only at this location, the ATN reach the maximum value (125) and a scheduled filter spot change occurred. These values were applied to the data collected at SIO to properly account for the loading effect.

With the correction factors, C and $R(ATN)$, the attenuation coefficient can be converted to the absorption coefficient, b_{abs}, according to Eq. 5.6:

$$b_{abs} = \frac{b_{ATN}}{C * R(ATN)} \qquad [5.6]$$

Additionally, the corrected equivalent black carbon mass concentration (EBC) can be calculated from the non-corrected equivalent black carbon mass concentration (EBC_{NC}) recorded by the aethalometer using the Eq. 5.7:

$$EBC = \frac{EBC_{NC}}{R(ATN)} = \frac{b_{abs}}{\sigma_{abs}} \; where \; \sigma_{abs} = \frac{\sigma_{ATN}}{C} \qquad [5.7]$$

5.9 Supplemental Figures

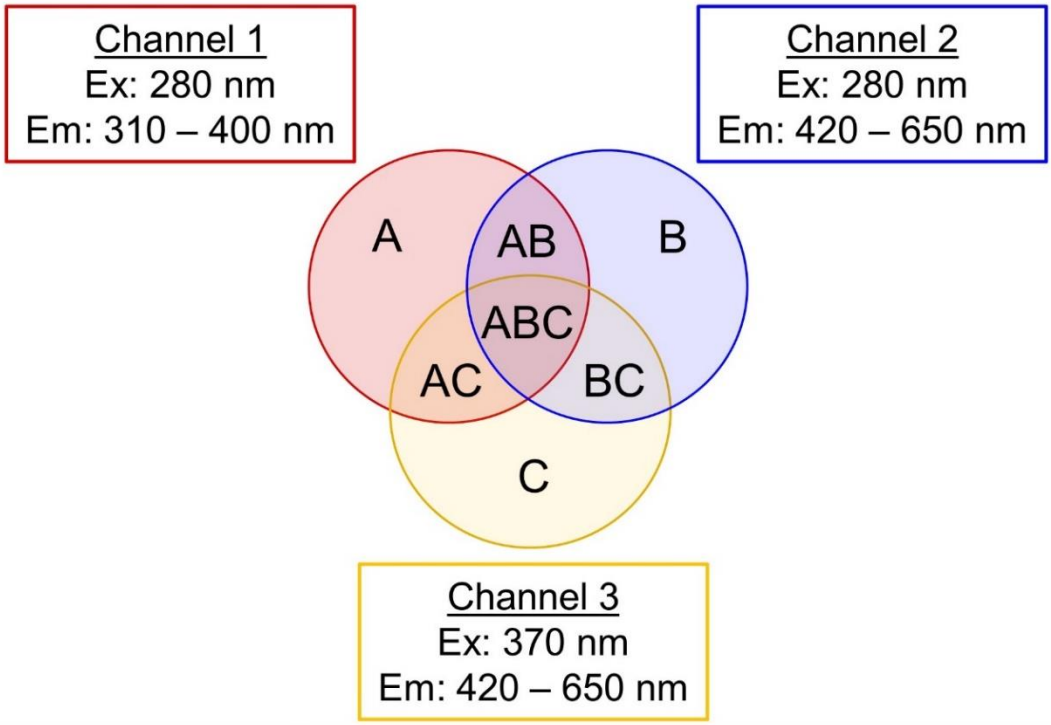

Fluorescence Class	Fluorescence Class Definition
A	Fluorescence in channel 1 but **not** channels 2 or 3
B	Fluorescence in channel 2 but **not** channels 1 or 3
C	Fluorescence in channel 3 but **not** channels 1 or 2
AB	Fluorescence in channels 1 **and** 2 but **not** channel 3
AC	Fluorescence in channels 1 **and** 3 but **not** channel 2
BC	Fluorescence in channels 2 **and** 3 but **not** channel 1
ABC	Fluorescence in channels 1, 2 **and** 3

Figure 5.8. Diagram of the different fluorescence classes defined by Perring et al. (2015) and the associated WIBS channels with excitation (Ex) and emission (Em) wavelengths. Included is a written description of each class and the fluorescence channels that comprise it.

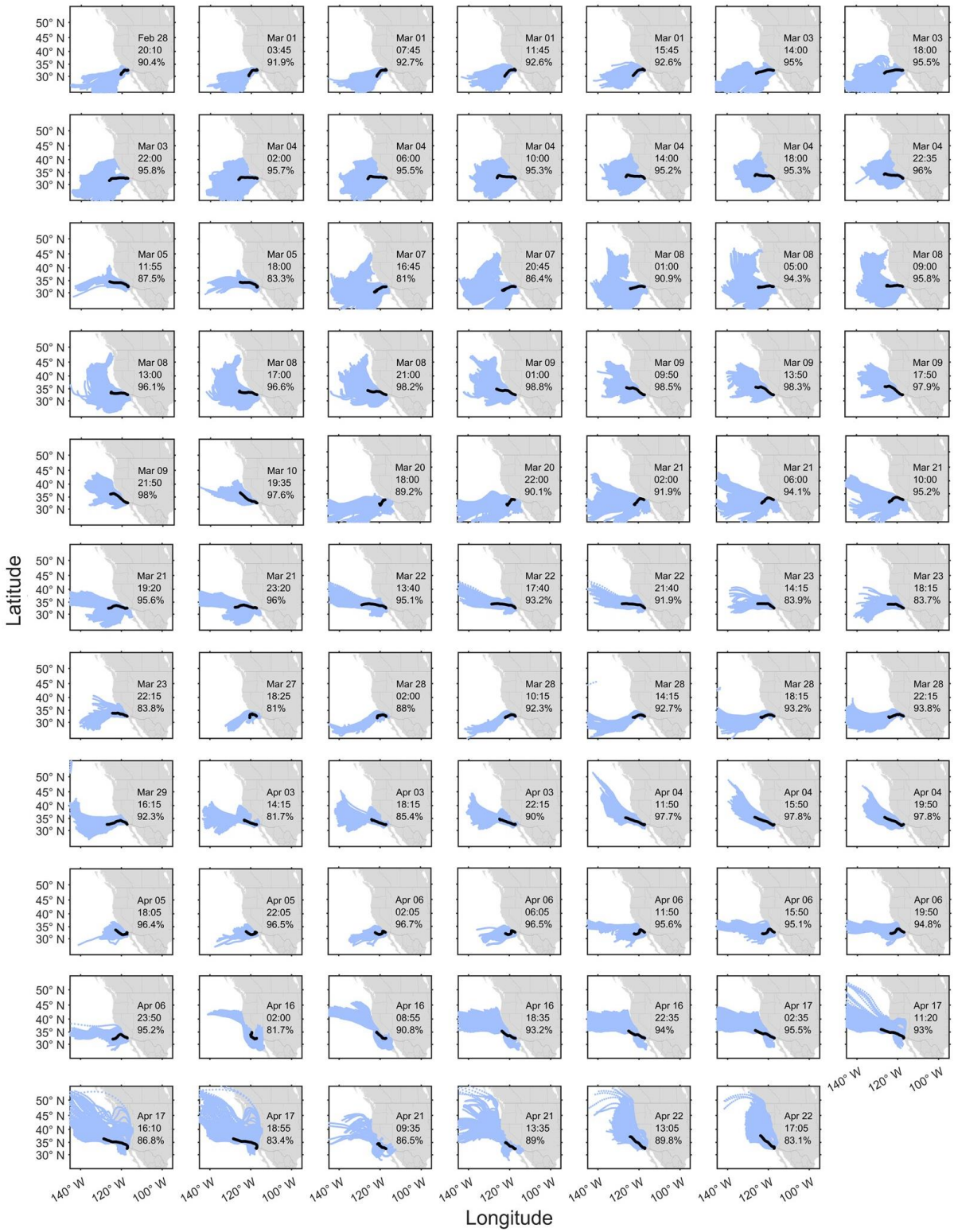

Figure 5.9. 72-hour back trajectories at BF showing the "air parcel" positions in blue and the mean positions in black. Included in each plot is the end date and time as well as the percentage of "air parcels" with coordinates over the ocean.

Figure 5.10. 72-hour back trajectories at SIO showing the "air parcel" positions in blue and the mean positions in black. Included in each plot is the end date and time as well as the percentage of "air parcels" with coordinates over the ocean.

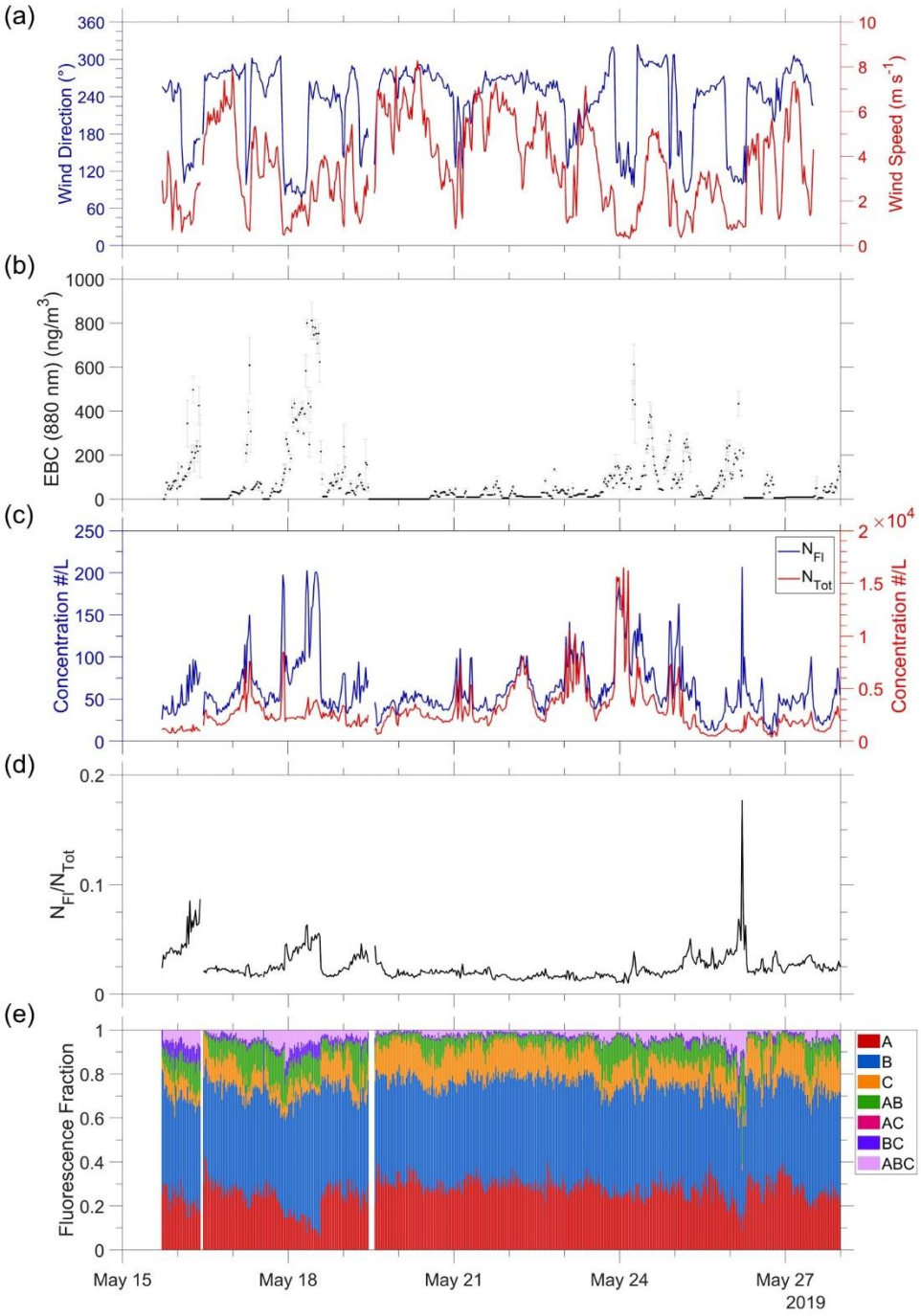

Figure 5.11. Timeseries of the sampling at the SIO location. Measurements include (a) 6-hour averages of wind speed (red) and wind direction (blue), and 30-minute averages of the following: (b) EBC concentration; (c) fluorescent particle (blue) and total particle (red) concentrations; (d) fluorescent fraction; (e) fluorescent class fraction.

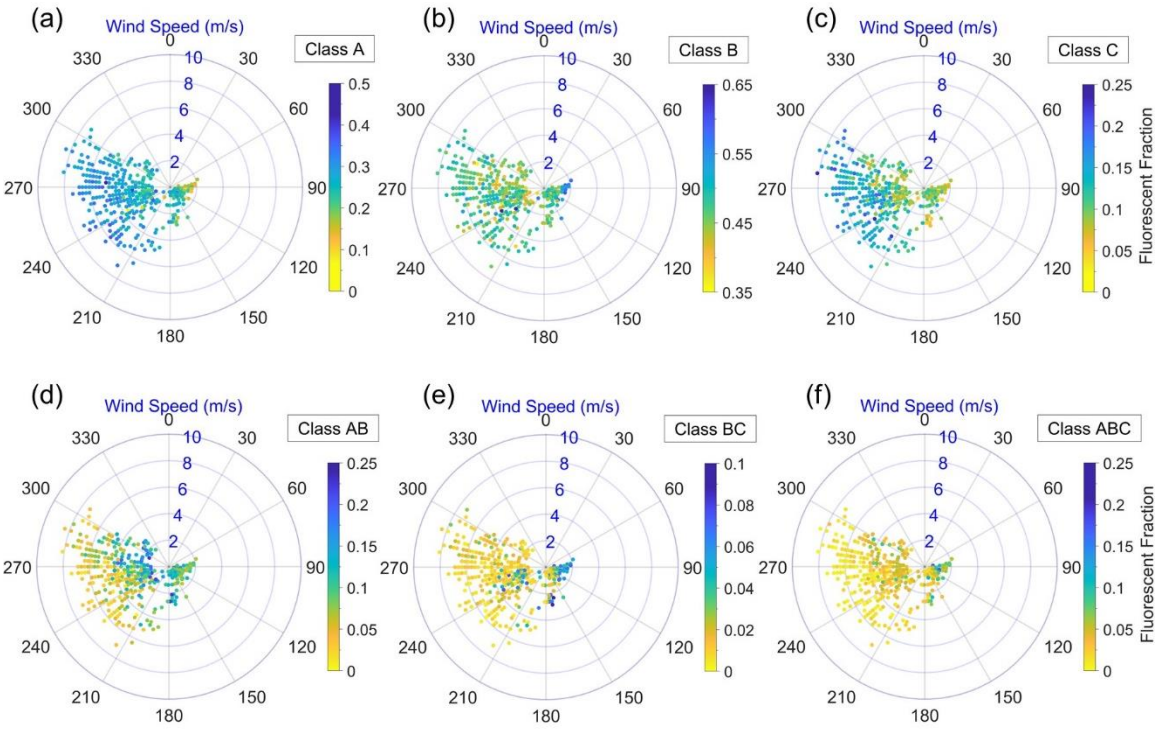

Figure 5.12. Polar plots of the fraction of fluorescent particles belonging to the fluorescent classes (a) A, (b) B, (c) C, (d) AB, (e) BC, (f) ABC over 30-minute time periods measured at the SIO location. The fluorescent class fraction is plotted as a function of wind direction (°; 0° N) and wind speed (blue concentric circles).

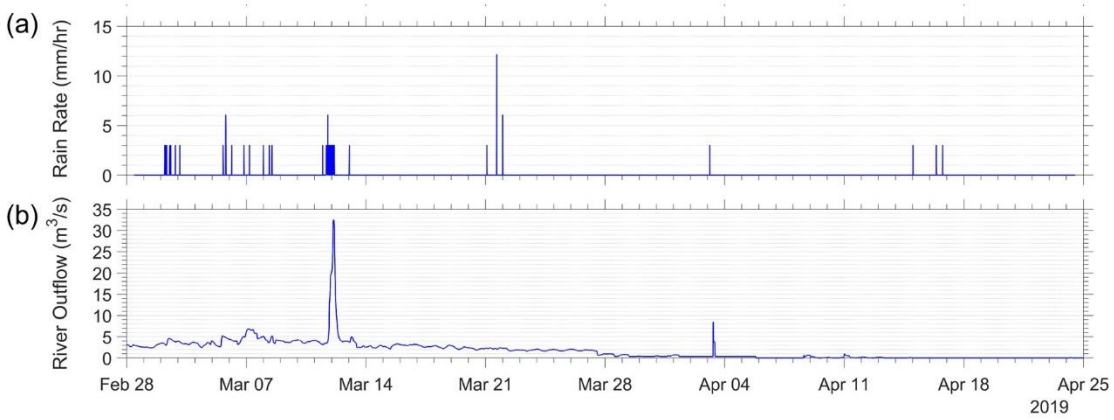

Figure 5.13. (a) Rain rate measured with the meteorological station at the BF sampling location. (b) Outflow of the Tijuana River at 5-minute intervals throughout the sampling period at BF.

5.10 Supplemental Tables

Table 5.1. Pearson correlation coefficients between aerosol measurements of BF Continental to meteorological variables. Bolded coefficients indicate significance with a *p-value* < 0.05.

Fluorescent Class Fraction:	RH (%)	Temperature (°C)	Wind Speed (m/s)
A	**0.223912575**	**0.311994125**	**-0.110479226**
B	**-0.173366169**	**0.571428372**	**-0.255889688**
C	-0.001281176	**-0.101035872**	0.037585335
AB	0.025755285	**0.163704889**	**0.075290978**
AC	0.00628246	**0.150603853**	**0.083386951**
BC	**-0.062812881**	**-0.451318622**	**0.080255004**
ABC	**0.144361285**	**-0.603519977**	**0.245300181**
Particle Characteristics:			
Diameter	**-0.445490097**	**0.34558695**	**-0.232120949**
AF	**-0.617357357**	-0.02270965	-0.008913887
Ch1 Intensity	**0.155155387**	**-0.283820812**	**0.164806786**
Ch2 Intensity	**0.208164904**	**-0.477132226**	**0.129379693**
Ch3 Intensity	**0.166244282**	**-0.502219682**	**0.135740938**
N_{Fl}	**-0.12187962**	**-0.2780541**	0.033443887
N_{Tot}	**0.107435067**	**0.240577254**	**-0.216368089**
Fluorescent Fraction	**-0.19064348**	**-0.414006406**	**0.232467077**

Table 5.2. Pearson correlation coefficients between aerosol measurements of BF Marine to meteorological variables and the Tijuana River outflow. Bolded coefficients indicate significance with a *p-value* < 0.05.

Fluorescent Class Fraction:	RH (%)	Temperature (°C)	Wind Speed (m/s)	River Flow (m^3/s)
A	**0.549479103**	**0.119974546**	**-0.097014293**	**-0.501663588**
B	**-0.219317609**	**0.505153427**	0.009455337	**-0.613641602**
C	**0.053664436**	**-0.599001885**	**0.149237911**	**0.792289823**
AB	**-0.253567036**	**0.363868505**	**-0.168885531**	**-0.284805776**
AC	0.023316564	**-0.436595212**	0.02784487	**0.609486087**
BC	**-0.361649972**	**-0.185791701**	**0.053352776**	**0.482947881**
ABC	**-0.405430559**	**-0.082892002**	-0.010134003	**0.37813505**
Particle Characteristics:				
Diameter	**-0.279801589**	**0.453644969**	**-0.233825173**	**-0.181103767**
AF	**-0.56597111**	**0.7037943**	0.039876038	**-0.199092139**
Ch1 Intensity	**-0.081895874**	**0.260679588**	-0.016066367	**-0.122861636**
Ch2 Intensity	**-0.385687661**	**0.364667482**	**-0.051322047**	**-0.214071161**
Ch3 Intensity	**-0.108778288**	**-0.379425361**	**0.068410721**	**0.506387045**
N_{Fl}	0.015237483	**-0.455643378**	**-0.121222909**	**0.632509173**
N_{Tot}	**0.398049263**	**-0.388097457**	**-0.258863523**	**0.151175279**
Fluorescent Fraction	**-0.314748191**	**-0.287581998**	0.041654959	**0.573153927**

Table 5.3. Pearson correlation coefficients between aerosol measurements of SIO Marine to meteorological variables. Bolded coefficients indicate significance with a *p-value* < 0.05.

Fluorescent Class Fraction:	RH (%)	Temperature (°C)	Wind Speed (m/s)
A	**0.218784389**	**-0.158436023**	**0.196266965**
B	0.04281251	**-0.130624714**	**0.169287614**
C	**0.138054874**	**-0.353811754**	**0.286103546**
AB	**-0.348640707**	**0.433512978**	**-0.452727373**
AC	-0.011991063	-0.038631721	0.012121215
BC	-0.040801878	**0.281738755**	**-0.164991799**
ABC	**-0.226546584**	**0.381950923**	**-0.403703419**
Particle Characteristics:			
Diameter	**-0.405559326**	**0.383284188**	**-0.414390315**
AF	**-0.515197183**	**0.490008229**	**-0.271378792**
Ch1 Intensity	**-0.055537266**	**0.092788788**	**-0.131864028**
Ch2 Intensity	**-0.160701215**	**0.495791818**	**-0.398720565**
Ch3 Intensity	0.009722235	**0.176600765**	**-0.199005323**
N_{Fl}	**0.209905448**	**-0.25037771**	**-0.093107609**
N_{Tot}	**0.308830953**	**-0.311586969**	0.030396647
Fluorescent Fraction	**-0.16392928**	**0.281403046**	**-0.35089682**

5.11 References

Aller, J. Y., Kuznetsova, M. R., Jahns, C. J., and Kemp, P. F.: The sea surface microlayer as a source of viral and bacterial enrichment in marine aerosols, J. Aerosol Sci., 36, 801–812, https://doi.org/10.1016/j.jaerosci.2004.10.012, 2005.

Bauer, H., Fuerhacker, M., Zibuschka, F., Schmid, H., and Puxbaum, H.: Bacteria and fungi in aerosols generated by two different types of wastewater treatment plants, Water Res., 36, 3965–3970, https://doi.org/10.1016/S0043-1354(02)00121-5, 2002.

Baylor, E. R., Baylor, M. B., Blanchard, D. C., Syzdek, L. D., and Appel, C.: Virus Transfer from Surf to Wind, Science (80-.)., 198, 575–580, 1977.

Bond, T. C., Doherty, S. J., Fahey, D. W., Forster, P. M., Berntsen, T., Deangelo, B. J., Flanner, M. G., Ghan, S., Kärcher, B., Koch, D., Kinne, S., Kondo, Y., Quinn, P. K., Sarofim, M. C., Schultz, M. G., Schulz, M., Venkataraman, C., Zhang, H., Zhang, S., Bellouin, N., Guttikunda, S. K., Hopke, P. K., Jacobson, M. Z., Kaiser, J. W., Klimont, Z., Lohmann, U., Schwarz, J. P., Shindell, D., Storelvmo, T., Warren, S. G., and Zender, C. S.: Bounding the role of black carbon in the climate system: A scientific assessment, J. Geophys. Res. Atmos., 118, 5380–5552, https://doi.org/10.1002/jgrd.50171, 2013.

Calvo, A. I., Baumgardner, D., Castro, A., Fernández-González, D., Vega-Maray, A. M., Valencia-Barrera, R. M., Oduber, F., Blanco-Alegre, C., and Fraile, R.: Daily behavior of urban Fluorescing Aerosol Particles in northwest Spain, Atmos. Environ., 184, 262–277, https://doi.org/10.1016/j.atmosenv.2018.04.027, 2018.

Collaud Coen, M., Weingartner, E., Apituley, A., Ceburnis, D., Fierz-Schmidhauser, R., Flentje, H., Henzing, J. S., Jennings, S. G., Moerman, M., Petzold, A., Schmid, O., and Baltensperger, U.: Minimizing light absorption measurement artifacts of the Aethalometer: Evaluation of five correction algorithms, Atmos. Meas. Tech., 3, 457–474, https://doi.org/10.5194/amt-3-457-2010, 2010.

Crawford, I., Gallagher, M. W., Bower, K. N., Choularton, T. W., Flynn, M. J., Ruske, S., Listowski, C., Brough, N., Lachlan-Cope, T., Fleming, Z. L., Foot, V. E., and Stanley, W. R.: Real-time detection of airborne fluorescent bioparticles in Antarctica, Atmos. Chem. Phys., 17, 14291–14307, https://doi.org/10.5194/acp-17-14291-2017, 2017.

Dancey, C. P. and Reidy, J.: Statistics Without Maths for Psychology, 5th ed., Prentice Hall, 2011.

Després, V., Huffman, Ja., Burrows, S. M., Hoose, C., Safatov, A., Buryak, G., Fröhlich-Nowoisky, J., Elbert, W., Andreae, M., Pöschl, U., Jaenicke, R., Huffman, A., Viviane Després S, B. R., Alex Huffman, J., Safatov, A. S., Fro, J., and Andreae, M. O.: Primary biological aerosol particles in the atmosphere: a review, https://doi.org/10.3402/tellusb.v64i0.15598, 2012.

Douwes, J., Thorne, P., Pearce, N., and Heederik, D.: Bioaerosol Health Effects and Exposure

Assessment: Progress and Prospects, Ann. Occup. Hyg., 47, 187–200, https://doi.org/10.1093/ANNHYG/MEG032, 2003.

Drinovec, L., Močnik, G., Zotter, P., Prévôt, A. S. H., Ruckstuhl, C., Coz, E., Rupakheti, M., Sciare, J., Müller, T., Wiedensohler, A., and Hansen, A. D. A.: The "dual-spot" Aethalometer: An improved measurement of aerosol black carbon with real-time loading compensation, Atmos. Meas. Tech., 8, 1965–1979, https://doi.org/10.5194/amt-8-1965-2015, 2015.

Feddersen, F., Boehm, A. B., Giddings, S. N., Wu, X., and Liden, D.: Modeling Untreated Wastewater Evolution and Swimmer Illness for Four Wastewater Infrastructure Scenarios in the San Diego-Tijuana (US/MX) Border Region, 5, https://doi.org/10.1029/2021GH000490, 2021.

Fennelly, M., Sewell, G., Prentice, M., O'Connor, D., and Sodeau, J.: Review: The Use of Real-Time Fluorescence Instrumentation to Monitor Ambient Primary Biological Aerosol Particles (PBAP), Atmosphere (Basel)., 9, https://doi.org/10.3390/atmos9010001, 2018.

Fialho, P., Hansen, A. D. A., and Honrath, R. E.: Absorption coefficients by aerosols in remote areas: A new approach to decouple dust and black carbon absorption coefficients using seven-wavelength Aethalometer data, J. Aerosol Sci., 36, 267–282, https://doi.org/10.1016/j.jaerosci.2004.09.004, 2005.

Forde, E., Gallagher, M., Walker, M., Foot, V., Attwood, A., Granger, G., Sarda-Estève, R., Stanley, W., Kaye, P., and Topping, D.: Intercomparison of Multiple UV-LIF Spectrometers Using the Aerosol Challenge Simulator, Atmos. 2019, Vol. 10, Page 797, 10, 797, https://doi.org/10.3390/ATMOS10120797, 2019.

Fröhlich-Nowoisky, J., Kampf, C. J., Weber, B., Huffman, J. A., Pöhlker, C., Andreae, M. O., Lang-Yona, N., Burrows, S. M., Gunthe, S. S., Elbert, W., Su, H., Hoor, P., Thines, E., Hoffmann, T., Després, V. R., and Pöschl, U.: Bioaerosols in the Earth system: Climate, health, and ecosystem interactions, Atmos. Res., 182, 346–376, https://doi.org/10.1016/j.atmosres.2016.07.018, 2016.

Gabey, A. M., Gallagher, M. W., Whitehead, J., Dorsey, J. R., Kaye, P. H., and Stanley, W. R.: Measurements and comparison of primary biological aerosol above and below a tropical forest canopy using a dual channel fluorescence spectrometer, Atmos. Chem. Phys. Atmos. Chem. Phys., 10, 4453–4466, https://doi.org/10.5194/acp-10-4453-2010, 2010.

Gabey, A. M., Stanley, W. R., Gallagher, M. W., and Kaye, P. H.: The fluorescence properties of aerosol larger than 0.8 μm in urban and tropical rainforest locations, Atmos. Chem. Phys., 11, 5491–5504, https://doi.org/10.5194/acp-11-5491-2011, 2011.

Gersberg, R. M., Rose, M. A., Robles-Sikisaka, R., and Dhar, A. K.: Quantitative detection of hepatitis A virus and enteroviruses near the United States-Mexico border and correlation with levels of fecal indicator bacteria, Appl. Environ. Microbiol., 72, 7438–7444,

https://doi.org/10.1128/AEM.01024-06, 2006.

Gosselin, M. I., Rathnayake, C. M., Crawford, I., Pöhlker, C., Fröhlich-Nowoisky, J., Schmer, B., Després, V. R., Engling, G., Gallagher, M., Stone, E., Pöschl, U., and Huffman, J. A.: Fluorescent bioaerosol particle, molecular tracer, and fungal spore concentrations during dry and rainy periods in a semi-arid forest, Atmos. Chem. Phys, 16, 15165–15184, https://doi.org/10.5194/acp-16-15165-2016, 2016.

Graham, K. E., Prussin, A. J., Marr, L. C., Sassoubre, L. M., and Boehm, A. B.: Microbial community structure of sea spray aerosols at three California beaches, FEMS Microbiol. Ecol., 94, 5, https://doi.org/10.1093/femsec/fiy005, 2018.

Griffin, D. W., Donaldson, K. A., Paul, J. H., and Rose, J. B.: Pathogenic human viruses in coastal waters, Clin. Microbiol. Rev., 16, 129–143, https://doi.org/10.1128/CMR.16.1.129-143.2003/FORMAT/EPUB, 2003.

Hagler, G. S. W., Yelverton, T. L. B., Vedantham, R., Hansen, A. D. A., and Turner, J. R.: Post-processing Method to Reduce Noise while Preserving High Time Resolution in Aethalometer Real-time Black Carbon Data, Aerosol Air Qual. Res., 11, 539–546, https://doi.org/10.4209/aaqr.2011.05.0055, 2011.

Hansen, A. D. A.: The Aethalometer--User Manual, Magee Sci. Company, California, USA, 2005.

Hansen, A. D. A., Rosen, H., and Novakov, T.: The aethalometer - An instrument for the real-time measurement of optical absorption by aerosol particles, Sci. Total Environ., 36, 191–196, https://doi.org/10.1016/0048-9697(84)90265-1, 1984.

Healy, D. A., O'Connor, D. J., Burke, A. M., and Sodeau, J. R.: A laboratory assessment of the Waveband Integrated Bioaerosol Sensor (WIBS-4) using individual samples of pollen and fungal spore material, Atmos. Environ., 60, 534–543, https://doi.org/10.1016/j.atmosenv.2012.06.052, 2012a.

Healy, D. A., O'Connor, D. J., and Sodeau, J. R.: Measurement of the particle counting efficiency of the "Waveband Integrated Bioaerosol Sensor" model number 4 (WIBS-4), J. Aerosol Sci., 47, 94–99, https://doi.org/10.1016/j.jaerosci.2012.01.003, 2012b.

Hernandez, M., Perring, A. E., McCabe, K., Kok, G., Granger, G., and Baumgardner, D.: Chamber catalogues of optical and fluorescent signatures distinguish bioaerosol classes, Atmos. Meas. Tech., 9, 3283–3292, https://doi.org/10.5194/amt-9-3283-2016, 2016.

Huffman, J. A., Sinha, B., Garland, R. M., Snee-Pollmann, A., Gunthe, S. S., Artaxo, P., Martin, S. T., Andreae, M. O., and Pöschl, U.: Size distributions and temporal variations of biological aerosol particles in the Amazon rainforest characterized by microscopy and real-time UV-APS fluorescence techniques during AMAZE-08, Atmos. Chem. Phys. Atmos. Chem. Phys., 12, 11997–12019, https://doi.org/10.5194/acp-12-11997-2012, 2012.

Huffman, J. A., Prenni, A. J., Demott, P. J., Pöhlker, C., Mason, R. H., Robinson, N. H., Fröhlich-Nowoisky, J., Tobo, Y., Després, V. R., Garcia, E., Gochis, D. J., Harris, E., Müller-Germann, I., Ruzene, C., Schmer, B., Sinha, B., Day, D. A., Andreae, M. O., Jimenez, J. L., Gallagher, M., Kreidenweis, S. M., Bertram, A. K., and Pöschl, U.: High concentrations of biological aerosol particles and ice nuclei during and after rain, Atmos. Chem. Phys., 13, 6151–6164, https://doi.org/10.5194/acp-13-6151-2013, 2013.

Huffman, J. A., Perring, A. E., Savage, N. J., Clot, B., Crouzy, B., Tummon, F., Shoshanim, O., Damit, B., Schneider, J., Sivaprakasam, V., Zawadowicz, M. A., Crawford, I., Gallagher, M., Topping, D., Doughty, D. C., Hill, S. C., and Pan, Y.: Real-time sensing of bioaerosols: Review and current perspectives, https://doi.org/10.1080/02786826.2019.1664724, 3 May 2020.

Hughes, D. D., Mampage, C. B. A., Jones, L. M., Liu, Z., and Stone, E. A.: Characterization of Atmospheric Pollen Fragments during Springtime Thunderstorms, Environ. Sci. Technol. Lett., 7, 409–414, https://doi.org/10.1021/acs.estlett.0c00213, 2020.

Jones, A. M. and Harrison, R. M.: The effects of meteorological factors on atmospheric bioaerosol concentrations - A review, Sci. Total Environ., 326, 151–180, https://doi.org/10.1016/j.scitotenv.2003.11.021, 2004.

Kawana, K., Matsumoto, K., Taketani, F., Miyakawa, T., and Kanaya, Y.: Fluorescent biological aerosol particles over the central Pacific Ocean: covariation with ocean surface biological activity indicators, Atmos. Chem. Phys., 21, 15969–15983, https://doi.org/10.5194/acp-21-15969-2021, 2021.

Kaye, P. H., Aptowicz, K., Chang, R. K., Foot, V., and Videen, G.: Angularly Resolved Elastic Scattering From Airborne Particles, in: Optics of Biological Particles, Springer Netherlands, 31–61, https://doi.org/10.1007/978-1-4020-5502-7_3, 2007.

Lewis, E. R. and Schwartz, S. E.: Sea salt aerosol production: Mechanisms, methods, measurements and models—A critical review, American Geophysical Union, Washington, D. C., 1–408 pp., https://doi.org/10.1029/152GM01, 2004.

Lieberherr, G., Auderset, K., Calpini, B., Clot, B., Crouzy, B., Gysel-Beer, M., Konzelmann, T., Manzano, J., Mihajlovic, A., Moallemi, A., O'connor, D., Sikoparija, B., Sauvageat, E., Tummon, F., and Vasilatou, K.: Assessment of real-time bioaerosol particle counters using reference chamber experiments, Atmos. Meas. Tech., 14, 7693–7706, https://doi.org/10.5194/amt-14-7693-2021, 2021.

Michaud, J. M., Thompson, L. R., Kaul, D., Espinoza, J. L., Richter, R. A., Xu, Z. Z., Lee, C., Pham, K. M., Beall, C. M., Malfatti, F., Azam, F., Knight, R., Burkart, M. D., Dupont, C. L., and Prather, K. A.: Taxon-specific aerosolization of bacteria and viruses in an experimental ocean-atmosphere mesocosm, Nat. Commun., 9, 2017, https://doi.org/10.1038/s41467-018-04409-z, 2018.

Moallemi, A., Landwehr, S., Robinson, C., and Simó, R.: Sources, Occurrence and Characteristics of Fluorescent Biological Aerosol Particles Measured Over the Pristine Southern Ocean, J. Geophys. Res., 2021.

O'Connor, D. J., Healy, D. A., and Sodeau, J. R.: A 1-month online monitoring campaign of ambient fungal spore concentrations in the harbour region of Cork, Ireland, Aerobiologia (Bologna)., 31, 295–314, https://doi.org/10.1007/s10453-015-9365-7, 2015.

Pendergraft, M. A., Grimes, D. J., Giddings, S. N., Feddersen, F., Beall, C. M., Lee, C., Santander, M. V., and Prather, K. A.: Airborne transmission pathway for coastal water pollution, PeerJ, 9, https://doi.org/10.7717/peerj.11358, 2021.

Perring, A. E., Schwarz, J. P., Baumgardner, D., Hernandez, M. T., Spracklen, D. V., Heald, C. L., Gao, R. S., Kok, G., McMeeking, G. R., McQuaid, J. B., and Fahey, D. W.: Airborne observations of regional variation in fluorescent aerosol across the United States, J. Geophys. Res. Atmos., 120, 1153–1170, https://doi.org/10.1002/2014JD022495, 2015.

Petzold, A., Ogren, J. A., Fiebig, M., Laj, P., Li, S. M., Baltensperger, U., Holzer-Popp, T., Kinne, S., Pappalardo, G., Sugimoto, N., Wehrli, C., Wiedensohler, A., and Zhang, X. Y.: Recommendations for reporting black carbon measurements, Atmos. Chem. Phys., 13, 8365–8379, https://doi.org/10.5194/acp-13-8365-2013, 2013.

Pöhlker, C., Huffman, J. A., and Pöschl, U.: Autofluorescence of atmospheric bioaerosols – fluorescent biomolecules and potential interferences, Atmos. Meas. Tech, 5, 37–71, https://doi.org/10.5194/amt-5-37-2012, 2012.

Pratt, K. A., Demott, P. J., French, J. R., Wang, Z., Westphal, D. L., Heymsfield, A. J., Twohy, C. H., Prenni, A. J., and Prather, K. A.: In situ detection of biological particles in cloud ice-crystals, Nat. Geosci. 2009 26, 2, 398–401, https://doi.org/10.1038/ngeo521, 2009.

Rastelli, E., Corinaldesi, C., Dell'anno, A., Lo Martire, M., Greco, S., Cristina Facchini, M., Rinaldi, M., O'Dowd, C., Ceburnis, D., and Danovaro, R.: Transfer of labile organic matter and microbes from the ocean surface to the marine aerosol: An experimental approach, Sci. Rep., 7, https://doi.org/10.1038/s41598-017-10563-z, 2017.

Resquin, M. D., Santágata, D., Gallardo, L., Gómez, D., Rössler, C., and Dawidowski, L.: Local and remote black carbon sources in the Metropolitan Area of Buenos Aires, Atmos. Environ., 182, 105–114, https://doi.org/10.1016/j.atmosenv.2018.03.018, 2018.

Sandradewi, J., Prévôt, A. S. H., Weingartner, E., Schmidhauser, R., Gysel, M., and Baltensperger, U.: A study of wood burning and traffic aerosols in an Alpine valley using a multi-wavelength Aethalometer, Atmos. Environ., 42, 101–112, https://doi.org/10.1016/j.atmosenv.2007.09.034, 2008.

Santander, M. V., Mitts, B. A., Pendergraft, M. A., Dinasquet, J., Lee, C., Moore, A. N., Cancelada, L. B., Kimble, K. A., Malfatti, F., and Prather, K. A.: Tandem Fluorescence

Measurements of Organic Matter and Bacteria Released in Sea Spray Aerosols, Environ. Sci. Technol., 55, 5171–5179, https://doi.org/10.1021/ACS.EST.0C05493/SUPPL_FILE/ES0C05493_SI_001.PDF, 2021.

Santarpia, J. L.: Bioaerosols in the environment: Populations, measurement and processes, in: Issues in Toxicology, The Royal Society of Chemistry, 219–247, https://doi.org/10.1039/9781849735940-00219, 2016.

Savage, N. J., Krentz, C. E., Könemann, T., Han, T. T., Mainelis, G., Pöhlker, C., and Alex Huffman, J.: Systematic characterization and fluorescence threshold strategies for the wideband integrated bioaerosol sensor (WIBS) using size-resolved biological and interfering particles, Atmos. Meas. Tech., 10, 4279–4302, https://doi.org/10.5194/amt-10-4279-2017, 2017.

Shaffer, B. T. and Lighthart, B.: Survey of culturable airborne bacteria at four diverse locations in Oregon: Urban, rural, forest, and coastal, Microb. Ecol., 34, 167–177, https://doi.org/10.1007/s002489900046, 1997.

Stohl, A., Hittenberger, M., and Wotawa, G.: Validation of the lagrangian particle dispersion model FLEXPART against large-scale tracer experiment data, Atmos. Environ., 32, 4245–4264, https://doi.org/10.1016/S1352-2310(98)00184-8, 1998.

Stohl, A., Forster, C., Frank, A., Seibert, P., and Wotawa, G.: Technical note: The Lagrangian particle dispersion model FLEXPART version 6.2, Atmos. Chem. Phys., 5, 2461–2474, https://doi.org/10.5194/ACP-5-2461-2005, 2005.

Tian, J. han, Yan, C., Nasir, Z. A., Alcega, S. G., Tyrrel, S., and Coulon, F.: Real time detection and characterisation of bioaerosol emissions from wastewater treatment plants, Sci. Total Environ., 721, 137629, https://doi.org/10.1016/j.scitotenv.2020.137629, 2020.

Wei, K., Zou, Z., Zheng, Y., Li, J., Shen, F., Wu, C. yu, Wu, Y., Hu, M., and Yao, M.: Ambient bioaerosol particle dynamics observed during haze and sunny days in Beijing, Sci. Total Environ., 550, 751–759, https://doi.org/10.1016/J.SCITOTENV.2016.01.137, 2016.

Weingartner, E., Saathoff, H., Schnaiter, M., Streit, N., Bitnar, B., and Baltensperger, U.: Absorption of light by soot particles: Determination of the absorption coefficient by means of aethalometers, J. Aerosol Sci., 34, 1445–1463, https://doi.org/10.1016/S0021-8502(03)00359-8, 2003.

Yu, X., Wang, Z., Zhang, M., Kuhn, U., Xie, Z., Cheng, Y., Pöschl, U., and Su, H.: Ambient measurement of fluorescent aerosol particles with a WIBS in the Yangtze River Delta of China: Potential impacts of combustion-related aerosol particles, Atmos. Chem. Phys., 16, 11337–11348, https://doi.org/10.5194/acp-16-11337-2016, 2016.

Yue, S., Ren, H., Fan, S., Sun, Y., Wang, Z., and Fu, P.: Springtime precipitation effects on the

abundance of fluorescent biological aerosol particles and HULIS in Beijing, Sci. Rep., 6, https://doi.org/10.1038/srep29618, 2016.

Yue, S., Ren, H., Fan, S., Wei, L., Zhao, J., Bao, M., Hou, S., Zhan, J., Zhao, W., Ren, L., Kang, M., Li, L., Zhang, Y., Sun, Y., Wang, Z., and Fu, P.: High Abundance of Fluorescent Biological Aerosol Particles in Winter in Beijing, China, ACS Earth Space Chem., 1, 493-502, https://doi.org/10.1021/acsearthspacechem.7b00062, 2017.

Yue, S., Ren, L., Song, T., Li, L., Xie, Q., Li, W., Kang, M., Zhao, W., Wei, L., Ren, H., Sun, Y., Wang, Z., Ellam, R. M., Liu, C. Q., Kawamura, K., and Fu, P.: Abundance and Diurnal Trends of Fluorescent Bioaerosols in the Troposphere over Mt. Tai, China, Spring, J. Geophys. Res. Atmos., 124, 4158–4173, https://doi.org/10.1029/2018JD029486, 2019.

Zimmer-Faust, A. G., Steele, J. A., Xiong, X., Staley, C., Griffith, M., Sadowsky, M. J., Diaz, M., and Griffith, J. F.: A Combined Digital PCR and Next Generation DNA-Sequencing Based Approach for Tracking Nearshore Pollutant Dynamics Along the Southwest United States/Mexico Border, Front. Microbiol., 12, https://doi.org/10.3389/fmicb.2021.674214, 2021.

Chapter 6. Optimization and Application of a Condensation Matrix-Assisted Aerosol Time-of-Flight Mass Spectrometer

6.1 Abstract

Aerosol time-of-flight mass spectrometry (ATOFMS) is a state-of-the-art, online method for measuring the size and chemical composition of single particles in real time. Historically, ATOFMS measurements have been limited to particles with diameters greater than ~100 nm due to the constraints of optically detecting incoming particles. However, recent development of a condensation Matrix Assisted Laser Desorption Ionization (cMALDI) system coupled with ATOFMS has enabled the growth of sub-100 nm analyte particles into the size range detected with ATOFMS. Here, we characterize several MALDI matrices using the condensation matrix-assisted ATOFMS (cMA-ATOFMS) system and optimize detection of sub-100 nm particles by varying laser intensities and matrix-to-analyte ratios. Secondary organic aerosol (SOA) particles generated from the oxidation of several gaseous precursors in an oxidative flow reactor were sampled as the analyte particles in these measurements. Mass spectral signatures associated with the SOA analyte were observed using seed particles with diameters as low as 20 nm, indicating the ability to probe the composition of particles from nucleation (< 30 nm) to accumulation (> 100 nm) size modes. Increased analyte signal and matrix fragmentation were observed with higher laser pulse energy. Additionally, analyte signals were optimized relative to matrix signatures using volumetric matrix-to-analyte ratios around 80-100:1. The cMA-ATOFMS distinguished the chemical composition of SOA particles generated from the oxidation of dimethyl sulfide (DMS) from secondary aerosols produced via SO_2 oxidation by identifying the presence of a $^{95}CH_3SO_3^-$ peak, indicative of the DMS byproduct methane sulfonic acid. These controlled laboratory experiments highlight the capabilities of this novel system for online analysis of ultrafine particles and emphasize the

potential to measure the particle mixing state of sub-100 nm aged aerosol populations in an ambient environment.

6.2 Introduction

Aerosols impact climate directly through scattering and absorbing solar radiation and indirectly by seeding clouds and affecting their radiative properties (Pöschl, 2005). Currently, the aerosol-cloud interaction remains one of the highest uncertainties in the global radiative budget (Boucher et al., 2013). Secondary organic aerosols (SOA), formed from the oxidation of volatile organic compounds (VOCs), comprise a significant number of particles and aerosol mass in the troposphere (Kroll and Seinfeld, 2008; Hallquist et al., 2009). The influence of SOA on cloud formation and global climate is dependent on the size, chemical composition, and concentration of these aerosols in the atmosphere (Seinfeld and Pandis, 2016). Therefore, it is important to understand the composition and size distribution of SOA released from various sources to better predict their impact on cloud radiative properties and global climate.

Mass spectrometry is an established technique for measuring the chemical composition of aerosols, and many instruments using mass spectrometry have been developed to study SOA (Pratt and Prather, 2012). A common, commercial mass spectrometer used for SOA detection is the aerosol mass spectrometer (AMS), which measures the chemical composition of non-refractory aerosols with vacuum aerodynamic diameters (D_{va}) ranging from 33 nm to 1500 nm (Jayne et al., 2000; Zhang et al., 2004a; DeCarlo et al., 2006). The AMS measures particle size distributions and bulk aerosol mass concentrations of species such as nitrate, sulfate, ammonium, and most organics. However, the AMS lacks the ability to measure individual particles, and therefore cannot determine particle mixing state.

Single-particle mass spectrometry (SPMS) has improved our understanding of atmospheric aerosols (Sullivan and Prather, 2005). The aerosol time-of-flight mass spectrometer (ATOFMS), a well-known SPMS, measures the vacuum aerodynamic diameter and the chemical composition of a single particle in real time (Prather et al., 1994; Gard et al., 1997). The ATOFMS is a mobile instrument, capable of measuring aerosols with D_{va} ranging from 70 nm to 3 μm (Gard et al., 1997; Pratt et al., 2009). Unlike the AMS, the ATOFMS also measures refractory particles including soot, minerals, and salts using laser desorption and ionization prior to chemical analysis. Due to the ability to detect individual particles, the ATOFMS has been used to characterize the chemical mixing state as a function of size and source for many different aerosol populations (Pratt et al., 2009; Gaston et al., 2010; Prather et al., 2013). However, the lower size limit of the ATOFMS has been limited by the fact it uses light scattering to detect individual particles. Therefore, it lacks the ability to measure SOA formed by nucleation as well as subsequent growth processes, which occurs at sizes below 100 nm (Fan et al., 2006).

Previous techniques to improve the hit rate and detection of small particles using ATOFMS include the addition of a matrix assisted laser desorption ionization (MALDI) matrix to an analyte solution prior to atomization and detection with the ATOFMS (Spencer et al., 2008; Kleefsman et al., 2007, 2008; Mcjimpsey et al., 2008; Whiteakert and Prather, 2003). This technique was further expanded to enable in-flight growth of incoming particles using condensation systems containing MALDI matrices. These systems, like condensation particle counters (Agarwal and Sem, 1980), grow particles through matrix addition using flow cells equipped with liquid or solid matrix reservoirs. Stowers et al. (2000) led these efforts by using an evaporation-condensation tube to coat matrix onto biological particles prior to single-polarity ATOFMS analysis (Stowers et al., 2000). Successful detection of antibiotics and bacterial spores was capable using the MALDI

matrices 3-nitrobenzyl alcohol, picolinic acid, and sinapinic acid. Subsequent experiments by this group achieved matrix addition through sublimation and condensation of a solid matrix onto incoming aerosols (van Wuijckhuijse et al., 2005). In this previous study, biological particles were grown with condensed ferulic acid (4-hydroxy-3-methoxycinnamic acid) and analyzed with a single-polarity ATOFMS. However, both studies used seed particles > 100 nm for their measurements. Like other MALDI experiments that target biological species, analysis was focused on mass ion markers exceeding 500 Da and avoided lower mass ions due to high background by the ionized matrix. Although traditional MALDI studies have focused on small molecule detection (Cohen and Gusev, 2002), characterization of molecules in the lower mass-to-charge range has yet to be performed with these condensation systems.

In this study, a recently designed sublimation-condensation system, similar in principle to that described by van Wuijckhuijse et al. (2005), was coupled with a dual-polarity ATOFMS to detect sub-100 nm aerosols (Li et al., *in prep*). SOA, generated from the oxidation of select VOCs using an oxidative flow reactor (Kang et al., 2007), were size-selected, grown in the sublimation-condensation system, and analyzed using the ATOFMS. Initial tests to verify the operation of this system involved condensation of ferulic acid onto 50 nm dimethyl sulfide (DMS) SOA particles prior to chemical analysis with an ATOFMS (Li et al., *in prep*). Here, the condensation matrix-assisted aerosol time-of-flight mass spectrometer (cMA-ATOFMS) system was further characterized using three different matrices, ferulic acid, 2,4-dihydroxybenzoic acid (2,4-DHB), and 1,8-bis(tetramethylguanidino)naphthalene (TMGN), for growth on secondary aerosols formed from multiple gaseous precursors including dimethyl sulfide (DMS), sulfur dioxide (SO_2), α-pinene, and toluene. Because the success of MALDI mass spectrometry relies on matrix material, matrix-to-analyte ratio, and laser fluence (Zenobi and Knochenmuss, 1998), this novel system was

characterized with different matrices, matrix-to-analyte ratios, and laser fluences to determine the optimal conditions for measuring the chemical composition of submicron SOA particles in real time. The cMA-ATOFMS system allows for real-time adjustment of sample parameters for targeted analysis of various analytes. Furthermore, we demonstrate the application of this system to detect differences in the secondary aerosol composition generated from the oxidation of different sulfur-containing gas mixtures.

6.3 Methods

6.3.1 cMA-ATOFMS System and Experimental Setup

The experimental setup for the cMA-ATOFMS is shown in Figure 6.2. SOA particles were generated from the oxidation of volatile organic compounds (VOCs) using an oxidative flow reactor (OFR). Following SOA formation, particles were dried through a silica diffusion drier (relative humidity < 20%) and size-selected using an Electrostatic Classifier (EC, TSI, Model 3080) and differential mobility analyzer (DMA, TSI, Model 308100). SOA were neutralized to a near steady-state charge distribution using a ^{34}Kr neutralizer and size-selected based on their electrical mobility diameter (Fuchs, 1963; Liu and Pui, 1974). Following size selection, analyte particles were grown using a custom laminar flow sublimation-condensation system (condenser) containing a solid MALDI matrix, as previously described (Li et al., *in prep*). The condenser produces both heterogeneously grown (matrix deposited onto analyte particles) and homogeneously nucleated (particle generation from matrix gas-to-particle transition) particles during the sublimation-condensation process. Homogeneously nucleated particles are generally in a neutral charge state, whereas the heterogeneously grown particles retain a charge from the neutralizer. A second DMA (TSI, Model 3082), bypassing the neutralizer, was used after the condenser to size select the charged, heterogeneously grown particles. Uncharged, homogenously

nucleated particles were not transmitted through the second DMA, thus filtering out these particles prior to detection. Additionally, the secondary size selection of heterogeneously grown particles maintained a consistent matrix-to-analyte ratio. Here, both DMAs were run in negative mode to ensure compatibility. After exiting the second DMA, particles were passed to the ATOFMS for chemical analysis. During homogeneous nucleation measurements, which acted as a baseline for the heterogeneous growth measurements, the second DMA was bypassed to allow chemical analysis of the matrices.

6.4 Results and Discussion

6.4.1 Evaluation of Matrices

Three matrices, ferulic acid, 2,4-DHB, and TMGN, were separately used in the condenser to induce particle growth and assist in stronger laser absorption and ionization of the analyte particles. The ability of each of these matrices to condense on KCl seed particles was previously characterized and growth curves were analyzed (Li et al., *in prep.*). Growth curves of these matrices onto SOA generated in the OFR represented those of KCl seeds (Figures 6.9, 6.10, 6.11) suggesting these techniques are applicable to many different analyte sources.

To compare the chemical signatures of the different matrices using a common analyte, 50 nm particles of DMS SOA were generated in the OFR and size selected with the first DMA. This particle diameter falls below the typical detection limit of the ATOFMS, however, growth with each of the matrices using the condenser system resulted in final particle vacuum aerodynamic diameters between 400 and 600 nm which were easily detected and hit with the ATOFMS (Pratt et al., 2009).

Figure 6.3 shows the representative dual-polarity mass spectra of 50 nm DMS SOA grown with each matrix. Within each spectrum, signatures of the MALDI matrix and the matrix

fragmentation products are distinct and were confirmed by measuring homogenously nucleated particles (Figure 6.12). For 2,4-DHB, major matrix ion peaks include the molecular ion peak at $^{154}M^{+}$, the protonated molecular ion peak at $^{155}[M+H]^{+}$, the deprotonated matrix, $^{153}[M-H]^{-}$, the protonated matrix with the loss of a water, $^{137}[M+H-H_2O]^{+}$, and the deprotonated matrix with the loss of a water, $^{135}[M-H-H_2O]^{-}$ (Figure 6.3a). In addition to these peaks, a major fragmentation product appears at *m/z* +85. The molecular ion marker and protonated molecular ion as a well as the peak at *m/z* +137 have been previously observed when using ATOFMS to analyze DHB (Morrical et al., 1998; Wenzel and Prather, 2004; Zhou et al., 2013).

When ferulic acid was used as the matrix, the main peaks associated with the matrix included the molecular ion peak, $^{194}[M]^{+}$, the protonated ($^{195}[M+H]^{+}$) and deprotonated molecular ions ($^{193}[M-H]^{-}$), and the markers $^{178}[M-H-CH_3]^{-}$ and $^{177}[M+H-H_2O]^{+}$ (Figure 6.3b). Additional high intensity peaks include those from the fragmentation of the matrix at *m/z* +46 and -135, and the presence of a matrix dimer at *m/z* -386, corresponding to $^{386}[M-H]_2^{-}$. The protonated molecular ion peak ($^{195}[M+H]^{+}$) and the ion formed from the subsequent loss of water ($^{177}[M+H-H_2O]^{+}$) agree with ion markers previously reported for another system utilizing laser desorption and ionization of vapor deposited ferulic acid (Kim et al., 1998). The presence of molecular ion peaks in the mass spectra for 2,4-DHB and ferulic acid likely resulted from a primary ionization mechanism, such as energy pooling, which is common with MALDI matrices (Zenobi and Knochenmuss, 1998).

Finally, for TMGN, the major peaks that corresponded to the matrix were $^{355}[M+H]^{+}$, $^{46}[NO_2]^{-}$, $^{62}[NO_3]^{-}$ and *m/z* +85, +311, and -125 (Figure 6.3c). Although TMGN is considered a proton-sponge and therefore should only represent positive ions in the mass spectra (Raab et al., 2002), it is clear from the negative mass peaks that desorption and ionization with this system results in fragmentation of the matrix (Figure 6.12). Additionally, due to the nitrogen species

within TMGN and appearance of $^{46}[NO_2]^-$ and $^{62}[NO_3]^-$, care should be taken when using this matrix to analyze particles, especially SOA, that may have reacted with NO_x. Nonetheless, the protonated molecular ion peak, which has been previously observed (Cao et al., 2011), suggests this matrix is a viable candidate for deprotonation of analyte particles.

Notably, in each of these spectra, the analyte signal was clear amongst the matrix peaks, suggesting successful growth and ionization of the target particles (Figure 6.3). Each spectrum showed a distinct peak at *m/z* -97 corresponding to $^{97}[HSO_4]^-$ and suggestive of sulfuric acid formation, a known secondary aerosol product following the oxidation of DMS (Barnes et al., 2006; Hopkins et al., 2008). The ATOFMS has been previously used to measure marine, sulfur-containing aerosols which often show a dominant $^{97}[HSO_4]^-$ peak, thus supporting the conclusion that DMS was oxidized in the OFR to sulfuric acid (Gaston et al., 2010).

6.4.2 Influence of Laser Power

To further optimize the new cMA-ATOFMS system and increase the intensity of the analyte peaks compared to those of the matrix, we systematically varied the pulse energy of the desorption/ionization laser. Figure 6.4 displays the mass spectra of 100 nm SOA particles produced from the oxidation of α-pinene and SO_2 gas in the OFR and grown to D_{va} ~500 nm using ferulic acid in the sublimation-condensation system. Particles were analyzed with the ATOFMS using average laser energies of approximately 200, 500, or 900 μJ. Sulfur dioxide gas was originally added to serve as an acidic seed and promote aerosol formation within the OFR (Zhao et al., 2021). However, SO_2 oxidation products acted as the main analytes in this experiment because SOA produced from the oxidation of α-pinene alone resulted in mass ion signatures that were indistinguishable from the organic fragments produced by ferulic acid.

The mass spectra presented in Figure 6.4 represent an average of all particles with dual polarity spectra in each respective dataset. Ionization at higher laser energy levels resulted in increased total positive ion intensities (TPII; i.e., the sum of all positive ion peaks from 0 to 500 *m/z*) (Figure 6.13) (Zelenyuk et al., 2008). At each laser energy, peaks associated with the ferulic acid matrix and the analyte seed are present. With increasing laser energy, higher mass peaks (> ±100 *m/z*) associated with the matrix decreased in intensity while lower mass peaks (< ±100 *m/z*) increased. These results suggest a higher degree of fragmentation of the matrix which is typical for laser desorption/ionization analysis of organic species using high laser energy (Noble et al., 1998; Silva et al., 1999). The fragmentation products from ferulic acid include hydrocarbon peaks from positive ions such as C^+, $C_2H_3^+$, $C_3H_3^+$, $C_4H_2^+$ and the negative ions C_2H^-, $C_3H_5^-$, and $C_5H_2^-$. Notables across all laser energies are the dominant intensities of the ion peaks attributed to the formation of sulfate species, $^{80}SO_3^-$ and $^{97}HSO_4^-$, following the oxidation of SO_2 gas in the OFR. The observations from the laser energy tests suggest that higher laser energies will help eliminate the higher mass peaks in the mass spectra at the potential cost of increased fragmentation and more matrix ions in the lower mass region.

To minimize matrix fragmentation and ensure less interference in the lower mass region, mass spectra with low TPII can be selected in FATES (Sultana et al., 2017b). Previous studies have demonstrated that TPII is an indicator of desorption and ionization, thus selecting for lower TPII ensures these processes are minimized (Sultana et al., 2017a; Zelenyuk et al., 2008). When mass spectra of SOA generated from α-pinene and SO_2 were selected for low TPII values at each laser energy tested in Figure 6.4, clear matrix peaks were observed with significantly less fragmentation and in addition to a prominent $^{97}HSO_4^-$ peak (Figure 6.14). Classification based on TPII may be a valuable method for future data analysis of the cMA-ATOFMS when analyzing

larger analyte particles (100 nm or above) or particles with low mass peaks that might overlap with matrix fragmentation.

To probe the impact of laser energy on the analyte signal of seed particles with diameters below 100 nm, tests were performed on 20 nm DMS SOA condensed with TMGN. Particles were desorbed and ionized using laser energies of approximately 100, 250, and 500 μJ (Figure 6.5). Like results from α-pinene and SO_2, as the laser energy increased, higher mass matrix peaks decreased along with a simultaneous increase in both the intensity and number of lower mass, fragmentation peaks. All spectra show the presence of the analyte particle at $^{97}HSO_4^-$ and $^{95}CH_3SO_3^-$, which are known products of DMS oxidation (Gaston et al., 2010; Ayers and Gillett, 2000). Unlike the 100 nm α-pinene and SO_2 particles which consistently showed intense analyte peaks, the 20 nm DMS particles show an increase in the relative peak area of the analyte signal with increased laser energies. At the highest laser energy tested (500 μJ), the relative peak area of the analyte (at *m/z* -97) was an order of magnitude higher than that at the lowest laser energy (100 μJ). These results agree with previous aerosol MALDI studies that found stronger analyte signals at higher laser pulse energies (van Wuijckhuijse et al., 2005; Murray and Russell, 1994), and suggest incomplete desorption and ionization of the analyte particle at low laser energies. Based on these tests, higher laser energies should be used when analyzing small particles (< 100 nm) to ensure full desorption and ionization of the analyte.

6.4.3 Effect of Matrix-to-Analyte Ratio

The effect of matrix growth on resulting mass spectra was observed with different matrix-to-analyte ratios throughout several experiments. To ensure consistency between the electrical mobility diameter, D_m, measured with the DMA (size-selecting the SOA), and the vacuum

aerodynamic diameter, D_{va}, measured with the ATOFMS, we converted from D_{va} to D_m using Equation 6.1:

$$D_m = \frac{D_{va}\chi\rho_0}{\rho_p} \quad [6.1]$$

Where χ is the dynamic shape factor, assumed to be 1 for spherical particles, ρ_0 is the standard density of a sphere (1 g/cm^3), and ρ_p is the particle density assumed to be the density of the matrix (DeCarlo et al., 2004). The conversion of the vacuum aerodynamic diameter sizes measured with the ATOFMS to the electrical mobility diameter is provided in Figure 6.15. The volume of the analyte particle was calculated assuming the volume of a sphere using the D_m measured with the DMA. The volume of the matrix was then calculated by finding the volume of a sphere using the D_m derived from the converted ATOFMS measurements and subtracting the volume of the seed particle. For the first tests, 100 nm SOA seed particles produced from the oxidation of toluene and SO_2 were grown to 350 and 400 nm, and 50 nm seed particles were grown to 400 nm using ferulic acid (all values reflect electromobility diameter). This resulted in a volumetric matrix-to-analyte ratio of approximately 50:1, 80:1, and 650:1, respectively. Assuming the density of sulfuric acid (1.83 g/cm^3) for the analyte seed (because this was the dominant peak) and the density of the matrix, ferulic acid (1.32 g/cm^3), the calculated molar matrix-to-analyte ratios for each dataset were around 20:1, 40:1, and 230:1, respectively. Figure 6.6 shows the mass spectra generated for particles pertaining to each of these matrix-to-analyte ratios. Like the laser power tests, the predominant analyte peaks in these tests were from the oxidation of SO_2, likely due to overlap of toluene oxidation products with matrix fragmentation peaks. Throughout these tests, the desorption/ionization laser pulse energy was 500 µJ.

The spectra related to particles with a molar matrix-to-analyte ratio of 20:1 show the highest degree of matrix interference between *m/z* 0–100 in both positive and negative polarity.

Additionally, the spectra of particles with a molar matrix-to-analyte ratio of 230:1 show some fragmentation peaks in the lower mass positive polarity as well as high intensity matrix peaks at *m/z* -178 and -135. Based on these results, to minimize matrix peaks relative the analyte peaks ($^{97}HSO4^-$ in this case), in-flight growth and ionization are optimized with a molar matrix-to-analyte ratio around 50:1. This ratio is in line with those previously reported for aerosol MALDI analysis (Zhou et al., 2013; Murray and Russell, 1994; Beeson et al., 1995). The matrix-to-analyte ratios required for aerosol MALDI is known to be much lower than those required for traditional surface MALDI, with ratios of 10^2–10^4:1, because of fast matrix crystallization in the aerosol phase and contact between the matrix and analyte (Murray and Russell, 1994; Beeson et al., 1995). These results suggest that condensation MALDI achieves similar interactions between the matrix and analyte particles, and thus requires minimal quantities of matrix to perform effectively. Minimizing excess matrix consumption is important for both operator safety and ensuring a sustainable, cost-efficient system.

The matrix-to-analyte ratio was further analyzed using DMS SOA particles that were condensed with TMGN. For these measurements, a clear increase in the analyte signature was observed with lower matrix-to-analyte ratios (Figure 6.7). DMS SOA particles were size selected at 20, 35, and 50 nm and grown through the condenser to D_m = 400–500 nm. This resulted in volumetric matrix-to-analyte ratios of approximately 10^4:1, 3000:1, and 1500:1 and molar matrix-to-analyte ratios (assuming the density of sulfuric acid) of approximately 2500:1, 500:1, and 170:1 for the 20, 35, and 50 nm particles, respectively. The particles were desorbed and ionized with a laser energy of ~100 µJ. At this low laser energy, the analyte signature shows a clear increase with decreasing matrix-to-analyte ratios, potentially because of higher analyte desorption and ionization. Although typical MALDI measurements report molar matrix-to-analyte ratios, when

analyzing an unknown particle source, this knowledge may not be readily available. Therefore, we propose using volumetric matrix-to-analyte ratios for this system to provide a method that is easily computed in a field environment. Based on the results from the two experiments, lower volumetric matrix-to-analyte ratios are preferred for higher analyte signal, with an optimal ratio of 80–100:1 when using higher laser energies (500 µJ).

6.4.4 Distinguishing Between Secondary Aerosol Sources

We assessed the ability of the cMA-ATOFMS to discriminate between secondary aerosols generated from different sources of sulfur: SO_2 which typically represents an anthropogenic source of inorganic sulfur (Smith et al., 2001), and DMS which is commonly produced from biogenic species and represents an organic source of atmospheric sulfur (Charlson et al., 1987; Bates et al., 1992). Secondary aerosols generated from SO_2 with electromobility diameters of 50 nm were grown using TMGN to a final D_{va} = 300 nm, while 50 nm seeds originated from DMS SOA were grown with TMGN to D_{va} = 450 nm. The laser was operated at a pulse energy of 500 µJ for both tests.

Both analytes showed the clear formation of sulfate species in the OFR, with peaks at $^{80}SO_3^-$ and $^{97}HSO_4^-$. Nearly all (95%) of the particles formed from the oxidation of SO_2 contained $^{97}HSO_4^-$ (Figure 6.8). Almost half of the particles containing $^{97}HSO_4^-$ from SO_2 oxidation had a relative peak area between 0.15 and 0.5, indicating this was a major ion marker in these particles. This contrasts with the DMS oxidation products where only ~50% of particles showed $^{97}HSO_4^-$, and 40% of those particles had a relative peak area between 0.01 and 0.05 for $^{97}HSO_4^-$. For particles in both datasets, the relative peak area of $^{80}SO_3^-$ was below 0.02, however, 84% of particles from DMS oxidation contained this signature compared to 52% of particles from SO_2. Only the DMS SOA showed a mass peak indicative of MSA formation in the OFR at $^{95}CH_3SO_3^-$. MSA was

measured in 93% of DMS SOA particles, with 76% of them having a relative peak area of 0.02–0.05 at this mass. MSA is a common product of DMS oxidation (Gaston et al., 2010), and will not form from SO_2. Therefore, the cMA-ATOFMS system, with its chemical analysis of secondary aerosols, represents a novel method to potentially distinguish between biogenic and anthropogenic sulfur sources in an ambient environment.

6.5 Conclusions

Here, we described the characterization, optimization, and application of a newly developed dual-polarity condensation matrix-assisted aerosol time-of-flight mass spectrometer (cMA-ATOFMS). Ferulic acid, 2,4-DHB, and TMGN were all analyzed as potential matrices for the growth and detection of oxidized aerosols with this system. TMGN, a matrix recently developed for small molecule analysis, consistently showed the least interference in negative mass spectra of analytes. The low sublimation temperature (excluding the need for recirculating water) makes TMGN a favorable matrix for future studies, though the presence of nitrogen containing species in the mass spectra may complicate use of TMGN for common atmospheric sampling. The highest analyte signatures were observed with laser energies around 500 μJ and volumetric matrix-to-analyte ratios of ~100:1. The cMA-ATOFMS system was shown to detect analyte signatures in SOA particles as small as 20 nm and distinguish between secondary aerosols generated from inorganic and organic sulfur containing species. Future improvements to this system will include the incorporation of a desorption/ionization laser with an even beam profile for better mass spectral consistency and enhanced control of desorption/ionization at low laser energies (Murray, 2021; Wenzel and Prather, 2004). Additionally, future directions will focus on expanding detection of small molecule organic species through new matrices, exploring lower matrix-to-analyte ratios, and matrix mixing (Cohen and Gusev, 2002; Guo and He, 2007).

The cMA-ATOFMS system represents a novel method for the direct analysis of single-particles with diameters below 100 nm. With this system, the particle mixing state of submicron aerosol populations can be measured, allowing for better predictions of aerosol-cloud interactions, and improving global climate modeling. Additionally, future applications of this system include the detection of biological aerosols in real time. Online detection and chemical analysis of small biological molecules, such as airborne viruses and bacteria, can expand our understanding of pathogen exposure and the influence of biological aerosols on the environment.

6.6 Acknowledgements

This work was supported by US National Science Foundation Grants GEO-2035847 and GEO-2035870.

Chapter 6, in full, is currently being prepared for submission for publication of the material. Kimble, K. A., Mitts, B. A., Li, L., Moore, A. M., Heilig, M., Hogan Jr., C. J., Prather, K. A. (2022). “Optimization and application of a condensation matrix-assisted aerosol time-of-flight mass spectrometer.” The dissertation author and Ke’La Kimble are co-first authors of this manuscript. The dissertation author contributed to experimental design and setup, designed and generated Figure 6.2, and was the lead writer for the abstract and results sections. The dissertation author contributed secondarily to writing the methods section and provided intellectual input and code for figure design. Ke’La Kimble was the primary experimenter, generated all other figures in the manuscript, was the lead writer of the methods section and secondary writer for the abstract and results sections. Both the dissertation author and Ke’La Kimble contributed equally to the writing of the introduction and conclusions, the generation of the graphical abstract, and to the review and editing process.

6.7 Figures

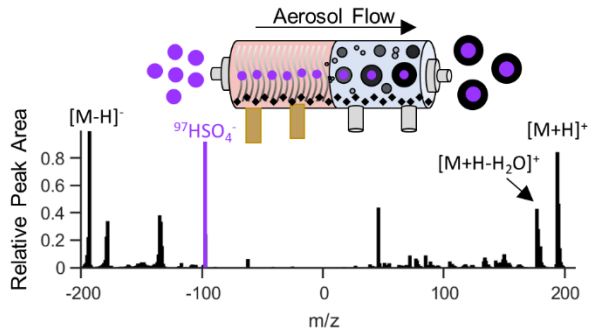

Figure 6.1. Graphical abstract.

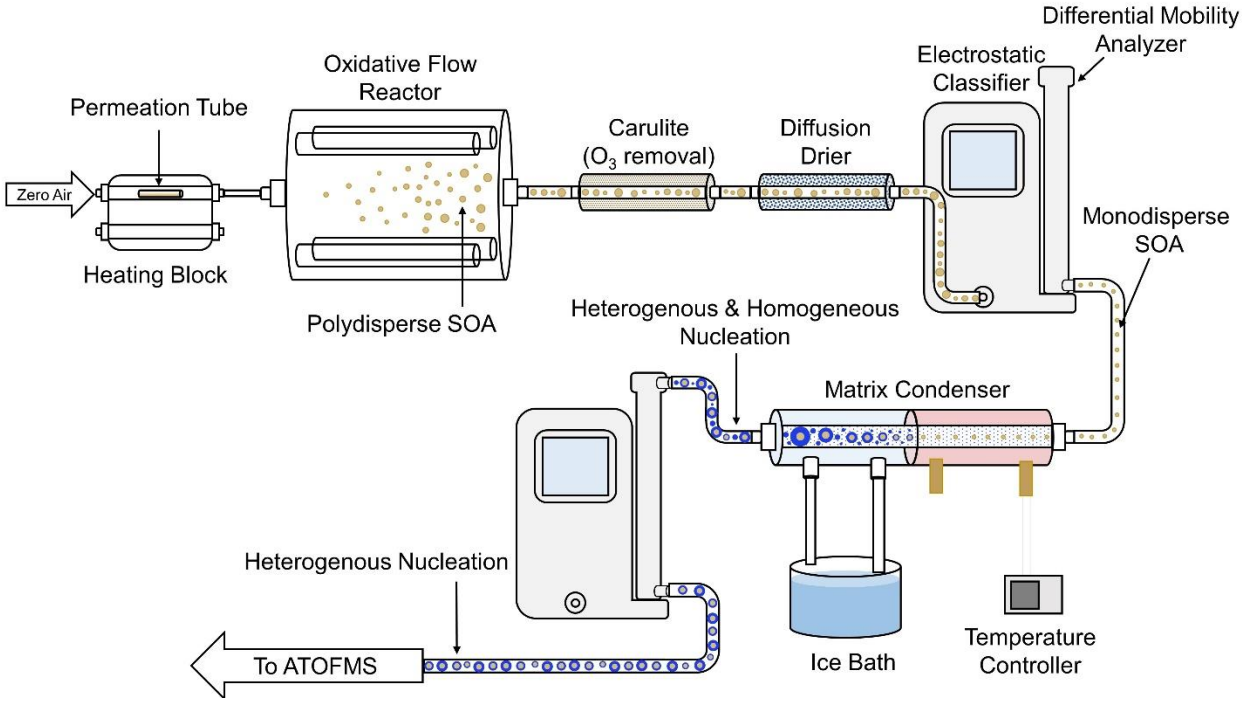

Figure 6.2. Schematic of the experimental setup showing new particle formation in the OFR from controlled gases followed by the tandem differential mobility analyzer system to isolate select particle sizes for growth in the matrix condenser and elimination of homogeneously nucleated particles before transport to the ATOMFS.

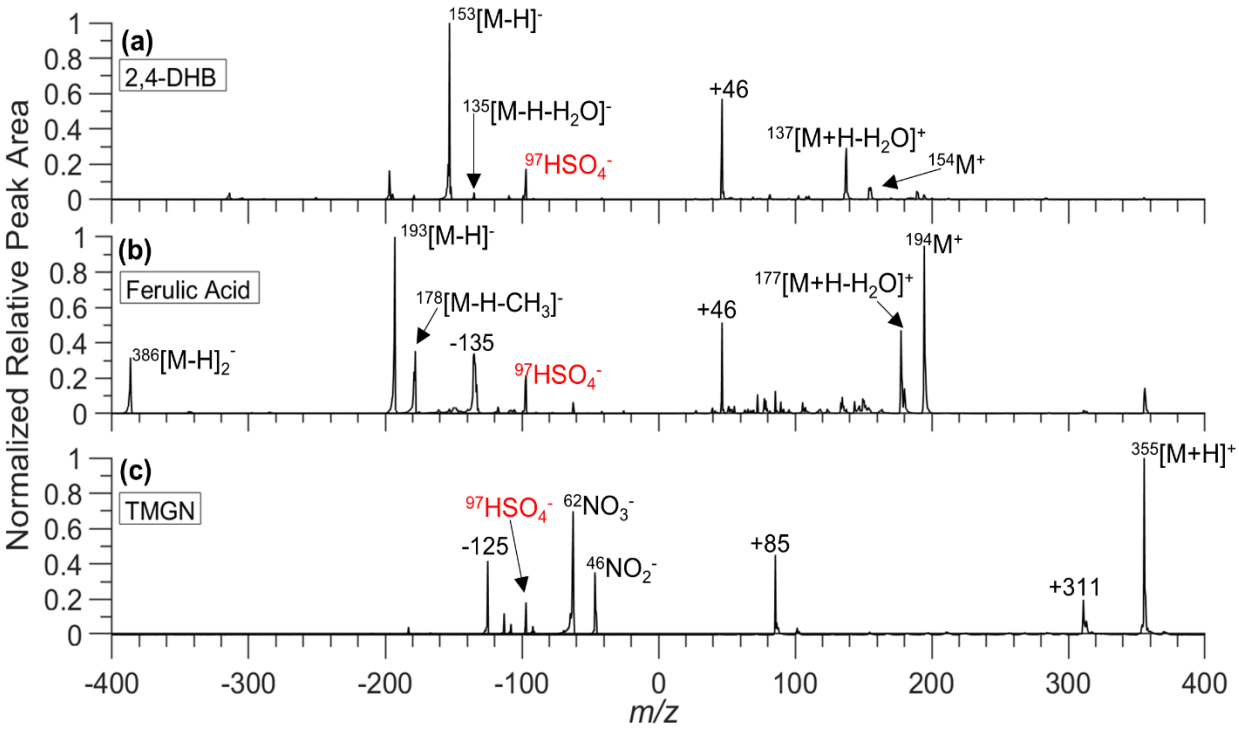

Figure 6.3. Average mass spectra of the chemical composition of 50 nm DMS SOA analyte particles after condensation with the MALDI matrix 2,4-DHB (a), ferulic acid (b), or TMGN (c).

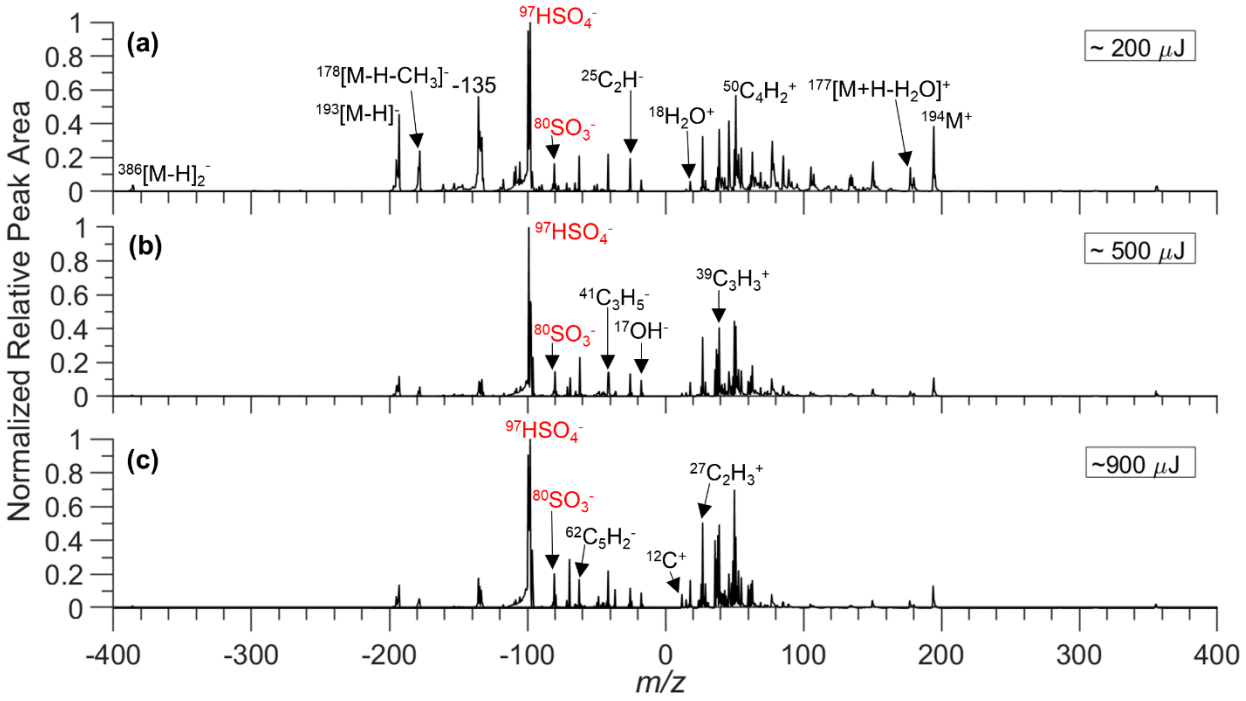

Figure 6.4. Representative mass spectra of the 100 nm SOA particles derived from oxidizing α-pinene and SO_2 together. Particles were condensed with ferulic acid and ionized using average laser energies of 200 (a), 500 (b), and 900 μJ (c).

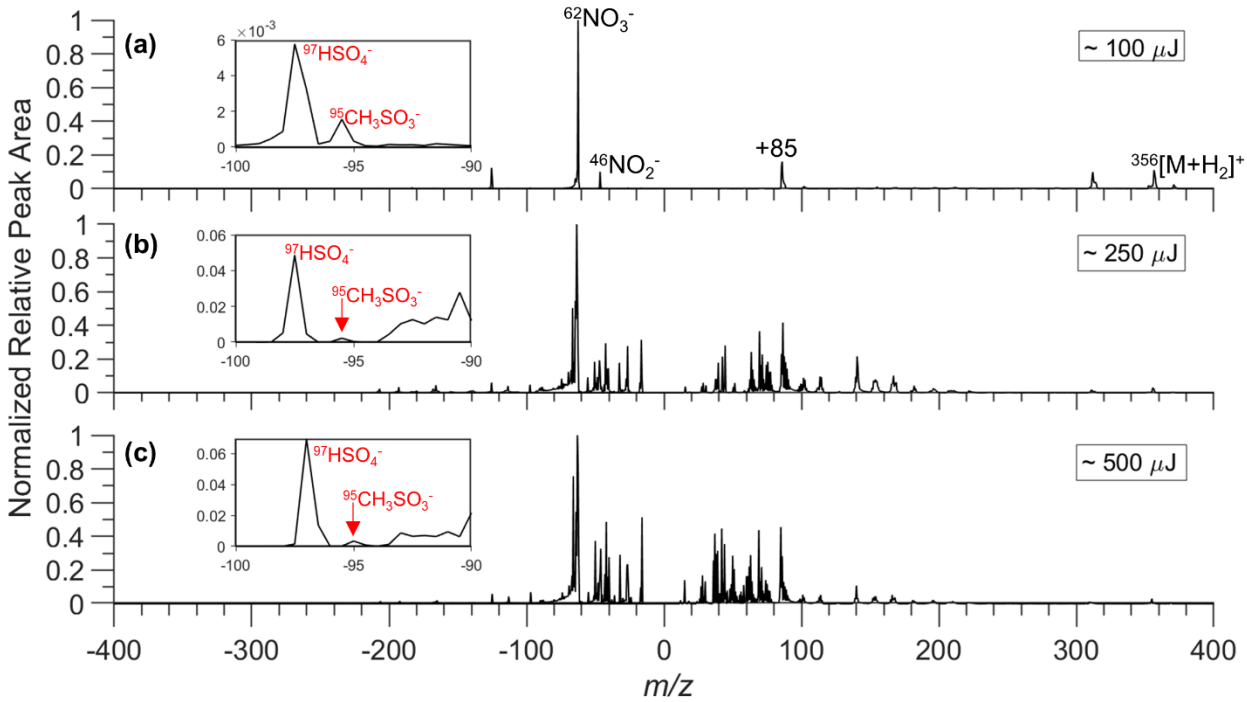

Figure 6.5. Representative mass spectra of the 20 nm DMS SOA particles condensed with TMGN and ionized using the laser powers of 100 (a), 250 (b), and 500 μJ (c).

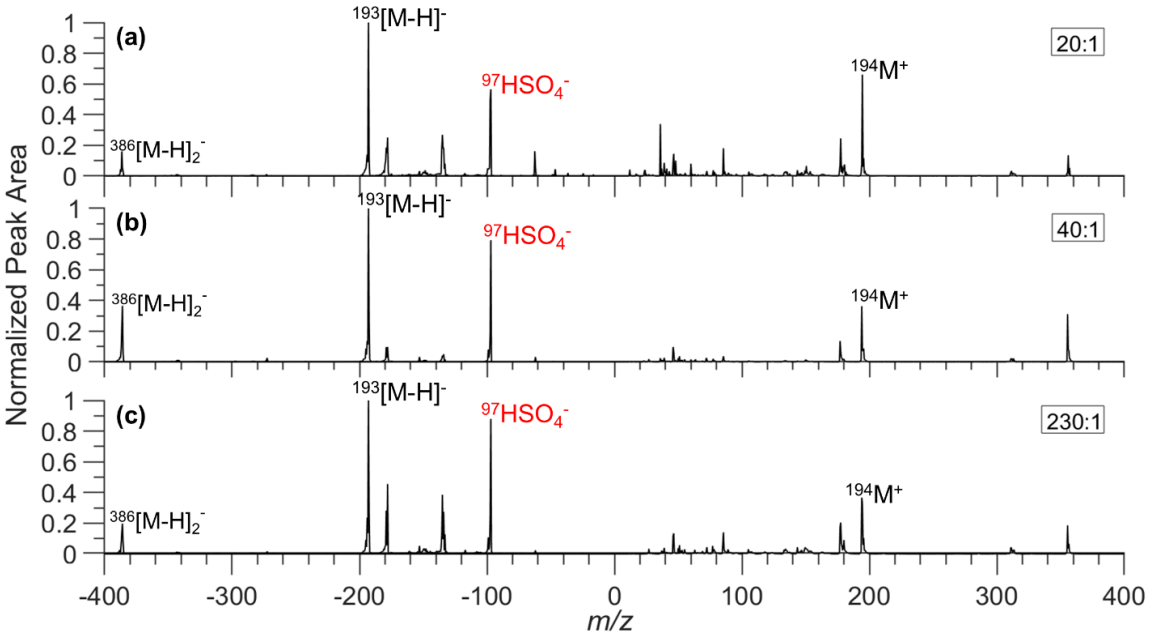

Figure 6.6. Mass spectra showing the effect of varying the molar matrix-to-analyte ratio from 20:1 (a), 40:1 (b), and 230:1 (c) for mixed toluene and SO_2 SOA analyte particles using ferulic acid as the MALDI matrix.

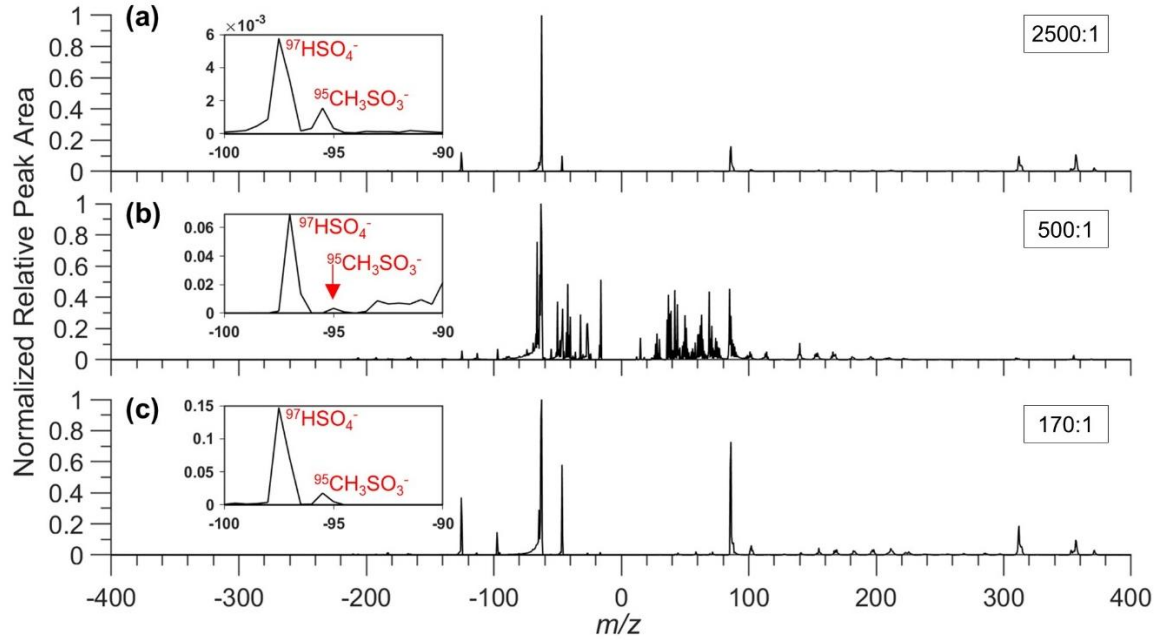

Figure 6.7. Mass spectra of the molar matrix-to-analyte ratio of 2500:1 (a), 500:1 (b), and 170:1 (c) for SOA particles derived from DMS oxidation and condensed with TMGN. All spectra were pre-selected for those containing presence of the analyte.

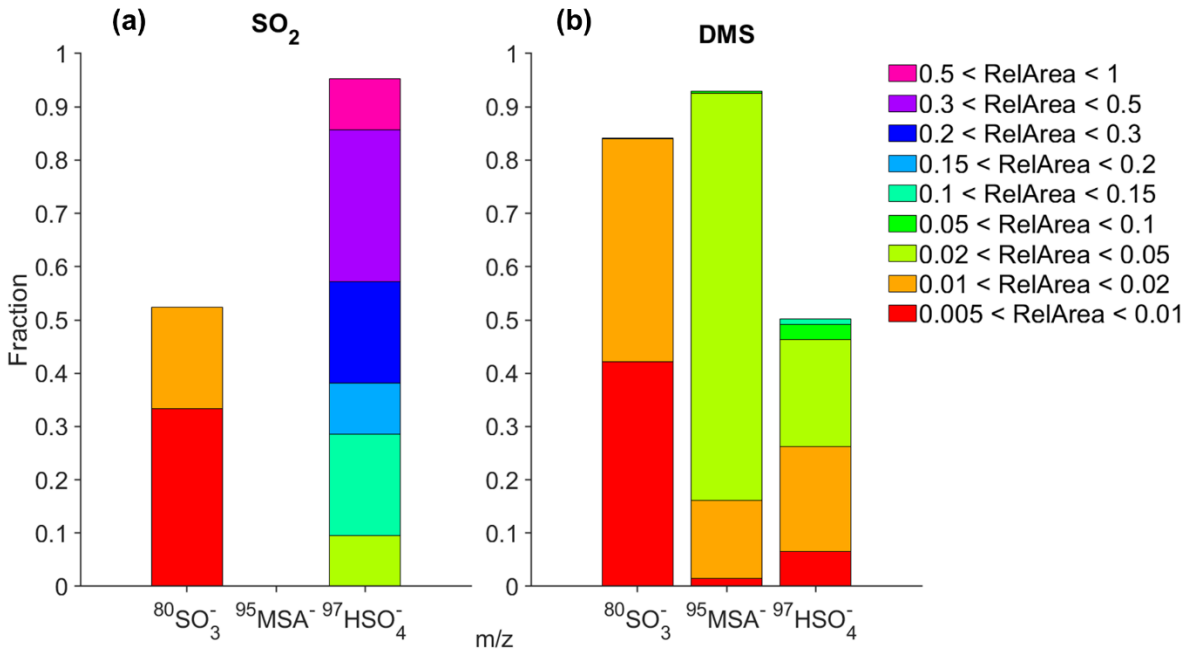

Figure 6.8. Fraction of particles with sulfur containing mass ion markers along with the relative peak area of these markers for secondary aerosols formed from the oxidation of SO_2 (a) and DMS (b).

6.8 Supporting Information

6.8.1 Secondary Organic Aerosol Formation

Permeation tubes (Metronics Dynacal) containing different volatile organic compounds (VOCs) were heated in a custom heating block at the temperatures recommend by the supplier. The VOCs chosen for this experiment were dimethyl sulfide (DMS), toluene, and α-pinene. They were heated at 30°C, 60°C, and 30°C, respectively, resulting in a permeation rate of 175 ng/min, 47 ng/min, and 345 ng/min. Zero-air (Sabio, Model 1001) flowed over the permeation tubes at a rate of 0.5 liters per minute (LPM) and a makeup flow of zero-air was added to reach a total flow of 5 LPM through a potential aerosol mass oxidative flow reactor (OFR, Aerodyne Research, Inc). The final concentrations of each VOC through the OFR were 0.0138 parts per million (ppm), 0.0025 ppm, and 0.0124 ppm, respectively.

Detailed descriptions of the OFR have been previously published (Kang et al., 2007; Lambe et al., 2011; Mayer et al., 2020). Briefly, the OFR can be used to simulate multiple days of atmospheric aging by generating high concentrations of ozone and hydroxyl radical (OH) which cause oxidation and heterogenous reactions. SOA formation occurs when the oxidized products of VOCs condense to form a new particle (nucleation) or condense onto a preexisting aerosol (Pandis et al., 1992). For this experiment, SOA generated in the OFR were formed through nucleation because particle-free air was used. SOA size distributions for each of the VOC sources as well as the addition of SO_2 with toluene and α-pinene are shown in Figure 6.16.

The OFR in this study was run in 185 nm mode, in which both 185 nm and 254 nm lamps are used to generate ozone and OH. OH exposure at a specific lamp voltage is determined from the loss of carbon monoxide, which has a known reaction rate with OH (Chen and Marcus, 2006), measured with a CO analyzer (APMA-370, Horiba Ltd.). A calibration curve of the lamp voltage

and OH concentration was generated and OH exposure was further converted to days of equivalent aging based on ambient OH concentrations (1.0×10^6 molec·cm^{-3}) (Figure 6.17) (Wolfe et al., 2019). Here, the lamp voltage was set to simulate ~1.87 days of equivalent aging in the OFR.

6.8.2 Laminar Flow Matrix Sublimation-Condensation

To achieve in-flight growth of sub-100 nm particles, a laminar flow matrix sublimation-condensation system was applied. This system, referred herein as the "condenser", has been previously described in detail (Li et al., *in prep*). Briefly, a stainless-steel tube was filled with a bed of solid matrix material and heated between 80-140°C using heating tape (BriskHeat, Columbus, OH, USA) to sublimate the matrix and create a matrix vapor-saturated region (the sublimation region). The second half of the condenser was cooled with circulating ice water around the surface walls, facilitating matrix supersaturation and condensation onto passing particles (the condenser region). Homogeneous nucleation of matrix particles also occurred in the system as a byproduct, as quantified by Li et al. (*in prep*). Ferulic acid, 2,4-DHB, and TMGN were chosen as matrices in this experiment due to their low melting temperatures and minimal toxicity. TMGN has a lower melting point than the other matrices, and a lower temperature gradient for condensation to occur, so it was used without ice water cooling to minimize homogeneous nucleation. SOA particles, flowing at ~0.25 LPM, were grown via condensation of the MALDI matrix to sizes detectable with the ATOFMS.

6.8.3 Size Distribution Measurements

The final size of heterogeneously grown particles depends on the temperature of the condenser, aerosol number concentrations, and the particle flow rate (Stowers et al., 2000). A scanning mobility particle sizer (SMPS) was used measure the particle size distributions before and after the sublimation-condensation system and observe the growth rates of particles at different

temperatures and with different matrices. The SMPS utilizes an electrostatic classifier and DMA (TSI, Model 3082), for particle size selection based on electrical mobility diameter, followed by particle detection via a condensation particle counter (CPC, TSI, Model 3787).

6.8.4 Measurements of SOA Composition using ATOFMS

The vacuum aerodynamic diameter and chemical composition of particles exiting the condenser were measured using an aerosol time-of-flight mass spectrometer (ATOFMS). This instrument has been thoroughly described in previous publications (Gard et al., 1997; Pratt et al., 2009). In brief, single particles pass through a Po-210 neutralizer prior to entering an aerodynamic lens that collimates the particle stream (Liu et al., 1995b, a; Zhang et al., 2002, 2004b). Particles are then optically detected upon scattering light from two, 532 nm continuous-wave lasers (JDSU, Model 21011871-200). The velocity of each particle is determined based on the time passed between the scattering signals of both lasers. The vacuum aerodynamic diameter is calculated using a calibration with polystyrene latex spheres of known diameters. The ATOFMS used in this study detects particles with diameters between 100 – 1000 nm with the peak detection efficiency between ~250 – 500 nm (Pratt et al., 2009). The scattering information is also used to trigger a Q-switched pulsed 266 nm, Nd:YAG laser (CFR200, Lumibird), with laser energies systematically varied between 0.1 – 1 mJ, a ~0.45 mm spot size, and 8 ns pulse width, that desorbs and ionizes incoming particles. Once ablated and ionized, positive and negative ion mass spectra for each particle are collected using a dual polarity reflectron time-of-flight mass spectrometer.

The mass spectra and sizing information generated by the ATOFMS were analyzed using the flexible analysis toolkit for the exploration of single-particle mass spectrometer data (FATES) software package within MATLAB (The MathWorks, Inc.) (Sultana et al., 2017b). Datasets were inspected visually using a graphical interface to remove any single-polarity particles. All spectra

presented in the manuscript are an average of dual polarity particles to help eliminate noise. A short discussion is provided in Section 6.8.5 detailing the selection of particles for figures shown throughout this paper. Peaks were assigned based on the most likely ion responsible for a mass-to-charge ratio (*m/z*) considering the analyte and matrix material.

6.8.5 Mass Spectral Data Analysis

This section describes the process of analyzing the various mass spectra shown throughout this manuscript. The FATES package in MATLAB was used to process all the ATOFMS data. First, each dataset was visually inspected in guiFATES, a graphical user interface within FATES, to remove single polarity spectra. Therefore, all spectra analyzed in this study contain ions from both positive and negative polarity.

For the homogeneous nucleation analysis (Figure 6.12) and the heterogeneous growth of DMS (Figure 6.3), particles were further selected based on their total positive ion intensity (TPII). TPII is an indication of the extent of desorption and ionization calculated based on the sum of all positive ion signals from 0-500 *m/z*. Due to the Gaussian beam profile of the desorption/ionization laser, TPII can be valuable for understanding the laser fluence experienced by a particle. Particle mass spectra with lower TPII (compared to the rest of the dataset) showed the least interference from fragmentation of the matrix between 0 and +/- 100 *m/z*, therefore the spectra for Figure 6.12 and Figure 6.3 were selected for low TPII values to best observe the matrix and analyte peaks. However, for Figures 6.4–6.7, all dual polarity particles were averaged (regardless of TPII) to properly show the effects of laser power and matrix-to-analyte ratio on the resulting spectra.

6.9 Supplemental Figures

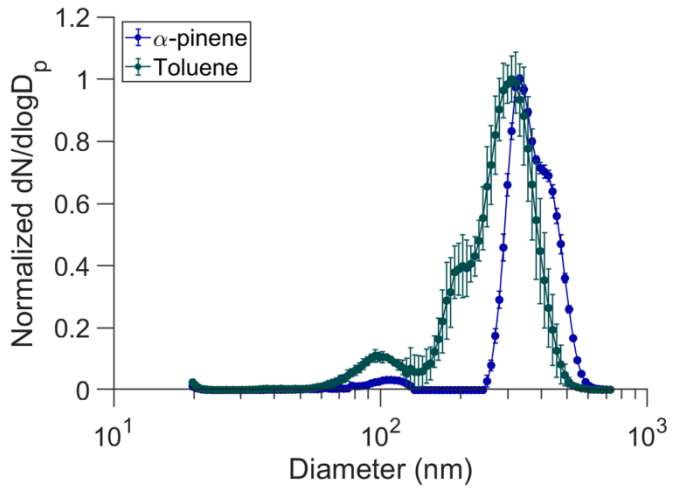

Figure 6.9. Normalized size distributions showing heterogeneous growth using 2,4-DHB. 35 nm seeds of SOA produced from α-pinene (green) and toluene (blue), individually, were grown at 140°C and resulted in peak concentrations at 332 nm and 309 nm, respectively.

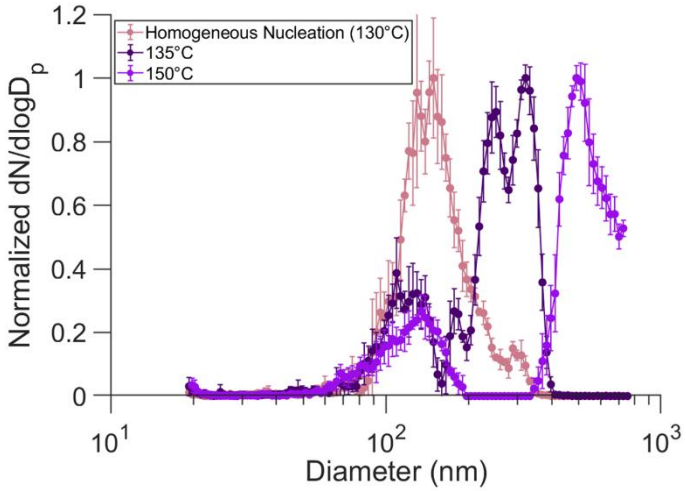

Figure 6.10. Normalized size distributions showing homogeneous nucleation (pink) and heterogeneous growth (dark purple, magenta) of ferulic acid. Homogeneous nucleation of the matrix was measured at 130°C (pink) producing a peak concentration at 148 nm. DMS SOA particles with diameters of 50 nm were heterogeneously grown at 135°C (dark purple) and 150°C (magenta) producing peak concentrations of 320 nm and 490 nm, respectively. Minor homogeneous nucleation modes were observed around 130 nm along with the heterogeneous growth at both temperatures.

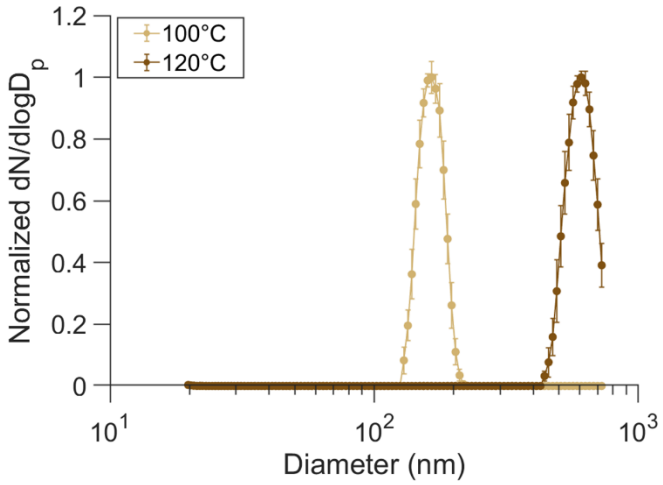

Figure 6.11. Normalized size distributions showing heterogeneous growth using TMGN. The SOA generated from an oxidized mixture of DMS, α-pinene, and toluene was size selected at 35 nm heterogeneously grown at 100°C (tan) and 120°C (brown). These growth profiles have peak concentrations at 164 nm and 607 nm, respectively.

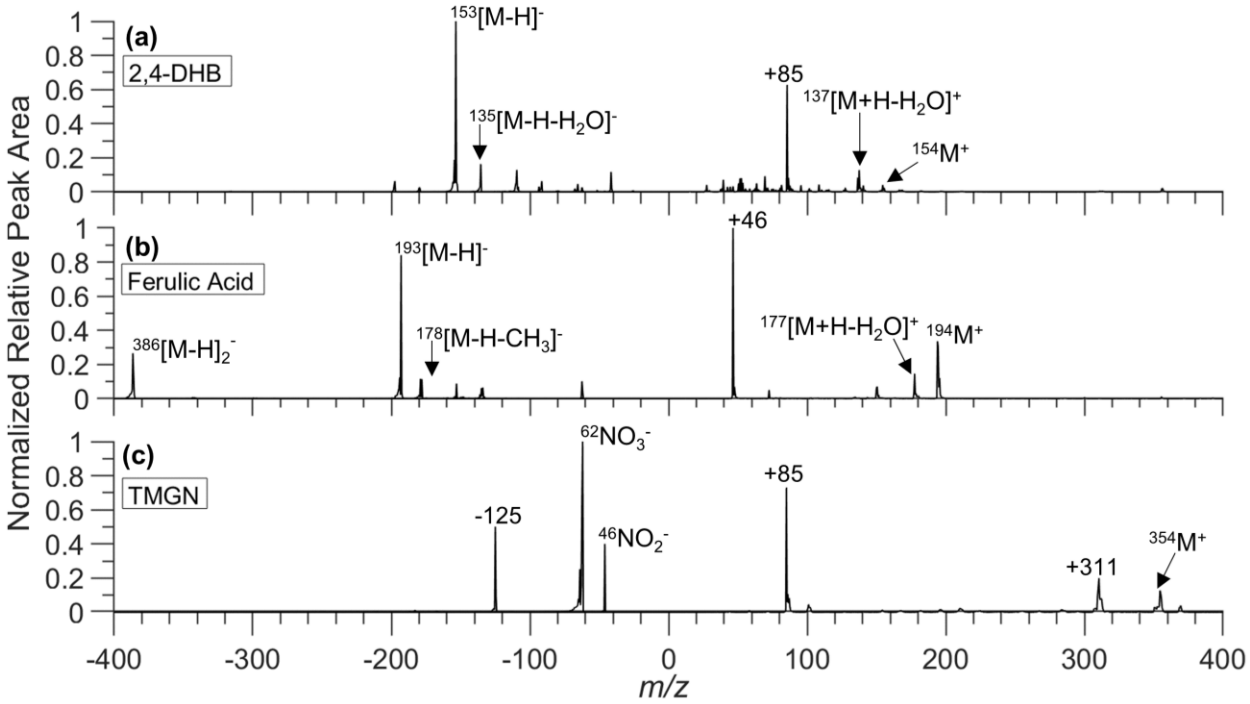

Figure 6.12. Representative mass spectra of homogeneously nucleated particles generated with 2,4-DHB (a), ferulic acid (b), and TMGN (c). The peaks are assigned to the most likely ion occurring at a mass-to-charge ratio.

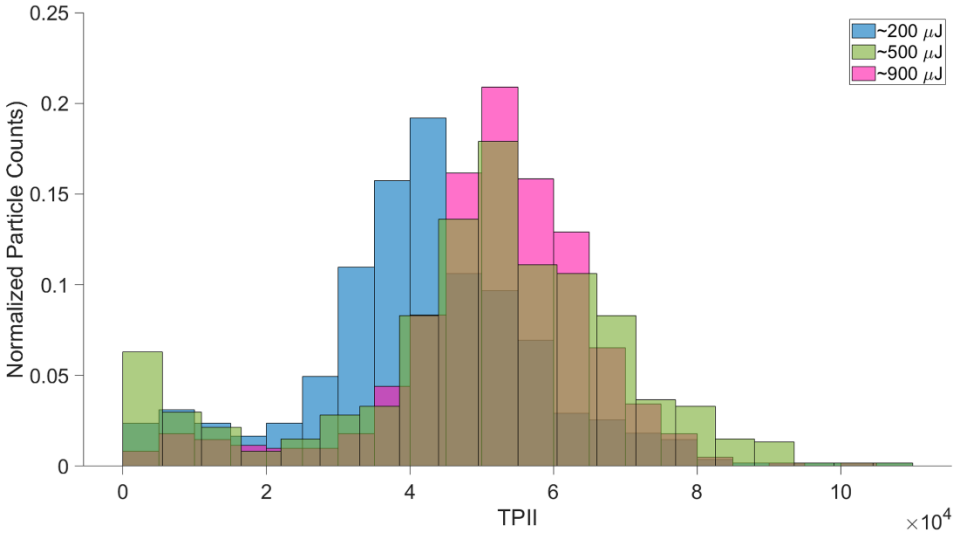

Figure 6.13. Distributions of total positive ion intensity (TPII) for spectra generated with average laser powers of approximately 200, 500, or 900 µJ.

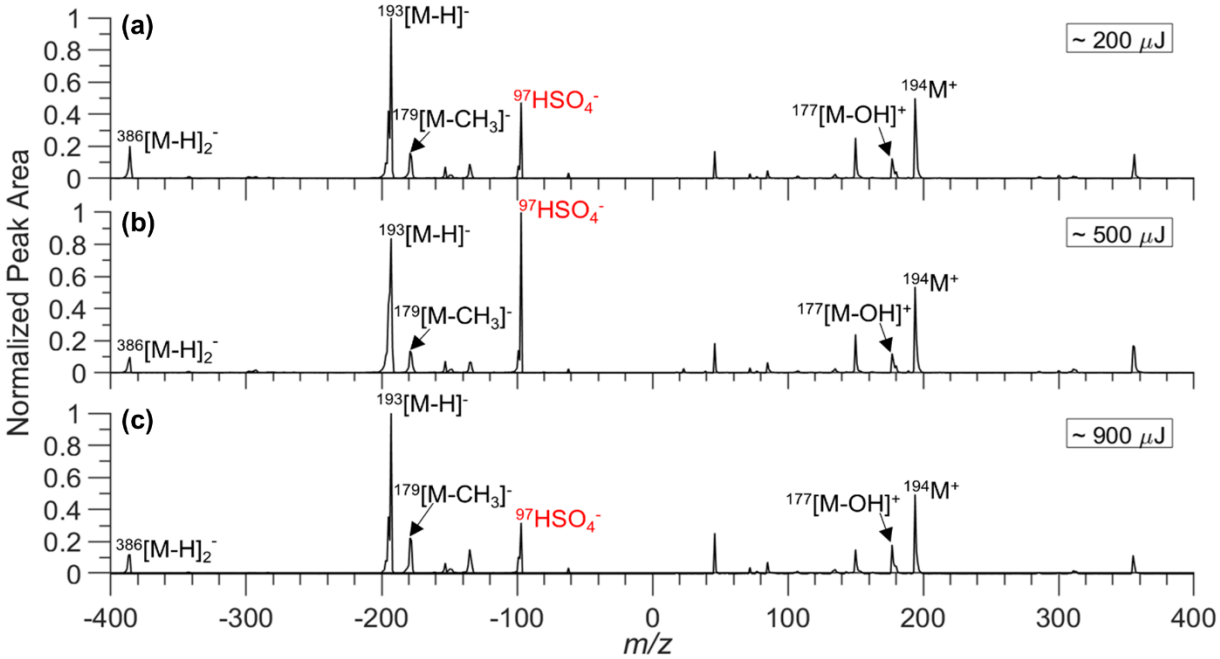

Figure 6.14. Representative mass spectra, pre-selected for low TPII values, of the 100 nm aerosols particles derived from α-pinene and SO_2 mixed coated with ferulic acid and ionized using the laser powers: ~200 (a), 500 (b), and 900 µJ (c).

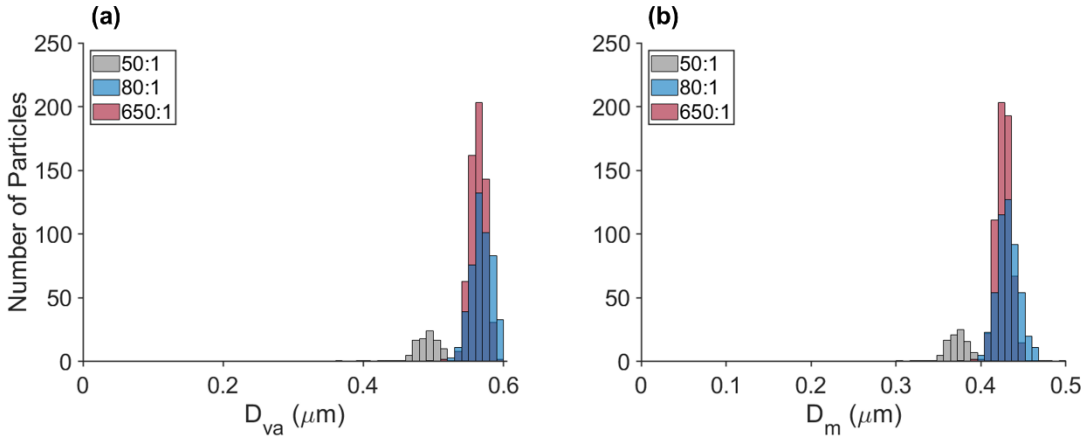

Figure 6.15. Size distributions showing the conversion of the vacuum aerodynamic diameter (D_{va}) recorded by the ATOFMS (a), to the equivalent electromobility diameter, D_m (b).

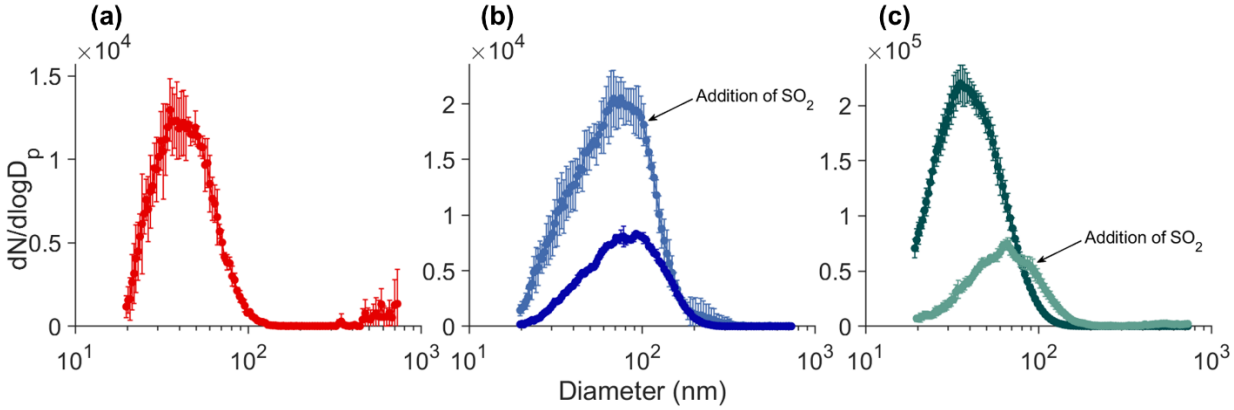

Figure 6.16. Size distributions of the secondary organic aerosols produced in the OFR of DMS (a), α-pinene (b), and toluene (c). These VOCs produce a Gaussian-like distributed SOA profile with the highest concentration of particles occurring at 35 nm, 92 nm, and 35 nm respectively. α-pinene and toluene were also measured with the addition of SO_2, and those peaks occur at 75 nm and 66 nm, respectively.

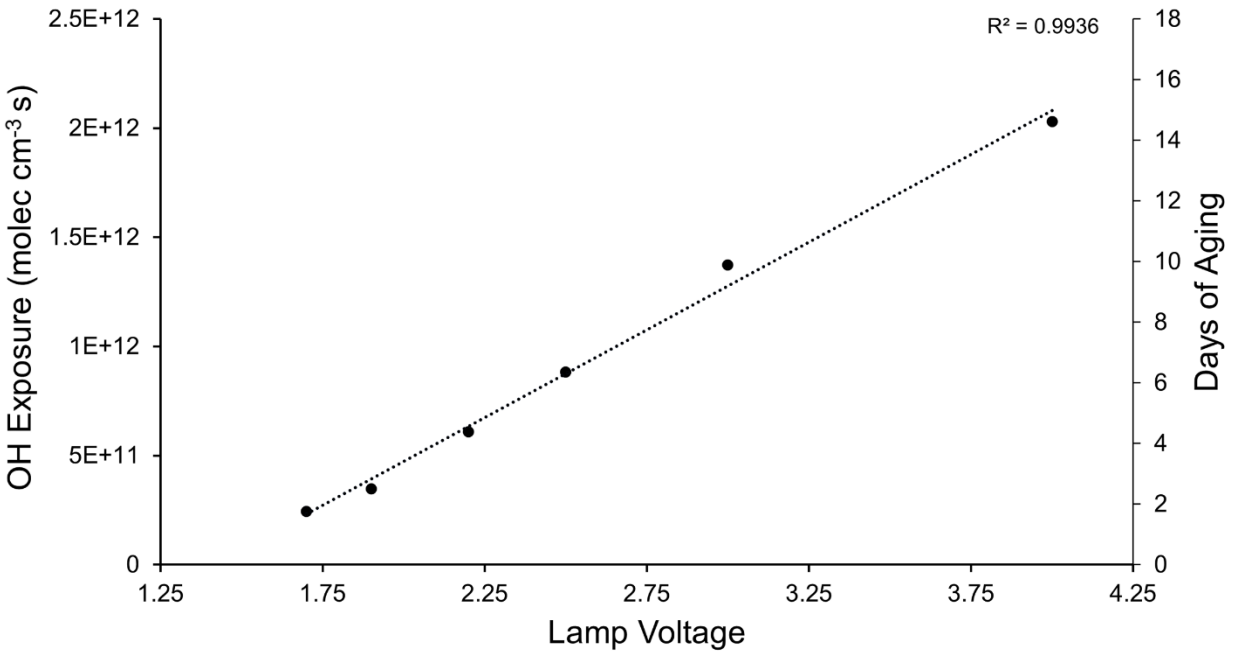

Figure 6.17. Calibration of the OFR performed to determine the days of equivalent atmospheric aging as a function of OH exposure. Lamp voltage was set to 1.7V for all experiments, resulting in ~1.87 days of equivalent aging imposed on particles inside the chamber.

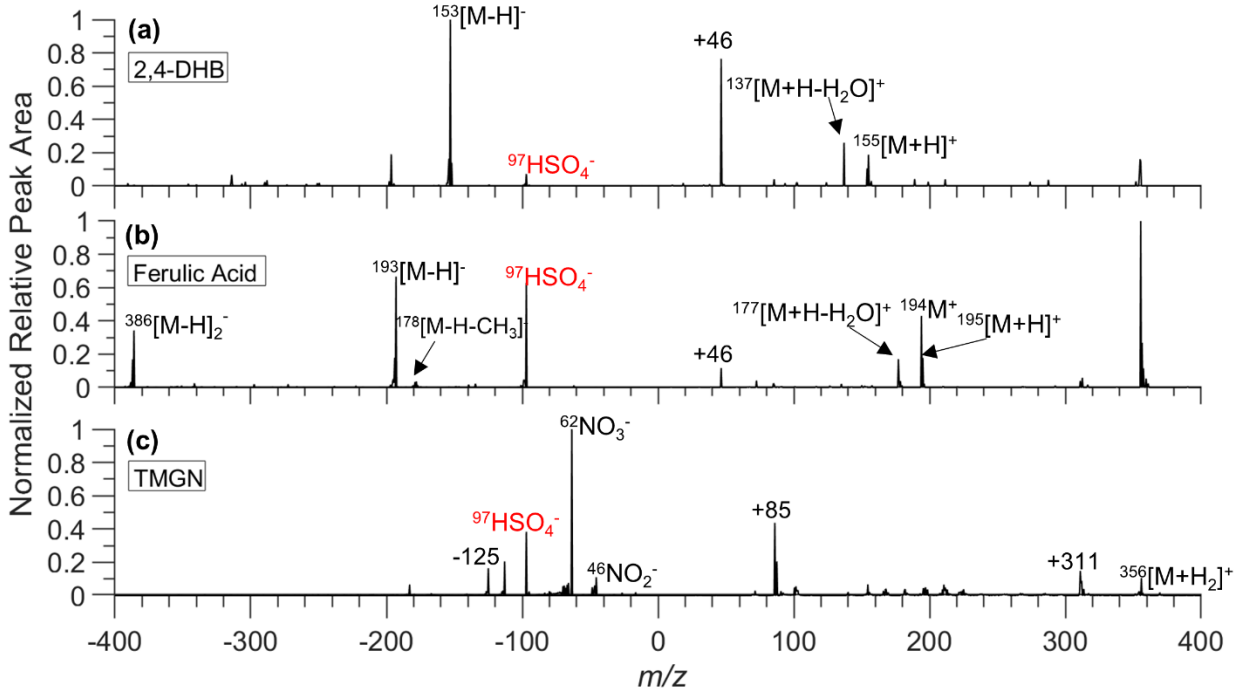

Figure 6.18. Representative mass spectra of the chemical composition of a single 50 nm DMS SOA analyte particle after condensation with the MALDI matrix 2,4 DHB (a), ferulic acid (b), or TMGN (c).

6.10 References

Agarwal, J. K. and Sem, G. J.: Continuous flow, single-particle-counting condensation nucleus counter, J. Aerosol Sci., 11, 343–357, https://doi.org/10.1016/0021-8502(80)90042-7, 1980.

Ayers, G. P. and Gillett, R. W.: DMS and its oxidation products in the remote marine atmosphere: Implications for climate and atmospheric chemistry, J. Sea Res., 43, 275–286, https://doi.org/10.1016/S1385-1101(00)00022-8, 2000.

Barnes, I., Hjorth, J., and Mihalapoulos, N.: Dimethyl sulfide and dimethyl sulfoxide and their oxidation in the atmosphere, Chem. Rev., 106, 940–975, https://doi.org/10.1021/cr020529, 2006.

Bates, T. S., Calhoun, J. A., and Quinn, P. K.: Variations in the methanesulfonate to sulfate molar ratio in submicrometer marine aerosol particles over the south Pacific Ocean, J. Geophys. Res. Atmos., 97, 9859–9865, https://doi.org/10.1029/92JD00411, 1992.

Beeson, M. D., Murray, K. K., and Russell, D. H.: Aerosol Matrix-Assisted Laser Desorption Ionization: Effects of Analyte Concentration and Matrix-to-Analyte Ratio, Anal. Chem, 67, 1981–1986, 1995.

Boucher, O., Randall, D., Artaxo, P., Bretherton, C., Feingold, G., Forster, P., Kerminen, V.-M. V.-M., Kondo, Y., Liao, H., Lohmann, U., Rasch, P., Satheesh, S. K., Sherwood, S., Stevens, B., Zhang, X. Y., and Zhan, X. Y.: Clouds and Aerosols, Clim. Chang. 2013 Phys. Sci. Basis. Contrib. Work. Gr. I to Fifth Assess. Rep. Intergov. Panel Clim. Chang., 571–657, https://doi.org/10.1017/CBO9781107415324.016, 2013.

Cao, D., Wang, Z., Han, C., Cui, L., Hu, M., Wu, J., Liu, Y., Cai, Y., Wang, H., and Kang, Y.: Quantitative detection of trace perfluorinated compounds in environmental water samples by Matrix-assisted Laser Desorption/Ionization-Time of Flight Mass Spectrometry with 1,8-bis(tetramethylguanidino)-naphthalene as matrix, Talanta, 85, 345–352, https://doi.org/10.1016/J.TALANTA.2011.03.062, 2011.

Charlson, R. J., Lovelock, J. E., Andreae, M. O., and Warren, S. G.: Oceanic phytoplankton, atmospheric sulphur, cloud albedo and climate, Nature, 326, 655–661, https://doi.org/10.1038/326655a0, 1987.

Chen, W. C. and Marcus, R. A.: On the theory of the reaction rate of vibrationally excited CO molecules with OH radicals, J. Chem. Phys., 124, 024306, https://doi.org/10.1063/1.2148408, 2006.

Cohen, L. H. and Gusev, A. I.: Small molecule analysis by MALDI mass spectrometry, Anal. Bioanal. Chem. 2002 3737, 373, 571–586, https://doi.org/10.1007/S00216-002-1321-Z, 2002.

DeCarlo, P. F., Slowik, J. G., Worsnop, D. R., Davidovits, P., and Jimenez, J. L.: Particle morphology and density characterization by combined mobility and aerodynamic diameter measurements. Part 1: Theory, Aerosol Sci. Technol., 38, 1185–1205, https://doi.org/10.1080/027868290903907, 2004.

DeCarlo, P. F., Kimmel, J. R., Trimborn, A., Northway, M. J., Jayne, J. T., Aiken, A. C., Gonin, M., Fuhrer, K., Horvath, T., Docherty, K. S., Worsnop, D. R., and Jimenez, J. L.: Field-deployable, high-resolution, time-of-flight aerosol mass spectrometer, Anal. Chem., 78, 8281–8289, https://doi.org/10.1021/AC061249N/SUPPL_FILE/AC061249NSI20060905_075156.PDF, 2006.

Fan, J., Zhang, R., Collins, D., and Li, G.: Contribution of secondary condensable organics to new particle formation: A case study in Houston, Texas, Geophys. Res. Lett., 33, https://doi.org/10.1029/2006GL026295, 2006.

Fuchs, N. A.: On the stationary charge distribution on aerosol particles in a bipolar ionic atmosphere, Geofis. Pura e Appl., 56, 185–193, https://doi.org/10.1007/BF01993343, 1963.

Gard, E., Mayer, J. E., Morrical, B. D., Dienes, T., Fergenson, D. P., and Prather, K. A.: Real-Time Analysis of Individual Atmospheric Aerosol Particles: Design and Performance of a Portable ATOFMS, Anal. Chem., 69, 4083–4091, https://doi.org/10.1021/ac970540n, 1997.

Gaston, C. J., Pratt, K. A., Qin, X., and Prather, K. A.: Real-Time Detection and Mixing State of Methanesulfonate in Single Particles at an Inland Urban Location during a Phytoplankton Bloom, Environ. Sci. Technol., 44, 1566–1572, https://doi.org/10.1021/es902069d, 2010.

Guo, Z. and He, L.: A binary matrix for background suppression in MALDI-MS of small molecules, Anal. Bioanal. Chem., 387, 1939–1944, https://doi.org/10.1007/S00216-006-1100-3/FIGURES/4, 2007.

Hallquist, M., Wenger, J. C., Baltensperger, U., Rudich, Y., Simpson, D., Claeys, M., Dommen, J., Donahue, N. M., George, C., Goldstein, A. H., Hamilton, J. F., Herrmann, H., Hoffmann, T., Iinuma, Y., Jang, M., Jenkin, M. E., Jimenez, J. L., Kiendler-Scharr, A., Maenhaut, W., McFiggans, G., Mentel, T. F., Monod, A., Prévôt, A. S. H., Seinfeld, J. H., Surratt, J. D., Szmigielski, R., and Wildt, J.: The formation, properties and impact of secondary organic aerosol: Current and emerging issues, Atmos. Chem. Phys., 9, 5155–5236, https://doi.org/10.5194/acp-9-5155-2009, 2009.

Hopkins, R. J., Desyaterik, Y., Tivanski, A. V, Zaveri, R. A., Berkowitz, C. M., Tyliszczak, T., Gilles, M. K., Laskin, A., Hopkins, C. :, Desyaterik, Y., Tivanski, A. V, Zaveri, R. A., Berkowitz, C. M., Tyliszczak, T., Gilles, M. K., and Laskin, A.: Chemical speciation of sulfur in marine cloud droplets and particles: Analysis of individual particles from the marine boundary layer over the California current, J. Geophys. Res. Atmos., 113, 4209,

https://doi.org/10.1029/2007JD008954, 2008.

Jayne, J. T., Leard, D. C., Zhang, X., Davidovits, P., Smith, K. A., Kolb, C. E., and Worsnop, D. R.: Development of an aerosol mass spectrometer for size and composition analysis of submicron particles, Aerosol Sci. Technol., 33, 49–70, https://doi.org/10.1080/027868200410840, 2000.

Kang, E., Root, M. J., Toohey, D. W., and Brune, W. H.: Introducing the concept of Potential Aerosol Mass (PAM), Atmos. Chem. Phys, 7, 5727–5744, https://doi.org/https://doi.org/10.5194/acp-7-5727-2007, 2007.

Kim, S. H., Shin, C. M., and Yoo, J. S.: First application of thermal vapor deposition method to matrix-assisted laser desorption ionization mass spectrometry: Determination of molecular mass of bis(p-methyl benzylidene) sorbitol, Rapid Commun. Mass Spectrom., 12, 701–704, https://doi.org/10.1002/(SICI)1097-0231(19980615)12:11<701::AID-RCM223>3.0.CO;2-B, 1998.

Kleefsman, I., Stowers, M. A., Verheijen, P. J. T., Van Wuijckhuijse, A. L., Kientz, C. E., and Marijnissen, J. C. M.: Bioaerosol analysis by single particle mass spectrometry, Part. Part. Syst. Charact., 24, 85–90, https://doi.org/10.1002/ppsc.200601049, 2007.

Kleefsman, W. A., Stowers, M. A., Verheijen, P. J. T., and Marijnissen, J. C. M.: Single particle mass spectrometry-bioaerosol analysis by MALDI MS, KONA Powder Part. J., 26, 205–214, https://doi.org/10.14356/kona.2008018, 2008.

Kroll, J. H. and Seinfeld, J. H.: Chemistry of secondary organic aerosol: Formation and evolution of low-volatility organics in the atmosphere, Atmos. Environ., 42, 3593–3624, https://doi.org/10.1016/j.atmosenv.2008.01.003, 2008.

Lambe, A. T., Ahern, A. T., Williams, L. R., Slowik, J. G., Wong, J. P. S., Abbatt, J. P. D., Brune, W. H., Ng, N. L., Wright, J. P., Croasdale, D. R., Worsnop, D. R., Davidovits, P., and Onasch, T. B.: Characterization of aerosol photooxidation flow reactors: heterogeneous oxidation, secondary organic aerosol formation and cloud condensation nuclei activity measurements, Atmos. Meas. Tech, 4, 445–461, https://doi.org/10.5194/amt-4-445-2011, 2011.

Liu, B. Y. H. and Pui, D. Y. H.: Electrical neutralization of aerosols, J. Aerosol Sci., 5, 465–472, https://doi.org/10.1016/0021-8502(74)90086-X, 1974.

Liu, P., Ziemann, P. J., Kittelson, D. B., and McMurry, P. H.: Generating particle beams of controlled dimensions and divergence: I. Theory of particle motion in aerodynamic lenses and nozzle expansions, Aerosol Sci. Technol., 22, 293–313, https://doi.org/10.1080/02786829408959748, 1995a.

Liu, P., Ziemann, P. J., Kittelson, D. B., and McMurry, P. H.: Generating particle beams of controlled dimensions and divergence: II. Experimental evaluation of particle motion in

aerodynamic lenses and nozzle expansions, Aerosol Sci. Technol., 22, 314–324, https://doi.org/10.1080/02786829408959749, 1995b.

Mayer, K. J., Wang, X., Santander, M. V., Mitts, B. A., Sauer, J. S., Sultana, C. M., Cappa, C. D., and Prather, K. A.: Secondary Marine Aerosol Plays a Dominant Role over Primary Sea Spray Aerosol in Cloud Formation, ACS Cent. Sci., 6, 2259–2266, https://doi.org/10.1021/acscentsci.0c00793, 2020.

Mcjimpsey, E. L., Jackson, W. M., Lebrilla, C. B., Tobias, H., Bogan, M. J., Gard, E. E., Frank, M., and Steele, P. T.: ARTICLES Parameters Contributing to Efficient Ion Generation in Aerosol MALDI Mass Spectrometry, https://doi.org/10.1016/j.jasms.2007.11.009, 2008.

Morrical, B. D., Fergenson, D. P., and Prather, K. A.: Coupling two-step laser desorption/ ionization with aerosol time-of-flight mass spectrometry for the analysis of individual organic particles, J. Am. Soc. Mass Spectrom., 9, 1068–1073, https://doi.org/10.1016/S1044-0305(98)00074-9, 1998.

Murray, K. K.: Lasers for matrix-assisted laser desorption ionization, J. Mass Spectrom., 56, e4664, https://doi.org/10.1002/JMS.4664, 2021.

Murray, K. K. and Russell, D. H.: Aerosol Matrix-Assisted Laser Desorption Ionization Mass Spectrometry, J Am Soc Mass Spectrom, 5, 1–9, 1994.

Noble, C. A., Prather, K. A., Noble, C. A., and Prnther, K. A.: Single Particle Characterization of Albuterol Metered Dose Inhaler Aerosol in Near Real-Time, Aerosol Sci. Technol., 29, 306, https://doi.org/10.1080/02786829808965570, 1998.

Pandis, S. N., Harley, R. A., Cass, G. R., and Seinfeld, J. H.: Secondary organic aerosol formation and transport, Atmos. Environ. Part A, Gen. Top., 26, 2269–2282, https://doi.org/10.1016/0960-1686(92)90358-R, 1992.

Pöschl, U.: Atmospheric aerosols: Composition, transformation, climate and health effects, Angew. Chemie - Int. Ed., 44, 7520–7540, https://doi.org/10.1002/ANIE.200501122, 2005.

Prather, K. A., Nordmeyer, T., Salt, K., and J Colloid, S. K.: Real-Time Characterization of Individual Aerosol Particles Using Time-of-Flight Mass Spectrometry, 66, 1403–1407, https://doi.org/https://doi.org/10.1021/ac00081a007, 1994.

Prather, K. A., Bertram, T. H., Grassian, V. H., Deane, G. B., Stokes, M. D., DeMott, P. J., Aluwihare, L. I., Palenik, B. P., Azam, F., Seinfeld, J. H., Moffet, R. C., Molina, M. J., Cappa, C. D., Geiger, F. M., Roberts, G. C., Russell, L. M., Ault, A. P., Baltrusaitis, J., Collins, D. B., Corrigan, C. E., Cuadra-Rodriguez, L. A., Ebben, C. J., Forestieri, S. D., Guasco, T. L., Hersey, S. P., Kim, M. J., Lambert, W. F., Modini, R. L., Mui, W., Pedler, B. E., Ruppel, M. J., Ryder, O. S., Schoepp, N. G., Sullivan, R. C., and Zhao, D.: Bringing the ocean into the laboratory to probe the chemical complexity of sea spray aerosol, Proc.

Natl. Acad. Sci. U. S. A., 110, 7550–7555, https://doi.org/10.1073/pnas.1300262110, 2013.

Pratt, K. A. and Prather, K. A.: Mass spectrometry of atmospheric aerosols-Recent developments and applications. Part II: On-line mass spectrometry techniques, Mass Spectrom. Rev., 31, 17–48, https://doi.org/10.1002/mas.20330, 2012.

Pratt, K. A., Mayer, J. E., Holecek, J. C., Moffet, R. C., Sanchez, R. O., Rebotier, T. P., Furutani, H., Gonin, M., Fuhrer, K., Su, Y., Guazzotti, S., and Prather, K. A.: Development and Characterization of an Aircraft Aerosol Time-of-Flight Mass Spectrometer, Anal. Chem., 81, 1792–1800, https://doi.org/10.1021/ac801942r, 2009.

Raab, V., Kipke, J., Gschwind, R. M., and Sundermeyer, J.: 1,8-Bis(tetramethylguanidino)naphthalene (TMGN): A new, superbasic and kinetically active "proton sponge," Chem. - A Eur. J., 8, 1682–1693, https://doi.org/10.1002/1521-3765(20020402)8:7<1682::AID-CHEM1682>3.0.CO;2-R, 2002.

Seinfeld, J. H. and Pandis, S. N.: Atmospheric chemistry and physics : From air pollution to climate change, 3rd ed., Wiley, 2016.

Silva, P. J., Prather, K., Noble, C. A., and Prather, K. A.: Size and Chemical Characterization of Individual Particles Resulting from Biomass Burning of Local Southern California Species Size and Chemical Characterization of Individual Particles Resulting from Biomass Burning of Local Southern California Species, Environ. Sci. Technol., 33, 3068–3076, https://doi.org/10.1021/es980544p, 1999.

Smith, S. J., Pitchera, H., and Wigley, T. M. L.: Global and regional anthropogenic sulfur dioxide emissions, Glob. Planet. Change, 29, 99–119, https://doi.org/10.1016/S0921-8181(00)00057-6, 2001.

Spencer, M. T., Furutani, H., Oldenburg, S. J., Darlington, T. K., and Prather, K. A.: Gold Nanoparticles as a Matrix for Visible-Wavelength Single-Particle Matrix-Assisted Laser Desorption/Ionization Mass Spectrometry of Small Biomolecules, J. Phys. Chem. C, 112, 4083–4090, https://doi.org/10.1021/jp076688k, 2008.

Stowers, M. A., Wuijckhuijse, A. L. Van, Marijnissen, J. C. M., Scarlett, B., and Baar, B. L. M. Van: Application of matrix-assisted laser desorption / ionization to on-line aerosol time-of-flight mass spectrometry, Rapid Commun. Mass Spectrom., 14, 829–833, 2000.

Sullivan, R. C. and Prather, K. A.: Recent advances in our understanding of atmospheric chemistry and climate made possible by on-line aerosol analysis instrumentation, Anal. Chem., 77, 3861–3885, https://doi.org/10.1021/ac050716i, 2005.

Sultana, C. M., Collins, D. B., and Prather, K. A.: Effect of Structural Heterogeneity in Chemical Composition on Online Single-Particle Mass Spectrometry Analysis of Sea Spray Aerosol Particles, Environ. Sci. Technol., 51, 3660–3668, https://doi.org/10.1021/acs.est.6b06399,

2017a.

Sultana, C. M., Cornwell, G. C., Rodriguez, P., and Prather, K. A.: FATES: A flexible analysis toolkit for the exploration of single-particle mass spectrometer data, Atmos. Meas. Tech., 10, 1323–1334, https://doi.org/10.5194/AMT-10-1323-2017, 2017b.

Wenzel, R. J. and Prather, K. A.: Improvements in ion signal reproducibility obtained using a homogeneous laser beam for on-line laser desorption/ionization of single particles, Rapid Commun. Mass Spectrom., 18, 1525–1533, https://doi.org/10.1002/rcm.1509, 2004.

Whiteakert, J. R. and Prather, K. A.: Detection of pesticide residues on individual particles, Anal. Chem., 75, 49–56, https://doi.org/10.1021/ac025771v, 2003.

Wolfe, G. M., Nicely, J. M., Clair, J. M. S., Hanisco, T. F., Liao, J., Oman, L. D., Brune, W. B., Miller, D., Thames, A., Abad, G. G., Ryerson, T. B., Thompson, C. R., Peischl, J., McCain, K., Sweeney, C., Wennberg, P. O., Kim, M., Crounse, J. D., Hall, S. R., Ullmann, K., Diskin, G., Bui, P., Chang, C., and Dean-Day, J.: Mapping hydroxyl variability throughout the global remote troposphere via synthesis of airborne and satellite formaldehyde observations, Proc. Natl. Acad. Sci. U. S. A., 116, 11171–11180, https://doi.org/10.1073/PNAS.1821661116, 2019.

van Wuijckhuijse, A. L., Stowers, M. A., Kleefsman, W. A., Van Baar, B. L. M., Kientz, C. E., and Marijnissen, J. C. M.: Matrix-assisted laser desorption/ionisation aerosol time-of-flight mass spectrometry for the analysis of bioaerosols: Development of a fast detector for airborne biological pathogens, J. Aerosol Sci., 36, 677–687, https://doi.org/10.1016/j.jaerosci.2004.11.003, 2005.

Zelenyuk, A., Juan, Y., Chen, S., Zaveri, R. A., and Imre, D.: “Depth-profiling” and quantitative characterization of the size, composition, shape, density, and morphology of fine particles with SPLAT, a single-particle mass spectrometer, J. Phys. Chem. A, 112, 669–671, https://doi.org/10.1021/jp077308y, 2008.

Zenobi, R. and Knochenmuss, R.: Ion formation in maldi mass spectrometry, Mass Spectrom. Rev., 17, 337–366, https://doi.org/10.1002/(sici)1098-2787(1998)17:5<337::aid-mas2>3.0.co;2-s, 1998.

Zhang, Q., Stanier, C. O., Canagaratna, M. R., Jayne, J. T., Worsnop, D. R., Pandis, S. N., and Jimenez, J. L.: Insights into the Chemistry of New Particle Formation and Growth Events in Pittsburgh Based on Aerosol Mass Spectrometry, Environ. Sci. Technol., 38, 4797–4809, https://doi.org/10.1021/ES035417U, 2004a.

Zhang, X., Smith, K. A., Worsnop, D. R., Jimenez, J., Jayne, J. T., and Kolb, C. E.: A numerical characterization of particle beam collimation by an aerodynamic lens-nozzle system: Part I. An individual lens or nozzle, Aerosol Sci. Technol., 36, 617–631, https://doi.org/10.1080/02786820252883856, 2002.

Zhang, X., Smith, K. A., Worsnop, D. R., Jimenez, J. L., Jayne, J. T., Kolb, C. E., Morris, J., and Davidovits, P.: Numerical characterization of particle beam collimation: Part II integrated aerodynamic-lens-nozzle system, Aerosol Sci. Technol., 38, 619–638, https://doi.org/10.1080/02786820490479833, 2004b.

Zhao, R., Zhang, Q., Xu, X., Zhao, W., Yu, H., Wang, W., Zhang, Y., and Zhang, W.: Effect of experimental conditions on secondary organic aerosol formation in an oxidation flow reactor, Atmos. Pollut. Res., 12, 205–213, https://doi.org/10.1016/J.APR.2021.01.011, 2021.

Zhou, L., Zhu, Y., Guo, X., Zhao, W., Zheng, H., Gu, X., Fang, L., and Zhang, W.: Effects of Matrix-to-analyte Ratio and Laser Energy on Peptides Ion Signals, Chinese J. Chem. Phys., 19, 207, https://doi.org/10.1360/CJCP2006.19(3).207.4, 2013.

Chapter 7. Conclusions

7.1 Synopsis

This dissertation investigates the detection of biological aerosols (bioaerosols) released in marine environments and the impact of these particles on clouds and climate. Chapter 2 describes the influence of supermicron-size sea spray aerosol (SSA) particles on ice nucleating particle (INP) concentrations released in marine systems. Chapter 3 demonstrates the use of single-particle fluorescence-based techniques to measure the composition and distribution of bioaerosols released in nascent SSA. Chapter 4 examines the effects of atmospheric aging on the fluorescence composition of SSA in an isolated ocean-atmosphere system. Chapter 5 describes online fluorescence measurements to distinguish marine and continental particles sources in an urban-coastal environment. Finally, Chapter 6 uses a novel single-particle system to measure the chemical composition of sub-100 nm secondary organic aerosols (SOA) produced from biogenic volatile organic compounds.

7.2 Conclusions

7.2.1 Importance of supermicron ice nucleating particles in nascent sea spray

Chapter 2 investigated the size-dependent influence of SSA on INP concentrations measured from a marine environment. Previous reports and modeling studies have placed a significant emphasis on the ice nucleating ability of submicron SSA (Burrows et al., 2013; Wilson et al., 2015; Huang et al., 2018; Vergara-Temprado et al., 2017) because organics are enriched in submicron SSA particles. However, field measurements have proposed that supermicron SSA may play an important role acting as INPs (Creamean et al., 2019; Ladino et al., 2019; Mason et al., 2015, 2016; McCluskey et al., 2018a, b; Si et al., 2018). In this study, supermicron SSA particles

were the dominant source of INPs at warm temperatures throughout all phases of a phytoplankton bloom, suggesting these particles are the primary source of INPs in the marine environment.

Additionally, the ice nucleating efficiency of each size population was investigated by analyzing the active site density and volume site density. It was shown that the concentration of INP active sites in SSA scaled with particle volume. While most studies investigate the surface-area normalized INP concentration (McCluskey et al., 2019; Niemand et al., 2012; DeMott et al., 2016), here, we found the volume normalized INP concentration showed comparable values between the submicron and total SSA particle populations. Thus, unlike dust particles which are often solid, the hydrated nature of nascent SSA allows for ice nucleating active sites in the interior of the particle. The results from this study enabled a new parameterization relating INP concentrations to SSA particle volume, which can be used in global climate models to better represent the impact of SSA on cloud processes and the global radiative balance.

7.2.2 Tandem fluorescence measurements of organic matter and bacteria released in sea spray aerosols

To investigate the release of bioaerosols in SSA, Chapter 3 focused on the detection of fluorescent SSA generated from natural seawater. Online SSA measurements were made using the WIBS in tandem with offline aerosol measurements with EEMS. Both fluorescence techniques recorded similar trends in SSA fluorescence intensities over the course of a phytoplankton mesocosm bloom, confirming the use of the WIBS to accurately detect fluorescent bioaerosols released in SSA. Additionally, EEMS of the bulk solution showed the fluorescence signature of SSA significantly differs from the bulk fluorescence profile, suggesting selective transfer and enrichment of certain fluorescent species into SSA.

Using the WIBS, size distributions of fluorescent, nascent SSA showed, for the first time, unique size profiles depending on the particle fluorescence signature. Particles with protein-like fluorescence in channel 1 (ex/em: 280 nm / 300–420 nm) had a primary size mode around 2–3 μm, suggestive of microbes such as marine bacteria, whereas particles fluorescent in channel 3 (ex/em: 370 nm / 420–650 nm) showed a dominant submicron mode, suggestive of dissolved HULIS (Benner et al., 1992). Additionally, marine bacteria aerosolized with a breaking wave proxy showed a similar protein-like fluorescence and size mode matching that of nascent SSA. This study was the first to definitively identify the fluorescence signature of marine bacteria in an aerosol and demonstrate the use of fluorescence techniques to measure the emission of bioaerosols in SSA.

7.2.3 Single-particle fluorescence properties of oxidized sea spray aerosol

In the ambient environment, nascent SSA particles undergo chemical reactions with atmospheric oxidants which can alter the chemical and morphological properties of these aerosols. Chapter 4 investigated the effect of atmospheric aging on the fluorescence profile of naturally produced SSA by exposing these particles to large concentrations of hydroxy radical using an oxidative flow reactor. Aged SSA showed a clear reduction of channel 1 fluorescence and an increase in channel 2 and channel 3 fluorescence compared to nascent SSA. This shift was attributed to the oxidative degradation of tryptophan in SSA particles and the formation of tryptophan oxidation products which fluoresce in channels 2 and 3 (Ignatenko et al., 1982; Fukunaga et al., 1982; Pan et al., 2014). These oxidative changes occurred for SSA particles across all sizes. Additionally, we observed a significant increase in the fraction of aged particles with humic-like fluorescence throughout the course of a phytoplankton bloom. These results suggest the reactivity of atmospheric oxidants and fluorescent molecules in SSA change throughout a phytoplankton bloom, potentially due to chemical changes in the seawater and the resulting SSA.

Furthermore, the reported changes highlight the importance of atmospheric aging on SSA for bioaerosol identification and climate implications.

7.2.4 Real-Time Fluorescence Measurements of Marine and Continental Aerosols in a Coastal Environment

Chapter 5 utilized the WIBS to investigate the fluorescence profile of aerosol populations in an urban-coastal environment in Southern California. Two sampling locations were chosen for this experiment: 1) Border Field (BF), located along the coast at the United States-Mexico border, and 2) on the Ellen Browning Scripps Memorial pier (Scripps Pier) in La Jolla, California. The BF site was influenced by anthropogenic aerosols from metropolitan Tijuana and SSA with potential sewage contamination from local wastewater runoff. The second sampling site, at the Scripps Institution of Oceanography (SIO), was chosen as a reference site for SSA measurements because of its distance from major metropolitan areas and wastewater runoff sources. The WIBS, combined with black carbon (a proxy for anthropogenic aerosols), wind speed, and wind direction measurements, was used to identify periods when potentially contaminated SSA particles were present at BF and understand the influence of various particle sources on the local communities.

We observed a significant difference between the fluorescent profile of continental/anthropogenic aerosols and marine aerosols. Marine air masses were characterized by a relatively low fluorescent particle fraction, often less than ~10%, containing class A and class C particles, resemblant of marine microbes and humic-like substances found in SSA, respeectively. The fluorescent particles from marine origins at BF had similar fluorescence profiles to the SIO marine air masses, but typically showed higher concentrations of microbial bioaerosols, indicative of the wastewater and pollution runoff in the coastal waters near BF. In contrast, continental air masses were classified by high fluorescent fractions that were predominantly class BC and class

ABC particles. At BF, particles from continental air masses exhibited high fluorescence intensities and small particle diameters, indicative of combustion related particles with fluorescence from polycyclic aromatic hydrocarbons. The particle fluorescent fractions from each source were consistent with previously observed trends (Kawana et al., 2021; Moallemi et al., 2021; Wei et al., 2016; Yue et al., 2017). The drastically different marine air mass profiles and continental/anthropogenic air mass profile demonstrate online fluorescence measurements can effectively distinguish between periods when SSA or anthropogenic sources are present in coastal communities. Additionally, WIBS class C fluorescent fractions at BF showed a strong correlation with the outflow of the Tijuana River, a source of wastewater contamination, suggesting a potential method for detecting the influence of sewage on SSA composition.

7.2.5 Optimization and Application of a Condensation Matrix-Assisted Aerosol Time-of-Flight Mass Spectrometer

Chapter 6 describes the characterization and optimization of a novel system which combines a sublimation-condensation laminar flow tube containing a solid MALDI matrix with an ATOFMS to make a condensation matrix-assisted aerosol time-of-flight mass spectrometer (cMA-ATOFMS) system for small molecule detection and chemical identification. This system was tested on SOA particles generated from the oxidation of VOCs in an oxidative flow reactor with particle diameters < 100 nm, falling below the typical detection limit of the ATOFMS (Pratt et al., 2009). Because of matrix growth on analyte particles in the sublimation-condensation flow tube, single-particle mass spectra were obtained for particles that were previously unable to be analyzed.

Utilizing this novel system, SOA particles generated from the oxidation of dimethyl sulfide (DMS) with diameters as low as 20 nm were able to be detected and chemically identified. The

cMA-ATOFMS system was characterized using three different MALDI matrices and showed higher laser powers and lower matrix-to-analyte ratios generally resulted in the highest analyte signal, in line with aerosol MALDI experiments (Murray and Russell, 1994). This system was shown to discriminate between secondary aerosols generated from different gaseous precursors by identifying differences in the chemical composition of secondary aerosols generated from SO_2 gas and from DMS. These gaseous precursors often represent anthropogenic and biogenic sulfur sources, respectively (Charlson et al., 1987; Bates et al., 1992; Smith et al., 2001). The identification of methanesulfonic acid, was observed solely in the SOA produced with DMS, suggesting this system may be useful for source apportionment in an ambient setting. Using this novel system, the mixing state of SOA particles can be analyzed and the chemical composition of small biological particles, such as viruses, can be measured.

7.3 Future Directions

7.3.1 Identification of ice nucleating species and selective transfer into SSA

Chapter 2 demonstrated how supermicron SSA particles were the dominant source of INPs across all phases of a phytoplankton bloom. However, the molecular composition of INPs in SSA has yet to be elucidated and will require future studies on the chemical and biological composition of INP samples to better understand the main components of ice nucleation in SSA. Additionally, it was demonstrated in this study that concentrations of ice nucleating entities (INEs) in the seawater increased with bloom progression, but the same trend was not observed in SSA. This disconnect suggests a selective transfer and enrichment of specific INPs in the aerosol phase emitted from the bulk seawater, likely due to the chemical composition of these particles. Future research on the ejection dynamics of INEs and tandem measurements comparing the chemical

composition of the INE bulk samples and INP aerosol samples will help determine the factors leading to INP selection.

7.3.2 Future studies on the emission of fluorescent biological aerosols in sea spray depending on wind speed and wave breaking

Chapter 3 observed the fluorescence profile of SSA produced in an isolated wave channel using natural seawater. This ocean-atmosphere system provides an accurate representation of natural SSA from a breaking wave (Deane and Stokes, 2002; Prather et al., 2013; Stokes et al., 2013), but it cannot generate SSA from high winds which are a well-known source of global SSA (Lewis and Schwartz, 2004). Future studies using a wind/wave channel and natural seawater would be able to determine any correlation between wind speed or wave height and fluorescent particle emissions in SSA. Additionally, previous measurements have shown that sea surface temperature can adjust the flux of SSA in a controlled environment (Forestieri et al., 2018). Further information regarding the influence of sea surface temperature on the production of fluorescent SSA particles would be beneficial for model simulations interested in the emission of bioaerosols in marine environments.

7.3.3 Future studies on the influence of heterogeneous reactions and atmospheric aging on fluorescent SSA

Chapter 4 investigated changes to the fluorescence signature of natural SSA following simulated atmospheric oxidation in a PAM-OFR. The PAM-OFR is a well characterized system for representing atmospheric aging, however, it can lead to the simulation of multiple heterogeneous reactions. Therefore, to better understand the influence of specific heterogeneous reactions on SSA fluorescence, future flow tube studies should be performed. These include

experiments focused on reactions with ozone, NO_x species, SOA interactions, and photo-oxidation reactions to align with previous bioaerosol studies (Pan et al., 2014; Ratnesar-Shumate et al., 2015; Santarpia et al., 2012; Kinahan et al., 2019). These future studies could utilize a rotating drum chamber to keep the bioaerosols aloft for extended periods of time (Pan et al., 2014). Lastly, future experiments on aged SSA would benefit from tandem WIBS fluorescence measurements with EEMS analysis, chemical compositional analysis, and INP measurements. Coupling to EEMS and chemical composition measurements would help elucidate the chemical transformation in SSA during atmospheric aging and better explain the variable reactivity observed in this study over the course of a phytoplankton bloom. Complimentary INP measurements would help identify correlations between fluorescent particle concentrations and INP concentrations released in SSA, as previously observed in other studies (Huffman et al., 2013; Mason et al., 2015; Wright et al., 2014). If a correlation was found, WIBS fluorescence measurements in marine environments could be used to constrain INP emissions in global climate models.

7.3.4 Measurements of the mixing state of secondary marine aerosols and small biological molecules using the cMA-ATOFMS

Chapter 6 highlights the characterization and application of the novel cMA-ATOFMS system measuring SOA generated in a controlled laboratory setting. This system, which expands the lower limit of the ATOFMS theoretically down to 7 nm, will enable the single-particle detection of many submicron aerosol populations. Significant interest is directed towards future studies focused on the mixing state of SOA produced in a marine environment and identifying the chemical composition of SSA with diameters below 100 nm. Additionally, this system can be applied to biological aerosols such as viruses, proteins, and other microbial fragments. The use of the MALDI matrix should enable the soft ionization of bioaerosols and the detection of specific

proteins and biomolecules (Stowers et al., 2000; van Wuijckhuijse et al., 2005). Future testing and optimization of this system on biological analytes could enable the online detection and chemical analysis of multiple biological species including airborne viruses, thus expanding bioaerosol identification and measurements for both health and climate implications.

7.4 Acknowledgements

Mitchell Santander is acknowledged for his assistance in editing this chapter.

7.5 References

Bates, T. S., Calhoun, J. A., and Quinn, P. K.: Variations in the methanesulfonate to sulfate molar ratio in submicrometer marine aerosol particles over the south Pacific Ocean, J. Geophys. Res. Atmos., 97, 9859–9865, https://doi.org/10.1029/92JD00411, 1992.

Benner, R., Pakulski, J. D., McCarthy, M., Hedges, J. I., and Hatcher, P. G.: Bulk chemical characteristics of dissolved organic matter in the ocean, Science (80-.)., 255, 1561–1564, https://doi.org/10.1126/science.255.5051.1561, 1992.

Burrows, S. M., Hoose, C., Pöschl, U., and Lawrence, M. G.: Ice nuclei in marine air: Biogenic particles or dust?, Atmos. Chem. Phys., 13, 245–267, https://doi.org/10.5194/acp-13-245-2013, 2013.

Charlson, R. J., Lovelock, J. E., Andreae, M. O., and Warren, S. G.: Oceanic phytoplankton, atmospheric sulphur, cloud albedo and climate, Nature, 326, 655–661, https://doi.org/10.1038/326655a0, 1987.

Creamean, J. M., Cross, J. N., Pickart, R., McRaven, L., Lin, P., Pacini, A., Hanlon, R., Schmale, D. G., Ceniceros, J., Aydell, T., Colombi, N., Bolger, E., and DeMott, P. J.: Ice Nucleating Particles Carried From Below a Phytoplankton Bloom to the Arctic Atmosphere, Geophys. Res. Lett., 46, 8572–8581, https://doi.org/10.1029/2019GL083039, 2019.

Deane, G. B. and Stokes, M. D.: Scale dependence of bubble creation mechanisms in breaking waves, Nature, 418, 839–844, https://doi.org/10.1038/nature00967, 2002.

DeMott, P. J., Hill, T. C. J., McCluskey, C. S., Prather, K. A., Collins, D. B., Sullivan, R. C., Ruppel, M. J., Mason, R. H., Irish, V. E., Lee, T., Hwang, C. Y., Rhee, T. S., Snider, J. R., McMeeking, G. R., Dhaniyala, S., Lewis, E. R., Wentzell, J. J. B., Abbatt, J., Lee, C., Sultana, C. M., Ault, A. P., Axson, J. L., Diaz Martinez, M., Venero, I., Santos-Figueroa, G., Stokes, M. D., Deane, G. B., Mayol-Bracero, O. L., Grassian, V. H., Bertram, T. H., Bertram, A. K., Moffett, B. F., and Franc, G. D.: Sea spray aerosol as a unique source of ice nucleating particles, Proc. Natl. Acad. Sci., 113, 5797–5803, https://doi.org/10.1073/pnas.1514034112, 2016.

Forestieri, S. D., Moore, K. A., Martinez Borrero, R., Wang, A., Stokes, M. D., and Cappa, C. D.: Temperature and Composition Dependence of Sea Spray Aerosol Production, Geophys. Res. Lett., 45, 7218–7225, https://doi.org/10.1029/2018GL078193, 2018.

Fukunaga, Y., Katsuragi, Y., Izumi, T., and Sakiyama, F.: Fluorescence characteristics of kynurenine and N'-formylkynurenine, their use as reporters of the environment of tryptophan 62 in hen egg-white lysozyme, J. Biochem., 92, 129–141, https://doi.org/10.1093/oxfordjournals.jbchem.a133909, 1982.

Huang, W. T. K., Ickes, L., Tegen, I., Rinaldi, M., Ceburnis, D., and Lohmann, U.: Global relevance of marine organic aerosol as ice nucleating particles, Atmos. Chem. Phys., 18, 11423–11445, https://doi.org/10.5194/acp-18-11423-2018, 2018.

Huffman, J. A., Prenni, A. J., Demott, P. J., Pöhlker, C., Mason, R. H., Robinson, N. H., Fröhlich-Nowoisky, J., Tobo, Y., Després, V. R., Garcia, E., Gochis, D. J., Harris, E., Müller-Germann, I., Ruzene, C., Schmer, B., Sinha, B., Day, D. A., Andreae, M. O., Jimenez, J. L., Gallagher, M., Kreidenweis, S. M., Bertram, A. K., and Pöschl, U.: High concentrations of biological aerosol particles and ice nuclei during and after rain, Atmos. Chem. Phys., 13, 6151–6164, https://doi.org/10.5194/acp-13-6151-2013, 2013.

Ignatenko, A. V., Tatarinov, B. A., Khovratovich, N. N., Khrapovitskii, V. P., and Cherenkevich, S. N.: Spectral-fluorescent investigation of the action of ozone on aromatic amino acids, J. Appl. Spectrosc., 37, 781–784, https://doi.org/10.1007/BF00663829, 1982.

Kawana, K., Matsumoto, K., Taketani, F., Miyakawa, T., and Kanaya, Y.: Fluorescent biological aerosol particles over the central Pacific Ocean: covariation with ocean surface biological activity indicators, Atmos. Chem. Phys., 21, 15969–15983, https://doi.org/10.5194/acp-21-15969-2021, 2021.

Kinahan, S. M., Tezak, M. S., Siegrist, C. M., Lucero, G., Servantes, B. L., Santarpia, J. L., Kalume, A., Zhang, J., Felton, M., Williamson, C. C., and Pan, Y. Le: Changes of fluorescence spectra and viability from aging aerosolized E. coli cells under various laboratory-controlled conditions in an advanced rotating drum, Aerosol Sci. Technol., 53, 1261–1276, https://doi.org/10.1080/02786826.2019.1653446, 2019.

Ladino, L. A., Raga, G. B., Alvarez, H., Rosas, I., Alvarez-Ospina, H., Andino-Enríquez, M. A., Martínez, L., Salinas, E., Miranda, J., Ramírez-Díaz, Z., Figueroa, B., Chou, C., Bertram, A. K., Quintana, E. T., Maldonado, L. A., García-Reynoso, A., Si, M., and Irish, V. E.: Ice-nucleating particles in a coastal tropical site, Atmos. Chem. Phys, 19, 6147–6165, https://doi.org/10.5194/acp-19-6147-2019, 2019.

Lewis, E. R. and Schwartz, S. E.: Sea salt aerosol production: Mechanisms, methods, measurements and models—A critical review, American Geophysical Union, Washington, D. C., 1–408 pp., https://doi.org/10.1029/152GM01, 2004.

Mason, R. H., Si, M., Li, J., Chou, C., Dickie, R., Toom-Sauntry, D., Pöhlker, C., Yakobi-Hancock, J. D., Ladino, L. A., Jones, K., Leaitch, W. R., Schiller, C. L., Abbatt, J. P. D., Huffman, J. A., and Bertram, A. K.: Ice nucleating particles at a coastal marine boundary layer site: Correlations with aerosol type and meteorological conditions, Atmos. Chem. Phys., 15, 12547–12566, https://doi.org/10.5194/acp-15-12547-2015, 2015.

Mason, R. H., Si, M., Chou, C., Irish, V. E., Dickie, R., Elizondo, P., Wong, R., Brintnell, M., Elsasser, M., Lassar, W. M., Pierce, K. M., Leaitch, W. R., Macdonald, A. M., Platt, A., Toom-Sauntry, D., Sarda-Estève, R., Schiller, C. L., Suski, K. J., Hill, T. C. J., Abbatt, J. P. D., Huffman, J. A., Demott, P. J., and Bertram, A. K.: Size-resolved measurements of ice-nucleating particles at six locations in North America and one in Europe, Atmos. Chem. Phys, 16, 1637–1651, https://doi.org/10.5194/acp-16-1637-2016, 2016.

McCluskey, C. S., Ovadnevaite, J., Rinaldi, M., Atkinson, J., Belosi, F., Ceburnis, D., Marullo, S., Hill, T. C. J., Lohmann, U., Kanji, Z. A., O'Dowd, C., Kreidenweis, S. M., and DeMott, P. J.: Marine and Terrestrial Organic Ice-Nucleating Particles in Pristine Marine to

Continentally Influenced Northeast Atlantic Air Masses, J. Geophys. Res. Atmos., 123, 6196–6212, https://doi.org/10.1029/2017JD028033, 2018a.

McCluskey, C. S., Hill, T. C. J., Humphries, R. S., Rauker, A. M., Moreau, S., Strutton, P. G., Chambers, S. D., Williams, A. G., McRobert, I., Ward, J., Keywood, M. D., Harnwell, J., Ponsonby, W., Loh, Z. M., Krummel, P. B., Protat, A., Kreidenweis, S. M., and DeMott, P. J.: Observations of Ice Nucleating Particles Over Southern Ocean Waters, Geophys. Res. Lett., 45, 11,989-11,997, https://doi.org/10.1029/2018GL079981, 2018b.

McCluskey, C. S., DeMott, P. J., Ma, P. -L., and Burrows, S. M.: Numerical Representations of Marine Ice-Nucleating Particles in Remote Marine Environments Evaluated Against Observations, Geophys. Res. Lett., 46, 7838–7847, https://doi.org/10.1029/2018GL081861, 2019.

Moallemi, A., Landwehr, S., Robinson, C., and Simó, R.: Sources, Occurrence and Characteristics of Fluorescent Biological Aerosol Particles Measured Over the Pristine Southern Ocean, J. Geophys. Res., 2021.

Murray, K. K. and Russell, D. H.: Aerosol Matrix-Assisted Laser Desorption Ionization Mass Spectrometry, J Am Soc Mass Spectrom, 5, 1–9, 1994.

Niemand, M., Möhler, O., Vogel, B., Vogel, H., Hoose, C., Connolly, P., Klein, H., Bingemer, H., Demott, P., Skrotzki, J., and Leisner, T.: A particle-surface-area-based parameterization of immersion freezing on desert dust particles, J. Atmos. Sci., 69, 3077–3092, https://doi.org/10.1175/JAS-D-11-0249.1, 2012.

Pan, Y. Le, Santarpia, J. L., Ratnesar-Shumate, S., Corson, E., Eshbaugh, J., Hill, S. C., Williamson, C. C., Coleman, M., Bare, C., and Kinahan, S.: Effects of ozone and relative humidity on fluorescence spectra of octapeptide bioaerosol particles, J. Quant. Spectrosc. Radiat. Transf., 133, 538–550, https://doi.org/10.1016/J.JQSRT.2013.09.017, 2014.

Prather, K. A., Bertram, T. H., Grassian, V. H., Deane, G. B., Stokes, M. D., DeMott, P. J., Aluwihare, L. I., Palenik, B. P., Azam, F., Seinfeld, J. H., Moffet, R. C., Molina, M. J., Cappa, C. D., Geiger, F. M., Roberts, G. C., Russell, L. M., Ault, A. P., Baltrusaitis, J., Collins, D. B., Corrigan, C. E., Cuadra-Rodriguez, L. A., Ebben, C. J., Forestieri, S. D., Guasco, T. L., Hersey, S. P., Kim, M. J., Lambert, W. F., Modini, R. L., Mui, W., Pedler, B. E., Ruppel, M. J., Ryder, O. S., Schoepp, N. G., Sullivan, R. C., and Zhao, D.: Bringing the ocean into the laboratory to probe the chemical complexity of sea spray aerosol, Proc. Natl. Acad. Sci. U. S. A., 110, 7550–7555, https://doi.org/10.1073/pnas.1300262110, 2013.

Ratnesar-Shumate, S., Pan, Y. Le, Hill, S. C., Kinahan, S., Corson, E., Eshbaugh, J., and Santarpia, J. L.: Fluorescence spectra and biological activity of aerosolized bacillus spores and MS2 bacteriophage exposed to ozone at different relative humidities in a rotating drum, J. Quant. Spectrosc. Radiat. Transf., 153, 13–28, https://doi.org/10.1016/j.jqsrt.2014.10.003, 2015.

Santarpia, J. L., Pan, Y.-L., Hill, S. C., Baker, N., Cottrell, B., McKee, L., Ratnesar-Shumate, S., and Pinnick, R. G.: Changes in fluorescence spectra of bioaerosols exposed to ozone in a

laboratory reaction chamber to simulate atmospheric aging, Opt. Express, 20, 29867, https://doi.org/10.1364/oe.20.029867, 2012.

Si, M., Irish, V. E., Mason, R. H., Vergara-Temprado, J., Hanna, S., Ladino, L. A., Yakobi-Hancock, J. D., Schiller, C. L., Wentzell, J. J. B., Abbatt, J. P. D., Carslaw, K. S., Murray, B. J., Bertram, A. K., and Bertram, A.: Ice-nucleating efficiency of aerosol particles and possible sources at three coastal marine sites, Atmos. Chem. Phys., 18, 15669–15685, https://doi.org/10.5194/acp-2018-81, 2018.

Smith, S. J., Pitchera, H., and Wigley, T. M. L.: Global and regional anthropogenic sulfur dioxide emissions, Glob. Planet. Change, 29, 99–119, https://doi.org/10.1016/S0921-8181(00)00057-6, 2001.

Stokes, M. D., Deane, G. B., Prather, K., Bertram, T. H., Ruppel, M. J., Ryder, O. S., Brady, J. M., and Zhao, D.: A Marine Aerosol Reference Tank system as a breaking wave analogue for the production of foam and sea-spray aerosols, Atmos. Meas. Tech., 6, 1085–1094, https://doi.org/10.5194/amt-6-1085-2013, 2013.

Stowers, M. A., Wuijckhuijse, A. L. Van, Marijnissen, J. C. M., Scarlett, B., and Baar, B. L. M. Van: Application of matrix-assisted laser desorption / ionization to on-line aerosol time-of-flight mass spectrometry, Rapid Commun. Mass Spectrom., 14, 829–833, 2000.

Vergara-Temprado, J., Murray, B. J., Wilson, T. W., O'Sullivan, D., Browse, J., Pringle, K. J., Ardon-Dryer, K., Bertram, A. K., Burrows, S. M., Ceburnis, D., Demott, P. J., Mason, R. H., O'Dowd, C. D., Rinaldi, M., and Carslaw, K. S.: Contribution of feldspar and marine organic aerosols to global ice nucleating particle concentrations, Atmos. Chem. Phys., 17, 3637–3658, https://doi.org/10.5194/acp-17-3637-2017, 2017.

Wei, K., Zou, Z., Zheng, Y., Li, J., Shen, F., Wu, C. yu, Wu, Y., Hu, M., and Yao, M.: Ambient bioaerosol particle dynamics observed during haze and sunny days in Beijing, Sci. Total Environ., 550, 751–759, https://doi.org/10.1016/J.SCITOTENV.2016.01.137, 2016.

Wilson, T. W., Ladino, L. A., Alpert, P. A., Breckels, M. N., Brooks, I. M., Browse, J., Burrows, S. M., Carslaw, K. S., Huffman, J. A., Judd, C., Kilthau, W. P., Mason, R. H., McFiggans, G., Miller, L. A., Najera, J. J., Polishchuk, E., Rae, S., Schiller, C. L., Si, M., Temprado, J. V., Whale, T. F., Wong, J. P. S., Wurl, O., Yakobi-Hancock, J. D., Abbatt, J. P. D., Aller, J. Y., Bertram, A. K., Knopf, D. A., and Murray, B. J.: A marine biogenic source of atmospheric ice-nucleating particles, Nature, 525, 234–238, https://doi.org/10.1038/nature14986, 2015.

Wright, T. P., Hader, J. D., McMeeking, G. R., and Petters, M. D.: High Relative Humidity as a Trigger for Widespread Release of Ice Nuclei, Aerosol Sci. Technol., 48, i–v, https://doi.org/10.1080/02786826.2014.968244, 2014.

van Wuijckhuijse, A. L., Stowers, M. A., Kleefsman, W. A., Van Baar, B. L. M., Kientz, C. E., and Marijnissen, J. C. M.: Matrix-assisted laser desorption/ionisation aerosol time-of-flight mass spectrometry for the analysis of bioaerosols: Development of a fast detector for airborne biological pathogens, J. Aerosol Sci., 36, 677–687,

https://doi.org/10.1016/j.jaerosci.2004.11.003, 2005.

Yue, S., Ren, H., Fan, S., Wei, L., Zhao, J., Bao, M., Hou, S., Zhan, J., Zhao, W., Ren, L., Kang, M., Li, L., Zhang, Y., Sun, Y., Wang, Z., and Fu, P.: High Abundance of Fluorescent Biological Aerosol Particles in Winter in Beijing, China, ACS Earth Space Chem., 1, 493-502, https://doi.org/10.1021/acsearthspacechem.7b00062, 2017.